Volume 9, Part A-2, No. 3, March 1971

Journal of Polymer Science

Part A-2: Polymer Physics

Contents

D. V. Rees and D. C. Bassett: Crystallization of Polyethylene at Elevated Pressures 385

S. Nomura, N. Nakamura, and H. Kawai: Graphical Representation of the State of Orientation of Polymer Systems 407

J. A. Cote and N. Shida: Long-Chain Branching in Low-Density Polyethylene 421

H. Ochiai, H. Shindo, and H. Yamamura: Side-Chain Relaxation in Stereoregular Poly(isobutyl Methacrylate) 431

Y. Udagawa and A. Keller: Liquid-Induced Reversible Long-Spacing Changes in Polyethylene Single Crystals and Their Implications for the Fold-Surface Problem 437

R. E. Robertson: Occurrence of Rippling During the Deformation of Oriented Polyethylene 453

R. C. Penwell and R. S. Porter: Effect of Pressure in Capillary Flow of Polystyrene 463

P. Vasudevan and M. Santappa: Fox-Flory Constant *K* Obtained by Viscometric Measurements for Poly(ethyl methacrylate) and Poly(methyl methacrylate) Systems 483

P. J. Phillips, G. L. Wilkes, B. W. Delf, and R. S. Stein: Dielectric and Rheo-optical Properties of Some Ethylene-Carbon Monoxide Copolymers 499

R. S. Stein and T. Hashimoto: Scattering of Light by Deformed Disordered Spherulites 517

A. M. Rijke, J. T. Hunter, and R. D. Flanagan: Morphology of Polyethylene Crystallized by Solution Stirring 531

L. A. Vermeulen, H. J. Wintle, and D. A. Nicodemo: Ultraviolet Photoelectric Effects in Polyethylene 543

B. Crist and A. Peterlin: Segmental Motion in Polyoxymethylene 557

G. McGibbon, A. J. Rostron, and A. Sharples: Photocurrents in Simple Polymer Systems. II 569

Published by INTERSCIENCE PUBLISHERS a division of John Wiley & Sons, Inc.

Journal of Polymer Science **Part A-2: Polymer Physics**

The Journal of Polymer Science is published in four sections as follows: Part A-1, Polymer Chemistry, monthly; Part A-2, Polymer Physics, monthly; Part B, Polymer Letters, monthly; Part C, Polymer Symposia, irregular.

Published monthly by Interscience Publishers, a Division of John Wiley & Sons, Inc., covering one volume annually. Publication Office at 20th and Northampton Sts., Easton, Pa. 18042. Executive, Editorial, and Circulation Offices at 605 Third Avenue, New York, N.Y. 10016. Second-class postage paid at Easton, Pa. Subscription price, $325.00 per volume (including Parts A-1, B, and C). Foreign postage $15.00 per volume (including Parts A-1, B, and C).

JOURNAL OF POLYMER SCIENCE: PART A-2 VOL. 9, 385–406 (1971)

Crystallization of Polyethylene at Elevated Pressures

D. V. REES and D. C. BASSETT,
J. J. Thomson Physical Laboratory,
University of Reading, Reading, United Kingdom

Synopsis

The crystallization from the melt of three sharp polyethylene fractions has been studied at 5 kbar. It has been shown that the thickness of so-called extended-chain lamellae is a function of time, temperature, and molecular weight. There is by no means just the fully extended molecular configuration present. Crystallization is qualitatively similar to that of chain-folded crystals at 1 bar, giving an optimum lamellar thickness which increases with time and decreasing supercooling. Fractional crystallization is widespread and is a major cause of disparate lamellar thickness. Isothermal thickening of lamellae during crystallization has been established directly. Morphological detail suggests further that layers can increase their thickness tenfold over their initial size.

INTRODUCTION

Interest in polyethylene crystallized from the melt under pressure centers upon the phenomenon of "extended-chain" crystallization following the work of Geil *et al.*[1] in which crystals as thick as 3 μ in the chain direction were identified. This is in marked contrast to the familiar chain-folded growth, where a dimension of ca. 200 Å is typical. Moreover, many of the properties of crystalline polymers are sensitive to the layer thickness because of the peculiar character of fold surfaces. When their proportion is reduced, as by crystallization under pressure, then melting point depression decreases, density increases, and chemical reactivity is reduced. All these effects and more have confirmed the much greater crystallite thicknesses of extended-chain crystals, but many of the most interesting questions regarding the phenomenon still require clarification.

Our work in this area began with annealing experiments under pressure, i.e., in which samples were raised to and held at a maximum temperature T_a. It was discovered that crystals could be formed whose appearance and high melting point corresponded to extended-chain samples.[2,3] Moreover, molecular orientation could be maintained throughout the process to lengths of several thousand Angstroms, much greater than is possible in similar experiments at 1 bar. The maintenance of molecular orientation is significant in that it is characteristically associated with the increase of lamellar thickness by annealing at atmospheric pressure.[4] A molecular description of this process is still obscure but it is generally recognized, on good grounds, as being a distinctive one and is known variously as lamellar, crystal, isothermal, or solid-state thickening. The relationship of lamellar thickening to melt crystallization is particularly interesting. The x-ray measurements of developing lamellar thickness in both show a logarithmic increase with time,[5,6] a phenomenon which is also, confusingly, known as isothermal thickening.

In the formation of extended-chain crystals, two main hypothetical explanations are suggested. One is that the large crystal thickness is formed on an extended-chain nucleus; the other, proposed most notably by Peterlin,[7] is that enhanced lamellar thickening is responsible. The constancy of molecular orientation to such high crystal thicknesses strongly suggests the latter,[2,3] a conclusion also reached by Wunderlich on several grounds.[8] In attempting to clarify the situation we found it imperative to examine the basic phenomena of crystallization from the melt at elevated pressures. In this paper, controlled crystallization of fractionated polyethylenes is reported, giving data on crystal thickness as functions of molecular length, crystallization temperature, and time.

EXPERIMENTAL

All high-pressure experiments have been carried out in a tetrahedral four-anvil press with pressure transmitted to a stainless steel capsule through a pyrophillite tetrahedron of 1 in. edge (Fig. 1) Specimens wrapped in platinum foil to aid identification and help achieve uniformity of temperature were immersed in water to provide an inert hydrostatic environment. The can acted as its own heater and the temperature of its contents was measured and controlled to better than ±1°C by a chromel–alumel thermocouple, piercing one of the Teflon end caps, in conjunction with an AEI TC3 control unit. This figure was also the maximum nonuniformity of temperature between the can wall and interior revealed by differential measurements.

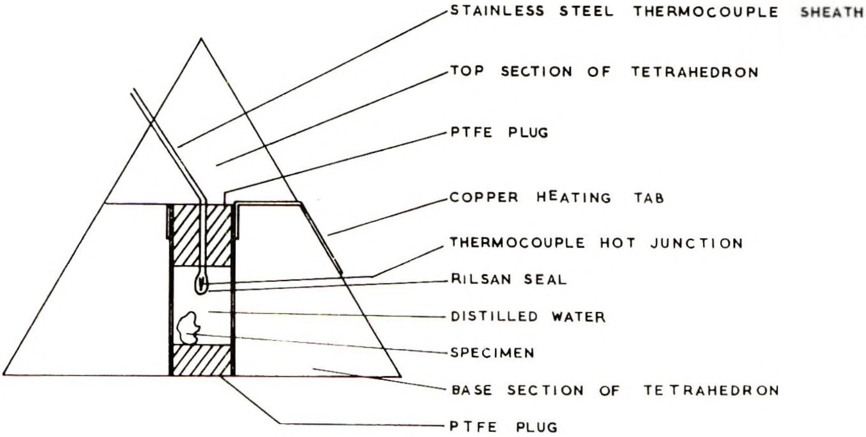

Fig. 1. High-pressure sample cell (schematic).

A special feature of the apparatus is the capsule's tiny thermal capacity which permits extremely rapid quenching. Switching off the heating current of some 200 A causes the temperature to plunge below 50°C within 15 sec. With this facility it is possible to determine the melting point of extended-chain samples experimentally as that temperature of annealing which first gives no high-melting material on quenching. Experimental values obtained in this way have been used in calculating supercooling. The major uncertainty in supercooling comes, however, not from this factor but from frictional effects and is probably 2–3°C. All experiments were conducted with the anvils at a constant load, maintained to 2%, but pressure is imperfectly transmitted through the pyrophillite and can to the sample. Values of ca. 0.5 kbar are not untypical of the pressure uncertainty from these causes in similar systems. Nevertheless, by careful attention to detail, such as machining all tetrahedra from the same block of mineral and especially by working with small samples occupying only a few per cent of the space available[3] (so that volume changes on fusion are negligible), it has been possible to achieve rather better reproducibility of pressure, and hence melting point, to the 2–3°C quoted.

Values of pressure in apparatus of this type have to come from calibration against known transitions. Initially[2] this information was not available for the particular arrangement used and pressure was estimated from values of melting point variation obtained by earlier workers.[9,10] In retrospect these gave values which were too low. Subsequently calibration has been achieved against phase transitions of bismuth at temperatures similar to those of the actual experiments. Data obtained in two ways, by changes of electrical resistance in the Bi I–II and II–III transitions and DTA measurements of the melting of Bi(I) fitted well together. From these, the pressure used in all experiments reported here was 4.9 ± 0.25 kbar. For an extended-chain melting point of 243°C, this value agrees with the direct measurements of others. Nevertheless, the melting of polyethylene itself is a still more sensitive function of pressure than these methods provide and would be a better means of assessing pressure were absolute values available.

Measurements of Crystal Thickness

The aim in crystallization experiments was to investigate any variation in lamellar thickness with time, temperature, and molecular weight and also to establish whether the so-called extended-chain crystals were truly that. For these purposes it was essential to work with fractionated material, and accordingly three column-fractionated samples of narrow distribution, designated A, B, and C, have been used almost exclusively. Their characteristics are shown in Table I. Wherever possible, two or more of these have been treated in the same capsule for optimum comparability. As no fraction is completely sharp, assessments of molecular extension have to come from comparisons of polydispersity, measured in this instance by gel-permeation chromatography (GPC), with distributions of crystal thicknesses taken here from fracture surfaces.

TABLE I

Sample	M_n	M_w	M_w/M_n	L_n, Å
A	21,600	24,700	1.14	1,960
B	50,100	57,100	1.14	4,550
C	280,000	518,000	1.85	25,400

Measurements on fracture surfaces can justifiably be criticized as being, in some degree, unrepresentative, because fracture occurs at special places in a sample. We do find that the larger crystal thicknesses, which would indeed be especially easy to fracture, tend to be revealed to the virtual exclusion of low-melting crystals which calorimetry shows also to be present. The method does, nonetheless, give close agreement with expectation for extended-chain crystals, and the differences we observe are in any case usually gross and insensitive, even to moderate bias in the data. We are confident, therefore, that our measurements are sufficiently reliable for present purposes.

Crystal thickness distributions have been computed from measurements with an Oscillograph Analyzer and Reader (OSCAR). Usually two, approximately orthogonal lines were drawn on prints of fracture surfaces. The thickness of all lamellae cut by the lines was taken, at their point of intersection, along the striation direction (i.e., molecular c axis) from the positions of the two relevant surfaces and punched out by OSCAR on tape ready for computation. The absolute values of length were checked by calibration of the electron microscope against a standard grating. Ultimately data were plotted as normalized histograms of frequency against chain length in 200 Å intervals, with means and standard deviations also recorded. This gives a number-average distribution, of mean $\bar{L}_n$, because each lamella is counted once.

With data of this kind, it is particularly necessary to establish their statistical significance. This has been checked with Student's t test on the hypothesis that the means of different distributions represent different sampling of the same population. The probability of this being so was evaluated from standard tables by using the statistic t defined as

$$t = \frac{(L_1 - L_2)\,(N_1N_2)^{1/2}}{(N_1\sigma_1^2 + N_2\sigma_2^2)^{1/2}}$$

where L_1,L_2 are means, σ_1^2, σ_2^2, variances, and N_1,N_2, the number of measurements in the two respective distributions. It has been gratifying to find throughout that all differences to be reported were significant at the 2.5% probability level or better. Conversely, differences between different areas of the same sample or different subsets of the same data, e.g., along one line only, were never significant, with a probability of 70% or (usually) better.

As a matter of routine, melting point and density of samples have also been determined. The former has been taken as the peak of the melting endotherm given by a Perkin-Elmer DSC1B instrument and is reproducible to within 1°C. For the latter, a gradient column with a mixture of isopropanol, diethylene glycol, and water gave acceptable measurements.

RESULTS

It is convenient to begin with sample B for which $\bar{L}_n$ = 4550 Å. A typical crystallization cycle for this and the other samples consisted of imposing pressure, heating to 270°C (27°C above T_m^0), cooling to the crystallization temperature T_c in about 45 sec., then holding for the stated times prior to quenching to ambient temperature and a final release of pressure. Figure 2 shows the consequence of varying crystallization temperatures on the distribution of observed lameller thicknesses. It was possible initially to quench from all these crystallization temperatures without forming high-melting material, giving reason to believe that the values of T_c quoted are those at which crystallization actually occurred. Significant increases in thickness occur above 210°C (33° of supercooling) at which temperature, with L_n = 2104 Å, an average molecule has one fold. Considerably more folding results from quenching, giving a low melting point of ca. 130°C, but crystallization then occurs so rapidly as not to be controllable. At 218 and 227°C all the sample crystallizes in the high-melting form. At 229°C, crystallization is only 70% complete after 30 min; and a second, lower, melting peak appears whose proportion is reduced at longer times. Figure 3 illustrates the point and shows, in particular, that higher thicknesses appear later. At 231°C (Fig. 4*b,c*) complete molecular extension is approached, especially for greater times, in a similar way to Figure 3. The consequences of more prolonged crystallization have still to be investigated in detail, but initial experiments cooling from the melting point at rates as low as 1.5°C/hr also confirm the trend shown in Figure 3. Greater thicknesses appear with increasing times of crystallization, i.e., slower cooling rates. For sample B, therefore, the observed mean thickness increases with crystallization time and temperature, qualitatively paralleling behavior at 1 bar.

Similar experiments have been carried out on the other two fractions. Sample A shows little change in distribution, which in the temperature range considered is close to the molecular length. There is, however, a small but highly significant increase on raising crystallization temperature from 227 to 231°C (Figs. 4*d*, 5). At the latter temperature the sample is very close to full molecular extension. Any time dependence is slight, the only evidence for it being perhaps an increased tail at 231°C for 40 min over 20 min crystallization, but there is no significant shift of the mean.

Detailed assessment of molecular extension is discussed in the following section, but its relative degree is qualitatively evident in the character of fracture obtained at liquid nitrogen temperature. For A samples, brittle fracture is the rule even at ambient temperatures while in B samples partial ductility is generally shown by pulled threads, especially for specimens crystallized at lower temperatures i.e. with more folding. When C samples

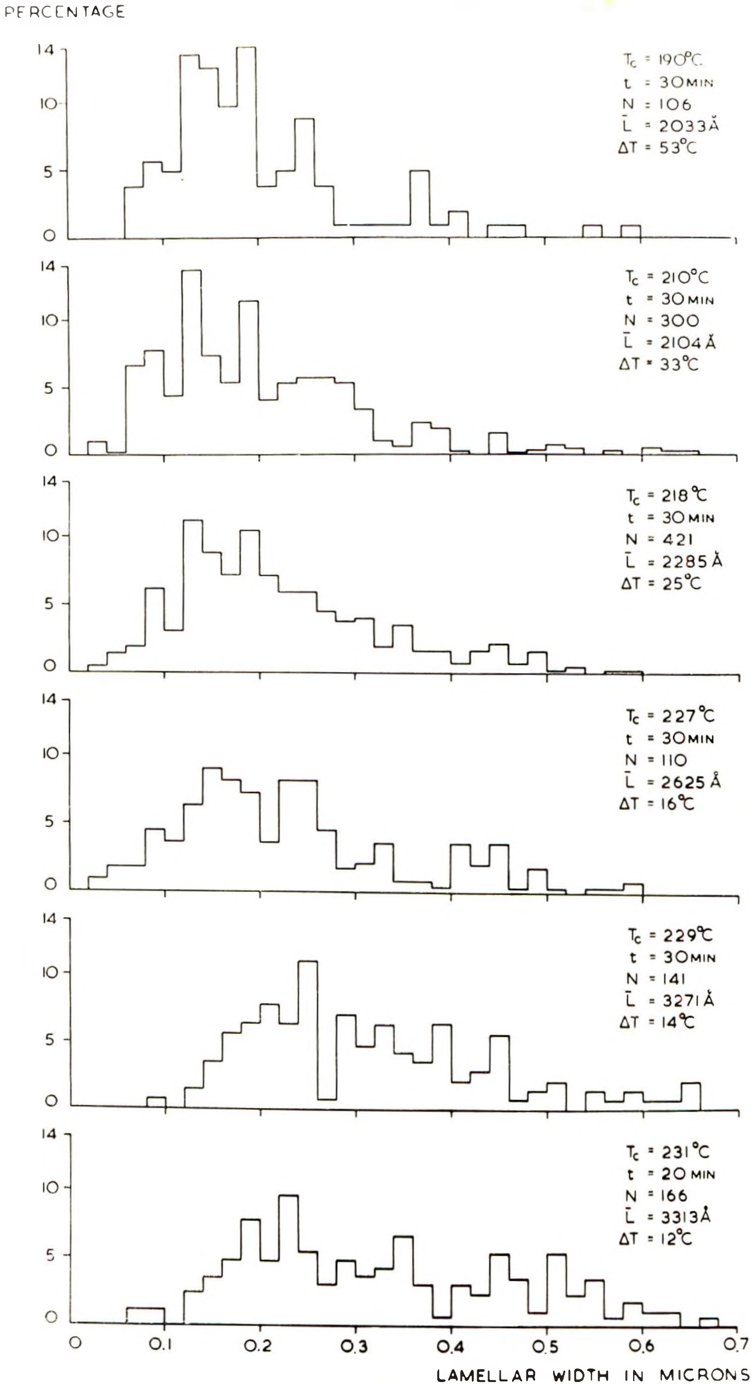

Fig. 2. Histograms of molecular extension against crystallization temperature for fraction B.

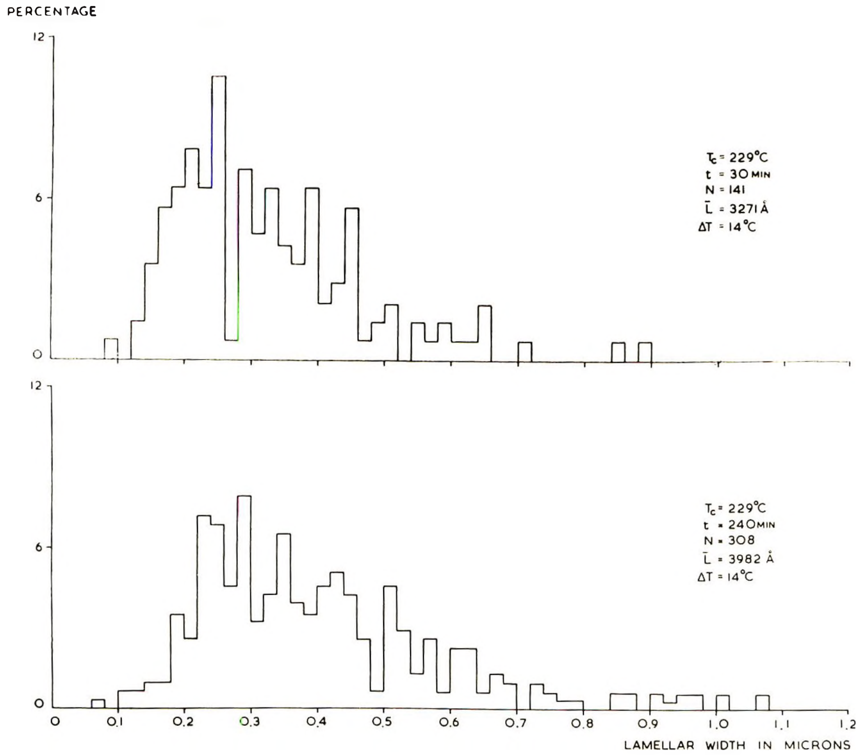

Fig. 3. Histograms showing the variation of molecular extension with time for fraction B crystallized at 229°C.

are examined, so ductile is the fracture that measurements of crystal thickness have not generally been possible. There is no doubt, however, that lamellar thicknesses are not commensurate with molecular lengths in C ($\bar{L}_n = 2.5\ \mu$) but rather are comparable with, or a little thicker than, those observed in B under the same conditions. Fraction C crystallized at 210°C for 30 min had an atmospheric melting point of 140°C, whereas identically treated B gave 139°C. In a few clearer areas of C (which we associate with internal flaws persisting, because of high melt viscosity, after attempted consolidation of the initially powdered sample by melting) the snaking lamellar morphology of Figure 6 predominates. These lamellae are thinner than in B, no more than 2000 Å thick and only microns wide. There are also a few isolated thick lamellae, which appear in greater numbers at 218°C (Fig. 7). At this temperature, B and C samples fully crystallized after 30 min gave melting points of 141 and 145°C, respectively. The thickest lamellae seen measured 0.9 μ in B and 1.1μ in C. (Somewhat similar lamellae are also evident in Figure 8 for whole Marlex 6002 polymer crystallized at 232°C for 30 min.) These lamellae are particularly noteworthy as representing the closest approach so far to isolated extended-chain crystals. Notice that they taper off towards their extremities down to below 1000 Å in cases (Fig. 7) and also their geometry when two lamellae touch (Figs. 7 and 8).

(*a*)

(*b*)

Fig. 4 (*continued*)

(*c*)

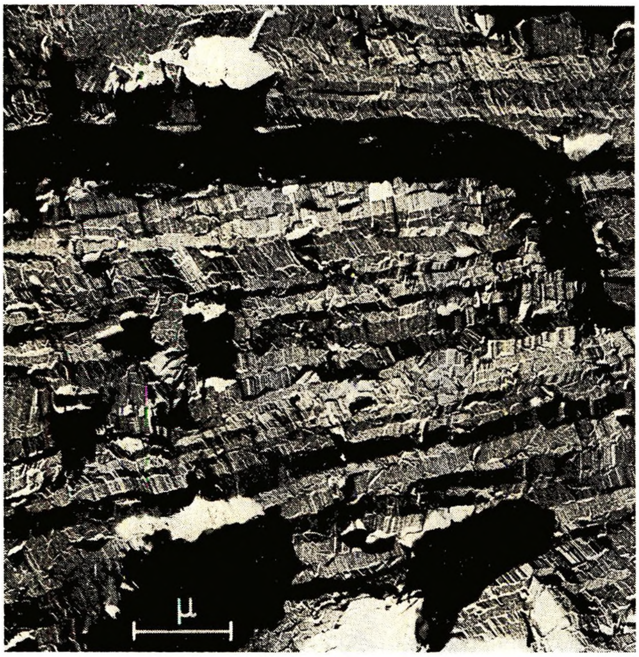

(*d*)

Fig. 4. Extended-chain morphology of fractured surfaces: (*a*) fraction B crystallized at 190°C for 30 min; (*b*) crystallized at 231°C for 20 min and (*c*) for 40 min; (*d*) fraction A after crystallization for 20 min at 231°C.

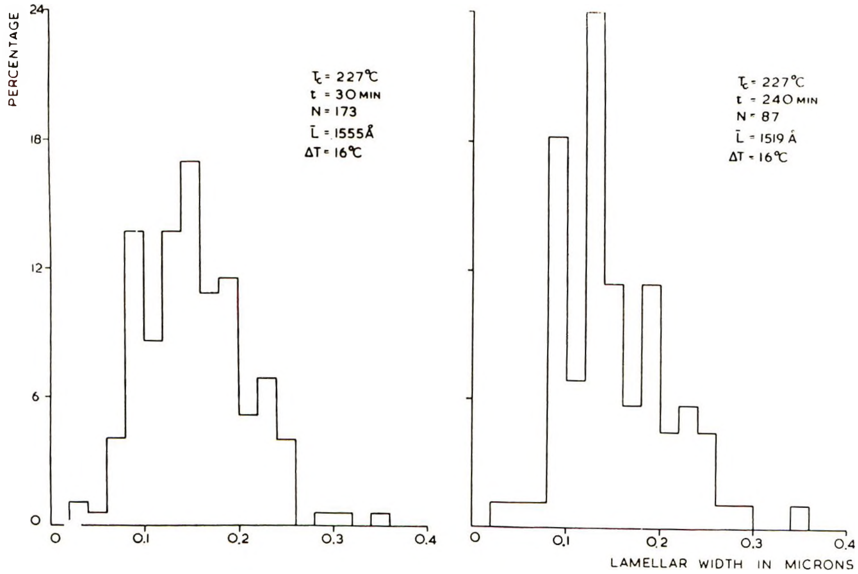

Fig. 5. Histograms of crystal thickness in fraction A.

Fig. 6. Snaking lamellae in fraction C crystallized at 210°C for 30 min.

Fig. 7. Thick lamellae with tapered ends in fraction C crystallized at 218°C for 30 min.

Fig. 8. Framework of thick lamellae in Marlex 6002 homopolymer crystallized at 232°C for 30 min.

Assessment of Molecular Extension

Although the term extended-chain has long been used to describe lamellae grown under pressure, the variability of spacing revealed with altered conditions shows that full molecular extension is not the general rule. It is of interest, though, to determine whether this state is reached in particular circumstances. For this purpose comparison has been made between the highest measured distributions for fractions A and B (crystallization at 231°C for 40 min in both cases) and their intrinsic polydispersities. The latter were constructed in histogram form from the integral molecular weight distributions derived from GPC measurements. There are two matters affecting a straightforward test, namely to what extent a fracture surface is representative of a sample, and secondly, the orientation of measured lengths to the viewing direction.

If it is assumed that fracture surfaces are representative, then the question of orientation can best be dealt with by stereoscopic measurement. A useful alternative is the construction of apparent distributions.

A length L which lies at an angle $(\pi/2) - \theta$ to the viewing direction will be measured as $l = L\cos\theta$. Let the probability of θ lying in $(\theta,\theta + d\theta)$ be $q(\theta)d\theta$ and correspondingly of l lying in $(l,l - dl)$ be $p(l)dl$. Then

$$\int_0^\theta q(\theta)d\theta = \int_L^l p(l)dl$$

and

$$\int_\theta^{\theta+d\theta} q(\theta)d\theta = \int_l^{l-dl} p(l)dl \tag{1}$$

whence

$$p(l) = -q(\theta)\, d\theta/dl = q(\theta)/(L\sin\theta) \tag{2}$$

Thus the distribution of any L among l can be constructed for a known angular probability. Note that although $p(l)$ is infinite at $\theta = 0$, the identity (1) ensures that the chance of L appearing in any range of lower lengths is finite. If L is randomly oriented in space then $q(\theta) = \cos\theta$ because $\cos\theta\, d\theta$ is the fractional surface area of a sphere in the angular interval $(\theta,0 + d\theta)$. The fracture process will tend to limit θ to lower values, making it necessary to truncate the angular range accordingly.

For present purposes a still simpler procedure has been adopted, that is the representation of each L as the average value, $\bar{L}$, it would have in the truncated angular range where

$$\bar{L} = \int_L^l lp(l)dl \Big/ \int_L^l p(l)dl$$

$$= L\int_0^{\theta_{\max}} \cos\theta\, q(\theta)d\theta \Big/ \int_0^{\theta_{\max}} q(\theta)d\theta$$

Putting $q(\theta) = \cos\theta$ gives

$$\frac{\bar{L}}{L} = \frac{2\theta_{\max} + \sin 2\theta_{\max}}{4 \sin (\theta_{\max})}$$

Taking $\theta_{\max}$ as $\pi/6$, $\pi/4$, and $\pi/2$, gives $\bar{L}/L = 0.961$, 0.909, and $\pi/4$ respectively.

Although the distributions so constructed must inevitably terminate at low values of l, nevertheless one can be confident that if a measured distribution falls below that constructed without angular truncation (i.e. $\theta_{\max} = \pi/2$) then full molecular extension has not been attained. If the reverse is true, then use must be made of a truncated distribution. Taking $\theta_{\max} = \pi/6$, however, only shifts the intrinsic distribution to lower lengths by 4%, which we ignore. On this basis Figure 9 shows the highest B distribution lying between the intrinsic and $\theta_{\max} = \pi/2$ distributions. We conclude that full molecular extension is near but has not quite been reached. In Figure 10, however, the measured distribution straddles the intrinsic one. Full extension must be very close, if indeed it has not already been reached. For a rigorous conclusion one cannot escape a more detailed comparison. We have not pursued this at present because two other points need quantifying.

The first is that because of fractional crystallization it is likely that a random plane through a sample would not reveal a representative distribu-

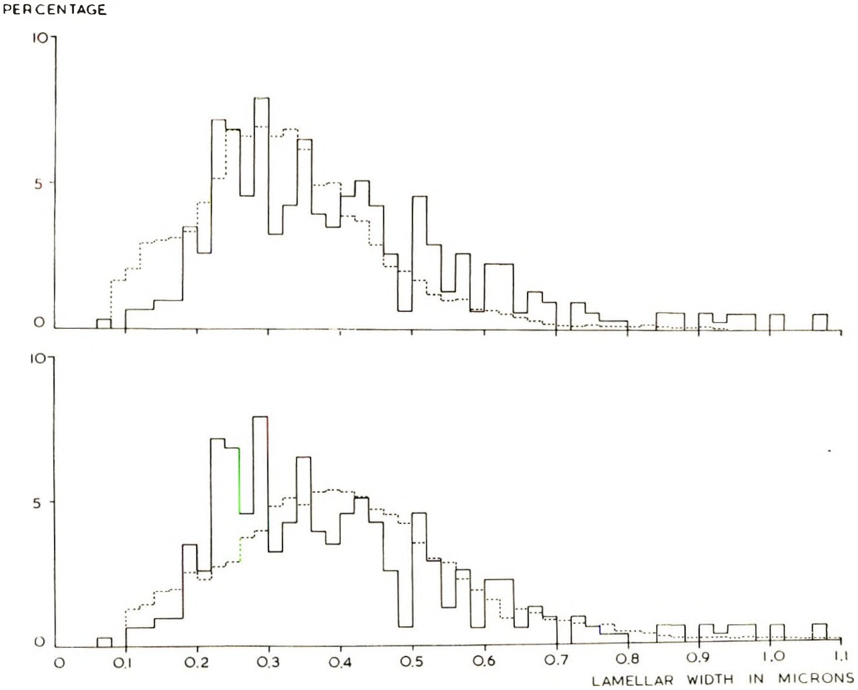

Fig. 9. Histograms of length distributions in fraction B: (——) measured after 40 min crystallization at 231°C; (– –) predicted distributions, upper with full angular dependence, lower without.

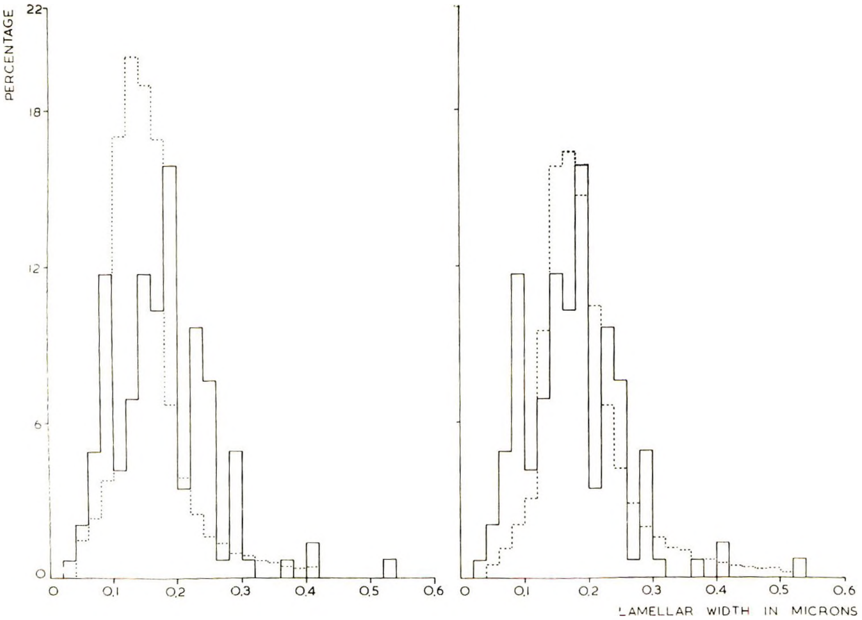

Fig. 10. Histograms of length distributions in fraction A: (——) measured after 40 min crystallization at 231°C; (– –) predicted distributions, with full angular dependence (left) and without (right).

tion of lamellar thicknesses. Fractional crystallization certainly occurs because of the wide disparity in thicknesses between different lamellae observed near full molecular extension. While there is also variability in the thickness of an individual lamellae, this lies, in our experience, in a much smaller range. Now a representative sampling of lamellar thicknesses would be revealed on a random surface were, for example, each molecular species distributed randomly through a specimen. When this is not so, there will be bias. Consider a case in which, as a consequence of fractional crystallization, each molecular species forms a disk of thickness corresponding to the molecular length L. Then the area of the disc must be proportional to $n(L)$, the number fraction of that species. For discs crystallized as a parallel array, as is frequently seen (eg., Fig. 4*d*), then the chance of any one intersecting an arbitrary surface normal to the discs will depend not on the area of the disc but on its diameter and thereby will depend upon $[n(L)]^{1/2}$. For sharp fractions such as ours, use of a normalized $[n(L)]^{1/2}$ instead of the $n(L)$ distribution has only a minor effect, especially by comparison with the effect of viewing orientation. With poorer fractions, increasing skewness towards lower molecular weights would be progressively introduced.

The second point is that the site of fracture is influenced by the degree of molecular extension as has been mentioned previously. One expects that fracture tends to occur where there is maximum extension. It follows that any inhomogeneity in a sample caused eg., by spread of molecular weight would influence which lamellae are exposed on a fracture surface. This effect will, however, diminish as all molecules reach full extension and, indeed, the agreement between observed and expected distributions in Figure 10 is evidence that this is so.

DISCUSSION

Temperature Dependence

The variability of crystal thickness revealed among what are loosely called extended-chain crystals is perhaps the most important feature of this work. It has been demonstrated that there is by no means just the one unique molecular extension but rather a whole range increasing with crystallization temperature, time and, where appropriate, molecular weight.

The three fractions used fall conveniently, at 5 kbar, into the three categories $L < l_c$, $L \approx l_c$, and $L > l_c$ where L is the molecular length and l_c the somewhat loosely defined crystal thickness given by an infinite molecule. Crystallization of the three will now be discussed in sequence.

Molecular extension in fraction A varies little but is always lower than that of B under identical conditions. One can be confident, therefore, that its molecular length is always below l_c. It is notable, therefore, that the crystals formed are not automatically of fully extended-chains, but incorporate some folding. The increase of some 250 Å in $\bar{L}_n$ in raising the crystallization temperature from 227 (or 229) to 231°C (Fig. 5) must mean that at least at 227°C (and 229°C) there was some folding. (Alternatives to this deduction such as a more fringed lamellar surface or fractional rejection of the shortest molecules at 231°C are ruled out respectively by higher density and a greater proportion of high-melting polymer at 231°C.)

The influence of lamellar thickening in this polymer is small, unlike that of B in similar circumstances, there being no significant change with time at 227°C where increased thickness can still be effected by raising the crystallization temperature is the major factor determining molecular extension in this fraction.

Fraction B is still brittle enough to reveal much morphological detail and gives the most documented behavior. With $L \approx l_c$, crystallization is analogous to that of oligomers at 1 bar. By and large, this is a little investigated region, and the factors affecting fold period are not well explored, although in one or two special cases[11,12] study has revealed quite complex situations. Here the temperature dependence of lamellar thickness (Fig. 11) has the upward curving shape typical of polymer crystallization in more usual circumstances. Moreover, work still in progress shows that this similarity may be more than qualitative, with crystallization of low molecular weight polyethylene at atmospheric pressure and fraction B at 5 kbar fitting the same reduced curve of $\bar{L}_n/L$ against $1/\Delta T$. This work will be described in detail in a subsequent publication, but at present it appears that although kinetic theories of chain folding cannot necessarily be

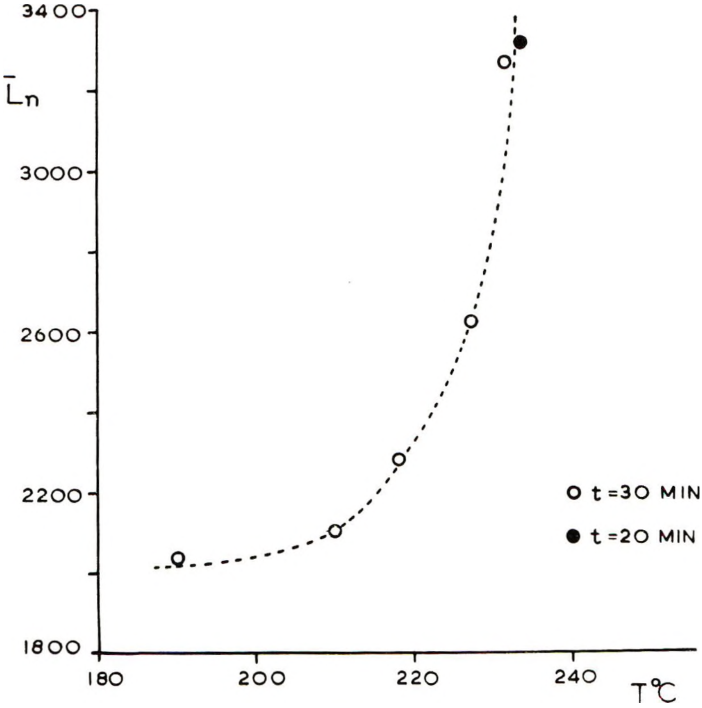

Fig. 11. Variation of mean molecular extension with crystallization temperature for fraction B.

expected to apply where chain ends may affect growth sequences, their general prediction[13] that

$$l_c = 2\sigma_e/\Delta S_f \Delta T + \delta l$$

where σ_e is the end surface free energy, ΔS_f the entropy of fusion per unit volume and ΔT the supercooling, does nevertheless fit data for oligomeric crystallization. This area of research merits, and is receiving, further investigation.

Time Dependence

Sample B shows pronounced time dependence of crystal lengths. At 229°C, Figure 3 shows $\bar{L}_n$ = 3271 Å after 30 min, when 70% of the sample had crystallized, and $\bar{L}_n$ = 3982 Å for 100% crystallized after 240 min. It will be argued that this is a fair indication of the extent of isothermal thickening, although there is a complication to be considered, namely that the 30% of material crystallizing between the two times may be fractionated. However, even on the worst possible (and unlikely) assumption, that the high tail of the 4-hr distribution is due to the precipitation of higher-molecular weight-rich polymer after the first 30 min, there is still irreducible evidence for isothermal thickening. We may find this by examining a differen-

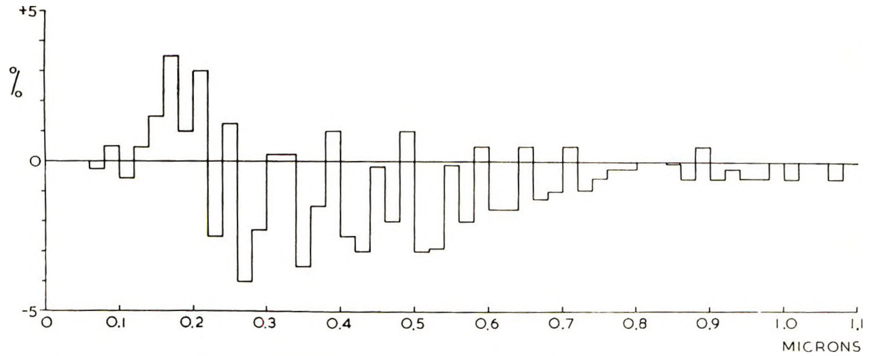

Fig. 12. Histogram of the difference between length distributions in B after 30 min and 4 hr crystallization at 229°C shown in Fig. 3. The earlier distribution is given 70% weight for all lengths.

tial distribution between the two times and looking especially at the lower end. To make the test as severe as possible, it must be assumed that the 30% of material still molten after 30 min contained none of the shortest molecules. Accordingly, the frequencies in Figure 3*a* at the low end refer only to 70% of the sample and must be multiplied by 0.7 to put them on an absolute basis. This done, the difference between the (fully scaled) 30-min and the 4-hr distributions is shown in Figure 12. There is an unmistakable initial positive region signifying lamellae which have thickened followed by a negative region (necessarily too large because of the scaling) corresponding to later-formed thicknesses. It follows that as well as fractional crystallization, isothermal thickening does occur during the formation of extended-chain lamellae by melt crystallization at 5 kbar. Furthermore, the true extent of thickening is almost certainly badly underestimated by Figure 12, because there is no evidence that longer molecules in the fraction do crystallize later under these conditions. On the contrary, one often sees, at in Figure 13, a network of lamellae ca. 1 μ thick, i.e., of molecules of at least this length, which must have formed first, filled in by thinner layers. It may be concluded with some confidence, therefore, that if fractional crystallization is indeed affecting the time dependence, it is by the shorter molecules crystallizing later, so that, if anything, the straightforward comparison of Figure 3 understates the case.

If Figure 3 is used to estimate the overall rate of thickening, the value of $d\bar{L}/d \log t$, t being in minutes, is approximately 300 Å, a figure several times more than is measured at 1 bar.[6,14] One may conclude, therefore, that there is substantial thickening of lamellae during crystalliztion, even at thicknesses of a few thousand Angstroms.

Effect of Pressure on Chain Extension

Consider now the implications of these results for the basic question of why high pressure increases chain extension so markedly. Firstly, there is no evidence whatsoever here for a single, unique, fully extended molecular configuration. There is rather a spectrum of chain extensions varying with temperature and time as do the thicknesses of lamellae formed at 1 bar. "Extended-chain" crystallization is thus to be thought of as an extension and modification of familiar chain-folded crystallization rather than as a rival process favored at low supercooling. Secondly, one particular hypothesis for the effect of pressure may be discounted. Because for chain-folded crystallization the curve of crystal thickness increases very rapidly with declining supercoooling, it might have been argued that high chain extension was a consequence of growth at high pressure occurring at smaller supercoolings than is normally possible. This is no longer tenable. Crystallization over the wide range of supercoolings of these experiments produces crystal thicknesses of some thousand Angstroms at 5 kbar, ten times the thickness at 1 bar. Lowered supercooling is, however, still effective in increasing spacing in all three fractions, and it is clearly part of the recipe for the growth of the highest extensions to go to the lowest supercoolings. Time is the other effective factor.

A second hypothesis stems from attempting to carry over the formalism of kinetic theories of crystallization. Crystals ten times thicker than at atmospheric pressure would result from a tenfold increase in σ_e to, say, 500–1000 erg/cm^2. While this parameter is expected to increase with pressure (because the density deficit associated with fold surfaces will give rise to a $p\Delta V$ term in the surface free energy) the effect will surely be too small, unless the character of the fold surface alters. Here ΔV is the extra volume required to accommodate a fold surface in a sample as compared to the same mass in a lamellar interior and may be estimated from the density and crystal thickness. For a lamella 200 Å thick of overall density 0.96 g/cm^3 as against the ideal 1.00, 4%, i.e., 8 Å will be due to the presence of the two fold surfaces. For each surface, therefore, the additional free energy at p kbar will be $4p$ kbar Å = $40p$ erg/cm^2. One would anticipate accordingly a rise in σ_e of some 200 erg/cm^2 at 5 kbar, an increase of 200–400%, but by no means enough directly to account for the observed crystal thicknesses. Increasing ΔV could overcome this discrepancy and would not be inconsistent with observed densities of 0.995 g/cm^3 or less, but such a proposal still raises problems, not the least of which is to explain why it should not apply equally to solution crystallization. Experimentally, according to Wunderlich[10] and our own unpublished work, the two are distinguished. High chain extensions have not been observed in crystals from solution.

A phenomenon which does differentiate crystallization from melt and solution is isothermal thickening, so far observed only for the former.[6] The time dependence of thickness in fraction B (Fig. 3) is firm direct evidence that lamellar thickening also occurs in high-pressure growth. The conclusion is reinforced by the tapered edges of lamellae in sample C (Fig. 7) and Marlex 6002 (Fig. 8) (c.f. also Wunderlich and Melillo)[8].

These narrowing edges lead to the conclusion that molecules are added to a crystal at much less extension than that obtained in the lamellar interior.

This follows if growth faces are at the extremities of such pointed profiles as those in Figures 7 and 8. The alternative, which we shall now exclude, is that the height of the growing face is more or less that observed away from the edges. If this were so, the tapering off must be due to special circumstances such as represent an early stage in the development of the height of the growth face, i.e., close to a nucleus and/or the proximity to the surface of another layer. Plausible though these particular suggestions may be on occasion, they are not able to provide a general explanation. In Figure 7 and 8 all edges are pointed, whether they abut on a second lamella or not. Moreover, interpenetrating layers growing around each other, as at the top of Figure 8 show no tapering. Evidently growth next to an existing crystal does not of itself generally restrict molecular extension. The presence of a nearby nucleus can similarly be ruled out because, in addition, both edges of layers narrow. Were both edges nucleated independently, they would in general lead to two lamellae rather than the one observed. No other special circumstances seem particularly likely, so we are forced to conclude that there is no reasonable alternative to the hypothesis that the edges (which, as only one kind is seen, must include the growth edges) of extended-chain lamellae narrow towards their extremities during growth from the melt. This implies that in general molecular extension and lamellar thickness increase rapidly behind the growth front.

In suitable circumstances, therefore, the profile of any edge may be a measure of the rate of thickening. One must use an isolated tip for this because edges terminating on a second layer will usually have had extra time available for thickening after impingement, and, as Figures 7 and 8 show, these latter do tend to have blunter profiles. Indeed, one really needs to account for the lack of complete thickening up. As has alreadv been pointed out, the constraints of one layer on the other are not a sufficient explanation because they do not cause tapering when layers grow around each other. Perhaps the difference in the orientation of the growth face is significant. In one case the edge falls on the first layer, leaving a taper, and in the other sweeps by it, with no evidence of narrowing. As lamellar thickening must involve mass transport, it is very likely that fixing the growing edge would affect the process, although the observed distances, of the order of microns, are considerable. Fig. 13 is of interest here, because in one photograph, not only is there clear evidence of competitive thickening of the enveloping lamellae in the Maltese cross, but also the thinner lamellae of fraction B show no general tapering of edges such as seen in Figures 7 and 8. It would appear that the shorter molecules of thinner lamellae have thickened up any tapering edges once present, which would be reasonable enough in terms of known behavior of laemllar thickening, where both theory[14] and experiment[6,15] indicate more rapid effects with diminishing molecular length. The relative rate of this short-term thickening is very high. Taking an isolated edge and assuming a uniform growth rate along the lamella during the entire thirty minutes crystallization, one ob-

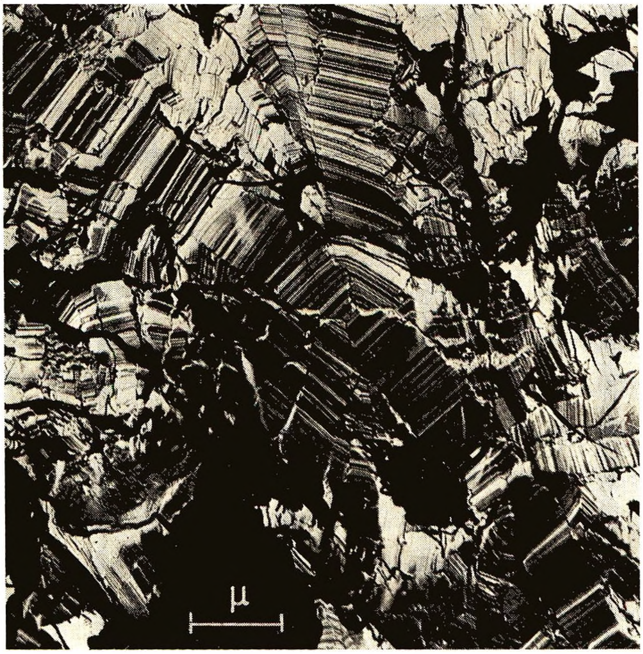

Fig. 13. Maltese cross of intersecting lamellae in fraction B crystallized at 218°C for 30 min.

tains values for $dL/d \log t$ of the order of 10^3–10^4 Å (where t is in minutes). This value is not only higher than that for the direct measurements of thickening in the longer term, but is quite unprecedented in behavior at atmospheric pressure.

There is then considerable evidence for isothermal thickening both direct and indirect, but the situation is not without its complications. For example, it has been objected that the reduction of annealing data to a common function of supercooling at both high and low pressures precludes thickening having an enhanced effect at high pressures.[16] In our view these data—with which we largely agree, though believing there to be a shift to lower supercoolings with pressure—are more a commentary on the nature of the thickening process than a fundamental objection. Certainly it is true that annealing does not give quite such high chain extensions as crystallization under identical conditions. Figure 14 shows lamellae in a B specimen annealed at 233°C for 30 min which satisfy the criteria of extended-chain crystals but are yet thinner than lamellae grown at lower temperatures (Fig. 4). Nevertheless we have demonstrated,[2] and it has been independently confirmed,[17] that much higher chain extensions, to several thousand Angstrom's can be achieved by annealing under elevated pressure. At the same time it has to be recognized that crystallization temperature also plays a role in the adoption of high thicknesses. To resolve this situation one has to enquire further into the nature of lamellar thickening.

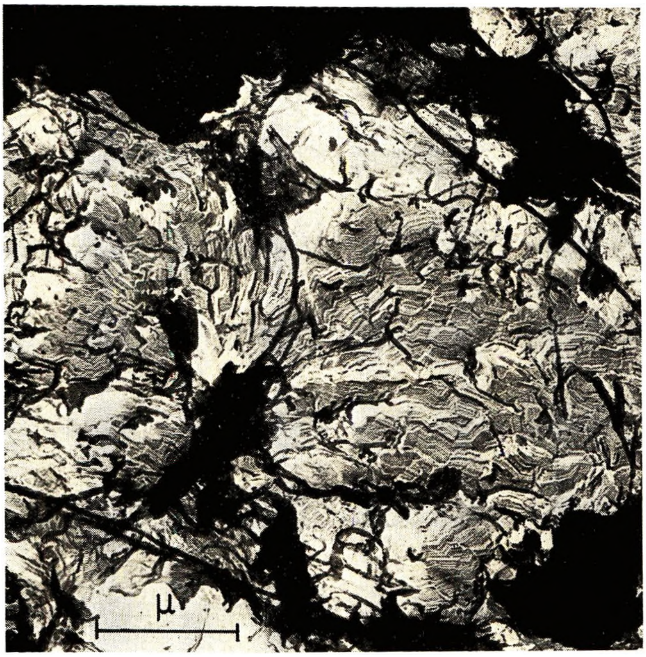

Fig. 14. Extended-chain lamellae produced by annealing fraction B at 233°C for 30 min.

At low temperatures we believe this to be more than the mere progressive melting and recrystallization which it is sometimes considered to be. Phenomenologically, crystallization and annealing treatments do give different results. The essential point is, however, that the state of the initial sample determines the final product, which would not be so if true melting had occurred. Not only is molecular orientation preserved on annealing[4] but, most importantly, the thinnest lamellae thicken fastest and reach higher extensions first.[18] We have confirmed this last effect by showing the crossing of annealing curves for different fold lengths for all three fractions A, B, and C, thereby removing a retrospective weakness in the earlier work where molecular weight differences due to fractional crystallization were present. Nevertheless, the distinction between annealing and crystallization blurs at higher temperatures. Regarding the origin of thick crystals, therefore, our present position is that faced with abundant evidence for thickening on one hand and clear observations of the importance of crystallization temperature on the other, it would seem probable that the relationship of lamellar thickening to crystallization and the attainment of high chain extension under pressure are different aspects of the same problem.

A recent series of articles by Wunderlich and co-authors[19] published while this paper was in preparation cover the same broad field of interest, but in our view, mostly in a complementary way. There is similar emphasis on fractional crystallization and lamellar thickening, but their preoccupation has been with the melting process and obtaining maximum chain extension while we have been concerned to elucidate the factors affecting lamellar thickness.

CONCLUSIONS

(1) The molecular extension in so-called extended-chain polyethylene crystals is a function of time, temperature, and molecular weight. There is by no means just the fully extended configuration present.

(2) Crystallization of polyethylene at high pressure gives lamellae of an optimum thickness which increases with crystallization temperature and time in a qualitatively similar way to the behavior of chain-folded crystals at 1 bar. Fractional crystallization is widespread.

(3) Isothermal thickening of lamellae during crystallization at high pressures has been directly established. Morphological detail suggests further that lamellae can thicken to ten times their initial size.

This work would not have been possible without the generous help of Mr. H. M. Hutchinson and Dr. K. S. Lawrence of B. P. Chemicals Ltd. who supplied the fractionated polyethylenes, and of Dr. R. G. Christensen and H. L. Wagner of the National Bureau of Standards who characterized them by gel-permeation chromatography.

D. V. Rees is also indebted to the Science Research Council for a postgraduate studentship.

References

1. P. H. Geil, F. R. Anderson, B. Wunderlich, and T. Arakawa, *J. Polym. Sci. A*, **2**, 3707 (1964).
2. D. V. Rees and D. C. Bassett, *Nature*, **219**, 368 (1968).
3. D. V. Rees and D. C. Bassett, *J. Polym. Sci. B*, **7**, 273 (1969).
4. W. O. Statton and P. H. Geil, *J. Appl. Polym. Sci.*, **3**, 357 (1960).
5. E. W. Fischer and G. F. Schmidt, *Angew. Chem.*, **74**, 551 (1962).
6. J. D. Hoffman and J. J. Weeks, *J. Chem. Phys.*, **42**, 4301 (1965).
7. A. Peterlin, *Polymer*, **6**, 25 (1965).
8. B. Wunderlich and L. Melillo, *Makromol. Chem.*, **118**, 250 (1968).
9. S. Matsuoka, *J. Polymer Sci.*, **57**, 569 (1962).
10. B. Wunderlich, *J. Polym. Sci. A*, **1**, 1245 (1963).
11. F. J. Baltá Calleja and A. Keller, *J. Polym. Sci. A*, **2**, 2151, 2171 (1964).
12. P. Spegt and A. Skoulios, *C.R. Acad. Sci.* (Paris), **C262**, 722 (1966).
13. J. I. Lauritzen and E. Passaglia, *J. Res. Nat. Bur. Stand.*, **71A**, 261 (1967).
14. A. Peterlin, *Makromol. Chem.*, **74**, 107 (1964).
15. M. Takayanagi and F. Nagatoshi, *Mem. Fac. Eng. Kyushu Univ.*, **24**, 33 (1965).
16. E. W. Fischer and H. Puderbach, *Kolloid Z.*, **235**, 1260 (1969).
17. C. L. Gruner, B. Wunderlich, and R. C. Bopp, *J. Polym. Sci. A-2*, **7**, 2099 (1969)
18. F. J. Baltá Calleja, D. C. Bassett, and A. Keller, *Polymer*, **4**, 269 (1963).
19. B. Wunderlich, and T. Davidson, *J. Polym. Sci. A-2*, **7**, 2043 (1969).

Received May 20, 1970
Revised August 24, 1970

JOURNAL OF POLYMER SCIENCE: PART A-2 VOL. 9, 407-420 (1971)

Graphical Representation of the State of Orientation of Polymer Systems*

SHUNJI NOMURA, NOBIRU NAKAMURA,† and HIROMICHI KAWAI, *Department of Polymer Chemistry, Faculty of Engineering, Kyoto University, Kyoto, Japan*

Synopsis

The orientation distribution function for noncrystalline structural units in polymer systems cannot be determined completely from any experimental source; only the second and/or fourth moments of the distribution function, i.e., the second and/or fourth orders of the generalized orientation factors $F_{lm}{}^j$, can be evaluated. It is therefore necessary to estimate the distribution function from $F_{2m}{}^j$ and $F_{4m}{}^j$. In this paper, a graphical representation of the state of orientation is first discussed in terms of plots of $F_{40}{}^j$ against $F_{20}{}^j$ for several types of distribution functions for uniaxial orientation. These are three types of extreme concentration of the distribution at particular polar angles θ_0 given by $\theta_0 = 0$, $0 < \theta_0 < \pi/2$, and $\theta_0 = \pi/2$; five types of rather realistic distributions having single maxima at $\theta_j = 0$, θ_0, $\pi/2$ and double maxima at $\theta_j = 0$, $\pi/2$, and a single minimum at $\theta_j = \theta_0$; and four types of more realistic distributions including Kratky's floating rod model in an affine matrix. Second, estimation of the distribution function for uniaxial orientation from $F_{40}{}^j$ and $F_{20}{}^j$ is discussed quantitatively in terms of the mean-square error by three approximation methods: (a) expansion of the distribution function in finite series of spherical harmonics through the fourth order, (b) approximation of the distribution function as a composite of two components, random orientation and a particular orientation distribution given by $N_a\ (\cos^2\theta_j)^a$, N_a being a constant, and (c) approximation of the distribution function by $N_a\ (\cos^2\theta_j)^a$ alone. It is concluded that when the orientation distribution is sharp, estimation by the second method of approximation gives a smaller error than the first.

Introduction

The degree of orientation of polymer molecules within an oriented system can be evaluated from optical quantities such as birefringence, and absorption and/or emission dichroism of polarized light.[1-5] These optical quantities, however, do not give the entire orientation distribution of the polymer molecules, but rather the second and/or fourth moments of the orientation distribution, i.e., the second and/or fourth orders of the generalized orientation factors.[6]

Actually, the only experimental technique which gives orientation factors

---

* Presented at the 19th Annual Meeting of the Society of Polymer Science, Japan, Tokyo, May 22, 1970.

† On leave from Research Center, Mitsui Petrochemical Industries, Ltd., Iwakuni, Yamaguchi-ken, Japan.

higher than the fourth order is x-ray diffraction, from which the complete orientation distribution, as well as any order of orientation factors of polymer molecules within the crystalline phase of the oriented system, can be evaluated. Consequently, the orientation distribution of molecules within the noncrystalline phase of the system cannot be obtained directly from any experimental sources.

In the previous paper[6] of this series of studies on the orientation of polymer systems, a mathematical procedure for estimating the orientation distribution function from generalized orientation factors was discussed. The method is based on expansion of the distribution function in a finite series of spherical harmonics, and graphical representation of the state of orientation has also been described in terms of the second-order and fourth-order orientation factors, $F_{20}{}^{j}$ and $F_{40}{}^{j}$, for rather extreme models for orientation distribution.

In this paper, the discussions will be extended to more realistic models for orientation distribution in order to permit better estimation of the orientation distribution function from the second-order and fourth-order orientation factors.

Mathematical Relation between Orientation Factors and Series Expansion of Orientation Distribution Function for Uniaxially Oriented System

Let the orientation distribution function for a given axis $\mathbf{r}_j$ within the bulk specimen be $N_j(\theta_j,\phi_j)$, where θ_j and ϕ_j are the polar and azimuthal angles of the $\mathbf{r}_j$ axis with respect to the x_3 axis of Cartesian coordinates fixed within the bulk specimen as shown in Figure 1. If we assume the system to have cylindrical symmetry with respect to the x_3 axis, then $N_j(\theta_j,\phi_j)$ is a function of θ_j only. The normalized orientation distribution function, $q_j(\zeta_j)$, can then be given by

$$q_j(\zeta_j) = N_j(\theta_j,\phi_j) \Big/ \left\{ 2\pi \int_{\theta_j=0}^{\pi} N(\theta_j,\phi_j) \sin \theta_j d\theta_j \right\} \tag{1}$$

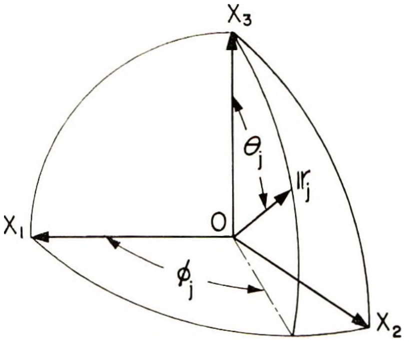

Fig. 1. Polar and azimuthal angles θ_j and ϕ_j specifying the orientation of the j th axis of the structural unit with respect to the Cartesian coordinates O–$x_1x_2x_3$ fixed with respect to the macroscopic specimen.

where $\zeta_j = \cos\theta_j$, and the normalization is performed over all of the specimen space:

$$\int_{\phi_j=0}^{2\pi}\int_{\zeta_j=-1}^{1} q_j(\zeta_j)d\zeta_j d\phi_j = 1 \tag{2}$$

The function $q_j(\zeta_j)$ can be expanded in a series of normalized Legendre functions, $\prod_l(\zeta_j)$, as follows:[7,8]

$$q_j(\zeta_j) = \sum_{l=0}^{\infty} Q_{l0}{}^j \prod{}_l(\zeta_j) \tag{3}$$

where l is even. Furthermore, the coefficient $Q_{l0}{}^j$ can be obtained from

$$Q_{l0}{}^j = \int_{-1}^{1} q_j(\zeta_j)\prod{}_l(\zeta_j)d\zeta_j \tag{4}$$

The coefficient $Q_{l0}{}^j$ is further related to the generalized orientation factor as follows:[6]

$$F_{l0}{}^j = \{2/(2l+1)\}^{1/2}\, 2\pi Q_{l0}{}^j \tag{5}$$

Thus, eq. (3) may be rewritten as

$$q_j(\zeta_j) = (1/2\pi)\sum_{l=0}^{\infty}\frac{2l+1}{2} F_{l0}{}^j P_l(\zeta_j) \tag{6}$$

where P_l is the Legendre function (not normalized)* given by

$$\int_{-1}^{1} \Pi_l(x)\Pi_m(x)dx = \delta_{lm}$$

and

$$\int_{-1}^{1} P_l(x)P_m(x)dx = \delta_{lm}\frac{2}{2l+1}$$

where δ_{lm} is the Kronecker delta.

$$P_l(x) = \left(\frac{2}{2l+1}\right)^{1/2}\cdot\prod{}_l(x) \tag{7}$$

Now, the mean-square error involved in approximating the distribution function with a finite series expansion through the kth order, in place of the infinite expansion as given by eq. (3), is given by

$$\sigma = \int_{\phi_j=0}^{2\pi}\int_{\zeta_j=-1}^{1} [q_j(\zeta_j) - q_j'(\zeta_j)]^2 d\zeta_j d\phi_j \tag{8}$$

where $q_j'(\zeta_j)$ is the approximate distribution function. Upon substituting the series expansion of eq. (3) through the kth order into eq. (8), the mean-square error can be written:

$$\sigma_k = \int_{\phi_j=0}^{2\pi}\int_{\zeta_j=-1}^{1}\left[q_j(\zeta_j) - \sum_{l=0}^{k} Q_{l0}{}^j\cdot\prod{}_l(\zeta_j)\right]^2 d\zeta_j d\phi_j \tag{9}$$

---

* $\Pi_l(x)$ and $P_l(x)$ have the orthogonality property.

$$= 2\pi \int_{-1}^{1} \{q_j(\zeta_j)\}^2 d\zeta_j - 2\pi \sum_{l=0}^{k} (Q_{l0}^j)^2 \qquad (10)$$

or

$$\sigma_k = 2\pi \int_{-1}^{1} \{q_j(\zeta_j)\}^2 d\zeta_j - (1/2\pi) \sum_{l=0}^{k} \frac{2l+1}{2} (F_{l0}^j)^2 \qquad (11)$$

For random orientation, $q_j(\zeta_j)$ equals $1/4\pi$, and $(Q_{l0}^j)^2$ is $1/8\pi^2$ or zero when l is zero or nonzero, respectively. Thus, σ_k is zero even when k is zero. On the other hand, the sharper the distribution function, the larger is the integral on the right-hand side of eq. (10) or (11), and the larger is the error. Therefore, larger k will be necessary to obtain a satisfactory approximation, especially for sharper orientation distributions of the jth axis.

The error of the finite series expansion for a particular distribution function involving uniaxial orientation, such as Kratky's model, a rod floating in an affinie matrix,[9] has been briefly discussed in the previous paper[6] and will be discussed in more detail in the following sections, together with the other types of distribution functions for uniaxial orientation.

Some Characteristic Orientation Distribution Functions and a Graphical Representation of the State of Orientation in Terms of a Plot of F_{40}^j against F_{20}^j

As discussed in the previous paper,[6] let us substitute the following relations given by

$$f(\zeta_j) = \zeta_j^2\{2\pi q_j(\zeta_j)\}^{1/2} \qquad (12)$$

and

$$g(\zeta_j) = \{2\pi q_j(\zeta_j)\}^{1/2} \qquad (13)$$

into the following Schwarz inequality:

$$\left\{\int_{-1}^{1} f(\zeta_j)g(\zeta_j)d\zeta_j\right\}^2 \leqq \int_{-1}^{1} \{f(\zeta_j)\}^2 d\zeta_j \int_{-1}^{1} \{f(\zeta_j)\}^2 d\zeta_j \qquad (14)$$

The relation between the second and fourth moments of the orientation distribution will then be given by

$$(\langle\cos^2\theta_j\rangle)^2 \leq \langle\cos^4\theta_j\rangle \qquad (15)$$

In addition, multiplying both sides of the inequality (16)

$$\cos^2\theta_j \geq \cos^4\theta_j \qquad (16)$$

by $2\pi g_j(\cos\theta_j)$ and integrating the both sides with respect to the angle θ_j, we obtain the relation (17):

$$\langle\cos^2\theta_j\rangle \geq \langle\cos^4\theta_j\rangle \qquad (17)$$

With eqs. (15) and (17), the relation between the second-order and fourth-order orientation factors will be given by

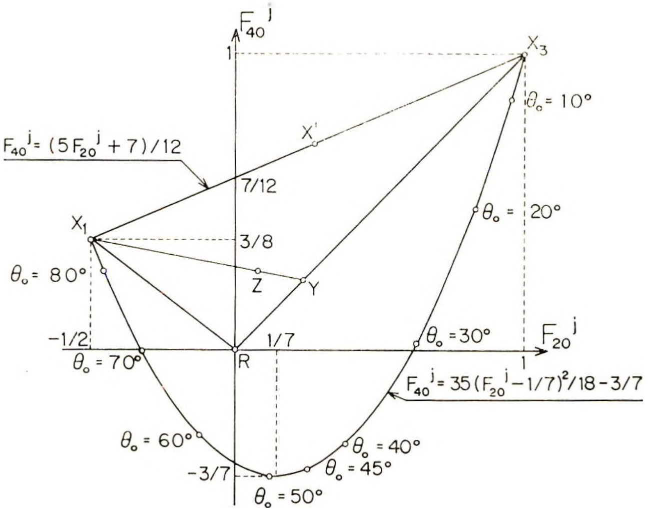

Fig. 2. Plots of F_{40}^j against F_{20}^j for three types of extreme concentration of orientation distribution at particular polar angles, as explained in the text.

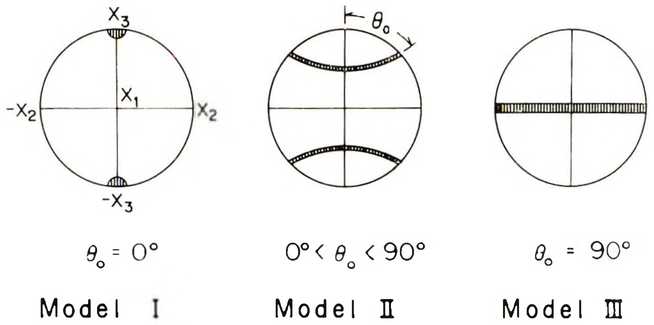

Fig. 3. Pole figures illustrating three extremes of concentration of orientation distribution, models I, II, and III.

$$(5F_{20}^j + 7)/12 \geq F_{40}^j \geq 35(F_{20}^j - 1/7)^2/18 - 3/7 \tag{18}$$

Therefore, a plot of the fourth-order orientation factor F_{40}^j against the second-order orientation factor F_{20}^j for any type of distribution function involving uniaxial orientation must, as is illustrated in Figure 2, fall within the area defined by eq. (18). In turn, any type of orientation distribution may be estimated, in principle, from comparison of a plot of F_{40}^j against F_{20}^j with plots of certain characteristic orientation distribution functions.

First of all, let us consider the extreme models for orientation distributions shown in Figure 3, where all of the vectors $\mathbf{r}_j$ orient uniaxially at a given polar angle θ_0 with respect to the x_3 axis. For model I, in which $\theta_0 = 0$, the plot degenerates to the point X_3 in Figure 2. For model III, in which $\theta_0 = \pi/2$, the plot degenerates to a point X_1, while for model II, in which $0 < \theta_0 < \pi/2$, the plot is given by the locus of the equation $F_{40}^j =$

$35[(F_{20}{}^{j} - 1/7)^2/18] - 3/7$. Further, an extreme orientation distribution composed of two components, represented by models I and III with relative amounts given by the ratio of straight-line segments $\overline{X_3X'}$ and $\overline{X'X_1}$ in Figure 2, is plotted at the point X'. The plot of another extreme orientation distribution composed of two components, model I and a random orientation (point R) in relative amounts $\overline{RY}$ and $\overline{YX_3}$, is given by the point Y, while an orientation distribution composed of two components, model III and the orientation distribution represented by the point Y with relative amounts $\overline{YZ}$ and $\overline{ZX_1}$, corresponds to a point Z. Therefore, any plot of $F_{40}{}^{j}$ against $F_{20}{}^{j}$ can be represented, in principle, by combinations of models I, II, and III and a random orientation, with appropriate fractions of each component.

Similar considerations may be applied to the simple, but more realistic, distribution functions given by

$$q_j(\cos\theta_j) = N_a N_j(\theta_j) \tag{19}$$

where $N_j(\theta_j)$ is distribution function of uniaxial orientation further defined for any of the orientation models (20)–(24)

Model IV:

$$N_j(\theta_j) = (\cos^2\theta_j)^a \tag{20}$$

Model V:

$$N_j(\theta_j) = (\sin^2\theta_j)^a \tag{21}$$

Model VI:

$$N_j(\theta_j) = (2\cos^2\theta_0\cos^2\theta_j - \cos^4\theta_j)^a \quad (0 < \theta_0 \leqq \pi/4) \tag{22}$$

Model VII:

$$N_j(\theta_j) = (2\sin^2\theta_0\sin^2\theta_j - \sin^4\theta_j)^a \quad (\pi/4 \leqq \theta_0 < \pi/2) \tag{23}$$

Model VIII:

$$N_j(\theta_j) = [(\cos^2\theta_j - \cos^2\theta_0)^2]^a \quad (0 < \theta_0 < \pi/2) \tag{24}$$

and N_a is a normalization constant given by

$$1/N_a = 2\pi\int_0^{\pi} N_j(\theta_j)\sin\theta_j d\theta_j \tag{25}$$

The function given by eq. (20) or (21) has a single maximum when θ_j is 0 or $\pi/2$, respectively. The functions given by eqs. (22) and (23) also give a single maximum at $\theta_j = \theta_0$, while eq. (24) gives maxima at $\theta_j = 0, \pi/2$ and a minimum at $\theta_j = \theta_0$. These features of the respective models are illustrated in Figure 4, by taking the value of a as unity or 2. The plot of

$F_{40}{}^j$ against $F_{20}{}^j$ for each of the orientation models illustrated in Figure 4 is depicted in Figure 5 by open circles; the notation is that of Figure 4.

When $a = 0$, every function defined by eqs. (20)–(24) represents the random orientation corresponding to point R in Figure 5. On the other

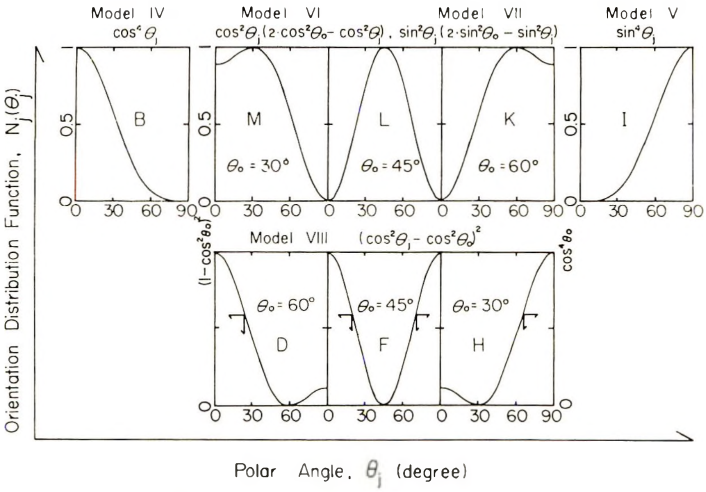

Fig. 4. Some examples of distribution functions for uniaxial orientation corresponding to models IV–VIII given by eqs. (20)–(24), respectively, where a is chosen as unity or 2.

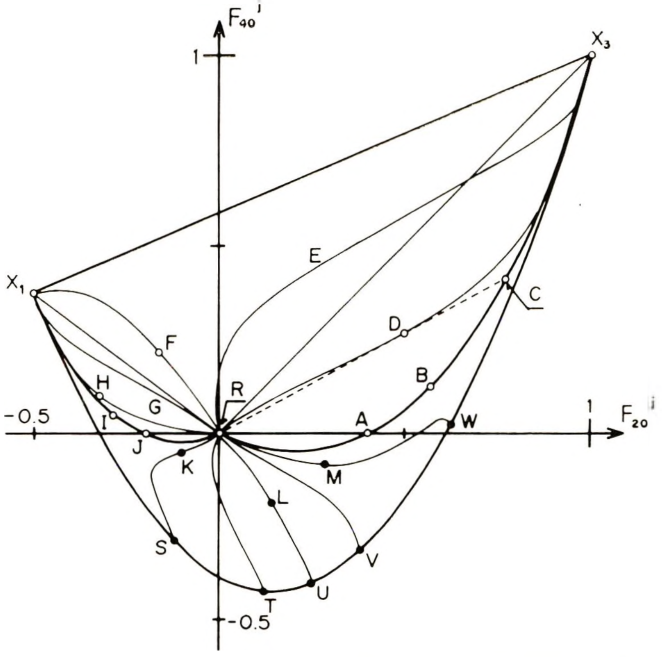

Fig. 5. Plots of $F_{40}{}^j$ against $F_{20}{}^j$ for models IV–VIII for $0 \leq a \leq \infty$ and θ_0 fixed as indicated.

hand, when $a = \infty$, the functions defined by eqs. (20) and (21) represent models I and III, which correspond to the points X_3 and X_1 in Figure 5, respectively. Equation (24) with $a = \infty$ represents model I or model III, depending on the choice of θ_0, and eqs. (22) and (23) with $a = \infty$ represent model II.

If the value of a is varied from 0 to ∞, the plot of F_{40}^j against F_{20}^j for model IV, eq. (20), gives curve $RABX_3$ in Figure 5, where $F_{40}^j = F_{20}^j(5F_{20}^j - 2)/(5 - 2F_{20}^j)$, while the plot for model V, eq. (21), gives curve $RJIX_1$, where $F_{40}^j = 3F_{20}^j(5F_{20}^j + 1)/(8F_{20}^j + 10)$. The corresponding plots for model VI, given by eq. (22) with $\theta_0 = 30°, 40°, 45°$, are represented by curves RMW, RV, and RLU, respectively. Plots for model VII, eq. (23) with $\theta_0 = 45°, 50°, 60°$, are curves RLU, RT, and RKS, respectively. Plots for the model VIII, eq. (24) with $\theta_0 = 30°, 40°, 45°, 50°, 60°$ are curves RHX_1, RGX_1, RFX_1, REX_3, and RDX_3, respectively.

Plots of F_{40}^j against F_{20}^j for models such as those given by eq. (24), or the combination of models I and III, which have double maxima at $\theta_j = 0, \pi/2$, fall in the region above curves X_1JR and $RABX_3$ in Figure 5, while the plots for models such as those given by eqs. (22) and (23) and model II, which have a single maximum at $\theta_j = \theta_0$ $(0 < \theta_0 < \pi/2)$ fall in the region below these curves.

Point D in Figure 5, the intersection of the curve RDX_3 and straight line RDC, corresponds to a distribution function given by eq. (24) or to an extreme distribution involving a combination of random orientation and the orientation corresponding to the point C with relative amounts $\overline{CD}$ and $\overline{DR}$, respectively. In other words, the point D may arise from two indistinguishable types of orientation. However, the distribution function for uniaxial orientation of a noncrystalline phase usually has a single maximum at $\theta_j = 0$; hence this ambiguity may not be of practical concern.

Estimation of the Uniaxial Orientation Distribution Function for the Noncrystalline Phase from Orientation Factors F_{20}^j and F_{40}^j

We now consider the error of estimating some specific distribution functions for uniaxial orientation of noncrystalline phases from F_{20}^j and F_{40}^j. The orientation distribution functions for so-called statistically equivalent chain segments proposed by Kuhn and Grün[10,11] will be omitted, both because a small error is expected because of relatively broad distribution characterized by the function and because a full discussion has been given by Roe and Krigbaum.[12]

The following four specific distribution functions will be considered.

Model IX:

$$q_j\,(\cos\theta_j) = (1/4\pi)\,\frac{\lambda^3}{[\lambda^3 - (\lambda^3 - 1)\cos^2\theta_j]^{3/2}} \tag{26}$$

Model X:

$$q_j(\cos\theta_j) = (N_b/2\pi)\,(\exp\{\cos^2\theta_j\})^b \tag{27}$$

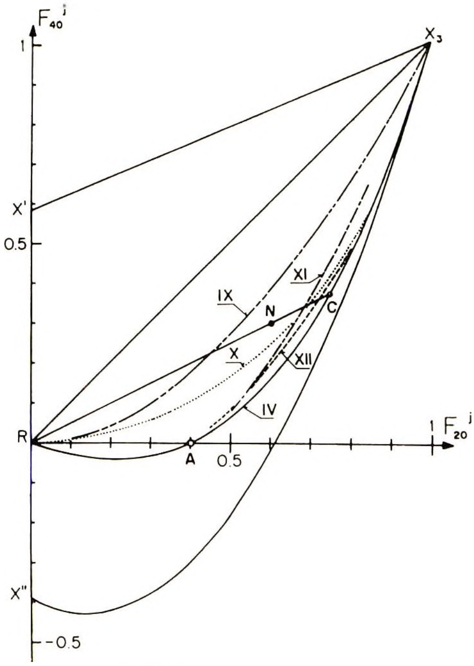

Fig. 6. Plots of F_{40}^j against F_{20}^j for four uniaxial orientation distributions, models IX–XII, given by eqs. (26)–(29), respectively, with b and c between zero and infinity, and λ between unity and infinity.

Model XI:

$$q_j\,(\cos\theta_j) = (N_\lambda/2\pi)\left\{\frac{\lambda^3}{[\lambda^3-(\lambda^3-1)\cos^2\theta_j]^{3/2}} - \frac{1}{\lambda^{9/2}}\right\} \tag{28}$$

Model XII:

$$q_j\,(\cos\theta_j) = (N_c/2\pi)\,[(\exp\{\cos^2\theta_j\})^c - 1] \tag{29}$$

Here N_b, N_λ, and N_c are normalization constants and λ is the elongation ratio of the affine matrix. Equation (26) is the distribution function proposed by Kratky for his floating rod model in an affine matrix,[9] and eqs. (28) and (29) are deduced by substracting the random component from eqs. (26) and (27), respectively.

Variation of b and c or λ from 0 to ∞, or from unity to ∞, gives plots of F_{40}^j against F_{20}^j represented by curves IX, X, XI, and XII in Figure 6 for these four models. Curve IV for model IV, given by eq. (20), has been added for comparison. The distribution function corresponding to curve IX is the sharpest of the four functions, as shown by the fact that it falls closest to line RX_3, which may be considered as a combination of random orientation and model I. With increasing F_{20}^j, curves X and XII converge to the point X_3 and approximate curve IV more closely than curves IX and XI. With decreasing F_{20}^j, on the other hand, curves IX and X converge to point R, while curves XI and XII approximate point A.

By analogy with eqs. (3) and (6), the distribution function $q_j(\zeta_j)$ can be approximated as a series expansion through the fourth order:

$$q_j'(\zeta_j) = \sum_{l=0}^{4} Q_{l0}^j \textstyle\prod_l(\zeta_j) = (1/2\pi) \displaystyle\sum_{l=0}^{4} \frac{2l+1}{2} F_{l0}^j P_l(\zeta_j) \tag{30}$$

and the mean-square error is given by eq. (11) with $k = 4$, i.e.,

$$\sigma_4 = 2\pi \int_{-1}^{1} [q_j(\zeta_j)]^2 d\zeta_j - (1/2\pi) \sum_{l=0}^{4} \frac{2l+1}{2} (F_{l0}^j)^2 \tag{31}$$

where l is even.

As another type of approximation, let us consider the distribution function to be composed of two components, a distribution given by model IV and by random orientation, with composition fractions f_a and $(1 - f_a)$, respectively; i.e.,

$$q_j''(\zeta_j) = f_a N_a(\zeta_j^2)^a + (1 - f_a)(1/4\pi) \tag{32}$$

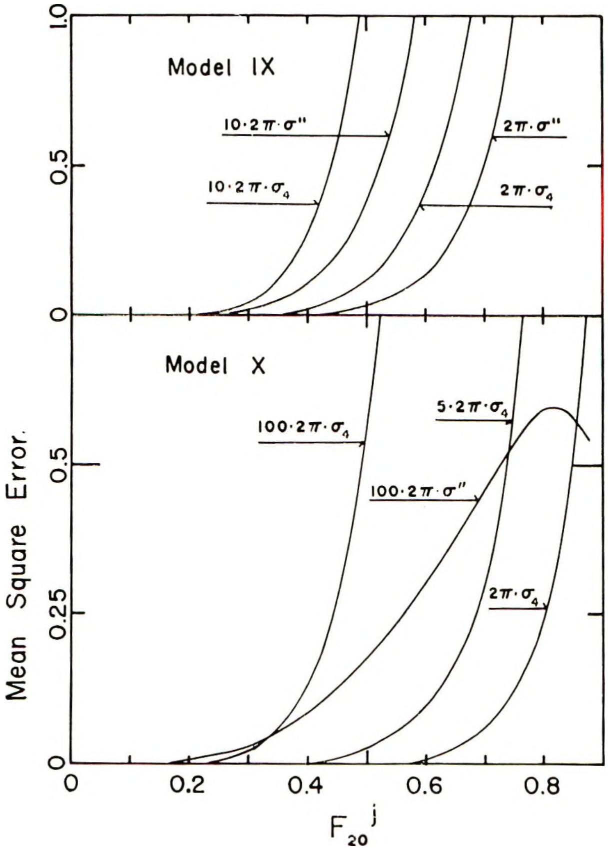

Fig. 7. Change of the mean-square error in calculation of the orientation distribution function by eq. (30) or eq. (32) with increase of F_{20}^j for two types of distribution functions for uniaxial orientation, models IX and X.

For the random component, we have

$$F_{20}{}^{j} = F_{40}{}^{j} = 0 \tag{33}$$

and for the component described by model IV,

$$F_{20}{}^{j} = 2a/(2a+3) \tag{34}$$

$$F_{40}{}^{j} = 4a(a-1)/(2a+3)(2a+5) \tag{35}$$

Upon eliminating a from eqs. (34) and (35), the following relation for $F_{40}{}^{j}$ in terms of $F_{20}{}^{j}$ (which was used for the plot of $F_{40}{}^{j}$ against $F_{20}{}^{j}$ for model IV in Figs. 5 and 6) is obtained:

$$F_{40}{}^{j} = F_{20}{}^{j}(5F_{20}{}^{j} - 2)/(5 - 2F_{20}{}^{j}) \tag{36}$$

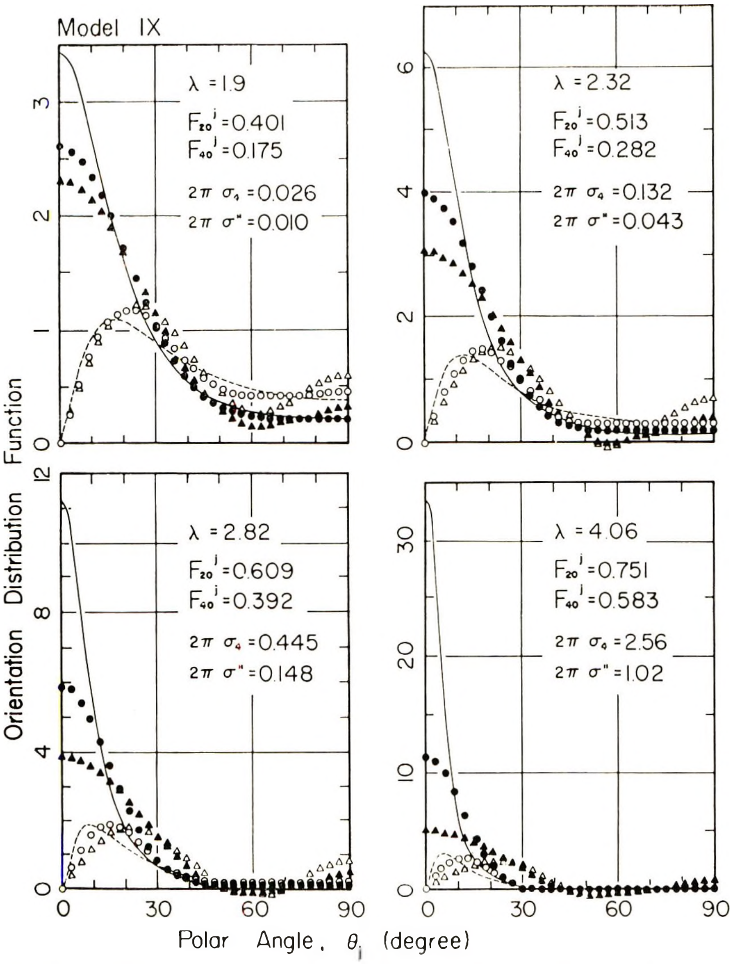

Fig. 8. Comparison of distribution functions approximated according to eqs. (30) and (32) with the exact distribution function given by the model IX for values of elongation ratio λ ranging from 1.90 to 4.06: (——) $2\pi q_j(\zeta_j)$; (--) $4\pi q_j(\zeta_j)\sin\theta_j$; (●) $2\pi q_j''(\zeta_j)$; (○) $4\pi q_j''(\zeta_j)\sin\theta_j$; (▲) $2\pi q_j'(\zeta_j)$; (△) $4\pi q_j'(\zeta_j)\sin\theta_j$.

The plot of F_{40}^j against F_{20}^j for the approximate distribution function $q_j''(\zeta_j)$ should appear within the area bounded by line RX_3 and curve IV in Figure 6. If the coordinates of the point N in Figure 6 are $= F_{20}^j\ x$, $F_{40}^j = y$, then a, f_a, and N_a are given by

$$a = (2x + 5y)/2(x - y) \tag{37}$$

$$f_a = x(5x + 2y)/(2x + 5y) \tag{38}$$

$$N_a = (2a + 1)/4 \tag{39}$$

The mean-square error for the latter type of approximation is given by

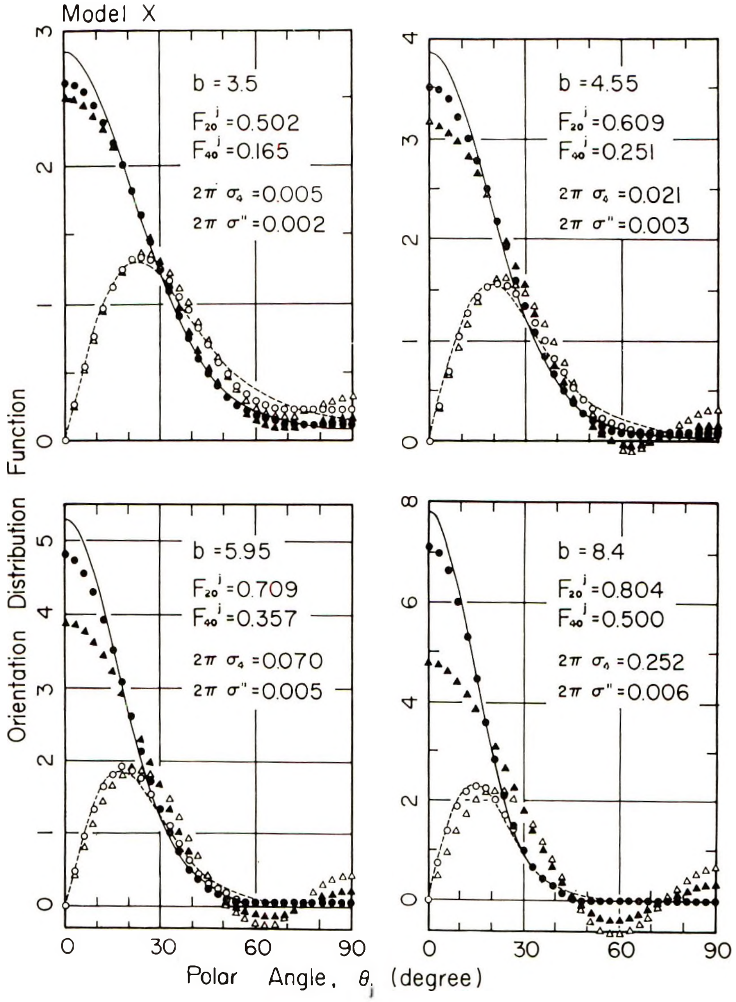

Fig. 9. Comparison of distribution functions approximated according to eqs. (30) and (32) with the exact distribution function given by the Model X for values of b ranging from 3.5 to 8.4: (——) $2\pi\ q_j(\zeta_j)$; (--) $4\pi\ q_j(\zeta_j) \sin\theta_j$; (●) $2\pi\ q_j''(\zeta_j)$; (○) $4\pi\ q_j''(\zeta_j) \sin\theta_j$; (▲) $2\pi\ q_j'(\zeta_j)$; (△) $4\pi\ q_j'(\zeta_j) \sin\theta_j$.

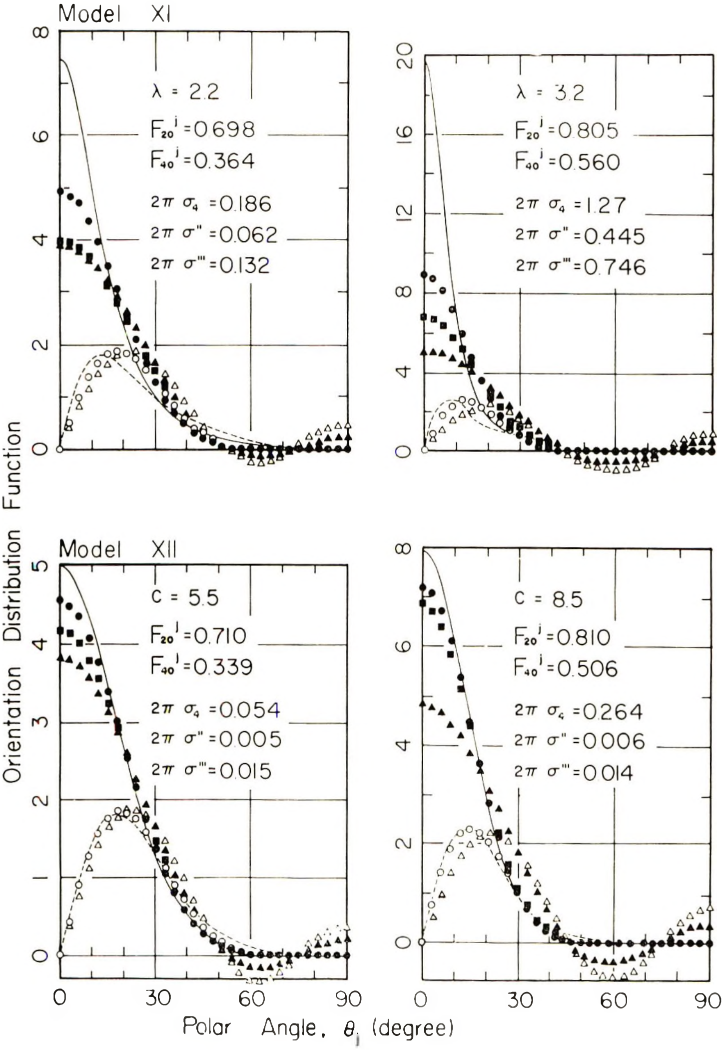

Fig. 10. Comparison of distribution functions approximated according to eqs. (30), (32), or (41) with the exact distribution functions given by the model XI with λ = 2.2 and λ = 3.2, and model XII with c = 5.5 and c = 8.5: (——) $2\pi\ q_j(\zeta_j)$; (--) $4\pi\ q_j(\zeta_j) \sin \theta_j$; (●) $2\pi\ q_j''(\zeta_j)$; (○) $4\pi\ q_j''(\zeta_j) \sin \theta_j$; (▲) $2\pi\ q_j'(\zeta_j)$; (△) $4\pi\ q_j'(\zeta_j) \sin \theta_j$; (■) $2\pi\ q''_j{}'(\zeta_j)$.

$$\sigma'' = 2\pi \int_{-1}^{1} [q_j(\zeta_j) - q_j''(\zeta_j)]^2 d\zeta_j \tag{40}$$

The two types of mean-square error, σ_4 and σ'', multiplied by appropriate factors for comparison, are plotted against F_{20}^j in Figure 7. The two illustrative models IX and X have distributions differing in sharpness, as illustrated in Figure 6. As can be seen in Figure 7, eq. (32) gives a smaller error than eq. (30) (the finite series expansion through the fourth order), especially for functions having a sharper distribution than that given by eq. (27).

The approximate functions, $q_j'(\zeta_j)$ and $q_j''(\zeta_j)$, as well as a further approximate function obtained by omitting the random component from eq. (32), i.e.,

$$q_j'''(\zeta_j) = N_a(\zeta_j^2)^a \tag{41}$$

are compared with the corresponding exact functions $q_j(\zeta_j)$ in Figures 8–10 for the four types of distribution functions given by eqs. (26)–(29). In each figure, the exact function, as well as the three approximate functions, are multiplied by factors 2π and $4\pi \sin \theta_j$. As is shown by the figures, the approximate function, $q_j'(\zeta_j)$ exhibits some negative regions arising from addition of the Legendre functions, $P_0(\zeta_j)$, $P_2(\zeta_j)$, and $P_4(\zeta_j)$. Upon comparing Figure 8 for model IX with Figure 9 for model X, the conclusion that $q_j''(\zeta_j)$ gives a smaller error than $q_j'(\zeta_j)$ for sharp distributions is reaffirmed. Further substantiation is provided by the results shown in Figure 10 for two models XI and XII, which are defined so as to eliminate the random component from models IX and X. Furthermore models XI and XII more differ in sharpness of distribution than do models IX and X.

When the above functions are multiplied by $\sin \theta_j$, $q_j (\cos \theta_j) \sin \theta_j$, for example, is the numbers of $\mathbf{r}_j$ within the angular element $d\theta_j$ at the polar angle θ_j, and the difference between the approximate functions and the exact functions becomes so small that the differences leading to the above conclusion are difficult to depict.

The authors are indebted to the Mitsui Petrochemical Industries, Ltd., the Nippon Gosei Kagaku Co., Ltd., and the Dai-Nippon Cellophane Mfg. Co., Ltd., for financial support through a scientific research grant.

References

1. P. H. Hermans and P. Platzek, *Kolloid-Z.*, **88**, 68 (1939).
2. R. S. Stein and F. H. Norris, *J. Polym. Sci.*, **21**, 381 (1956).
3. R. S. Stein, *J. Polym. Sci.*, **31**, 335 (1958).
4. S. Nomura, H. Kawai, I. Kimura, and M. Kagiyama, *J. Polym. Sci. A-2*, **5**, 479 (1967).
5. I. Kimura, M. Kagiyama, S. Nomura, and H. Kawai, *J. Polym. Sci. A-2*, **7**, 709 (1969).
6. S. Nomura, H. Kawai, I. Kimura, and M. Kagiyama, *J. Polym. Sci. A-2*, **8**, 383 (1970).
7. R. J. Roe and W. R. Krigbaum, *J. Chem. Phys.*, **40**, 2608 (1964).
8. R. J. Roe, *J. Appl. Phys.*, **36**, 2024 (1965).
9. O. Kratky, *Kolloid-Z.*, **64**, 213 (1933).
10. W. Kuhn and F. Grün, *Kolloid-Z.*, **101**, 248 (1942).
11. L. R. G. Treloar, *Trans. Faraday Soc.*, **50**, 881 (1954).
12. R. J. Roe and W. R. Krigbaum, *J. Appl. Phys.*, **35**, 2215 (1964).

Received April 20, 1970
Revised September 8, 1970

JOURNAL OF POLYMER SCIENCE: PART A-2 VOL. 9, 421-430 (1971)

Long-Chain Branching in Low-Density Polyethylene

J. A. COTE and M. SHIDA, *Chemplex Company, Rolling Meadows, Illinois 60008*

Synopsis

A method is given for the analysis of long-chain branching in polymers by using combined GPC and intrinsic viscosity measurements. A computer program was written to evaluate branching indices by a tabular, iterative method. The method was applied to the evaluation of long-chain branching in low-density polyethylene.

INTRODUCTION

A branched polymer molecule occupies a smaller volume in solution than a linear molecule of the same molecular weight. Gel-permeation chromatography (GPC) is known to separate molecules by hydrodynamic volume,[1-3] and therefore any independent measure of molecular weight can be combined with GPC data to yield information on branching in polymer systems.[4,5]

Tung[5] has proposed the use of concurrent GPC and sedimentation velocity measurements. Drott[4] has proposed the simpler technique of evaluation of intrinsic viscosity of the whole polymer combined with GPC measurements. The branching indices obtained are based on a specific branch distribution—that proposed by Zimm and Stockmayer.[6] Drott assumed that the branch density (the ratio of the number of branches per molecule to molecular weight) is independent of molecular weight. For this distribution, the branch density is proportional to molecular weight for species of low molecular weight and asymptotically constant only at high molecular weights. The arbitrariness of this assumption has been pointed out in a recent paper by Shultz.[7] In his work, by specifying the branch distribution, he can evaluate branching indices solely from molecular weight measurements.

In this paper, we will present our method for the analysis of branching by combined GPC and intrinsic viscosity measurements.

Theoretical

For an ideal polymer solution, the ratio of the intrinsic viscosity of a branched molecule (B) to that of a linear molecule (L) of the same molecular weight is equal to the ratio of the two hydrodynamic volumes:

$$[\eta]_B = \Phi \langle r^2\rangle_B^{3/2}/M_B \tag{1}$$

$$[\eta]_{\mathrm{L}} = \Phi\ r\langle{}^{2}\rangle_{\mathrm{L}}^{3/2}/M_{\mathrm{L}} \tag{2}$$

$$[\eta]_{\mathrm{B}}/[\eta]_{\mathrm{L}} = \langle r^2\rangle_{\mathrm{B}}^{3/2}/\langle r^2\rangle_{\mathrm{L}}^{3/2} \tag{3}$$

where $\langle r^2\rangle$ denotes the mean square molecular radius and Φ is a constant. The ratio g is defined by:

$$g = \langle r^2\rangle_{\mathrm{B}}/\langle r^2\rangle_{\mathrm{L}} \tag{4}$$

giving, therefore:

$$[\eta]_{\mathrm{B}}/[\eta]_{\mathrm{L}} = g^{3/2} \tag{5}$$

For real polymer solutions, eq. (5) must be modified to include effects of excluded volume, shielding and polymer–solvent interactions. In this modification, the exponent is changed:

$$[\eta]_{\mathrm{B}}/[\eta]_{\mathrm{L}} = g^{\epsilon} \tag{6}$$

Zimm and Stockmayer[6] state that the value of the exponent is given by:

$$\epsilon = 2 - a \tag{7}$$

where a is the Mark-Houwink exponent appearing in the expression for the intrinsic viscosity of a linear molecule:

$$[\eta]_{\mathrm{L}} = KM^{a} \tag{8}$$

If $[\eta]_{i\mathrm{B}}$ represents the intrinsic viscosity of a single fraction, appearing as a point on the GPC curve with concentration C_i (in units of mass/volume), then the intrinsic viscosity of the whole polymer will be given by:

$$[\eta]_{\mathrm{B}} = \sum_i [\eta]_{i\mathrm{B}}C_i/\sum_i C_i \tag{9}$$

Equations (6), (7) and (9) can be combined to give:

$$[\eta]_{\mathrm{B}} = K \sum_i g_i^{\epsilon} M_i^{a}\, C_i/\sum_i C_i \tag{10}$$

For the distribution[6] to be considered here, g_i is a function of the molecular weight M_i and a branch index λ. Thus, from eq. (10), a knowledge of M_i, C_i and $[\eta]_{\mathrm{B}}$ is sufficient to evaluate the branch index λ. In practice, we do not know M_i since the separation in GPC is by hydrodynamic volume. The calibration curve gives $[\eta]_i M_i$ as a function of elution volume. (The product $[\eta]_i M_i$ is proportional to the hydrodynamic volume of species i.) It has been demonstrated that this curve is "universal"; it holds for both linear and branched polymer.[1,7]

Since for a given λ we can evaluate $[\eta]_i$ as a function of M_i, this curve is sufficient to give the additional information required to evaluate λ. The method requires a knowledge of the g factor as a function of degree of branching and molecular weight and the relation between the degree of branching and the molecular weight. For an arbitrary distribution, these relations are not known; however, they have been set forth by Zimm and Stockmayer for a distribution originally treated by Flory,[8] hereafter referred to as the FZS distribution.

In this distribution, it is assumed that the location of branch points, number of branches and branch lengths are completely random variables. We consider only the case, appropriate to polyethylene, of trifunctional branch points. Two parameters, α and q, describe the distribution. The parameter α is the probability that a chain starting from a branch unit ends in another branch unit. If a chain is selected at random, the probability that both ends are branched is α^2, while the probability that such a chain has a branch at one end and terminates in an endgroup at the other is $\alpha(1 - \alpha)$. The second parameter q is the probability of continuation of a chain equal, in kinetic terms, to the average propagation rate divided by the average termination rate. The quantity $(1 - q)q^{x-1}$ is the probability that a chain branch consists of x monomer units. The g factor and the number of branches per molecular depend on α, q, and molecular weight. For other distributions, other g factors would apply, which might differ markedly in their functional dependence on degree of branching and molecular weight.

Certain properties of this distribution are known. For fractions of uniform molecular weight from it, we have

$$\lambda M \equiv y = 2[\alpha^{1/2}(1 - \alpha)^{1/2}(1 - q)/M_0 q]M \tag{11}$$

and m, the average number of branch points per molecule, is given by:[6]

$$m = (y/2)I_3(y)/I_2(y) \tag{12}$$

where I_3 and I_2 are modified Bessel functions of order 3 and order 2:

$$I_3(y) = \sum_{n=0}^{\infty} \frac{(y/2)^{2n+3}}{n!(n + 3)!} \tag{13}$$

$$I_2(y) = \sum_{n=0}^{\infty} \frac{(y/2)^{2n+2}}{n!(n + 2)!} \tag{14}$$

At large values of m (>5) and y, m is proportional to M; but at low values of m, m varies as the square of the molecular weight (Fig. 1). Thus, the assumption that the branch density m/M is constant, used by Drott,[4] holds only for large M.

Equations relating averaged g factors to the number of branch points per molecule are known for: (a) material monodisperse in molecular weight and number n of branch points per molecule:

$$g = 3/2(\pi/n)^{1/2} - 5/(2n) \tag{15}$$

(b) fractions of the original distribution homogeneous in molecular weight and containing an average number m of branch points per molecule:

$$\langle g \rangle = [(1 + m/7)^{1/2} + 4m/9\pi]^{-1/2} \tag{16}$$

and (c) polydisperse materials (the original distribution),

$$\langle g \rangle_w = \frac{6}{n_w}\left[\left(\frac{2 + n_w}{4n_w}\right)^{1/2} \ln \frac{(2 + n_w)^{1/2} + n_w^{1/2}}{(2 + n_w)^{1/2} - n_w^{1/2}} - 1\right] \tag{17}$$

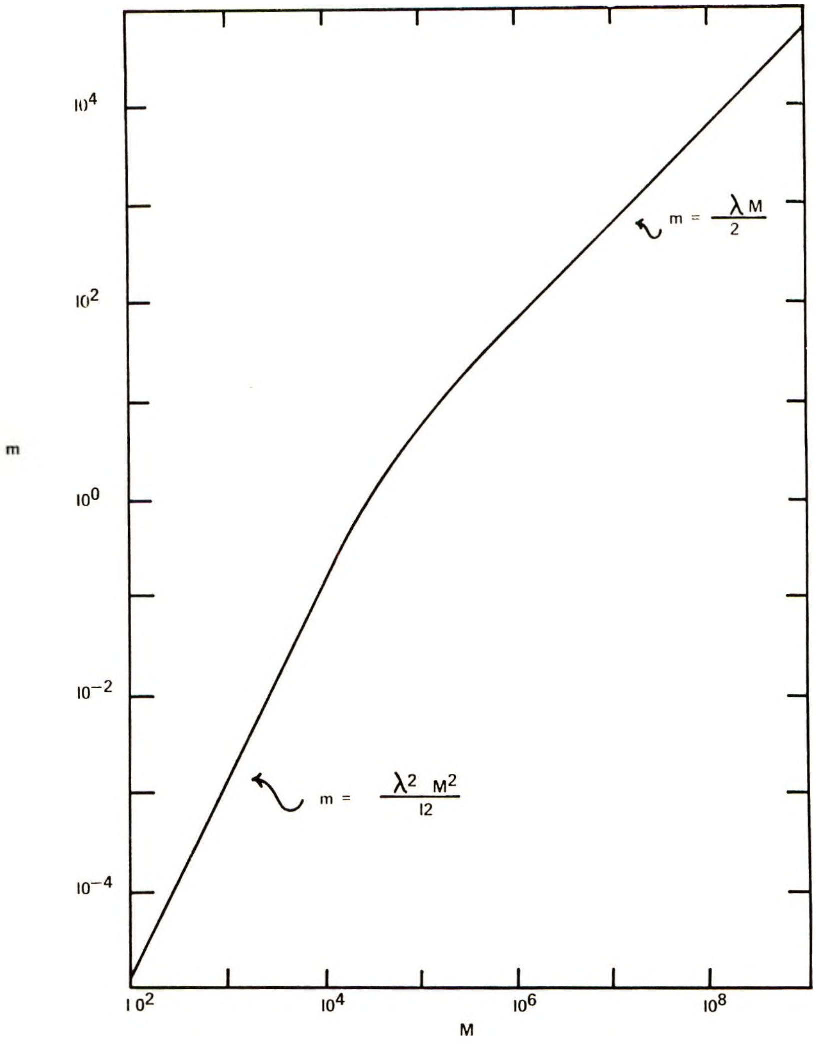

Fig. 1. Branch points per molecule vs. molecular weight for fractions homogeneous in molecular weight from the FZS distribution; $\lambda = 1.24 \times 10^{-4}$.

in which n_w is the weight-average number of branch points per molecule. Since the species comprising the distributions corresponding to eqs. (15) and (16) are uniform in molecular weight, $\langle g \rangle$ represents the arithmetic mean, but $\langle g \rangle_w$ is a weight average.[6] Equations (15) and (16) are analytical approximations to series expressions that cannot be written in closed form.

None of these forms for g is appropriate for GPC, which separates by hydrodynamic volume. A g for fractions of the FZS distribution having constant hydrodynamic volume, not constant molecular weight, should be used. This expression is not known; it is assumed that case (b) is closest to it. It is also assumed in the computer program that at any given elution volume, the molecular weight of the eluent is fixed, and the degree of branching is a nonlinear function of molecular weight.

The relation between the branching index λ and the parameters α and q is:

$$\lambda = [2^{1/2}(1 - \alpha)^{1/2}/M_0][(1 - q)/q] \tag{18}$$

where M_0 is the monomer molecular weight.

Because of the assumptions inherent in the treatment, branching indices obtained should be considered relative, not absolute, numbers.

Applicability of the method is based on the validity of the assumed distribution (the FZS distribution) for polyethylene. If polyethylene were found to have a branching distribution other than this, the equations for the g functions would have to be modified.

Experimental

The branched polyethylene samples used in this study are commercially available resins. All resins used were of the high pressure, low density type. Properties of these resins are shown in Table I.

TABLE I
Polyethylene Samples Used in This Study[a]

Resin	Density g/cc[b]	Melt index[c]
LD 100	0.924	1.4
LD 101	0.933	3.5
LD 102	0.919	0.6
LD 103	0.915	3.2
LD 109	0.922	2.6
LD 110	0.922	2.8
LD 111	0.925	29.0
LD 108	0.916	12.0
LD 106	0.926	22.0
LD 104	0.917	4.1
LD 107	0.915	23.0
LD 112	0.922	55.9
LD 114	0.923	2.0
LD 115	0.925	2.0
LD 116	0.926	1.5

[a] All polyethylenes synthesized by the high-pressure process.
[b] ASTM D1505-57T.
[c] ASTM D1238-57T.

A Waters Associates Model 200 gel-permeation chromatograph was used in this study. Four columns were used, packed with Styragel of pore sizes 10^6, 10^5, 10^4 and 10^3 Å. The operating temperature was 135°C; 1,2,4-trichlorobenzene was used as the solvent. The flow rate was 1.0 ml/min; 2.0 ml of a 0.25% polymer solution was injected after filtering at 135°C.

Calibration was carried out with anionic polystyrene standards supplied by the Pressure Chemical Company. The values of M_w and M_n are taken from data issued by the manufacturer and were obtained by light scattering and osmometry, respectively. Data on these standards are shown in Table II. The calibration curve is approximately linear on a log molecular weight–elution volume plot. Polystyrene and linear and branched poly-

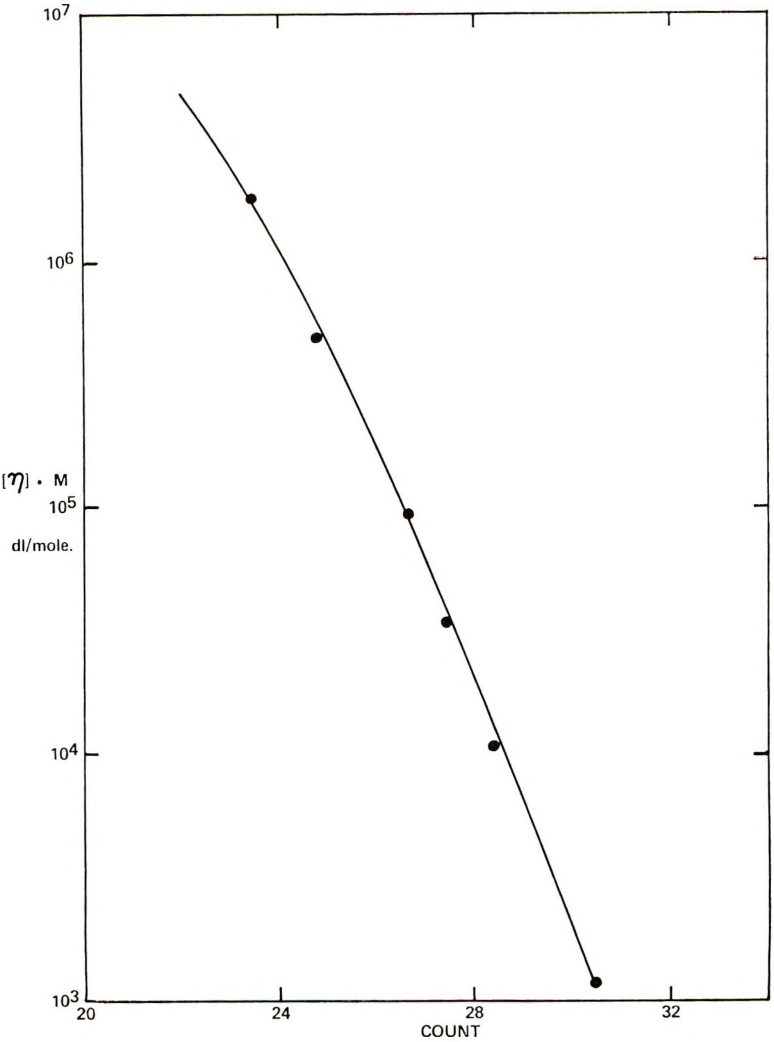

Fig. 2. Universal calibration curve; $[\eta]M$ vs. count. Data points are for polystyrene fractions.

TABLE II
Polystyrene Calibration Samples

Molecular weight		Intrinsic viscosity		
$\bar{M}_n$	$\bar{M}_w$	$[\eta]$, dl/g[a]	$[\eta]\bar{M}_w$, dl/mole	Elution volume, count
19650	19850	0.060	1190	30.5
49000	51000	0.214	10900	28.5
96200	98200	0.336	33000	27.5
104000	173000	0.544	94100	26.7
352000	411000	1.130	464000	24.8
773000	867000	1.960	1700000	23.5

[a] In 1,2,4-trichlorobenzene (TCB) at 135°C.

ethylenes will give the same master curve if log $([\eta]M)$ is plotted as a function of elution volume, as has been pointed out by Benoit[1] and by Wild and Guliana.[9] A plot of this type is shown in Figure 2.

Intrinsic viscosities were measured in trichlorobenzene at 135°C; results are reported in deciliters/gram. Intrinsic viscosities of fractions of linear polyethylene gave the following Mark-Houwink constants:

$$K = 7.1 \times 10^{-4}$$

$$a = 0.67$$

Computer Evaluation of Data

A computer program using a tabular, iterative method to evaluated λ was written in Fortran IV. The steps in the program are summarized below.

A table of forty M_i values is set up, each equally spaced logarithmically over the range $10 < M_i < 3 \times 10^{12}$. For each M_i and an assumed value of λ, the program calculates m_i from eqs. (11) and (12), $g_i^{1/3}$ from eq. (16), $[\eta]_{i\mathrm{L}}$ from eq. (8), $[\eta]_{i\mathrm{B}}$ from eq. (6) and the product $[\eta]_{i\mathrm{B}}M_i$.

Counts corresponding to the products $[\eta]_{i\mathrm{B}}M_i$ are obtained by interpolation of the universal calibration curve. Concentration versus count data from GPC measurements are stored in the computer. Interpolation of the count versus $[\eta]_{i\mathrm{B}}$ table provides concentration versus $[\eta]_{i\mathrm{B}}$ data. Equation (9) is then used to calculate the intrinsic viscosity $[\eta]_\mathrm{B}$ of the whole polymer for comparison with the experimental value.

If the values differ, a new λ is chosen and the process is repeated until the experimental and calculated values of $[\eta]_\mathrm{B}$ agree to within ±0.005 dl/g. The iteration of λ is such that λ converges to the correct value. Once this point has been reached, the table of M_i versus count can be used to determine other molecular weight averages: $\bar{M}_n$, $\bar{M}_w$, $\bar{M}_z$, and $\bar{M}_{z+1}$.

Results and Discussion

While the mode of fractionation in GPC is by hydrodynamic volume, not molecular weight, we have assumed that the proper equation to use for g is that for fractions of constant molecular weight, eq. (16).

Data of Wild and Guliana[7] on fractions of branched polyethylene were fitted by adjusting λ values to plots of g^ϵ versus m. Figure 3 shows these plots for $\epsilon = 1/2$, $4/3$, and $3/2$. The fit is best for $\epsilon = 4/3$ and $\epsilon = 3/2$ and poorest for $\epsilon = 1/2$. We believe that a choice of $\epsilon = 4/3$ rather than $3/2$ is more reasonable, for the following reasons. From eqs. (12) and (16), at large molecular weights,

$$g^\epsilon \rightarrow [(2\lambda/9\pi)M]^{-\epsilon/2} \tag{19}$$

With $[\eta]_\mathrm{B}$ given by eq. (6) and a Mark-Houwink exponent of $2/3$, we should observe the following behavior at large molecular weight: if $\epsilon = 4/3$, $[\eta]_\mathrm{B}$ is constant; if $\epsilon < 4/3$, $[\eta]_\mathrm{B}$ should increase with increasing molecular weight; if $\epsilon > 4/3$, $[\eta]$ should pass through a maximum and then decrease with increasing molecular weight. On physical grounds, the decrease of $[\eta]_\mathrm{B}$

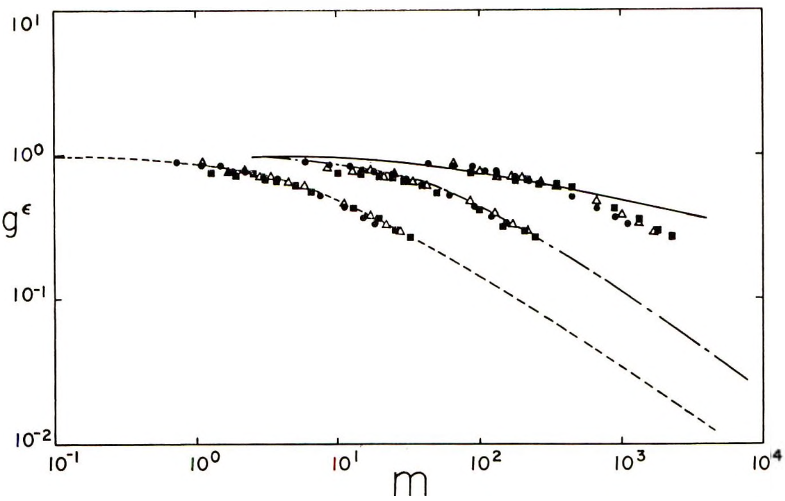

Fig. 3. g^ϵ vs. branch points per molecule, m: (--) $g^{3/2}$; (■) resin A, $\lambda = 0.97 \times 10^{-4}$; (△) resin B, $\lambda = 0.93 \times 10^{-4}$; (●) resin C, $\lambda = 0.67 \times 10^{-4}$; (– – –) $g^{4/3}$; (■) resin A, $\lambda = 1.24 \times 10^{-4}$; (△), resin B, $\lambda = 1.14 \times 10^{-4}$; (●) resin C, $\lambda = 0.82 \times 10^{-4}$; (——) $g^{1/2}$; (■) resin A, $\lambda = 85.1 \times 10^{-4}$; (△) resin B, $\lambda = 81.6 \times 10^{-4}$; (●) resin C, $\lambda = 45.4 \times 10^{-4}$.

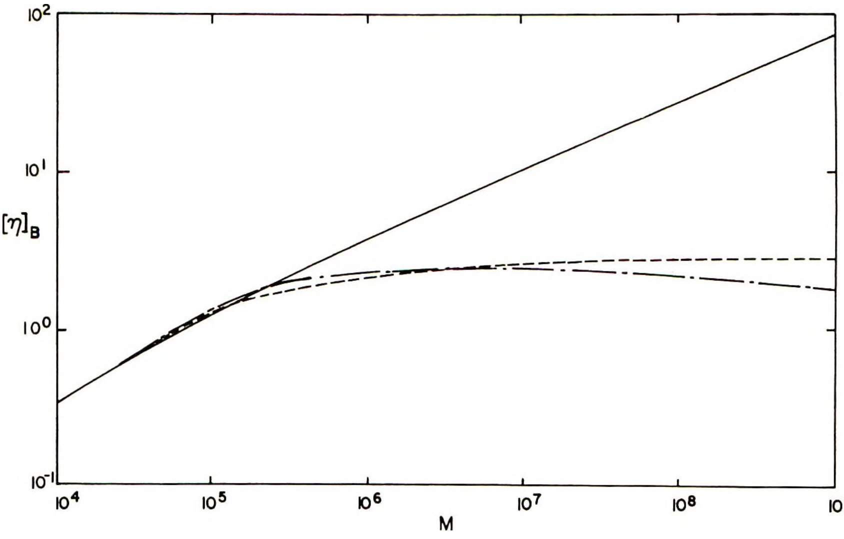

Fig. 4. $[\eta]_B$ vs. molecular weight M for resin LD 114: (——) $\epsilon = 1/2$; (--) $\epsilon = 4/3$; (– – –) $\epsilon = 3/2$.

with increasing molecular weight is improbable, and therefore, $^4/_3$ was chosen as the value for ϵ.

This behavior is shown in Figure 4 for $\epsilon = {}^1/_2$, $^4/_3$, and $^3/_2$ for LD 114 resin. (Similar curves are obtained for other resins, with shifts in the position of the maximum and plateau levels.)

Computer evaluation of the branching indices λ and n_w for the low-density polyethylenes are shown in Table III for $\epsilon = {}^1/_2$, ${}^4/_3$, and ${}^3/_2$. Because of the nonlinear dependence of M on molecular weight,

$$n_w = \lambda \bar{M}_w$$

does not hold. Although λ values vary greatly, there is some consistency in the relative ranking of the branch indices. Thus, if only relative figures are desired, any ϵ from ${}^1/_2$ to ${}^3/_2$ could be used. The absolute values of N_w for $\epsilon = {}^1/_2$ data appear to be too high. The calculated molecular weight averages for $\epsilon = {}^4/_3$ are shown in Table IV.

TABLE III
Branching Data

Resin	$[\eta]$ (135°C, TCB), dl/g	$\lambda \times 10^{-4}$			n_w		
		$\epsilon = {}^3/_2$	$\epsilon = {}^4/_3$	$\epsilon = {}^1/_2$	$\epsilon = {}^1/_2$	$\epsilon = {}^4/_3$	$\epsilon = {}^1/_2$
LD 107	0.732	1.32	2.02	58.97	45.83	62.52	1103
LD 103	0.974	0.81	1.25	43.07	38.22	54.77	1293
LD 104	0.935	0.82	1.26	43.07	37.75	53.48	1227
LD 102	1.015	0.72	1.11	33.92	32.12	46.78	990
LD 106	0.677	1.35	2.05	41.47	27.14	38.05	504
LD 108	0.892	0.75	1.06	28.80	25.54	32.09	631
LD 111	0.648	1.25	1.95	23.85	15.11	22.81	193
LD 112	0.531	2.17	3.19	33.07	14.78	20.90	160
LD 109	0.770	1.11	1.70	18.74	13.80	20.82	171
LD 110	0.778	1.10	1.69	17.95	13.59	20.54	163
LD 115	0.834	1.03	1.51	10.67	7.63	11.45	71
LD 101	0.792	0.77	1.16	7.50	6.66	9.87	48
LD 116	0.854	0.84	1.23	7.50	5.74	8.64	47
LD 100	0.789	0.85	1.25	7.11	4.72	7.23	37
LD 114	0.986	0.37	0.60	1.38	1.08	2.11	5

TABLE IV
Molecular Weight Data

Resin	$\bar{M}_n \times 10^{-4}$	$\bar{M}_w \times 10^{-5}$	$\bar{M}_z \times 10^{-6}$	$\bar{M}_z + 1 \times 10^{-6}$
LD 100	1.614	1.306	0.746	2.058
LD 101	1.745	1.864	3.198	8.632
LD 102	2.368	8.574	6.056	10.489
LD 103	2.640	8.948	6.380	11.470
LD 104	2.331	8.619	6.606	11.609
LD 106	1.636	3.803	4.758	12.264
LD 107	1.911	6.303	6.803	13.095
LD 108	1.359	6.248	5.498	9.738
LD 109	2.037	2.568	2.210	5.516
LD 110	2.287	2.558	2.111	4.983
LD 111	1.348	2.442	2.829	6.492
LD 112	1.606	1.377	1.497	4.256
LD 114	2.045	0.955	0.316	0.635
LD 115	2.929	1.657	0.854	2.483
LD 116	2.509	1.562	0.950	2.911

The computer also provides several other branching indices. The weight-average and number-average molecular weights of linear chain elements are determined. These are the weight-average and number-average molecular weights of the distribution which would result if the molecule were broken at each branch point so as to create three chain ends, i.e.,

$$\langle M_s\rangle_w = \sum_i \frac{M_i C_i}{2m_i + 1} \Big/ \sum_i C_i \tag{20}$$

$$\langle M_s\rangle_n = \sum_i C_i \Big/ \sum_i (2m_{i+1}) C_i / M_i \tag{21}$$

The intrinsic viscosity which would result if the molecules were all linear with the same molecular weight distribution is also calculated. The ratio of this to the observed intrinsic viscosity provides another branching index.

References

1. Z. Grubisic, P. Rempp and H. Benoit, *J. Polym. Sci. B*, **5**, 753 (1967).
2. E. Drott, paper presented at the 4th International Seminar on GPC, Miami Beach, May 1967.
3. L. Wild and R. T. Guliana, paper presented at the 6th International Seminar on GPC, Miami Beach, October 1968.
4. E. Drott and R. A. Mendelson, paper presented at the 6th International Seminar on GPC, Miami Beach, October 1968.
5. L. H. Tung, *J. Polym. Sci. A-2*, **7**, 47 (1969).
6. B. H. Zimm and W. H. Stockmayer, *J. Chem. Phys.*, **17**, 1301 (1949).
7. A. R. Shultz, *Europ. Polym. J.*, **6**, 69 (1970).
8. P. J. Flory, *J. Amer. Chem. Soc.*, **63**, 3091 (1941).
9. L. Wild and R. T. Guliana, *J. Polym. Sci. A-2*, **5**, 1087 (1967).

Received April 2, 1970
Revised September 15, 1970

JOURNAL OF POLYMER SCIENCE: PART A-2 VOL. 9, 431-435 (1971)

Side-Chain Relaxation in Stereoregular Poly(isobutyl Methacrylate)

HIROSHI OCHIAI, HEISABURO SHINDO, and HITOSHI YAMAMURA, *Department of Chemistry, Faculty of Science, Hiroshima University, Hiroshima 730, Japan*

Synopsis

The effects of stereoregularity on the low-temperature relaxation processes were studied by dynamic mechanical measurements on isotactic and syndiotactic polyisobutyl methacrylates (iso-PiBMA and syn-PiBMA). The α, β, and γ relaxation processes were observed in both stereoregular forms. Both the α and β loss peaks were at lower temperatures for iso-PiBMA than for syn-PiBMA. The γ loss peak was observed at about $-155°C$ at 30 Hz for both forms, and the apparent activation energy of this process was same for both samples within experimental error (6.7 ± 0.5 kcal/mole). It was reduced from these results that the α and β processes are both considerably influenced by the isotactic configuration but the γ process is not.

INTRODUCTION

It is well known that in alkyl methacrylate polymers several relaxation processes can be observed by mechanical and dielectric measurements.[1] They are designated the α, β, γ relaxation processes, and so on, in order of decreasing temperature. In these relaxation processes, the loss peak of the γ process ordinarily appears at a temperature between -100 and $-200°C$ for alkyl methacrylate polymers with fairly long side chains such as *n*-propyl and *n*-butyl,[2] but cannot be observed in this temperature range for methacrylate polymers with fairly short (methyl, ethyl) side chains. Even so, the detailed mechanism for the effect of the side chain on the γ relaxation process is not known.

One can conceive of the following characteristics as dominating the mechanism of the γ process: (1) the length and/or bulkiness of the side chain, and (2) the mobility of the backbone chain, which plays a major role in the appearance of the glass-transition phenomenon. The effect of the dimensions of the side chain can be examined by changing the ester alkyl group in the polymers. Studies of these polymer series have revealed that the location of the γ loss peak is essentially independent of the length of the ester alkyl group.[2,3] However, in these cases it must be remembered that the substitution of ester alkyl groups may also have serious effects on the mobility of the backbone chain. For instance, the glass transition temperatures become lower as the length of the ester alkyl group is increased. Thus the decreased mobility of the ester alkyl group as a whole with increasing length may be counteracted by a contribution from the increased mobility of the backbone chain.

As to the effects of the mobility of the backbone chain on the γ process, Wada et al.,[4] have shown for copolymers of methyl methacrylate (MMA) with *n*-butyl methacrylate (*n*-BMA) that the location of the γ loss peak assigned to the motion of the *n*-butyl group does not change for *n*-BMA content up to about 50 mole-%. In stereoregular methacrylate polymers, one can change the glass transition temperature over a fairly wide range by varying the stereoregularity without changing the chemical species,[5] and hence it may be possible to study the effects of the mobility of the backbone chain on the γ process somewhat independently of the other effects. From this point of view, we here discuss the effects of the mobility of the backbone chain on the γ process as revealed by dynamic measurements on isotactic (iso-PiBMA) and syndiotactic (syn-PiBMA) poly(isobutyl methacrylates).

Materials and Methods

The iso-PiBMA was prepared in toluene solution at −70°C with lithium aluminum hydride as the initiator, and the syn-PiBMA was obtained by polymerization in THF solution at −70°C with lithium aluminum hydride. The products were repeatedly purified by reprecipitation with a cooled water–methanol mixture. The characteristics of the samples are listed in Table I.

TABLE I
Some Characteristics of Stereoregular Poly(isobutyl Methacrylates)

	Tacticity from NMR spectra, %		Density (25°C),	
Sample	Isotactic	Syndiotactic	g/cc	T_g, °C
iso-PiBMA	90	10	1.0487	7
syn-PiBMA	20	80	1.0412	53

The apparatus used here was a forced-oscillation type of viscoelastic spectrometer (Iwamoto Seisakusho Co. Ltd.). Films cast from benzene solutions of the sample (about 0.2 mm thick) were cut into the form of rectangular strips (about 5 × 50 mm) for dynamic mechanical measurements. Some care was taken to keep the initial extension imposed on the sample sufficiently small to stay in the linear region. The dynamic Young's storage modulus E' and the loss modulus E'' for each sample were obtained as a function of temperature over the range of −175 to 100°C at fixed frequencies of 5, 30, and 80 Hz.

Results and Discussion

For iso-PiBMA and syn-PiBMA, log E' and log E'' at 5 Hz are plotted against temperature in Figure 1. Three types of relaxation processes can be discerned in the curves of the loss modulus for each sample. The loss

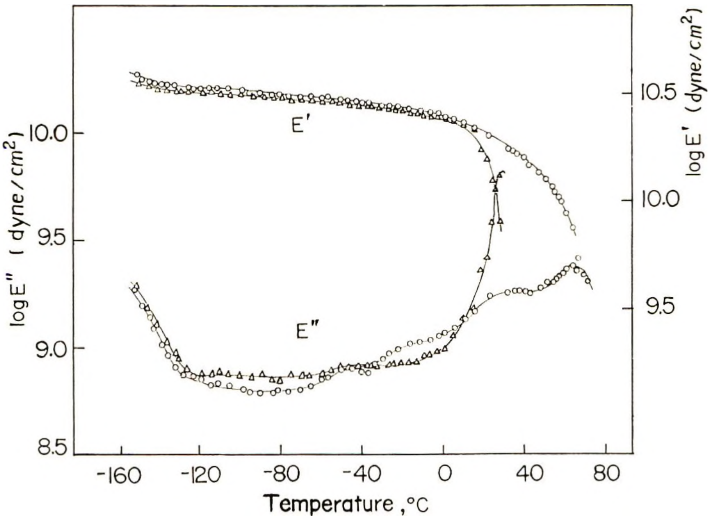

Fig. 1. Temperature dependence of the dynamic storage modulus E' and loss modulus E'' for (△) isotactic and (○) syndiotactic poly(isobutyl methacrylate).

peak at high temperature can be attributed to the micro-Brownian motion of the chain backbone (the α process). By comparing the glass transition temperature of the two samples listed in Table I, the α loss temperature can be assigned to the glass transition temperature of each polymer. It is lower by about 40°C for the isotactic sample (25°C at 5 Hz) than for the syndiotactic sample (65°C at 5 Hz). The β loss attributed to the motion of the ester oxycarbonyl group can be clearly observed in the temperature range -20 to 50°C for syn-PiBMA as a shoulder of the large α loss peak, but for iso-PiBMA it is observed as a small, broad peak at about -40°C.

In higher alkyl methacrylate polymers, the β loss peak tends to be submerged in the large α loss peak, since the β process is considerably influenced by the α process,[1] which shifts to lower temperature as the length of the alkyl side group increases. This implies that the mobility of the backbone chain is increased by the longer alkyl side group. Similar results have been reported for some isotactic stereoregular polymers;[6,7] however Heijboer[8] and Mikhailov[9] have clearly observed the β loss peak in isotactic methyl and *tert*-butyl methacrylate polymers, respectively. Their results show that both the α and β loss peaks appear at higher temperatures for syndiotactic than for isotactic samples and that the magnitude of the β peak of isotactic polymer is smaller than that of the syndiotactic polymer. Accordingly, our results in PiBMA suggest that the mobilities of the backbone chain and the side chain are increased for the isotactic configuration as in PMMA and PtBMA. However it should be noted that it is open to some question whether the small peak observed in iso-PiBMA may be attributed merely to adsorbed water and accordingly whether the β loss may in fact be submerged in the large α peak.

The increase in loss modulus as the temperature is lowered below -120°C has been attributed to the γ relaxation process.[2] The temperature de-

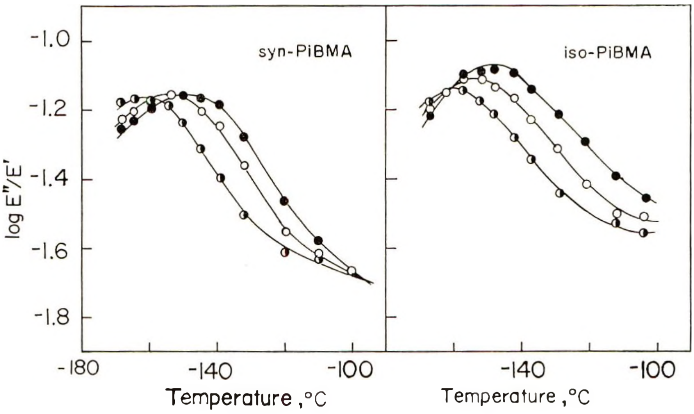

Fig. 2. Temperature dependence of log (E''/E') at (◑) 5 Hz, (○) 30 Hz, and (●) 80 Hz for isotactic and syndiotactic poly(isobutyl methacrylate).

pendence of the loss tangent E''/E' at frequencies of 5, 30, and 80 Hz are shown for the γ process in Figure 2. Stereoregularity affects the γ process in two ways: the height of the γ loss peak is slightly greater in the isotactic polymer, and it increases with increasing frequency only for iso-PiBMA. On the other hand, both the location of the γ loss peak (−155°C at 30 Hz) and the apparent activation energy of the corresponding process (6.7 ± 0.5 kcal/mole) are independent of the stereoregularity.

Generally in methacrylate polymers, including the PiBMA in Figure 1, both the α and β processes are greatly affected by stereoregularity.[10-12] Furthermore, from NMR studies[13,14] it has been deduced that the mobility of the α methyl group is increased in the isotactic configuration. However in our study, since both the location and the activation energy of the γ process were found to be independent of the stereoregularity, the above-mentioned differences seem not to be essential. Thus it may be concluded that the γ process is practically independent of the differences in the stereoregularity (independent, especially, of the glass transition temperature) and also that it is scarcely affected by the mobility of the backbone chain. Consequently, we suggest that the γ process is due to the motion of the ester alkyl group farthest away from the backbone chain.

It still seems necessary to make more systematic studies of the γ process in order to interpret experimental results in view of the possible effects of the length and/or bulkiness of the side chain, and of the presence of dipolar groups and of substituents at the α position on the main chain.

References

1. N. G. McCrum, B. E. Read, and G. Williams, *Anelastic and Dielectric Effects in Polymeric Solids*, Wiley, New York–London, 1967, p. 238.

2. E. A. W. Hoff, D. W. Robinson, and A. H. Willbourn, *J. Polym. Sci.*, **18,** 161 (1955).

3. J. Bareš and J. Janáček, *Coll. Czech. Chem. Commun.*, **30,** 1604 (1965).

4. Y. Kawamura, S. Nagai, J. Hirose, and Y. Wada, *J. Polym. Sci. A-2*, **7**, 1559 (1969).
5. T. G. Fox et al., *J. Amer. Chem. Soc.*, **80**, 1768 (1958).
6. W. G. Gall and N. G. McCrum, *J. Polym. Sci.*, **50**, 489 (1961).
7. T. I. Borisova, L. L. Burshtein, and G. P. Mikhailov, *Vysokomol. Soedin.*, **4**, 1479 (1962).
8. J. Heijboer, in *Physics of Noncrystalline Solids*, J. A. Prins, Ed., North Holland, Amsterdam, 1965, p. 231.
9. G. P. Mikhailov, in *Physics of Noncrystalline Solids*, J. A. Prins, Ed., North Holland, Amsterdam, 1965, p. 270.
10. G. P. Mikhailov and T. G. Borisova, *Polym. Sci. USSR*, **2**, 287 (1961).
11. Y. Ishida, S. Togami, and K. Yamafuji, *J. Polym. Sci. B*, **5**, 745 (1968).
12. H. Shindo, I. Murakami, and H. Yamamura, *J. Polym. Sci. A-1*, **7**, 297 (1969).
13. J. P. Powles, B. I. Hunt, and D. J. H. Sandiford, *Polymer*, **4**, 401 (1963).
14. A. Odajima, A. E. Woodward, and J. A. Sauer, *J. Polym. Sci.*, **55**, 181 (1961).

Received June 25, 1970
Revised August 31, 1970

JOURNAL OF POLYMER SCIENCE: PART A-2 VOL. 9, 437-451 (1971)

Liquid-Induced Reversible Long-Spacing Changes in Polyethylene Single Crystals and Their Implications for the Fold-Surface Problem

Y. UDAGAWA and A. KELLER, *H.H. Wills Physics Laboratory, University of Bristol, Bristol BS8 1TL, England*

Synopsis

The long spacing of single-crystal mats of polyethylene was found to increase reversibly on addition of liquids which normally act as swelling agents. The magnitude of the increase follows the sequence of the solvent power which these liquid exhibit at higher temperatures. The increase in long spacing depends to a minor extent on crystallization conditions, such as concentration and crystallization temperature, but increases very markedly with the molecular weight of the polymer. Heat treatment reduces the amount of swelling, even in the range of low treatment temperatures which do not produce a fold-length increase, implying a reorganization of the fold surface. It is inferred that there is a layer along the fold surface which expands by swelling which in turn implies a disordered amorphous component. Nevertheless, such disordered material need not be an intrinsic consequence of chain folding, as its amount can be reduced to insignificant proportions, e.g., by taking molecules which are short but still fold. Thus both, the presence of amorphous disorder and the nonunique nature of such a disorder along the surface is demonstrated. Further implications for the fold-surface problem are discussed.

As has long been established, sedimented mats of single crystals give discrete x-ray reflections in the low-angle region which correlate with the thickness of the crystals and hence provide a measure of the fold length.[1] While the long period determined in this way has proved to be one of the most characteristic and reproducible parameters in the characterization of crystalline polymers, at least in the form of solution-grown single crystals, it must be remembered that it is not a direct measure of the fold length as such, but that of the layer periodicity. The latter may be affected both by additional features of the surface structure and by the mode of packing and sedimentation of the layers themselves. The present note contains some observations of the variability of the long periods due to such factors. This is of consequence for the fold-length values as derived from the long spacings and for studies on the nature of the fold surface itself, which is a subject of current topicality.

The experiments to be reported consisted of the determination of the long spacings when the polymer was wetted with different liquids. Such liquids were xylene, octane, and decalin, all three of which dissolve the crystals at suitably high temperatures but are nonsolvents at room temperature where the long spacing determination was performed. In one case silicone oil was used, which is a nonsolvent under all circumstances.

EXPERIMENTAL

The experiments to be reported here were carried out on the linear polyethylene Rigidex 50 crystallized from an 0.025% xylene solution by slow cooling and sedimented so as to yield an oriented mat in the usual manner. The long spacing was determined to an accuracy of ±1 Å by means of a slit-collimated Kratky and/or point-collimated Franks focussing camera in which the mat was placed horizontally on a suitable support. After recording the low-angle x-ray diffraction pattern, drops of the appropriate liquid were placed onto the mat, until the mat lay completely covered beneath a layer of liquid, when the diffraction pattern was again recorded. In order to keep the sample under the liquid, losses due to evaporation were replaced during exposure when necessary. In the following stage the liquid was exchanged with acetone which could then be readily removed by evaporation. The dried sample was examined again as regards low-angle diffraction.

RESULTS

The addition of the liquid to the crystal had two effects. The intensity of the reflection increased and the reflection angle decreased, i.e., the corresponding spacing increased in the wet state. The intensity effect will be only briefly mentioned, while the change of spacing will form the main body of the paper.

Intensity Changes

Figure 1*a* illustrates the photometer trace of the low-angle pattern, dry and wet, while Figure 1*b* shows the corresponding traces for the 110 reflection in the wide-angle region with decalin as the liquid. As can be seen, there is a very large increase of the low-angle intensity on wetting. If we attribute the decrease of the wide-angle intensity to increased adsorption due to the liquid drop placed on the specimen (a point which would need further check) and take its intrinsic scattering power unaltered, hence use it as a standard, we still obtain an intensity increase of 3.6× in the scattering in the low-angle pattern. This effect was reversible: the intensity reverted to the original on drying of the sample. As seen from Figure 1*a*, the continuous central scattering became greatly reduced under the effect of the added liquid.

Spacing Changes with Time

Figure 2 shows the effect of the time of immersion on the long spacing. The abscissa gives the time of separate immersion prior to exposure. In

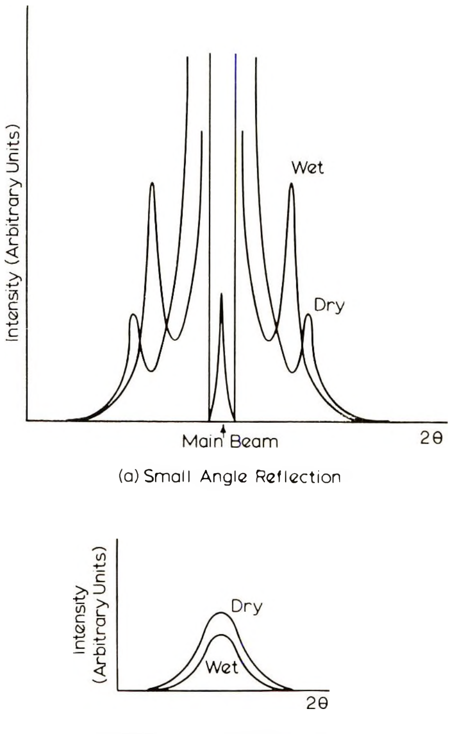

Fig. 1. Photometer traces from x-ray diffraction pattern of dry and wet single-crystal mats of polyethylene: (*a*) small-angle reflection; (*b*) 110 wide-angle reflection.

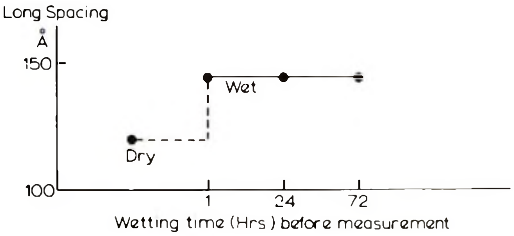

Fig. 2. Effect of wetting with decalin on the long spacing of a single-crystal mat as a function of time.

this case the exposure itself required a further 1 hr with the liquid drop placed on the specimen. As can be seen, there was no change between 1 and 72 hr immersion time; the long spacing took up its final value after the shortest treatment employed here. The lower time limit was not explored, but it was noted that the initially opaque sample became translucent immediately on immersion; hence on our time scale at least, the liquid penetration was instantaneous.

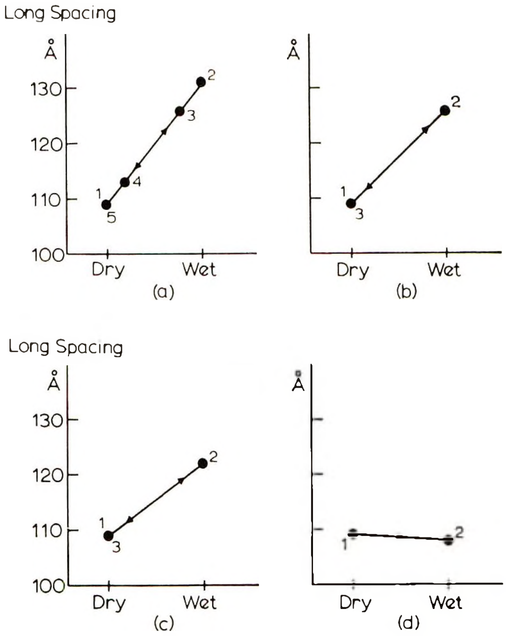

Fig. 3. Long spacing changes in single-crystal mats produced by different addition liquids: (*a*) decalin; (*b*)xylene; (*c*) octane; (*d*) silicone oil.

Effect of Different Addition Liquids

The results are shown in Figure 3. Points *1* and *2* compare the long spacings in the dry and wet states, respectively, for four different liquids. As seen the spacing increase was largest with decalin (22 Å) and diminished in the sequence of xylene (17 Å) octane (15 Å) and silicone oil (−1 Å) (the −1 Å in the last case is within experimental error, consequently the effect of silicone oil can be taken as zero).

Reversibility of Spacing Changes

Points *3* in Figures 3*b* and 3*c* were obtained after the two samples exposed to xylene and octane were washed in acetone and dried in a vacuum oven. The original starting value of the long spacing was regained.

In the case of Figure 3*a* the removal of the liquid was done in three stages which could be readily performed in this case in view of the low vapor pressure of decalin. This allows the removal of the liquid to be readily spaced out. For the same reason the intermediate amounts of liquid at each stage can be retained during the exposure without special precautions.

Point *3* corresponds to a sample which, after having yielded point *2*, was cleared from overlaying liquid and kept in air for 1 hr prior to exposure. As noted, there is a small but noticeable decrease in the long spacing. A further, much greater decrease was obtained when this same sample was placed in acetone and allowed to dry in air (point *4*). The initial starting

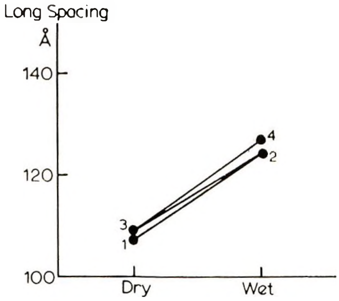

Fig. 4. Effect of repeated wetting on the long spacing of single-crystal mats: (*1*) initial dry state; (*2*) after first wetting with xylene; (*3*) after subsequent drying; (*4*) after second wetting with xylene.

spacing was fully regained on repeated immersion in acetone and subsequent drying in a vacuum oven (point *5*).

In all these experiments complete reversibility has been achieved. In one instance with xylene as a swelling agent a cycling experiment was also carried out. The results with the explanatory caption are given by Figure 4. As is seen, the swelling effect can be repeated. (The points of the second cycle lie 2–3 Å above the first (which is only just above experimental error).) Comparison with Figure 3*b* carried out on the same preparation, indicates that points *1* and *2*, i.e., those of the first cycle may be low owing to some systematic error. As this small discrepancy was of no further consequence, it was not pursued further.

Effect of Crystallization Conditions and Sample Treatment on the Spacing Changes

Effect of Concentrations. Figures 5*a* and 5*b* show the effect of the concentration of the crystallizing solution. All preparations were obtained from xylene crystallized at 80°C. The subsequent swelling liquid was decalin. In agreement with existing experience, the long spacing was unaffected by concentration[2,3] (Fig. 5*a*). There is only a small but nevertheless noticeable variation in the long spacing increase on addition of decalin: samples crystallized from higher concentration gave a slightly larger long spacing increase. The effect is about 6 Å over two decades of concentration.

Effect of Crystallization Temperature. The crystals were prepared from 0.02% xylene solution by crystallizing at different temperatures. They were subsequently immersed in decalin. As seen from Figure 6*a*, the long spacing increases with the crystallization temperature, which is the well established fundamental behavior of chain-folded crystallization.[1] At the highest crystallization temperature of 90°C, two spacings are obtained simultaneously. As is well known,[2] this arises from the fact that some material remains uncrystallized at these high temperatures and precipitates during cooling at a lower temperature with a correspondingly lower spacing. (The

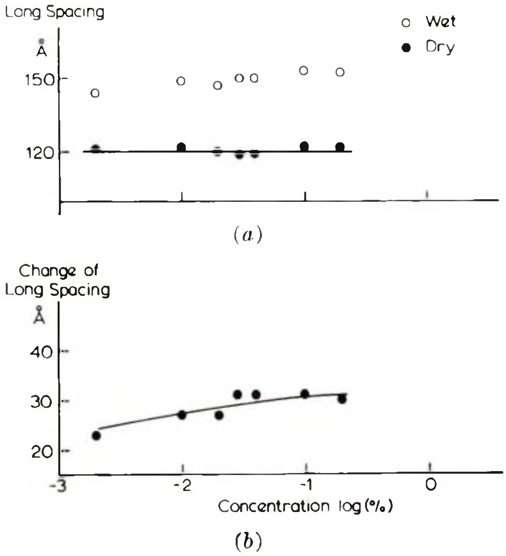

Fig. 5. Plots of (*a*) the effect of added decalin on the long spacing of single-crystal mats as a function of the concentration of the solution from which the crystals had been precipitated; (*b*) long-spacing increments from (*a*).

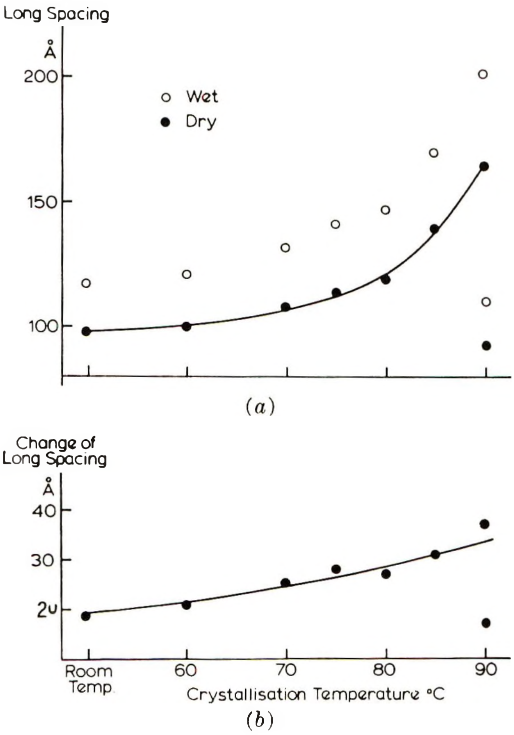

Fig. 6. Plots of (*a*) the effect of added decalin on the long spacing of single-crystal mats as a function of the crystallization temperature; (*b*) long-spacing increments from (*a*).

higher spacing can be obtained on its own if the precipitate is filtered off at 90°C, which was not done in the present experiment.)

The long-spacing increment on addition of decalin increases with increasing crystallization temperature (Fig. 6*b* ranging from 20 Å to 32 Å). The second, shorter spacing in the sample nominally crystallized at 90°C is lower than any of the isothermally obtained points. It is very noteworthy that the corresponding spacing increment is also the lowest (8 Å).

Effect of Heat Treatment (Annealing). The starting material was obtained by crystallization at 80°C from a 0.1% xylene solution by means of the self-seeding technique (T_s = 102.1°C).[4,5] The dried crystals were annealed at different temperatures for 24 hr, a fresh sample being used for each heat treatment. The long spacings were measured first dry, then after immersion in decalin. The results are shown by Figure 7.

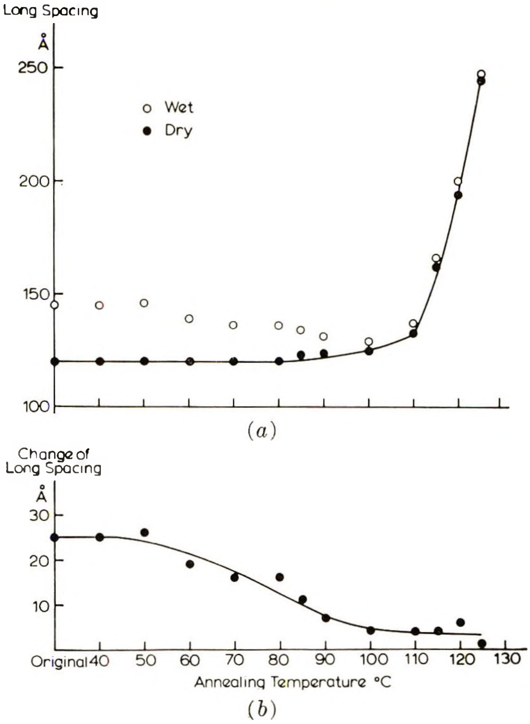

Fig. 7. Plots of (*a*) the effect of added decalin on the long spacing of annealed single-crystal mats as a function of the annealing temperature; (*b*) long-spacing increments from (*a*).

It is seen from Figure 7*a* that the long spacing of the dry mat starts to increase when the annealing temperature exceeds 80°C, i.e., the temperature of the original crystallization. Up to an annealing temperature of 100°C this effect is slight (less than 5 Å), but there is a large increase beyond, at higher annealing temperatures. This of course is in agreement with extensive past experience on annealing behavior.[6] The long-spacing increment due to addition of decalin (Fig. 7) remains constant up to an annealing temperature of 50°C but then decreases markedly. It is to be noted that it decreases to about half its value for the unannealed sample before any change in long spacing in the dry samples is observed. At 80°C, when the dried long spacing is still completely unaltered, this increment has reduced to about 15 Å from an initial value of 25 Å, and at the stage when the long spacing increase in the dried samples becomes definite (100°C), this increment has been reduced to a bare 4–5 Å. It stays at such a small value and finally falls to a negligible amount at the higher annealing temperatures, where most of the long-spacing increase of the initial dry material occurs.

Effect of Molecular Weight. The fractions available for this study, together with their special characteristics as made available to us, and source of supply are listed in Table I.

TABLE I

Molecular Weight		M_w/M_n	Supplier[a]
2.6×10^3	$\bar{M}_n$	—	P
9×10^3	$\bar{M}_w$	1.13	P
1.6×10^4	$\bar{M}_w$	1.60	P
7.6×10^4	$\bar{M}_v$	1.13	M
1.4×10^5	$\bar{M}_w$	1.10	P
3.5×10^5	$\bar{M}_v$	2.25	M
1.4×10^6	$\bar{M}_v$	Broad distribution (Not fraction)	A

[a] Suppliers: P = Dr. A. J. Pennings, Central Laboratory, Staatsmijnen/DSM., Geleen, The Netherlands; M = Dr. J. Mann, Shell Chemical Company, Carrington Plastics Laboratory, Manchester; A = Allied Chemical Co.

The fractions were crystallized from 0.02% solution of xylene by cooling in a 150-ml flask to room temperature. The long spacings of dried samples were not quite identical; they increased slightly with molecular weight (Fig. 8*a*). (This means that the longer molecules must have crystallized at a lower supercooling during the cooling process, which in turn implies higher rates of crystallization at comparable undercoolings.)

Decalin was used as an immersion liquid. It was noticed that the samples of lowest molecular weight did not imbibe decalin readily, and for this reason an immersion time of 24 hr was adopted. The effect on the long spacing is shown by Figures 8*a* and 8*b*. As it is seen, the long-spacing increment is larger and increasingly so for the higher molecular weights. This increase ranges from 8 to 38 Å for $M = 2.6$ to $M = 1.4 \times 10^6$ i.e., we have a difference of 30 Å. It is true that by Figure 6 the increasing long period of the starting material should be partly responsible for this effect. However, even if the relation shown by Figure 6 held equally for all the molecular weights involved, the change in the long-spacing increment

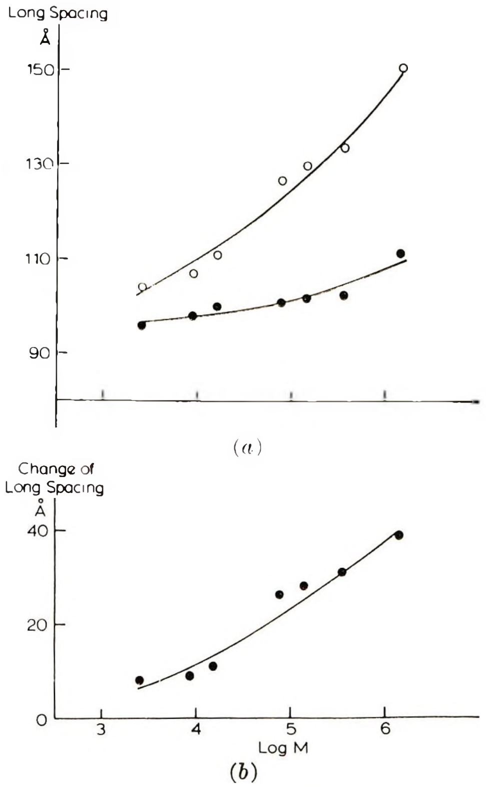

Fig. 8. Plots of (*a*) the effect of added decalin on the long spacing of single-crystal mats as a function of molecular weight of the polymer as stated in Table I; (*b*) long-spacing increment from (*a*). ○ = wet state; ● = dry state.

caused by decalin due to differences in the initial long spacings would be within 10 Å. Consequently, there remains a very sizeable effect attributable to differences in molecular weight.

DISCUSSION

Evidence for Swelling of Crystals

The principal effect under discussion is the reversible increase of the long period on addition of appropriate liquids. The question could be asked whether the spacing increase is just one transient stage in the process of disintegration of the lamellar stack into its constituents. However, the observations are definitely against this possibility. The ultimate spacing value for the wet mats could not be increased by the addition of more liquid, neither was it seen to increase with time (Fig. 2). It appears, therefore, that the increased separation of the layers on the addition of liquid corresponds to an equilibrium state.

One may suggest an absorption layer on the crystal interface causing the spacing increase. However, an increase of 22 Å (i.e., 11 Å per surface) would be too high for the low molecular weight liquids involved. Further, variations for samples of different chain length speak against simple surface absorption, as the basic absorption characteristics of a particular liquid–polymer pair are not expected to depend on the molecular weight of the polymer. It appears therefore that the effect in question may be due to the structure of the surface layer itself.

The most obvious suggestion is that the surface swells. This is borne out by the fact that the three liquids producing the effect are swelling agents, the swelling power as assessed from the solvent power at elevated temperatures, increasing in the sequence octane–xylene–decalin. We see that the effect on the long spacing increases is in the same order. Silicone oil is not expected to swell polyethylene, neither is any change of the long spacing observed on its addition.

The observed intensity increase of the low-angle reflections is consistent with the picture. Scattering is due to a variation in the electron density which in the present case of dried crystals corresponds to an alternation of a wide crystal portion of high and a narrow interfacial region of low electron density. The widening of the region of low electron density caused by the swelling agent will increase the intensity of the diffraction peak, more exactly, dependent on the amount and electron density of the swelling agent itself.

Structural Implications Concerning the Fold Surface

It is self evident that the crystals themselves do not swell, and therefore the swelling must involve disordered material which is tied to the crystal so as to exhibit the effect of limited swelling, as is familiar in crosslinked elastomers. There are two possibilities: (*a*) there are loose surface regions on the crystal to begin with; (*b*) such regions form under the action of the swelling agent at the expense of the crystal, i.e., the lattice breaks up surface downwards. Of course (*a*) and (*b*) could pertain simultaneously. Irrespective whether the cause is (*a*) or (*b*) it is important to note that it varies with the kind of material and sample preparation involved.

We may now consider the type of surface looseness which can be envisaged in a chain-folded crystal. There could be loose hairs; large loose loops due to nonreentrant folds; individual, protruding, adjacently reentrant folds taking up a loose configuration; a distinct defective surface region due to fold stems of uneven length, hence folds terminating beneath the layer boundary; and possibly loose tie molecules between consecutive layers. All these have been discussed elsewhere.[7,8] Even so, it will be stated that the model of uneven fold length has been recently receiving increasing experimental support and emphasis[9,10] in addition to previous theoretical predictions.[11] It emerges that this factor is a general one for crystals obtained under a variety of circumstances and is likely to be the principal cause of the crystallinity deficiency observed in crystals obtained from dilute solution to which other sources of looseness listed above may contribute to varying extents. Accordingly, the crystal layer would consist of a comparatively perfect central core with a gradually increasing number of terminating folds as the surface is approached. These buried folds will need to be adjacently reentrant, folds with nonadjacent reentry—so far as they are present—being necessarily confined to the top stratum of the crystallinity-deficient layer. Irrespective of structural detail, this model will result in a surface region of decreasing density on going outwards from the interior. Relatively few folds terminating deep inside the crystal will cause only dislocations, but as the number of such folds increases further towards the layer surface, the lattice will have to break up gradually and will virtually cease to exist at a level where the average density becomes equal to that of the amorphous material.

More specifically, if we confine ourselves to adjacent reentry, folds will have increasingly fewer neighbors until they will represent single fold protrusions. The average amorphous density, however, will be preserved, as such folds with few or no neighbors will bulge out in a random configuration and lie down on the folds terminating at a lower level around them. Further isolated protrusions will then lie flat on such disordered material already present, together with such nonadjacently reentrant large loops and loose hairs as might be present in the uppermost crystal level.

There is evidence that in the absence of much overlying material, surfaces of superposed layers containing uneven folds may intermesh, which under some circumstances can lead to crystal continuity between the layers (crystals with dislocation networks).[12]

With the above picture in mind, the effect of swelling agents can be readily visualized even without invoking destruction of more lattice. Accordingly, all the overlying loose elements would swell by virtue of preferred interaction with solvent and the accompanying increase in entropy, due to the larger number of configurations available for the loose elements when protruding in the solution as compared with lying on the crystal surface. Further, the swelling agent will penetrate into the layer of uneven folds and will produce swelling of all those folds which have loosely collapsed on their lower-lying fold environment as deep down as such are present, thus contributing further to the thickness increase of the layer. A certain amount of mobilization may still occur deep down in the layer of buried folds but its contribution to the thickness increase will be rapidly diminishing.

In the light of the foregoing, certain variations of the swelling effect fall readily in line. Large loose loops, hairs, loose intermolecular ties— that is, all those features of surface disorder which we consider as adventitious irregularities in the deposition of long chains—are expected to increase in number with molecular weight. The corresponding increase in swelling is in fact observed (Fig. 8). Increase in concentration is expected to give the same trend; this again seems to be observed even if the magnitude of the effect is unexpectedly small (Fig. 5). Increase in crystallization temperature could have several opposing effects, the results of which are not readily predicted. It is likely to lead to long excluded hairs owing to the larger length of chains which is expected to be in equilibrium with a deposited chain-folded ribbon. Also, the surface roughness caused by uneven folds should be larger as far as these are due to equilibrium roughness. However, the kinetically determined unevenness of folds should become smaller, leading to an opposite dependence on crystallization temperature.[11]

Annealing is seen to reduce the amount of swelling (Fig. 7). Two distinct temperature regions where such a reduction occurs can be specified: region A, in which the long spacing of the dried crystals is unaffected, and region B, where the long spacing of the dried crystals is increased. The effect in region A is potentially very significant because it is direct evidence that the fold surface can alter without change in long spacing, and, conversely, that a given long spacing obtained at a given crystallization temperature for a given material need not uniquely define the fold surface. More specifically, the reduction of the swelling between 50 and 85°C in Figure 7 is indicative of a regularization of the fold surface, a point of great interest requiring further exploration.[13] The total reduction of swelling in region B may appear surprising. It could well be due to intermeshing of folds in the course of fold-length increase which would both impede liquid penetration and reduce swelling, as interpenetrating folds will not be able to extend along the stem direction; for this the chains need to have a component lying parallel to the basal faces.

On the Possibility of Partial Lattice Disruption

So far the possibility that more material capable of swelling is created by the solvent has not been invoked. The possibility of this occurring is implicit in the interfacial premelting theories by Zachmann[14] and Fischer.[15] These authors consider that the usual broad melting range of polymer crystals is attributable to a gradual increase of the amorphous portion at the crystal surface. These arguments are based on the following considerations. The chain portions within the folds have a restricted configuration and hence lower entropies than the amorphous material in the melt but do not have the lowered enthalpy associated with the crystal proper. If the loops get larger, these constraints are released and the entropy increased. Up to a point this can lead to a decrease of the total free energy of the system, even when the increase of the loop occurs at the expense of the crystal; that is, the total amount of crystalline material is reduced. The extent to which the loops can increase at the expense of the crystal with a net reduction of free energy will depend on the temperature; with increasing temperature the equilibrium loop size will increase and the equilibrium crystallinity will decrease. The issue is more straightforward in case of nonadjacently reentrant large loops.[8] With adjacently reentrant loops this process can only take place in case of folds of sufficiently unequal length so as to provide an additional entropy of mixing.[16] (When the folds are equal the effect should not only be absent but even superheating may occur as far as interfacial melting is concerned. See comment in Ref. 8.)

Structurally, the increase of surface looseness can in principle occur in two ways: (1) the crystal thickness is reduced from the surface downwards, (2) the crystal thickness stays unaltered but more material is being fed into the fold region by movements equivalent to a refolding mechanism of the whole chain; (1) should lead to no appreciable change in the total layer thickness, while (2) should make it larger. It is suggested that reversible long-spacing changes observed in some special instances may be accountable in this way.[15]

As in the presence of solvents all melting phenomena are shifted to lower temperatures, the possibility arises that the observed surface melting effects may be due to this cause. As an increase in layer thickness is involved, it would need to be by mechanism (2). If such a mechanism does occur at all —it is unproven even in dry crystals—it would necessitate movement of the chain through the lattice. Chain mobility necessary for this is implied by all refolding phenomena but only at temperatures close to the melting range of the dry crystals. Solvent is not expected to increase the chain mobility within the lattice. Consequently, by this argument refolding, such as implied by the above interfacial premelting considerations, is not expected to occur at room temperature. We conclude, therefore, that our swelling effect involves only material which is present in a form accessible to the solvent to begin with, and not disordered material created by the solvent at the expense of the crystal.

Correlation with Other Effects

Evidence for swelling of crystals has been obtained previously by different techniques, namely by NMR and by direct electron microscope observation of gold-decorated crystals.

NMR. It has been reported[17] that the proton resonance absorption peak narrowed on addition of swelling agents, the effect being reversible. This implies increase of chain mobility on liquid addition, hence swelling. The experiments as they stand do not define the location of this mobilizable material. However, the observation that the thinning of the crystal by selective oxidation[18,19] eliminates this mobilization effect strongly suggests that it is situated along the fold surface. The method should in principle give the quantity of mobilizable material; however, this is sensitively dependent on the procedure by which the peaks are isolated in the resonance curve. Earlier results imply only 2–6% of mobilizable material;[17,19] however, more recent separation methods put these figures up to 10% and beyond.[20]

Electron Microscopy of Gold-Decorated Crystals. As described elsewhere,[21] a thin layer of gold, not sufficient to cover the surfaces, produces a deposit of fine gold grains appearing as dark spots along the crystal surface. These dots align preferentially along edges and steps and hence can be used to show up such discontinuities. On surfaces with no such structural features they form a random pattern of dots. When such decorated crystals are flooded with xylene, the random dot pattern changes, acquiring a coarser distribution.[8,22] Evidently the solvent affects the crystal surface in so far as it must mobilize material along it, which implies swelling. It can be seen further that this mobilization effect is not uniform, e.g., crystal portions grown at the early stages, that is within the crystal interior, are more effected. Current exploration of such effects reveal that higher molecular weight material leads to more mobilizable fold surface and hence must give rise to more loose material, which is in line with expectations.[23]

To sum up, the three completely different methods all reveal the same phenomenon: partial swelling of the crystals. The three methods are complementary. NMR tells us about changes in molecular mobility as a result of swelling, and at least in principle it should be able to give quantitative information. The low-angle x-ray method reveals the volume increase associated with the swelling and attributes the effect to the material lying between the lamellae, hence by implication along the lamella interface. Electron microscopy provides direct visual evidence for the presence of mobilizable material along the crystal face and provides means of distinguishing between individual crystals and crystal portions as regards mobilizability. However, this test is only qualitative.

We see that the present low-angle x-ray studies occupy a central position among the other methods of detecting solvent-induced swelling and mobility in single crystals. Studies of this kind have obviously an important part to play in the elucidation of fold-surface problems and in combination with other techniques offer some obvious new points of departure. Such are the quantitative assessment of solvent uptake, evaluation of the low-angle x-ray intensities, and correlation with selective degradation studies.

CONCLUSIONS

The observed liquid-induced long-spacing increase is consistent with swelling of the crystal surface. This implies the presence of material there capable of swelling, which by necessity must be in a disordered state with a sizeable chain component along the plane of the basal surface of the crystal. Nevertheless, such material cannot be a unique attribute of chain folding as the amount of this swelling effect depends on molecular weight, crystallization conditions, and heat treatment of otherwise chain-folded systems and in fact can be altered within one and the same sample without change in fold length. Neither can it be the only or even the main source of crystallinity deficiency in chain-folded crystals, as such crystals of low molecular weight material show hardly any swelling, possibly only absorption, while still possessing crystallinity deficiency as assessed by conventional methods.[12] We suggest that the material responsible for the swelling is a variable component of surface looseness overlying the rest of the fold surface which contains other, possibly more intrinsic, sources of crystallinity deficiency.

We are greatly indebted to Professor S. Okajima, Tokyo Metropolitan University, who first suggested the investigation of the effect of swelling agents on single crystals. The first positive effect was obtained by one of us (Y.U.) in the course of a trial experiment in his laboratory. Also we wish to thank Dr. H. Hendus, Ludwigshafen, for drawing our attention to the effect of residual solvents on the long spacing. Our thanks are due to Dr. A. J. Pennings, Dutch State Mine Laboratories, Geleen and Dr. J. Mann, Shell, Carrington Laboratories, Manchester for supply of fractions.

References

1. A. Keller and A. O'Connor, *Discussions Faraday Soc.*, **25**, 114 (1958).
2. D. C. Bassett and A. Keller, *Phil. Mag.*, **7**, 1553 (1962).
3. T. Kawai, *Makromol. Chem.*, **113**, 282 (1968).
4. D. J. Blundell, A. Keller, and A. J. Kovacs, *J. Polym. Sci. B*, **4**, 481 (1966).
5. D. J. Blundell and A. Keller, *J. Macromol. Sci. B*, **2**, 337 (1968).
6. W. O. Statton and P. H. Geil, *J. Appl. Polym. Sci.*, **3**, 357 (1960).
7. A. Keller, *Kolloid Z. Z. Polym.*, **231**, 386 (1969).
8. A. Keller, *Repts. Progr. Phys.*, **31**, Part 2, 623 (1968).
9. A. Keller, E. Martuscelli, D. J. Priest, and Y. Udagawa, paper presented at IUPAC Symposium, Leiden, 1970; *Preprint V6*, submitted to *J. Polymer Sci. A-2*.
10. D. M. Sadler, T. Williams, A. Keller, and I. M. Ward, *J. Polym. Sci. A-2*, **7**, 1819 (1969).
11. J. I. Lauritzen and E. Passaglia, *J. Res. Nat. Bur. Stand.*, *A-71*, 261 (1967).
12. D. M. Sadler and A. Keller, *Kolloid Z. Z. Polym.*, **239**, 641 (1970).
13. J. D. Hoffman, J. I. Lauritzen, E. Passaglia, G. S. Ross, L. J. Frolen, and J. J. Weeks, *Kolloid Z. Z. Polym.*, **231**, 564 (1969).
14. H. G. Zachmann, *Kolloid Z. Z. Polym.*, **231**, 504 (1969).
15. E. W. Fischer, *Kolloid Z. Z. Polym.*, **231**, 458 (1969).
16. H. G. Zachmann and A. Peterlin, *J. Macromol. Sci. B*, **3**, 493 (1969).
17. E. W. Fischer and A. Peterlin, *Makromol. Chem.*, **74**, 1 (1964).
18. A. Peterlin, G. Meinel, and H. G. Olf, *J. Polym. Sci. B*, **4**, 399 (1966).
19. D. J. Blundell, A. Keller, and T. Connor, *J. Polym. Sci. A-2*, **5**, 991 (1967).
20. K. Bergman and K. Nawotky, *Kolloid Z. Z. Polym.*, **219**, 132 (1967).
21. G. A. Bassett, D. J. Blundell, and A. Keller, *J. Macromol. Sci. B*, **1**, 161 (1967).
22. D. J. Blundell, Ph.D. Thesis, University of Bristol (1967).
23. A. Keller and D. M. Sadler, to be published.

Received July 13, 1970

JOURNAL OF POLYMER SCIENCE: PART A-2 VOL. 9, 453-462 (1971)

Occurrence of Rippling During the Deformation of Oriented Polyethylene

RICHARD E. ROBERTSON,* *General Electric Research and Development Center, Schenectady, New York 12301*

Synopsis

Rippling is another mode, in addition to kink-band formation, by which oriented polyethylene can deform and results in a profuse and irregular waviness in the fibrils. For the medium-density and high-density polyethylenes investigated, rippling tended to occur only at strain rates below about 1 min^{-1} at 25°C. Above this rate, kink bands tended to form. It is suggested that rippling results from easy slip between the fibrils of the oriented polymers and from the resistance of the fibrils to shortening under a compressive stress. The applied shear stress is reduced by the easy slip to a simple compression along the fibrils, and this distorts the fibril into the series of waves that constitutes rippling. Stress-strain measurements confirm that fibril slip is considerably easier under the rates at which rippling occurs than at the rates at which kink bands form.

INTRODUCTION

It was previously reported[1] that kink bands formed when oriented polyethylene was sheared along directions in which the fibrils of the oriented polymer were compressed. The kink bands appear in the specimen at low magnification as lines that run more or less parallel with planes of maximum shear stress. At higher magnification the lines are seen to be bands within which the fibrous texture of the polymer changes direction. The striking characteristics of the kink bands are the sharpness of the band edges and the mirror symmetry of the fibrous texture within the band compared to that without. The sharpness of the edges is due to the abruptness with which the fibrils entering the band change direction, often within a width of about 100 Å.

We now wish to report on a type of deformation we call "rippling" that occurs during a similar shearing of oriented polyethylene. An example of rippling is shown in Figure 1 in a specimen that had been sheared about 15%. The photograph shows the gauge section or the section of the specimen between the two clamps of the shearing device. The clamps were positioned just beyond the side edges of the picture, and during the shearing the left-hand clamp moved downward and the right-hand clamp upward. It is the periodically recurring dark bands that we

---

* Present address: Scientific Research Staff, Ford Motor Co., Dearborn, Michigan 48121.

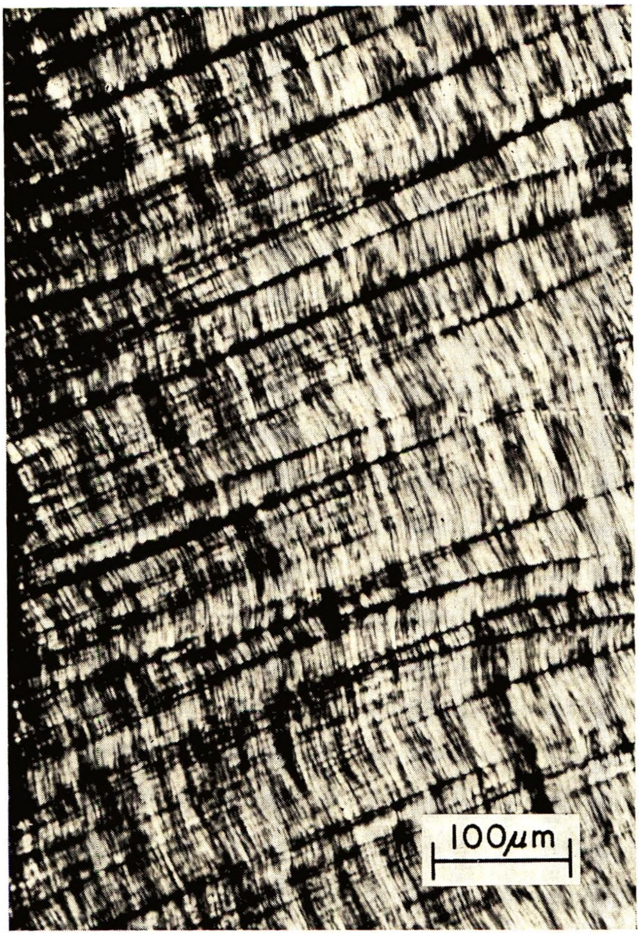

Fig. 1. Annealed, oriented high-density polyethylene after being sheared at the rate of 10^{-2} min^{-1}, as seen with transmitted light. During shearing the left edge of the specimen had moved downward and the right edge had moved upward.

call rippling. We see that these bands are just perpendicular to the background texture of the specimen due to the orientation, which runs from upper left to lower right. In the following we shall describe the rippling texture in more detail, give the conditions for its occurrence, and present a mechanism for it.

EXPERIMENTAL

Two polyethylenes were studied: a high-density polyethylene (Marlex 6050) and a medium-density polyethylene that contained a small amount of butylene (Marlex 5065). Both were made by the Phillips Petroleum Co., Bartlesville, Oklahoma. The polymers were pressed into $^1/_{32}$-in.-thick sheets and stretched about 700% after a few minutes exposure in an air oven. The temperature of the oven for the high-density polyethylene was 135°C and that for the medium-density polyethylene was 130°C. After stretching, the polymers were quickly cooled to room temperature under tension. The medium-density polyethylene was used as stretched, but the high-density polyethylene was usually annealed free for $^1/_2$ hr at 125°C after stretching. However, the occurrence of rippling was independent of whether the specimen had or had not been annealed before shearing.

The specimens were deformed in simple shear with devices described previously.[1,2] The specimens shown in the light and electron micrographs were sheared with our "improved" device.[1] These specimens were about 0.25 mm thick and were sheared across a gap of a width about 0.5 mm. The stress–strain measurements were made with our first shearing device.[2] The specimens for this were about 0.1 mm thick and were sheared across a gap of nominal width 0.1 mm. A variable in all of our studies has been the angle between the plane across which shearing occurs and the axis along which the specimen had been previously stretched. All of the shearing was done at approximately 25°C.

RESULTS

Rippling and the Conditions for Its Occurrence

The specimen that was shown in Figure 1, which was taken with transmitted light, is shown with a combination of transmitted and reflected light and at higher magnification in Figure 2. We see that the fibrils follow, more or less together, an irregular, weaving path, though before shearing the fibrils were straight. In general, this waviness exists throughout the gauge section of the specimen. A similar texture is seen at higher resolution in the electron micrograph shown in Figure 3. This micrograph was obtained from a shadowed replica of the surface of another rippled specimen. The dark bands in Figure 1 are found to be correlated with the changes in fibril directions. The darkness of the bands seems to arise from scattering of light being transmitted through the specimen.

As occurs when kink bands form, continued shearing eventually reestablishes the fibrous texture, though in the mirror image of the initial texture; i.e., if the angle between the shear plane and the axis of orientation initially is α, the angle becomes $-\alpha$ after the re-establishment of the texture. Shearing the specimens beyond the amounts shown in Figures 1–3 often causes the fibrils to bend sharply enough that the waves collapse into kinks. Such a result is shown in Figure 4. Following the collapse of the waves into kinks, further shearing often causes the angle between the fibrils on the two sides of the kink to decrease. This continues until the two ends of each fibril, where they pass under the two clamps, are brought just opposite each other across the gauge gap. At this point the fibrils will have been compressed as much as they will be in the reorientation process, and further shearing causes the angle between the fibrils on the two sides of the kink to increase. The increase in angle then continues until

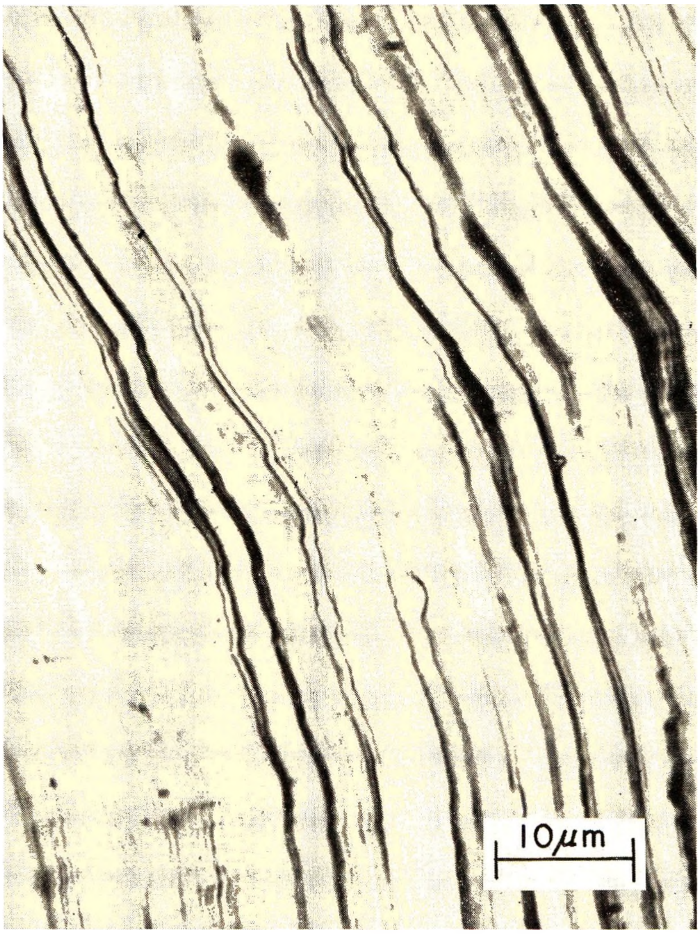

Fig. 2. Same specimen with the same orientation as in Fig. 1, here seen at higher magnification with a combination of transmitted and reflected light.

the kinks essentially disappear and the texture obtained is the mirror image of the initial texture.

The effect on the deformation, of the angle between the axis of orientation and the direction of shear is shown in Figure 5. For each of the photographs shown in Figure 5 the clamp just out of the left edge of each picture had moved downward and that outside the right edge had moved upward during shearing. We see that essentially the same deformation pattern was produced for the range of angles shown. This is almost the whole range of angles for which the fibrils are compressed by shearing. Regardless of the initial angle between the shearing direction and the orientation axis, the dark bands are all seen to be more or less perpendicular to the fibrous texture of the oriented polymer, and the texture seen at higher magnification in each specimen was similar to that in Figure 2. However, as the specimens differ in the extent to which the fibrils are

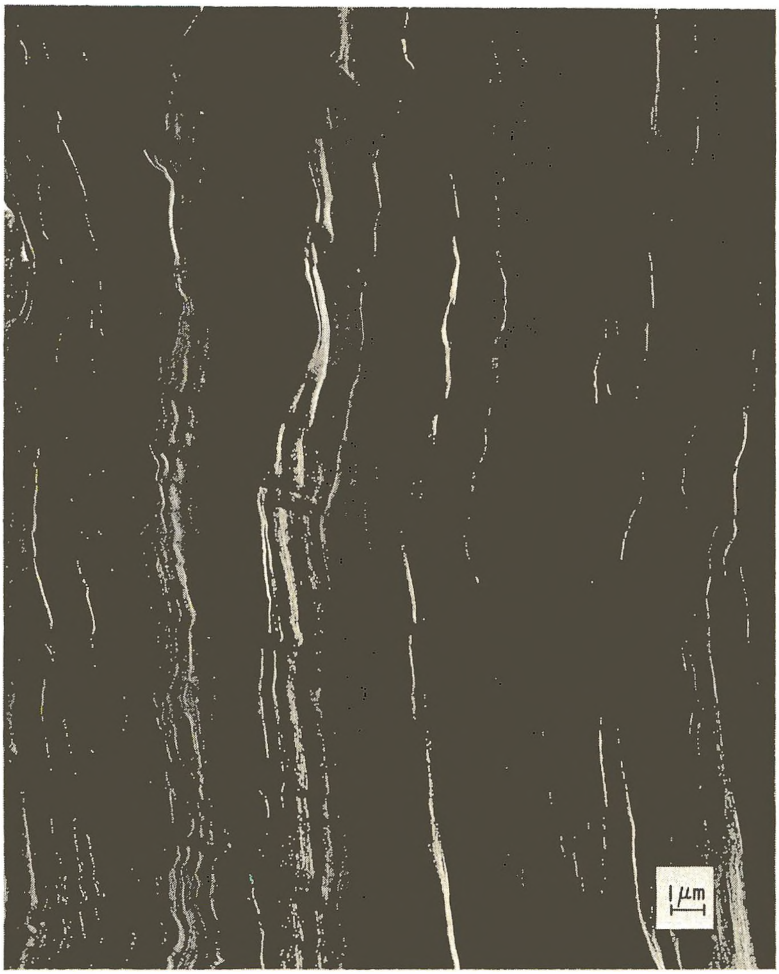

Fig. 3. Electron micrograph of a rippled surface; oriented high-density polyethylene, not annealed.

compressed in the reorientation process, the collapse of the fibril waves into kinks, as in Figure 4, does not occur in all specimens. The kinks develop only in the specimens for which the angle between the shear plane and the axis of orientation is less than about 45°.

For the polymers studied we found that rippling occurred when the strain rate was below about 1 min^{-1}. Figure 6 indicates the change in the type of deformation as the strain rate is varied through 1 min^{-1}. The narrow band or line extending upward from the bottom center of Figure 6 is a kink band that was produced as the specimen was strained 10% at the rate of about 10 min^{-1}. The kink band initiated at a flaw (actually a razor cut) just below the area photographed. Following the 10% strain at the rate of 10 min^{-1}, the specimen was strained 20% at the rate of 0.1 min^{-1}. It was during this latter rate that the rippling occurred.

Fig. 4. Electron micrograph of a rippled surface after about twice the strain as that in Fig. 3; annealed, oriented high-density polyethylene.

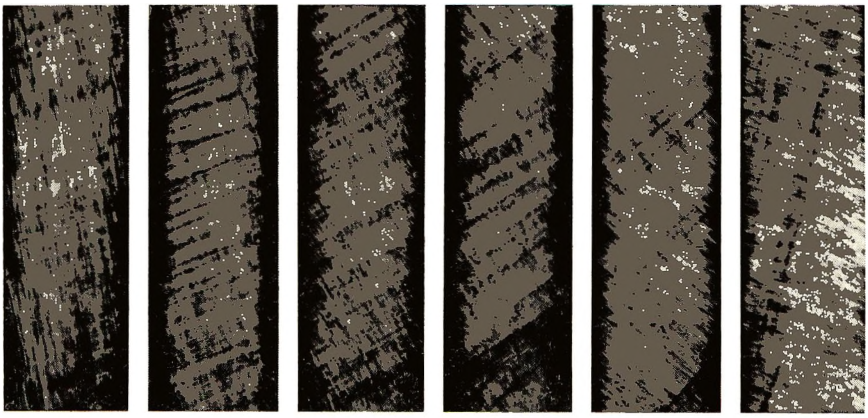
10° 20° 30° 40° 50° 60°

Fig. 5. A series of rippled specimens sheared with the angles indicated between the initial orientation axis and the shear plane, which was vertical in these pictures. The shear rate used was about 10^{-2} min^{-1}. The width of each picture is about 400 μ.

Fig. 6. A specimen containing both a rippled region and a kink band. This specimen had been sheared (right side upward, left side downward) 10% at the rate of approximately 10 min^{-1} and then 20% at approximately 0.1 min^{-1}. The marker represents 10 μ.

Straining other specimens at strain rates intermediate between 0.1 and 10 min^{-1} gave mixtures of rippling and kink bands; occasionally mixtures were obtained even outside the range 0.1–10 min^{-1}, but kink bands clearly predominated at rates above and rippling below about 1 min^{-1}.

Change in the Anisotropy of Oriented Polyethylene with Strain Rate

Previous[3] shear stress–strain measurements had been made on annealed, oriented high-density polyethylene strained at a rate of 0.001 in./min. These were extended to the medium-density polyethylene, and the measurements for both materials were extended to the rate of 0.050 in./min. Shown in Table I are the yield stresses for shear parallel to the orientation axis for both the unannealed medium-density and the annealed high-density polyethylenes at the two rates. Because of an uncertainty in the gap width between the clamps, though it was nominally 0.004 in., we are uncertain of the actual strain rates, but they do straddle 1 min^{-1} and correspond in order of magnitude to 0.1 and 10 min^{-1}, respectively. For both polyethylenes the yield stresses are seen to be considerably smaller at the slower rate.

TABLE I
Shear Yield Stress Parallel to Orientation Axis and Anisotropy Ratio versus Rate

Polyethylene	Clamp displacement, rate, in./min.	Yield stress $\times 10^8$, dyne/cm^2	B_2/B_0	
			$\epsilon \rightarrow 0$	$\epsilon =$ 0.002 in.
Marlex 5065	0.001	0.70	0.39	0.42
"	0.05	1.15	0.28	0.36
Marlex 6050-annealed	0.001	1.30	0.22	0.31
" "	0.05	1.65	0.17	0.25

A perhaps more appropriate measure of the effect of rate on the shear stress is the mechanical anisotropy, which was obtained as follows. Stress–strain curves were plotted for many different angles between the orientation axis and the shear direction. The stresses from each at given amounts of strain were then fitted to the following equation, which is the simplest equation that fits the data at all well:

$$\sigma = B_0 + B_1 \cos 2(\alpha - \delta) - B_2 \cos 4\alpha$$

where σ is the stress at a particular level of strain, α is the angle between the axis of orientation and the shear plane, and B_0, B_1, B_2, and δ are constants. An example of the data and the fitted curve is shown in Figure 7. These data for annealed, oriented high-density polyethylene deformed at the rate of 0.001 in./min are the same as given previously,[3] though the sense of the angle α has here been reversed to conform to general usage. The

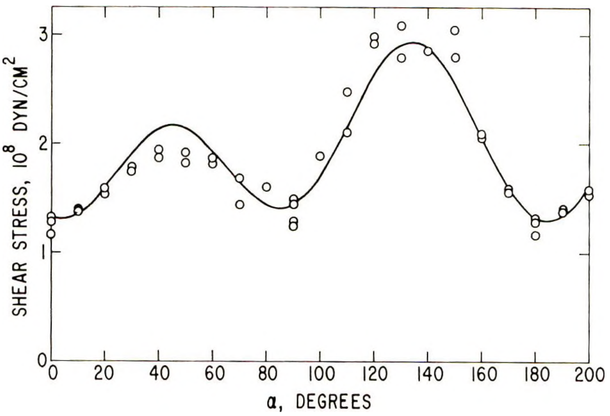

Fig. 7. Shear stresses after shearing annealed, oriented high-density polyethylene specimens to a clamp displacement of 0.0015 in.

anisotropy is given essentially by the ratio B_2/B_0. The term B_1 arises from the difference in response between stretching and compressing the fibrils and extrapolates to zero at zero strain.[3] Included in Table I are both the limiting values of B_2/B_0 at zero strain and the values after a displacement of the clamps by 0.002 in., which corresponds to a nominal strain of 50%. We see for both polymers that the anisotropy is larger at the slower rate.

DISCUSSION

We can readily understand the origin of rippling if we assume that (a) the fibrils of the oriented polyethylene are relatively free and (b) that they do not shorten on being compressed. In effect, we are viewing the oriented polyethylene as a collection of threads. The shear strain applied to the specimen in Figure 8*a* then becomes a compression along the fibrils. In response, the fibrils, like threads, become slack and tend to loop back and forth. It is because the fibrils are packed together that they tend to weave in concert with their neighbors as indicated in Figure 8*b*.

The assumption that the fibrils do not shorten when they are compressed is more or less confirmed by the results. The contour length of the fibrils after the deformation remains approximately the same as before shearing. Nor do the fibrils seem to shorten during the formation of kink bands either. The constancy of fibril length is believed to be the reason for the

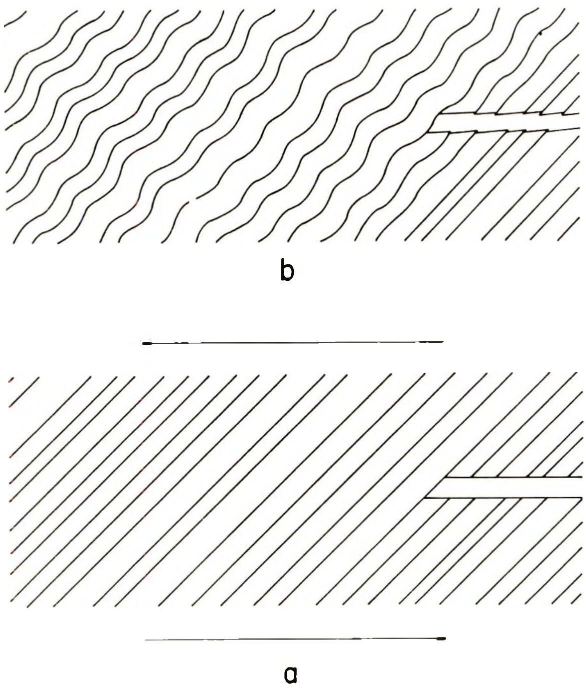

Fig. 8. Mechanism of rippling.

mirror symmetry of the fibrous texture within the kink band as compared with the texture without.[1]

Support for the assumption that the fibrils are relatively free under the conditions during which rippling occurs is given by the data in Table I. Of course, the fibrils are not completely free, for then the yield stress for shear parallel to the orientation axis would be zero. Nonetheless, it is seen in Table I that over the range of strain rates for which the deformation changes from kink band formation to rippling that the yield stress decreases considerably and the anisotropy increases significantly. This suggests that rippling replaces the formation of kink bands because of the relative ease of fibril slip. The converse suggestion is that kink band formation replaces rippling at higher strain rates because of the inhibition of fibril slip. Without easy fibril slip the shear stress can concentrate at flaws of the type shown in Figure 8, leading to a localized deformation of the fibrils adjacent to the flaw, and thence to the kink band.

We wish to acknowledge the help of Mrs. C. W. Joynson with the stress-strain measurements and W. J. Barnes with the electron micrographs.

References

1. R. E. Robertson, *J. Polym. Sci. A-2*, **7**, 1315 (1969).
2. R. E. Robertson and C. W. Joynson, *J. Appl. Phys.*, **37**, 3969 (1966).
3. R. E. Robertson and C. W. Joynson, *J. Polym. Sci. A-2*, **6**, 1673 (1968).

Received July 13, 1970

JOURNAL OF POLYMER SCIENCE: PART A-2 VOL. 9, 463–482 (1971)

Effect of Pressure in Capillary Flow of Polystyrene

RICHARD C. PENWELL and ROGER S. PORTER, *Polymer Science and Engineering, University of Massachusetts, Amherst, Massachusetts 01002*

Synopsis

Several corrections possibly required for capillary flow are based on the existence of a linear relationship between the pressure drop along the capillary and the length-to-diameter ratio at a given temperature and shear rate. Recently, the appearance of nonlinearities in this relationship has created some concern as to the cause of this behavior. The occurrence and an explanation of the nonlinearities for polystyrene form the basis of this study. A narrow-distribution, low molecular weight (20,400) polystyrene was tested in eight capillaries at temperatures of 140 and 160°C to initiate the discussion of the nonlinearity in a ΔP (pressure) versus L/D (length/diameter of capillary) plot. The sample exhibits negligible extrudate swelling at all pressures which reinforces the idea that pressure is influencing the flow. The pressure dependence of viscosity is determined using the equivalent expression of the WLF equation derived from free volume theory. Justification for its use is presented. A pressure correction, representing the increased shear stress necessary for flow of the higher viscosity material, is found to linearize the ΔP versus L/D data. A narrow-distribution, high molecular weight polystyrene (670,000) is subjected to a similar analysis at 165°C by using nine capillaries. The situation is quite different, as the high molecular weight sample is not nearly as ideal as the low molecular weight polystyrene.

INTRODUCTION

In a previous work,[1] a possible pressure effect on polymer viscosity in capillary flow was considered. Narrow-distribution polystyrenes of low (20,400) and high (670,000) molecular weight were studied. Pressure was thought to decrease the free volume available for flow and thereby increase the glass transition temperature T_g. Variations in the viscosity resulting from a shift in the glass transition were calculated by using the WLF equation. A more critical view of the use of the WLF equation for this purpose, based on its derivation from Doolittle's free volume expression, is discussed in the present work.

Nonlinearities occurring in pressure versus L/D (length-to-diameter ratio of a capillary) plots, frequently called Bagley plots, for polystyrenes have consistently been reported in the literature.[1–4] The nonlinear data were disregarded in one case,[2] while in another, the possibility of hydrostatic pressure affecting the results was suggested, without analysis.[4] Although McLuckie and Rogers have chosen to analyze their nonlinear pressure versus L/D plots as due to elastic energy effects,[3] there is much evidence to suggest that the nonlinearities could very well be due to the pressure dependence of the apparent viscosity.[1,3–15]

The present work is concerned with an attempt to clarify the cause for the nonlinearities which have appeared in Bagley plots for polystyrene, as have been mentioned many times recently. A low molecular weight (20,400) polystyrene of narrow distribution (hereafter called the 20.4K polymer) was selected for initial study, as it represents a model system in many respects. The apparent viscosity exhibits Newtonian behavior in the absence of pressure effects,[1] it gives no indication of elastic energy storage and it is comparatively stable to shear and thermal degradation for the conditions used. The influence of pressure is evaluated from any nonlinearities appearing in Bagley plots by utilizing the WLF equation.

Conclusions drawn from the study of the low molecular weight polystyrene are applied to the analysis of the nonlinearities in Bagley plots for a high (670,000) molecular weight polystyrene of narrow distribution (hereafter called the 670K polymer). This represents a more complicated system, as it is highly susceptible to thermal and shear degradation.[16] It is also a power-law fluid and exhibits appreciable elastic energy effects. The total entrance correction is of such magnitude that it must be accounted for before a pressure correction can be applied. Pressure-corrected capillary data are presented and compared with data from a cone-and-plate viscometer.

EXPERIMENTAL

The low and high molecular weight polystyrene standards used in the tests were obtained from Pressure Chemical Company, Pittsburgh, Pennsylvania. The 20.4K polymer has $\bar{M}_w/\bar{M}_n \leq 1.06$ and the 670K polymer has $\bar{M}_w/\bar{M}_n \leq 1.10$. Sufficient material of each molecular weight was available to make reuse unnecessary and thus minimizing thermal, shear, and oxidation effects.

All flow measurements were made through tungsten carbide capillaries in an Instron capillary rheometer (Instron Corporation). Several capillaries, necessary to obtain data for the Bagley plots, were used and are listed in Table I. The various capillaries gave a span of length to diameter

TABLE I
Capillary Dimensions, Entry Angle 90°

Diameter, in.	Length/diameter
0.02000	12.20
0.02000	50.32
0.03020	30.53
0.03015	66.57
0.03018	99.67
0.05035	39.01
0.06026	4.26
0.06040	33.11
0.06014	49.88

ratios from approximately 4 to 100. The temperature variation along their lengths was estimated to be within 1°C.

It is desirable to eliminate voids in samples packed in the capillary reservoir. This was accomplished by careful packing of the polymer powder and flakes. The test temperatures were 140°C and 160°C for the low molecular weight polystyrene and 165°C for the high molecular weight polystyrene. Thermal degradation at these temperatures was negligible inside the rheometer.[16] This was important, as the time required for stress equilibrium was large compared to the time required for thermal equilibrium. The limitation in most of the tests was the maximum recommended load that the instrument would sustain, 1900 kg/cm.[2] Data points rechecked at various times within the same run and on different runs indicated a reproducibility of approximately 5%.

Several corrections possibly required for capillary flow measurements were considered. Pressure losses in the barrel region were measured, by using the barrel as a capillary, for all crosshead speeds and were found to be negligible except for the capillary of lowest L/D. This matter is discussed in a later section. The kinetic energy correction was assumed to be negligible for the conditions of these tests. In the absence of pressure effects, the end correction from a linear extrapolation of a Bagley plot[17] and the Rabinowitsch correction[18] are easily obtained. However, as found earlier,[1] deviations from Newtonian and power-law behavior caused by pressure effects make both corrections fatuous. The possibility of making the Bagley corrections under conditions of pressure effects forms the basis for this work.

A Weissenberg Rheogoniometer (Model No. 17) was used to measure the apparent viscosity of the 670K polymer for comparison with the corrected capillary data. To insure the removal of air, the powder was placed on the plate of the rheometer and was maintained at 185°C in a nitrogen atmosphere for several hours. Upon attainment of thermal equilibrium at 165°C, measurements were made with a 5.0-cm plate and a 2° angle cone. The viscosity values calculated, by comparison with the literature,[19] were for a polystyrene with a molecular weight of 67,000. Molecular degradation reduced the molecular weight by a decade, in agreement with the work of Arisawa and Porter.[16] The thermal degradation problem was circumvented by preforming the test sample in a press at 165°C until all voids were eliminated. The time required for thermal equilibrium at 165°C had little effect on the degradation of the sample in the rheometer.[16]

DISCUSSION

Free-Volume Model

The pressure dependence of the apparent viscosity and related properties for amorphous polymers has received considerable attention recently.[1,3,5–15,20–23] A discussion appropriate to the present work can be initiated by considering Doolittle's[24] relation between viscosity and free volume. Doolittle found a linear relation when $\ln \eta$ was plotted as a function of v_0/v_f. He originally defined η as the coefficient of viscosity and v_f/v_0 as the relative free volume. He suggested that changes in the relative free volume could result from changes in pressure and temperature. This appeared to be a very convenient means of relating viscosity to free volume rather than temperature.

Williams[25] used a form of Doolittle's equation

$$\log \eta = \log A + \frac{B}{2.303\left[\dfrac{v_g - v_0}{v_0} + \dfrac{1}{v_0}\dfrac{dv}{dT}(T - T_g)\right]} \tag{1}$$

$$= \log A + \frac{B}{2303f}$$

where f is the relative free volume, A and B may be considered constants, and v_g is the volume at the glass transition temperature T_g, to calculate the free volume parameters from the data of Fox and Flory on polystyrene fractions.[26] Since $\log a_T \approx \log \eta_T - \log \eta_{T_g}$, as mentioned by Williams,[25] the following equivalent form of the WLF equation results:

$$\log a_T = -\frac{\dfrac{B}{2.303f_g}(T - T_g)}{f_g/\alpha + T - T_g} \tag{2}$$

where the glass transition temperature T_g is taken as the reference temperature, α is the thermal expansion coefficient, and f_g is the relative free volume at T_g.

Ferry and Stratton subsequently attempted to include the pressure dependence of viscosity by using the following modified form for the relative free volume:[21]

$$f = f_g + \alpha(T - T_g) - \beta P \tag{3}$$

where, in their development, α and β are considered as constants.

Haward[5] has considered the compressibility of polymers as being the sum of a free-volume compressibility and a molecular compressibility, noting that molecular compressibilty occurs only at high pressure (>3000 bars). He uses his modified van der Waals equation to calculate compressibility coefficients.

Martynyuk and Semenchenko[6] studied the temperature dependence of compressibility of amorphous polymers, defining three regions: a region of low compressibility ($T < T_g$), a region in which β changes rapidly with T ($T \approx T_g$) and a region of high compressibility ($T > T_g$) in which the compressibility is a linear function of T. They used x-ray techniques to verify that the polymers were amorphous at various pressures.

Matheson has used his modified free-volume approach to show that the pressure dependence of viscosity for liquids can be calculated from free-volume theory.[10] He suggests that the viscous flow must be determined by the probability of sufficient free volume being available to the flow molecule rather than the probability of a molecular jump which predominates at higher temperatures.

Ito, using a Westover-type extrusion rheometer, reported the effect of hydrostatic pressure on viscosity for several polymers.[9] At 190°C, the viscosity of polystyrene showed an increase by approximately a factor of 10 when subjected to a hydrostatic pressure of 500 kg/cm^2.

Holliday ran tension tests on polystyrene under hydrostatic pressure and noted a change from brittle to ductile failure as the pressure was increased.[15] He concluded that the increase in the maximum load with pressure was caused by hydrostatic pressure increasing the glass transition temperature. Mears, Pae and Sauer also noted an increase in the modulus and ductility with pressure.[14] They also concluded that high pressure can decrease the free volume and shift the glass transition temperature.

Matsuoka and Maxwell have made extensive measurements of the compressibility of polystyrene.[13] They observed that the shift in the glass transition, or identically the transition from a rubber to glass, depends on the rate of pressure application. They found no indication of crystallization occurring.

Previously, the suggestion was made that the apparent viscosity of narrow-distribution polystyrenes, measured in a capillary viscometer, was strongly pressure-dependent.[1] Considering the conditions of the tests in the earlier study, the free-volume approach to explain the pressure dependence of viscosity seemed to be generally valid. The WLF equation was used as given in eq. (2), where the relative free volume is:

$$f = f_g + \alpha(T - T_g) \tag{4}$$

with α (thermal expansion coefficient), T_g, and β (compressibility coefficient) pressure-dependent. The pressure functions for the above parameters for polystyrene have been given by Gee and appear to be based on sound analysis.[20] He has used the Tait equation to describe the compression of polystyrene in the form:

$$V_0 - V = V_0 C \ln [1 + (P/B)] \tag{5}$$

where V is the volume at pressure P, V_0 is the volume at zero pressure, C is a constant, and B is a temperature-dependent parameter (constant under isothermal conditions).

Differentiation of the Tait equation with respect to temperature and pressure gives the following expressions for the coefficient of expansion and the compressibility coefficient:[20]

$$\alpha_l = \alpha_{0l} + P\beta_l(d \ln B_l/dT) \tag{6}$$

$$\beta = V_0 C/V(P + B) \tag{7}$$

where $\alpha_{0l} = 5.34 \times 10^{-4}$ deg^{-1} (subscript l refers to values above T_g) and the other parameters are as defined previously. The pressure dependence of the glass transition is presented graphically by Gee[20] and in equation form by Miller.[27] Sasabe and Saito have recently used the Tait equation to successfully calculate the pressure dependence of v_l, v_g, and α for poly(vinyl chloride) and poly(methyl methacrylate).[8]

With the relations for the pressure dependence of the free volume parameters available,[20] eqs. (3) and (4) may now be compared as shown in Table II. The value of f_g selected is for a polystyrene fraction with a molecular weight of 19,300.[25] The value is comparable to the widely accepted value of 0.025 and certainly in agreement with the work of Bondi[28] and Plazek.[29] Gee[20] and Miller[27] present values of approximately 0.927 for v_g at a temperature of 140°C. For the values of α and β selected (Gee's values[20]), calculations of the relative free volume were made at a temperature of 140°C. The pressure was increased until the volume was reduced to v_g. The value of the relative free volume F_2 is 0.025 at $v = 0.925$ according to eq. (4). With α and β constant at $P = 0$, the relative free volume F_1, given by eq. (3), decreases much too rapidly. The resulting values of F_1 and F_2 as the pressure is increased reinforce the use of eq. (2) to describe the pressure dependence of viscosity.

TABLE II
Free Volume Parameters for Polystyrene at $T = 140°C$

v_l, cc/g[a]	$\alpha_l \times 10^4$, deg^{-1} [b]	$\beta \times 10^5$, bars^{-1}	Pressure, bars	Relative free volume	
				F_1[c]	F_2[d]
1.000	5.34	6.84	0	0.05120	0.05120
0.993	5.02	6.40	100	0.04436	0.04818
0.982	4.48	5.67	300	0.03068	0.04313
0.971	4.05	5.10	500	0.01700	0.03908
0.962	3.70	4.63	700	0.00332	0.03575
0.953	3.40	4.25	900		0.03294
0.945	3.15	3.93	1100		0.03055
0.938	2.94	3.66	1300		0.02849
0.932	2.75	3.42	1500		0.02670
0.925	2.58	3.21	1700		0.02512

[a] $v_g = 0.927$ (data of Gee and Miller[20,27]).
[b] $\alpha_{0l} = 5.34 \times 10^{-4}$ (data of Gee[20]).
[c] $F_1 = f_g + \alpha_{0l}(T - T_{g0}) - \beta P;\ T_{g0} = 90°C, f_g = 0.0245$ (data of Williams[25]).
[d] $F_2 = f_g + \alpha_l(T - T_g)$.

The relative free volume is most dependent on the initial values of α and β selected. The different values for these two parameters found in the literature for polystyrene[5,6,11,12,20,27–31] cause some change in the computed relative free volume. Equation (4), nonetheless, gave the better results in all cases. Slight variations in v_0, v_l, $\partial T_g/\partial P$, and v_{g0} found in the literature affect the values of the relative free volume very little. Considering all the parameters involved, the work of Gee[20] and Miller[27] appears to be the most consistent and was used in the calculations presented in Table II.

Considering the results of Table II, the derived WLF expression as represented by eq. (2) appears valid for determining the pressure dependence of viscosity for polystyrene. For temperature shifts of viscosity data, $C_1 = B/2.303f_g$ and $C_2 = f_g/\alpha$ are constants for a given system. However, since α is pressure-dependent, C_2 will vary somewhat with pressure. In the average pressure ranges encountered in the present study ($P_{\text{avg}} < 300$ bars), C_2 changes very little and was assigned a fixed value. The variation in C_2 with the pressure ranges encountered was less than the variation in using the different values of α in the literature.

Table III lists the values of C_1 and C_2 used in the calculations involving the two polystyrenes. The procedure for obtaining C_1 and C_2 has been described elsewhere.[32] The necessary zero-shear viscosity data to obtain C_1 and C_2 for the low molecular weight sample was presented earlier.[1] Zero-shear viscosity data were not available for the 670K polymer. Plazek[33] and Ballman and Simon[19] have obtained sufficient zero-shear data for a polystyrene of molecular weight 600,000 to permit a precise calculation of C_1 and C_2. These values of C_1 and C_2, evaluated in the immediate range of the test temperature, were used in the calculations involving the 670K polymer. The values of the constants C_1 and C_2 derived from free volume parameters selected from the data of Williams[25] and Gee[20] are also included in Table III.

TABLE III
WLF Parameters for Narrow-Distribution Polysytrenes

Molecular weight	C_1	C_2	$B/2.303f_g$	f_g/α
20,400	14.4	36.2		
600,000	16.6	158.2		
			16.13	41.67

Capillary Viscometry

Capillary extrusion studies of polymers are of continuing interest as normally the measurements are comparatively simple to make and the data straightforward to analyze. However, several possible problems arise when pressure losses at the entrance of the capillaries become appreciable. Bagley[17] first suggested a means of eliminating the entrance loss from capillary data by extrapolation of the linear relation between pressure and length-to-diameter ratio of many capillaries. Middleman[18] suggests an alternate approach to the problem which involves plotting the flow rate of the polymer versus the pressure drop for capillaries of the same diameter but different length. The latter method has the advantage of requiring less data for determination of the end correction. Philippoff and Gaskins[34] have suggested a means of determining elastic energy losses incurred in capillary flow of viscoelastic fluids. The several methods for considering the entrance losses in tubular flow all involve the necessity of a linear relation between the pressure drop and L/D ratio at given shear rates and temperatures. Complications arise when the relation is no longer linear.

Sakiadis[22] has derived equations for determining the shear stress and two normal-stress differences in the equilibrium flow of a general fluid through a cylindrical tube. He presents a measurement of the axial pressure distribution in a tube in which the pressure drop is nonlinear. He also states that the residual pressure cannot be used directly to measure normal pressures. Arai et al.[23] have measured the pressure distribution along the die axis for a commercial-grade polystyrene. The pressure drops at a given shear rate (12 $\sec^{-1}$) and three temperatures (170, 180, 200°C) are nonlinear and all indicates a residual pressure at the exit. This residual pressure and its relation to extrudate swelling are discussed.

Toelcke et al.,[2] in their study of the effects of molecular weight distribution on the flow properties of polystyrene, obtained nonlinear pressure versus L/D curves by using three capillaries. They chose to ignore the data for the highest L/D in their analysis and thus eliminated the nonlinearity problem. Thomas and Hagan,[4] in their discussion of the effects of molecular weight distribution on the flow properties of polystyrene, also encountered the nonlinear pressure versus L/D curves. Without detailed analysis, they suggested the effect might be due to hydrostatic pressure. McLuckie and Rogers[3] discuss the nonlinearity as due to elastic back pressure. They state that the relaxation of the polymer creates an elastic back pressure which results in nonlinear behavior as L/D increases.

RESULTS

The situation in which pressure may affect the apparent viscosity has been discussed and an appropriate model which predicts the pressure dependence of viscosity analyzed. The problem is best represented by the nonlinearities appearing in capillary data plotted in the form of a Bagley plot. To initiate the study of this problem, the 20.4K polymer was selected. The molecular weight of this sample is below the critical molecular weight for chain entanglement in polystyrene. Shear, oxidative, and thermal degradation are negligible for the test conditions used.[16] In the absence of pressure effects, the sample is Newtonian and exhibits insignificant extrudate swelling.

The average pressure attainable in these tests rarely exceeded 300 bars. According to Table II, this results in a maximum volume change of less than 2%. This is in agreement with Figures 1 and 2 which represent a comparison of the calculated and measured flow rates Q. The points represent measured flow rates and the solid lines the calculated values. (In Fig. 1, the calculated curve for the capillary with $L/D = 39.1$ extends beyond the indicated points, as an additional point lies off scale.) Within experimental error, it is impossible to detect any difference between the measured and calculated flow rates at the two temperatures indicated and for the several capillaries used. This might lead to the false conclusion that the material is incompressible. However, as can be seen in Table II and as calculated by eq. (2), a small volume change increases the viscosity by a large factor.

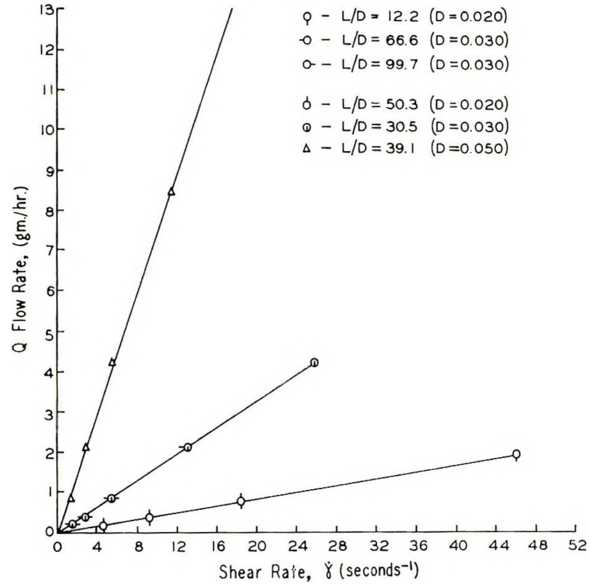

Fig. 1. Comparison of calculated and measured flow rates for narrow-distribution, low molecular weight polystyrene (20.4K polymer): $\bar{M}_w = 20{,}400$, $\bar{M}_w/\bar{M}_n \leq 1.06$ at 140°C.

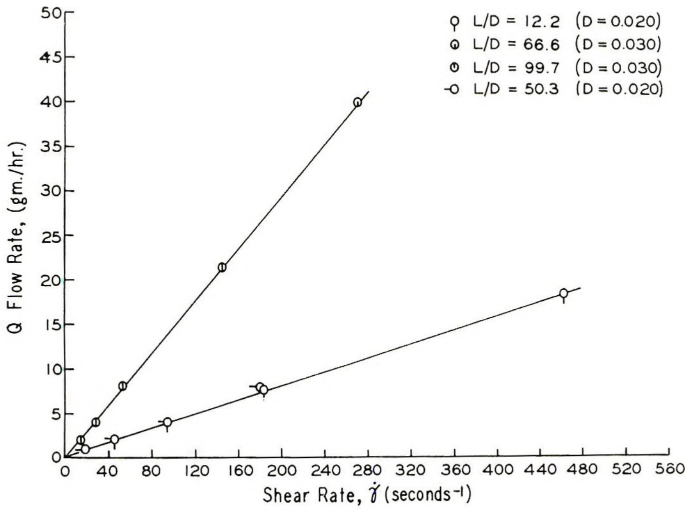

Fig. 2. Calculated and measured flow rates at 160°C, 20.4K polymer.

Figure 3 is a plot of the pressure drop versus shear rate at a temperature of 160°C for eight capillaries. Additional data should be obtainable for all the capillaries if the material continued to exhibit Newtonian behavior. However, the next higher point for all the curves exceeded the limit of 1900 kg/cm^2 for the instrument. Similar results were obtained at a temperature of 140°C.

One of the most obvious manifestations of elastic energy storage in

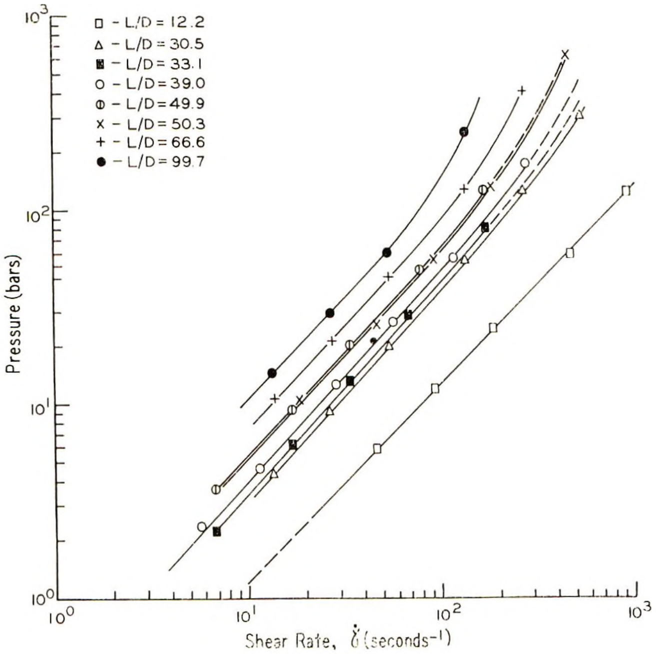

Fig. 3. Flow data at 160°C for several capillaries, 20.4K polymer.

capillary flow is the observation of extrudate swelling on exit from the die.[4,23,34,35] In view of the work by McLuckie and Rogers,[3] the tremendous increases in the pressure with shear rate indicated in Figure 3 should be accompanied by appreciable swelling of the extrudate. However, no significant die swell was observed at the test temperatures of 140 and 160°C for any of the capillaries at any shear rate. Any prominent dependence of the entrance loss on pressure should appear as a slight separation of the pressure data for capillaries with the same *L/D* ratio but different dimensions. This is not observed in Figure 3, and thus it is likely that entrance losses are negligibly dependent on pressure.

Figure 4 illustrates the nonlinear Bagley plot for the low molecular weight polystyrene at a temperature of 160°C. The curves are linear at low shear rates and their extrapolation produces very small end corrections. As the shear rate is increased the curves gradually become nonlinear at low *L/D* ratios. Importantly, the best linear extrapolation of these curves still indicates a small entrance loss. Data were not taken on the capillary with $L/D = 4.26$ as the uncertainties involved are a large percentage of the total reading.

Figure 5 is a plot similar to Figure 4 but for 140°C. It may be noted that the nonlinear effect is more pronounced as the temperature is decreased, first appearing at a shear rate of 2 sec^{-1}. Tremendous increases in the pressure (or stress) are evident in Figures 4 and 5, while concurrently the extrudate swelling is negligible and the extrapolated end corrections small. The indication is, therefore, that the increase in pressure

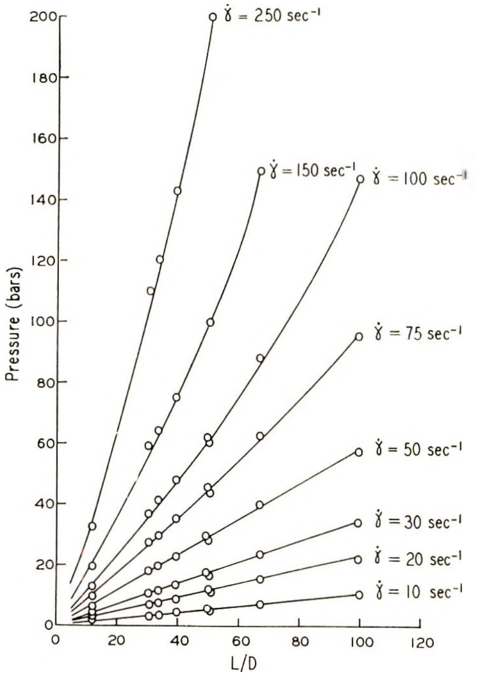

Fig. 4. Pressure required for flow at 160°C at various shear rates versus the length/diameter ratio of several capillaries, 20.4K polymer.

above that required for Newtonian flow is needed to generate greater stresses to move the higher viscosity material at the same rate. The procedure for calculating the increased viscosity by using the WLF equation has been described elsewhere[1] and is only briefly reconsidered. The pressure dependence of the glass transition temperature is known[20,27] and is used to calculate the change in T_g with pressure. Any shift in T_g can be inserted into the WLF equation and the resulting change in viscosity determined. The stress necessary to accommodate any viscosity determined. The stress necessary to accommodate any viscosity increase can then be calculated and applied as a correction to the nonlinear data in Figures 4 and 5.

The average pressure used to calculate a shift in T_g was half the total pressure drop over the entire capillary. This assumption involves little error, as the deviations from a linear pressure drop, cited earlier,[22,23] are small. Residual pressures reported for capillary flow are negligible compared with the total pressure drop as they are of the magnitude of normal stresses generated by the shear field.[22,23] The viscosity was then calculated as a function of pressure at several intervals along the capillary. The average viscosity calculated in this manner varied less than 1% from the viscosity calculated by using the mean value of the pressure drop over the entire capillary.

Applying the pressure correction described earlier to the data in Figure

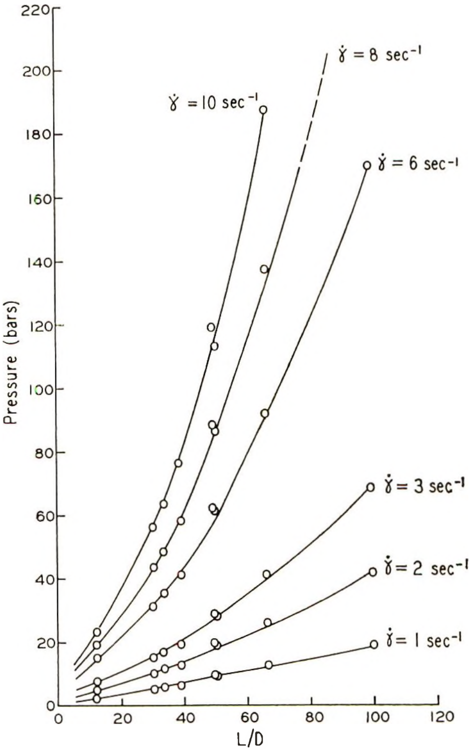

Fig. 5. Plot as in Fig. 4, but for 140°C.

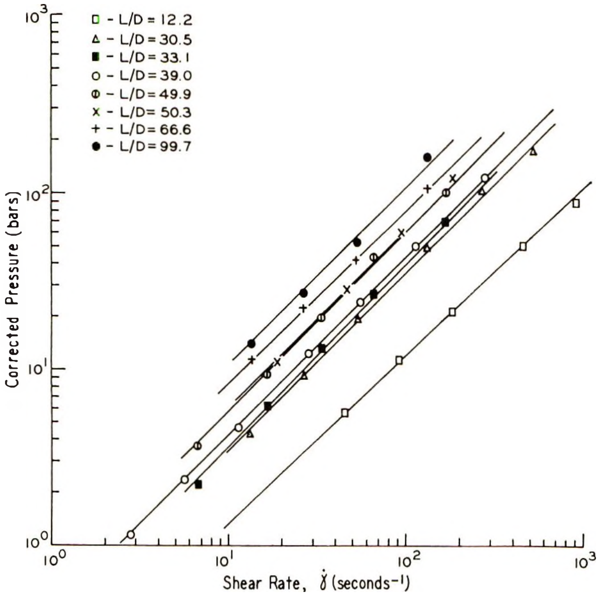

Fig. 6. Flow data of Fig. 3 corrected for pressure effects.

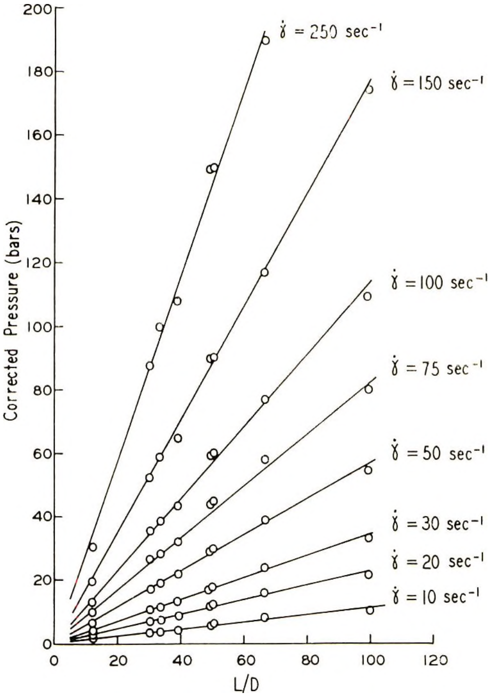

Fig. 7. Corrected pressure vs. length/diameter ratio of several capillaries at 160°C for 20.4K polymer.

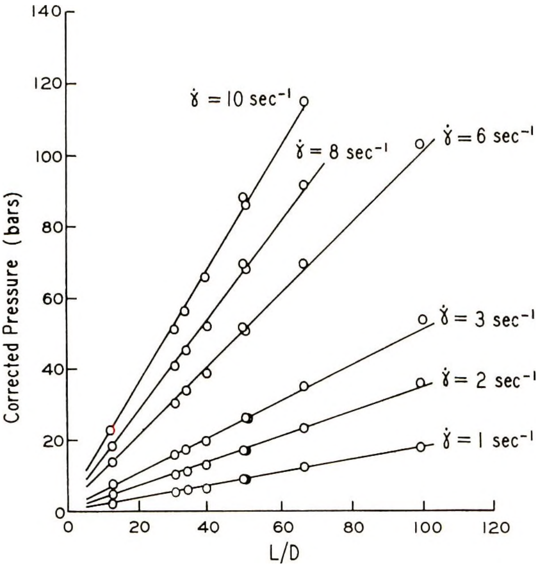

Fig. 8. Corrected pressure vs. length/diameter ratio as in Fig. 7, but at 140°C.

3 produces the linear curves of Figure 6. Similar results were obtained for the data at 140°C. The magnitude of the pressure correction becomes quite apparent when comparisons of Figure 7 and Figure 4 are made. The corrected data in Figure 7 are linear at all the shear rates and L/D ratios given. At 140°C, the linear curves in Figure 8 result from applying the pressure correction to the data of Figure 5. Thr nonlinearities in Figures 4 and 5 have been eliminated and appear, then, to be due to the excess pressure required for flow of the higher viscosity material.

Figures 3–8 and previous work[1] indicate that moderate pressures can definitely influence the capillary flow of low molecular weight polystyrene. The effect of pressure on flow can be incorporated into a pressure correction factor. However, the low molecular weight material was ideal in that it was a stable system, sustained small losses in the entrance region of the capillaries, and gave no indication of appreciable elastic energy storage as witnessed by negligible swelling of the extrudate. It would be meaningful to study a high molecular weight polystyrene to see if the same pressure dependence applies in a system of practical processing interest and not nearly as ideal.

The 670K polymer behaves quite differently than the low molecular weight sample under similar test conditions. From studies of Arisawa and Porter[16] on an identical sample, it was shown to be quite susceptible to shear and thermal degradation. Polystyrenes of similar molecular weights have also demonstrated the ability for considerable elastic energy storage.[4] The entrance losses are expected to be larger than those encountered with the low molecular weight sample. These factors tend to make the analysis of the high molecular weight polystyrene much more difficult.

Figure 9 represents the pressure required for flow of the 670K polymer in nine capillaries as a function of shear rate at 165°C. For all but the capillary of lowest L/D, the pressure increases nonlinearly as the shear rate is increased. The rapid increase in pressure with increasing shear rate and L/D ratio is more easily seen in Figure 10. The data for the lowest L/D seemingly deviates considerably from the other data at lower shear rates. The force requirements for this capillary are much less than the other eight capillaries and the various losses associated with capillary flow become appreciable. As an example the losses in the barrel represent only a small error for the capillaries of larger L/D but can approach 30% and possibly more of the total force for the lowest L/D. At higher shear rates, the pressure losses become a smaller percentage of the total pressure and there is less tendency for curvature parallel to the L/D axis. The present analysis is concerned with the nonlinearities appearing in Figure 10 at the higher L/D ratios and therefore the behavior as the L/D ratio approaches zero is of interest only as a total end correction.

The separation of the pressure curves in Figure 9 with L/D ratios of approximately 50 might be an indication that the losses in the barrel and entrance region of a capillary are pressure dependent. In Figure 10, however, this possible pressure dependence of the losses is not as obvious or as large as first indicated in Figure 9 and will be neglected for the present.

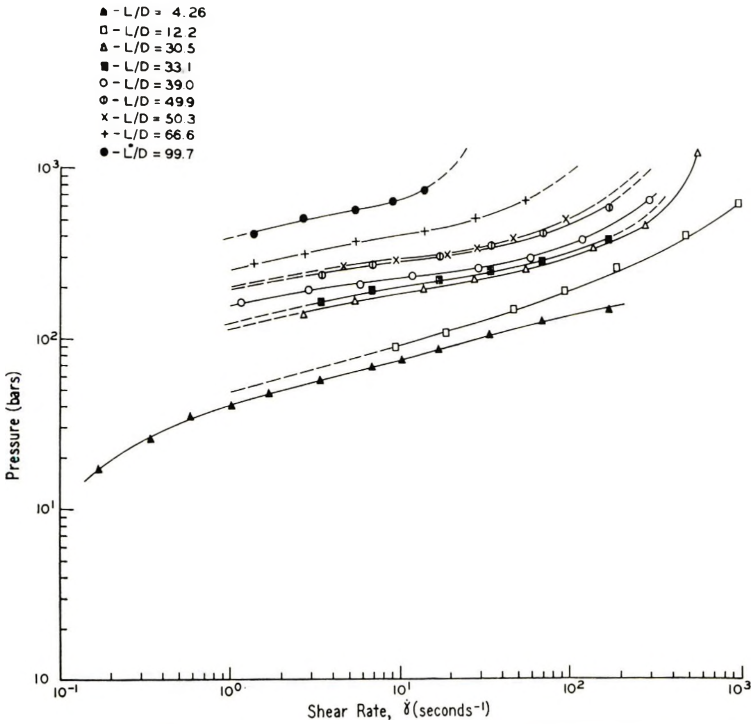

Fig. 9. Flow data at 165°C in several capillaries for narrow-distribution, high molecular weight polystyrene (670K polymer): $\bar{M}_w = 670{,}000$, $\bar{M}_w/\bar{M}_n \leqslant 1.06$.

The calculated pressure correction represents the pressure necessary to generate the shear stress to move the higher viscosity material. The magnitude of the additional shear stress depends on the increase in viscosity, which is quite sensitive to pressure. Therefore, an attempt to determine the pressure correction with included entrance losses would result in overcorrecting the data. To avoid this, the entrance losses must be estimated for each shear rate in Figure 10 and eliminated from the data. No attempt is made to separate the various components of the entrance loss as the entrance to a capillary is a very complex region. Appreciable extrudate swelling observed for this polymer indicates elastic energy storage in addition to Couette losses.

With the exception of the lowest value, the lower L/D ratios can be used to approximate the entrance losses. A least-squares analysis of as many points as approximated straight lines in Figure 10 gave an estimate of the entrance losses at each shear rate. The approximate end corrections were applied to the curves of Figure 10, shifting them as shown in Figure 11. The apparent viscosity was calculated by using the data of Figure 11 and is shown in Figure 12. The separation of the curve in Figure 12 at a shear rate of 1 sec^{-1} is small and increases with shear rate. The upturns suggested at the highest shear rates for each capillary are justified by recalling that the next increment in shear rate is inaccessible experimentally as indicated by Figure 9. The capillary having the highest L/D ratio requires

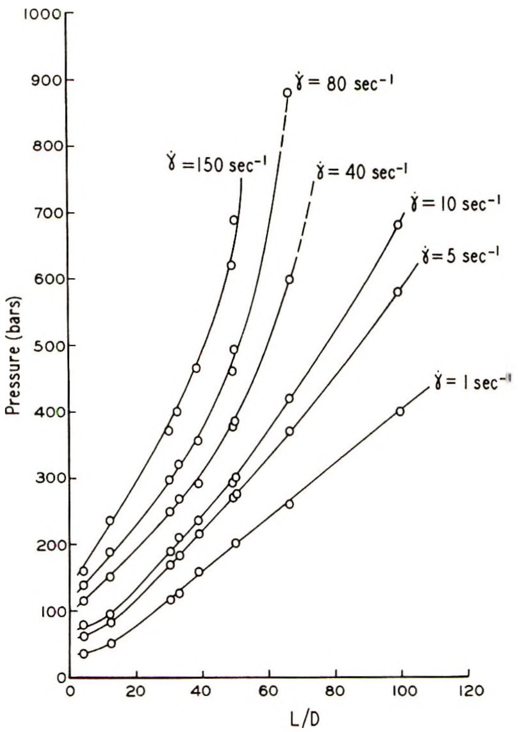

Fig. 10. Pressure required for flow at 165°C at various shear rates versus the length/diameter ratio of several capillaries, 670K polymer.

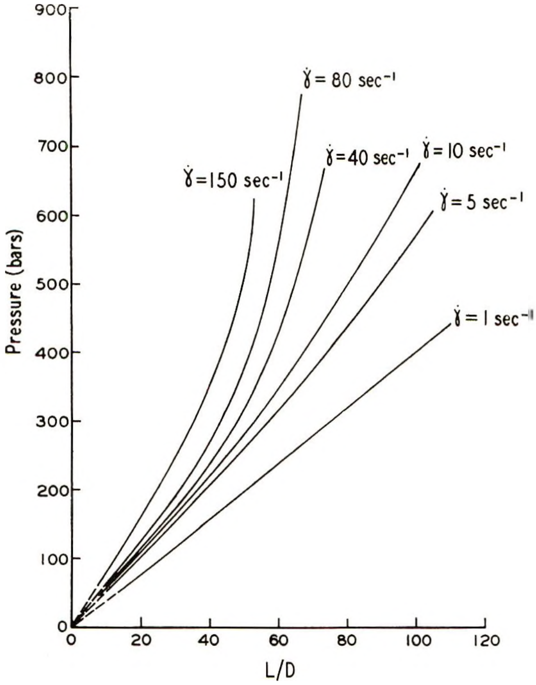

Fig. 11. Data of Fig. 10 shifted by an amount which approximates the end correction.

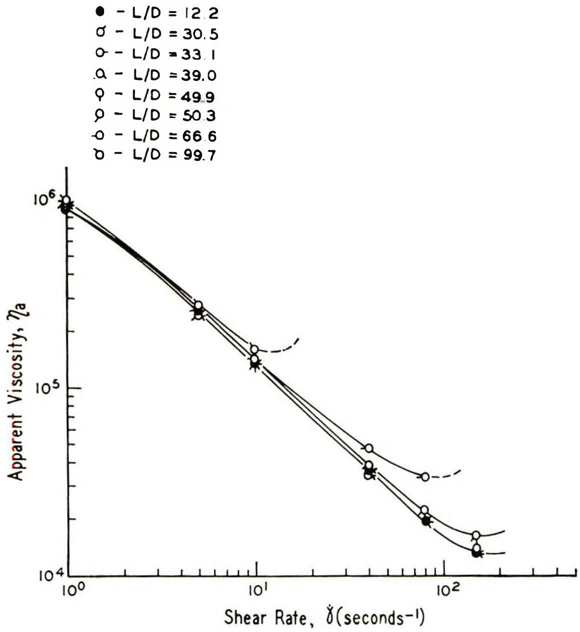

Fig. 12. Apparent viscosity vs. shear rate at 165°C for 670K polymer.

the greatest pressure at a given shear rate and is the first to exceed the capacity of the Instron capillary rheometer. As the *L/D* ratio decreases, the pressure effect does also, as can be seen in Figure 12.

The problem in applying the WLF equation to determine the pressure dependence of the high molecular weight polystyrene is that it does not include a shear-thinning contribution. However, it can be used to calculate a relative viscosity increase starting with the experimental points at the lowest shear rates recorded for each capillary. Any relative viscosity increase can then be converted to a pressure correction in a procedure similar to that used for the low molecular weight polystyrene.

Applying the pressure correction to the curves in Figure 11 gives the plots shown in Figure 13. Essentially linear plots are obtained at the lower shear rates but a large overcorrection occurs at higher shear rates. As mentioned earlier, the viscosity is very sensitive to the pressures encountered in these tests. Any pressure loss not accounted for will tend to predict too great an increase in viscosity. This will then result in pressure corrections which are too large. A pressure-dependent viscosity suggests the possibility that the entrance losses may also be pressure-dependent. This means that the Couette loss may not be the same for capillaries of equal diameter. Earlier, this possibility was acknowledged, but the effect was assumed to be small compared to the total pressure drops in these tests. Considering the results in Figure 13, this may be a limiting assumption.

The pressure-corrected viscosity is compared in Figure 14 to data obtained from the Weissenberg rheometer and to data generated from reduced coordinates. From a plot of the data on zero-shear viscosity versus temperature^{-1} by Ballman and Simon[19] and Plazek and O'Rourke[33] for a

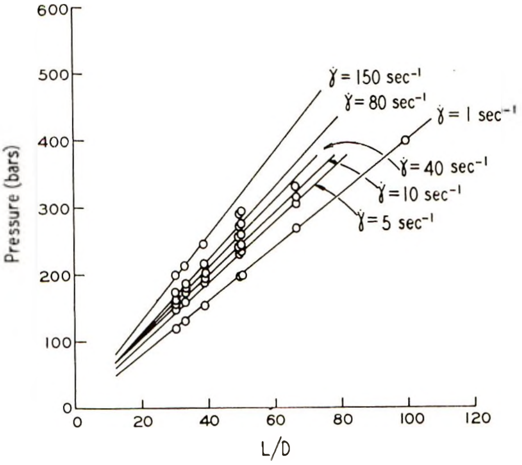

Fig. 13. Corrected pressure vs. length/diameter ratio for several capillaries, 670K polymer at 165°C.

narrow-distribution sample of molecular weight 600,000, the zero shear viscosity at 165°C can be obtained. With the reduced coordinates log η/η_0 and log $(\dot{\gamma}\eta_0 M/T)$ as presented by Ballman and Simon[19] for narrow-distribution polystyrenes, the apparent viscosity curve in Figure 14 was calculated. This curve was generated for reference only, and it is not necessary to discuss the value of the exponent of M in the reduced coordinates since it is not a variable.[36] The overcorrection of the pressure appears in Figure 14 as a greater decrease in the apparent viscosity with shear rate than is expected.

CONCLUSIONS

Examination of the equivalent form of the WLF equation derived from Doolittle's relation between viscosity and free volume indicates that it can be used to describe the pressure dependence of viscosity of polystyrene. In the pressure ranges encountered in these tests ($P_{\text{avg}} < 300$ bars), no modification of the equation is necessary.

It is virtually impossible to detect any difference in the measured and calculated flow rates encountered in this study. The conclusion that the polymer is therefore incompressible is false even though the volume change is less than 2%. The viscosity is quite sensitive to small volume changes at the test temperatures used and varied considerably in this work. However, in considering the equation of continuity, it may be possible to neglect the small change in the density and make the assumption that the system is incompressible.

The 20.4K polymer was ideal for an initial study of the nonlinearity in a Bagley plot. The observation of negligible end effects and extrudate swelling, while pressures prematurely exceeded the capacity of the vis-

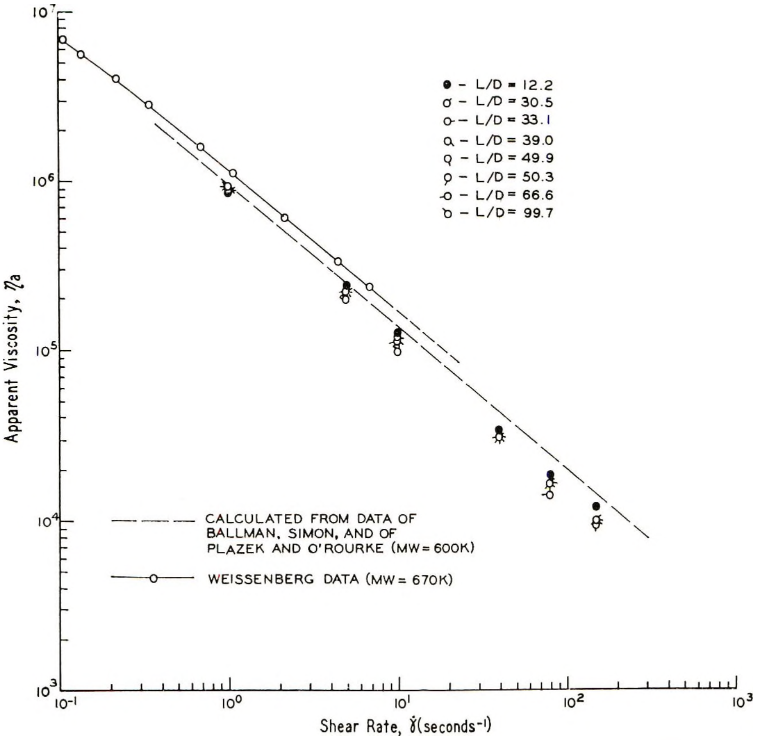

Fig. 14. Pressure-corrected apparent viscosity vs. shear rate for 670K polymer at 165°C.

cometer, supported the idea that pressure was influencing the flow. Pressure corrections, based on the pressure needed to generate the increased stress to move the higher viscosity material, linearized the Bagley plots.

To perform a similar analysis of a high molecular weight polystyrene, it is necessary first to estimate the end effect as its magnitude will significantly affect the results. In doing this, the assumption is made that the pressure dependence of the losses in the entrance region of the capillaries can be neglected. The calculated pressure corrections tended to linearize the Bagley plots and predict power law behavior of the apparent viscosity. There is a tendency to overcorrect the data, possibly a consequence of the limiting assumption that the entrance losses are constant at a given shear rate and temperature.

The results on both the low and high molecular weight polystyrenes indicate that pressure definitely influences the flow. It would be of interest to apply the same approach to other amorphous systems exhibiting similar phenomena. It would also be of interest to further examine the limits of the pressure dependence of viscosity by using a free-volume model. One would expect this model to fail once the probability of sufficient free volume being available to the flow molecule ceases to be the controlling factor. In view of the pressure dependence of the free volume, this limit may be deceivingly higher than might be expected.

We wish to express our appreciation to the U.S. Army, Durham, and to the Paint Research Institute for support of this study.

References

1. R. C. Penwell and R. S. Porter, *J. Appl. Polym. Sci.*, **13**, 2427 (1969).
2. G. A. Toelcke, C. G. Gogas, and J. A. Biesenberger, *SPE 13th ANTEC*, 98 (1967).
3. C. McLuckie and M. G. Rogers, *J. Appl. Polym. Sci.*, **13**, 1049 (1969).
4. D. P. Thomas and R. S. Hagan, *Polym. Eng. Sci.*, **9**, 164 (1969).
5. R. N. Haward, *J. Polym. Sci. A-2*, **7**, 219 (1969).
6. M. M. Martynyuk and U. K. Semenchenko, *Kolloid. Zh.*, **26**, 83 (1964).
7. I. Duvdevani, *SPE 13th ANTEC*, 80 (1967).
8. H. Sasabe and S. Saito, *Rept. Progr. Polym. Phys. Japan*, **12**, 265 (1969).
9. K. Ito, *Rept. Progr. Polym. Phys. Japan*, **12**, 131 (1969).
10. A. J. Matheson, *J. Chem. Phys.*, **44**, 695 (1966).
11. R. N. Haward, H. Bruer, and G. Rehage, *J. Polym. Sci. B*, **4**, 375 (1966).
12. A. A. Miller, *J. Polym. Sci. A-2*, **4**, 415 (1966).
13. S. Matsuoka and B. Maxwell, *J. Polym. Sci.*, **32**, 131 (1958).
14. D. R. Mears, K. D. Pae, and J. A. Sauer, *J. Appl. Phys.*, **40**, 4229 (1969).
15. L. Holliday, *Nature*, **202**, 381 (1964).
16. K. Arisawa and R. S. Porter, *J. Appl. Polym. Sci.*, **14**, 879 (1970).
17. E. B. Bagley, *J. Appl. Phys.*, **28**, 624 (1957).
18. S. Middleman, *The Flow of High Polymers*, Interscience, New York, 1968, p. 15.
19. R. L. Ballman and R. H. Simon, *J. Polym. Sci., A*, **2**, 3557 (1964).
20. G. Gee, *Polymer*, **7**, 177 (1966).
21. J. D. Ferry and R. A. Stratton, *Kolloid-Z.*, **171**, 107 (1960).
22. B. C. Sakiadis, *AIChE J.*, **8**, 317 (1962).
23. T. Arai, I. Suzuki, and N. Akino, *Proc. Fujihara Mem. Fac. Eng. Keio Univ. Tokyo*, **20**, 39 (1967).
24. A. K. Doolittle, *J. Appl. Phys.*, **22**, 1471 (1951).
25. M. L. Williams, *J. Appl. Phys.*, **29**, 1395 (1958).
26. T. G. Fox and P. J. Flory, *J. Appl. Phys.*, **21**, 581 (1950).
27. A. A. Miller, *J. Polym. Sci. A-2*, **6**, 1161 (1968).
28. A. Bondi, *J. Polym. Sci. A*, **2**, 3159 (1964).
29. D. J. Plazek, *J. Phys. Chem.*, **69**, 3480 (1965).
30. T. G. Fox and S. Loshaek, *J. Polym. Sci.*, **15**, 371 (1955).
31. K. Ueberreiter and G. Kanig, *J. Colloid Sci.*, **7**, 569 (1953).
32. J. D. Ferry, *Viscoelastic Properties of Polymers*, Wiley, New York, 1961, p. 212.
33. D. J. Plazek, private communication.
34. W. Philippoff and F. H. Gaskins, *Trans. Soc. Rheol.*, **2**, 263 (1958).
35. R. S. Spencer and R. E. Dillon, *J. Colloid Sci.*, **3**, 163 (1948).
36. R. A. Stratton, *J. Colloid Interfac. Sci.*, **22**, 517 (1966).

Received March 26, 1970
Revised August 24, 1970

JOURNAL OF POLYMER SCIENCE: PART A-2 VOL. 9, 483–497 (1971)

Fox-Flory Constant *K* Obtained by Viscometric Measurements for Poly(ethyl methacrylate) and Poly(methyl methacrylate) Systems

PADMA VASUDEVAN* and M. SANTAPPA,
Department of Physical Chemistry
University of Madras, Madras 25, India

Synopsis

Poly(ethyl methacrylate) and poly(methyl methacrylate) prepared by benzoyl peroxide-catalyzed polymerization were fractionated. The Fox-Flory constant *K* was determined for these polymers by viscometry in several good and bad solvents. Application of some empirical methods for evaluation of *K* are also briefly discussed in relation to our results.

INTRODUCTION

Viscometric studies of high polymer solutions at and above the Flory temperature Θ have been widely used in determining the Fox-Flory constant *K*. Some of the methods of determination of *K* from measurements in good solvents were reviewed by Cowie.[1] Comparatively little work[2] has been done on poly(ethyl methacrylate) (PEMA) solutions and it would be of interest to compare its unperturbed dimensions with those of poly(methyl methacrylate)[2–15] (PMMA). In this paper, we report values of *K* by viscometry for PEMA in ten solvents and for PMMA in six solvents by various extrapolation procedures for good solvents, as well as by direct measurements at $T = \Theta$ for ideal solvents. Recently many empirical and semiempirical methods[16–31] for estimation of *K* from viscometric measurements in good solvents have been proposed. An application of these methods to our data has been attempted in order to see how far *K* values obtained by empirical methods agree with those from direct methods.

THEORETICAL

In the theory developed by Flory and Fox[32] and Kurata et al.[33,34] the intrinsic viscosity $[\eta]$ is related to the Fox-Flory constant *K*, molecular weight *M*, and the hydrodynamic expansion factor α_η by:

---

* Present address: Chemistry Department, Indian Institute of Technology, New Delhi 29, India.

$$[\eta] = \Phi\left(\frac{\overline{r_0^2}}{M}\right)^{3/2} M^{1/2}\alpha_n^3 = KM^{1/2}\alpha_n^3 \tag{1}$$

where Φ is a universal parameter and $\overline{r_0^2}$ denotes the unperturbed mean-square end-to-end distance.

The thermodynamic parameters χ and z are defined[15,35] by:

$$\chi = \frac{Z\Delta W_{12}x_1}{kT} \tag{2}$$

where ΔW_{12} is the change in energy for the formation of an unlike contact pair, x_1 is the number of segments in the solvent molecule, and Z is the lattice coordination number, and

$$z = (^3/_2\pi)^{3/2}B\left(\frac{\overline{r_0^2}}{M}\right)^{-3/2} M^{1/2} \tag{3a}$$

where

$$B = (2\bar{v}^2/N_AV_1)(^1/_2 - \chi) \tag{3b}$$

$\bar{v}$ is the (partial) specific volume of the polymer; V_1 is the molar volume of the solvent; and N_A denotes Avogadro's number. The linear expansion factor α ($\alpha^2 = \overline{s^2}\ \overline{s_0^2} = \overline{r^2}/\overline{r_0^2}$, $\overline{s^2}$ denoting the mean square molecular radius) for linear polymers has been related to χ (or z) through many theoretical and semiempirical equations, notably by Fox and Flory[32] [eq. (4)]; Stockmayer and Fixman[35] [eq. (6)]; Kurata and Stockmayer[36,37] [eq. (7a)]; Berry[38] [eq. (8)], and others:[39,40]

$$\alpha^5 - \alpha^3 = 2C_M(^1/_2 - \chi)M^{1/2} \tag{4}$$

where

$$C_M = (27/2^{5/2}\pi^{3/2})(\bar{v}^2/V_1N_A)(M/\overline{r_0^2})^{3/2} \tag{5}$$

$$\alpha^3 = 1 + 2z \tag{6}$$

$$\alpha^3 - \alpha = (^4/_3)zg(\alpha) \tag{7a}$$

where

$$g(\alpha) = 8\alpha^3(3\alpha^2 + 1)^{-3/2} \tag{7b}$$

$$\alpha^3 = 2 + 0.325z \qquad 2 < z < 11 \tag{8}$$

The exact relation between α and z is still an open question and a large number of other recent publications[41-49] are devoted to the excluded volume effect and its relation to solution properties. The equations developed have been widely used with partial success. Similarly, the exact relation between α and α_n has not been fully established:[44,50] the relations $\alpha = \alpha_n$ due to Flory,[32] $\alpha_n^3 = \alpha^{2.5}$ due to Kurata and Yamakawa,[33] $\alpha_n^3 = \alpha^{1.95\pm0.15}$ near Θ due to Norisuye et al.[50] have been suggested. In any case, at Θ, for any polymer–solvent system, $\alpha = \alpha_n = 1$ holds and hence evaluation of K at Θ is the most accurate method.

On the other hand for evaluation of K from $[\eta]$ at $T > \Theta$ (in good solvents), a number of equations relating $[\eta]$ and M through K (after eliminating α, α_n, z, etc.) have been suggested. Fox and Flory (F-F) obtained:[32]

$$[\eta]^{2/3}/M^{1/3} = K^{2/3} + K^{5/3}C_T(M/[\eta]) \tag{9}$$

Kurata and Stockmayer[36,37] (K-S) arrived at:

$$[\eta]^{2/3}/M^{1/3} = K^{2/3} + 0.363\Phi B[g(\alpha_n)(M^{2/3}/[\eta]^{1/3})] \tag{10}$$

Stockmayer and Fixman[35] (S-F) and others derived[51,52]

$$[\eta]/M^{1/2} = K + 0.51\Phi BM^{1/2} \tag{11}$$

Berry[38] proposed:

$$([\eta]/M^{1/2})^{1/2} = K^{1/2} + 0.42K^{3/2}B(\overline{r_0^2}/M)^{-3/2}(M/[\eta]) \tag{12}$$

Besides these, several other equations[53,54] proposed have had partial success. According to all these equations the value of K is obtained from the intercepts on the ordinates of the plots of the quantity on the left-hand side versus a function of M and $[\eta]$ on the right-hand side (see Figs. 2–5). .

EXPERIMENTAL

Polymers

Both PMMA and PEMA were prepared by polymerization of the distilled monomers at 60°C with benzoyl peroxide as the initiator. The polymers were fractionated by standard precipitation procedures using benzene as solvent and n-hexane as non-solvent. As a result of two or three repeated fractionations, fairly sharp $(\bar{M}_w/\bar{M}_n) \approx 1.2$ for PEMA[55]) fractions were obtained. The molecular weights $(10^5 \leq \bar{M}_w \leq 10^6)$ of PMMA fractions were determined by viscometry in benzene at 30°C, by using the relation,[56] $[\eta] = 5.2 \times 10^{-5}\bar{M}_w^{0.76}$ for $\bar{M}_w \geqslant 35{,}000$ and of PEMA fractions in methyl ethyl ketone at 23°C by using the relation[57] $[\eta] = 2.83 \times 10^{-5}\bar{M}_w^{0.79}$

Solvents

n-Butyl bromide (Riedel, AnalaR), isoamyl acetate (B.D.H. L.R. and M&B AnalaR), o-xylene (Riedel AnalaR), m-xylene (Merck, A.G., Darmstadt; AnalaR), p-xylene (Riedel, AnalaR), n-butyl chloride (Riedel AnalaR), ethyl acetate (B.D.H. AnalaR), isopropanol (Merck, AnalaR), n-butanol (B.D.H., AnalaR), benzene (Sarabhai Merck Ltd., India, Merck, AnalaR), methyl n-propyl ketone (Riedel, AnalaR), petroleum ether (n-hexane, boiling range 60–80°C) were purified by standard procedures and freshly distilled before use.

Viscometry

An Ubbelohde suspended-level dilution viscometer was used. The viscometric constants C and B in the equation $\eta/\rho = Ct - B/t$ were determined[55] with doubly distilled water and were used in making kinetic energy

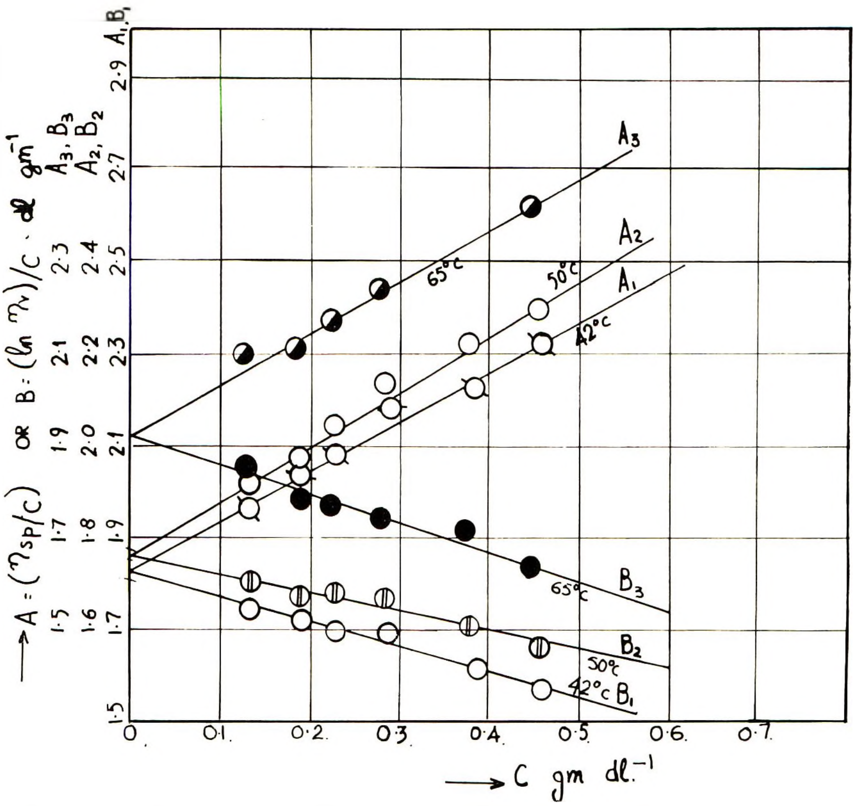

Fig. 1. Plot of η_{sp}/c vs. c and ln η_r/c vs. c for PEMA, fraction Ib, in n-butyl bromide: (A_1, A_2, A_3) η_{sp}/c vs. c at 42, 50, and 65°C; (B_1, B_2, B_3) to (ln η_r)/c vs. c at 42, 50, and 65°C.

corrections where necessary. The intrinsic viscosity was evaluated as an average of the intercepts of the plots of η_{sp}/c and (ln η_r)/c versus concentration c, both graphically and by the least-square method. The values by the two extrapolation procedures agreed to ±0.001 (Fig. 1). The temperature of the viscometric bath was controlled to ±0.05°C.

DISCUSSION

The Fox-Flory constant K may be obtained from viscosity data by three methods: (a) in theta solvents, i.e., by direct measurement of $[\eta]$ at Θ; (b) in good solvents by using suitable extrapolation procedures based on equations relating α, α_n, and z; and (c) by certain empirical and semiempirical methods.

K from $[\eta]_\Theta$

The most direct estimate of K is from $[\eta]_\theta$ ($[\eta]$ at $T = \Theta$) the reliability of the value being dependent on the accuracy of measurement of $[\eta]$ and Θ and in overcoming the experimental difficulties due to poor solubility of the

TABLE I
Intrinsic Viscosity Data at Θ for PMMA and PEMA Systems[a]

System	Θ, °C	log ($[\eta]_\Theta \times 10$)	$^1/_2$ log ($M_w \times 10^{-5}$)	$K \times 10^4$
PMMA-*p*-xylene	50	0.683	0.533	4.9
		0.644	0.487	
		0.620	0.455	
		0.602	0.421	
		0.562	0.352	
		0.491	0.320	
PMMA-*m*-xylene	30	0.663	0.485	4.9
		0.664	0.487	
		0.623	0.455	
		0.591	0.381	
		0.512	0.352	
PMMA-isoamyl acetate	50	0.634	0.445	4.5
		0.558	0.381	
		0.550	0.343	
		0.342	0.202	
PMMA-*n*-butyl bromide[b]	35	0.773	0.533	4.6
		0.671	0.487	
		0.625	0.467	
		0.637	0.467	
		0.615	0.445	
		0.610	0.421	
		0.592	0.415	
		0.574	0.381	
		0.352	0.257	
		0.248	0.100	
PEMA-isopropanol[b]	36.9	0.942	0.641	6.4
		0.924	0.580	
		0.836	0.516	
		0.766	0.415	
		0.711	0.415	
		0.692	0.419	
PEMA-*n*-butanol[b]		0.668	0.388	5.8
		0.644	0.385	
		0.602	0.300	
		0.474	0.223	

[a] Intrinsic viscosity $[\eta]$ in dl/g.
[b] Θ checked by precipitation studies.

polymer under theta conditions etc. Our values of $[\eta]$ as estimated by Huggins and Kramer plots (Fig. 1) are accurate to within ±0.001 dl/g. Wherever possible we have measured Θ directly by the precipitation method involving extrapolation of $1/T_c$ versus $[(1/x^{1/2}) + (^1/_2x)]$, where T_c is the critical solution temperature of a given polymer fraction in the solvent, and x represents the ratio of the molar volume of the polymer to that of the solvent. Repeated sets of experiments give Θ values to within ±1°C. For other systems, on which precipitation measurements were not made, Θ was found by viscometry.[55] These extrapolations give a rather inaccurate estimate of Θ for systems where $T \gg \Theta$, but a fairly accurate value ($\pm 2°$C) for systems for which $T \approx \Theta$. Even if measurements of $[\eta]$ are not made exactly at Θ but at one or two degrees higher, the accuracy in the measurement of K as determined by $[\eta]/M^{1/2}$ versus $M^{1/2}$ plots would not be significantly affected, for, in effect, such plots instead of being perfectly horizontal would show a slight positive slope (cf. in Fig. 2, the plot for the PMMA/*n*-butyl bromide system at $T = 35°$C, while the exact Θ, as measured by precipitation, may be less by ca. 1°C). Results of $[\eta]_\Theta$, K (Table I) for PMMA and PEMA are given.

In view of the above limitations, our K values obtained by measurements under theta conditions for PMMA are comparable to the literature values;[2,6] K values for PEMA, on the other hand, are somewhat larger than those reported by Chinai.[58] No explanation is available at present for this discrepancy except that the preliminary work with other mixed solvent systems from our laboratory seems to indicate that our K values are higher than those of Chinai. Only further work on more theta systems of PEMA and evaluation of the exact effect of temperature and solvent (single and or mixed etc.) could lead to any definite conclusion.

K from [η] in Good Solvents

This method has the merit that the convenient tool of viscometry may be employed for good solvents with facility. Since the exact relations among α, and α_η and z are still not established, the values of K and Θ obtained are at best approximate, but serve at least as a good estimate of K, the accuracy being greater, the closer T is to Θ. Keeping the approximations involved in view, we have chosen the widely used plots of K-S (Fig. 2), F-F (Fig. 3), S-F (Fig. 4) and Berry (Fig. 5) for getting an estimate of K. From the nature of extrapolations involved not much meaning may be attached to ap-

TABLE II

K Values of Poly(methyl methacrylate) by Measurement of $[\eta]$ at $T \geqslant \Theta$

				$K \times 10^4$			
No.	Solvent	Θ, °C	T, °C	From $[\eta]_\Theta$	From S-F plots	From F-F plots	From Berry plots
1	*m*-Xylene	30	30.0	4.9	—	—	—
			40.0–70.0		4.4	4.1	—
2	*n*-Butyl bromide	35	35.0	4.6	—	—	—
			42.0–58.0		4.6	4.4	4.6
3	*p*-Xylene	50	50.0	4.9	—	—	—
			60.0–70.0		4.6	4.6	—
4	Isoamyl acetate	50	50.0	4.5	—	—	—
			65.0–80.0		3.7–3·5	2.7–2.4	
5	*o*-Xylene	−3	40.0–70.0	—	4.4	4.1	—
6	Cyclohexanone	−10	40·0–70·0	—	7·0	4·6	4·6

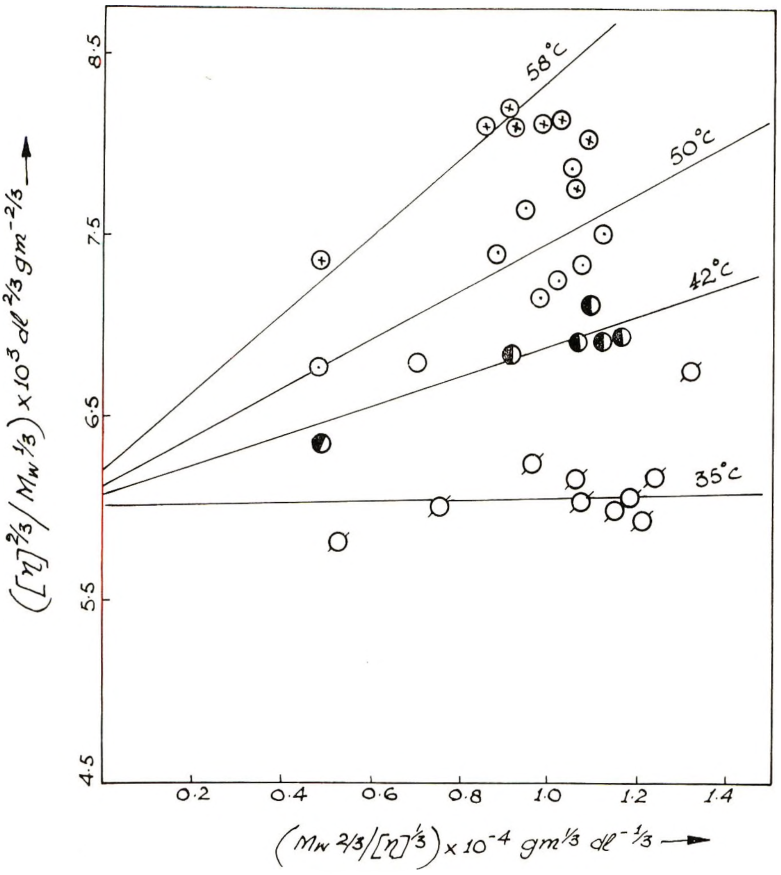

Fig. 2. Kurata-Stockmayer plots for PMMA in *n*-butyl bromide at 35, 42, 50, and 58°C.

parent variation of K with T. When K was evaluated from $[\eta]$ at $T > \Theta$ for PMMA systems, the extrapolation methods gave values of K comparable to those obtained at T close to Θ (in relatively poor solvents) (Table II). In better solvents like cyclohexanone, the values of K by the S-F method were higher than those obtained by other methods. For PEMA systems, K was obtained mainly by the S-F method (graphical and method of least squares) and the values of K in solvents like methyl *n*-propyl ketone, obtained by the former were higher than those at Θ (Table III). Such deviations were observed by others[59] also and were attributed to the fact that the parent equations relating α and z hold good only at very low values of z; higher K (the S-F method) being attributed[60] to the tendency of the $[\eta]/M^{1/2}$ versus $M^{1/2}$ plots to bend downwards (at higher M or z) and give a higher intercept on the ordinate (hence higher K) on extrapolation to $M = 0$. It was also noted[36,37] that the points in F-F plots, $[\eta]^{2/3}/M^{1/3}$ versus $M/[\eta]$ were usually scattered and the method yielded low values of K. Since at $T > \Theta$, large extrapolations are involved, various methods may not predict correctly, the small variations in K with temperature or solvent.

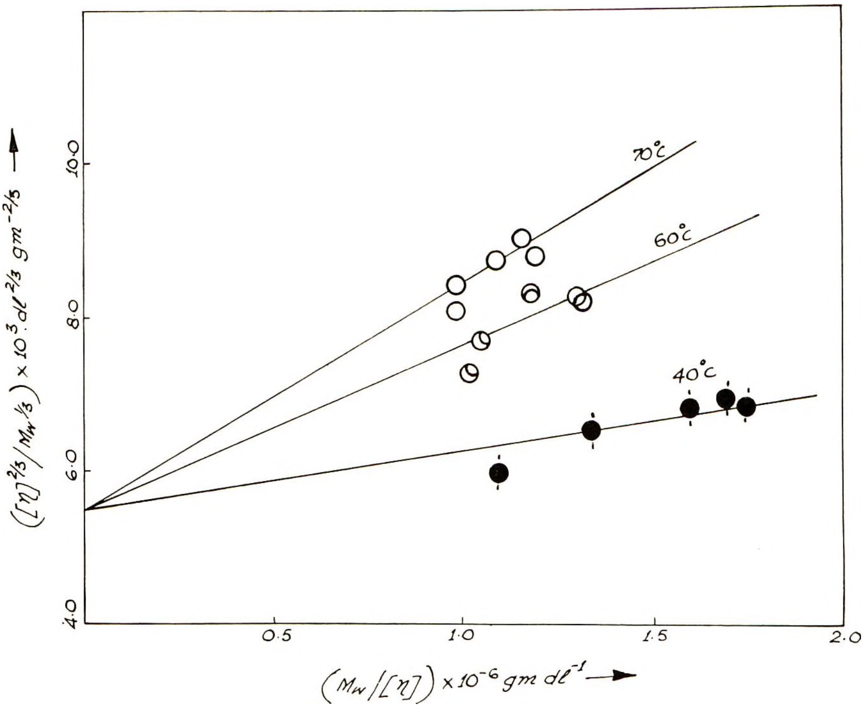

Fig. 3. Fox-Flory plots for PMMA in *m*-xylene at 40, 60, and 70°C.

Values of K obtained at $T = \Theta$ may be understood in terms of the combined effect of solvent and temperature on K. The effect of the solvent is explained[61-70] on the basis of the influence of the former on the nature of the potential energy barrier to rotation about the skeletal and other bonds, polarity of solvent, etc.

The effect of temperature is rather interesting. With increase of temperature, $\overline{r_0^2}$ (and hence K) is expected to decrease[15] due to a greater freedom of rotation around the skeletal bonds. On the other hand, an increase of $\overline{r_0^2}$ (and K) with temperature may be explained[51,69] on the basis of the increased freedom of rotation of the side chains. Our present knowledge of these effects does not warrant the separation[70] of solvent and temperature effects on K determined by viscosity measurements, even at $T = \Theta$. Often the temperature coefficient of K from stress–strain measurements on the bulk polymer is found[70,71] to be not only different in magnitude but even opposite in sign to that deduced by viscometry. To a first approximation,[65,66] the variation of K with Θ, for a set of chemically similar solvents, may be taken to reflect the temperature coefficient of K.

Recently, Flory[72] and others[73] obtained the temperature coefficient of K from variations of intrinsic viscosity with temperature in a given solvent and by making use of eq. (13):

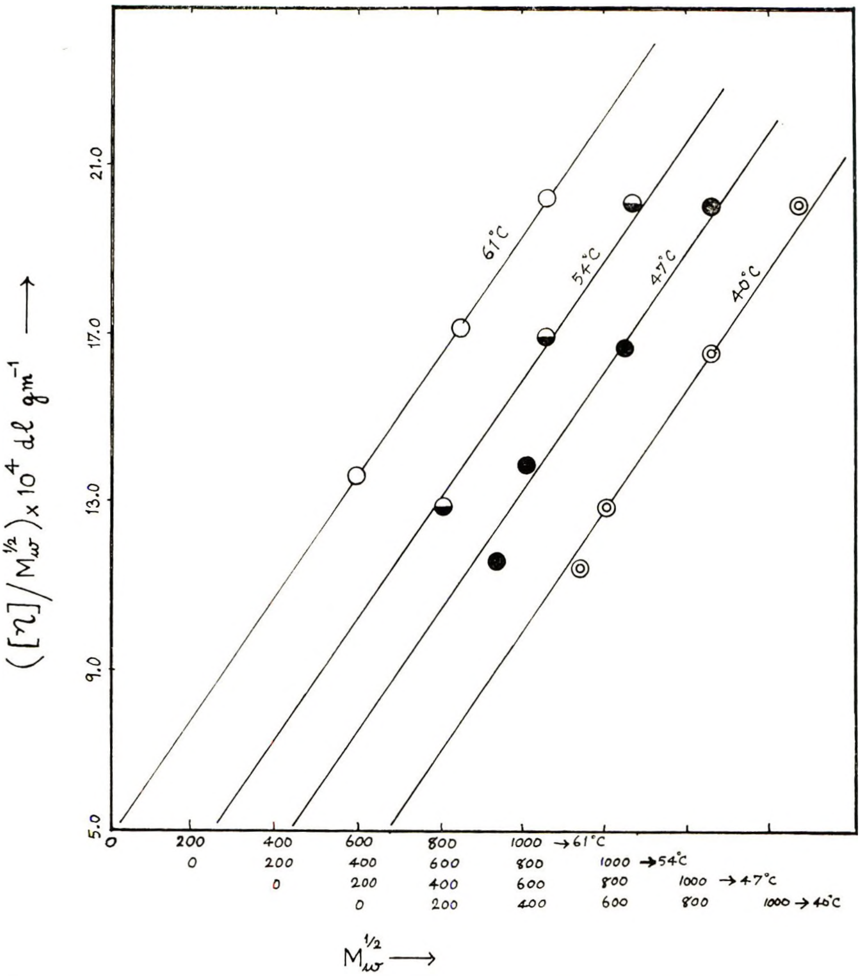

Fig. 4. Stockmayer-Fixman plots for PEMA in *n*-butyl chloride at 40, 47, 54, and 61°C.

$$\frac{d \ln \overline{r_0^2}}{dt} = 2\left(\frac{5\alpha^2}{3} - 1\right)[(5-\gamma)\alpha^2 - (3-\gamma)]^{-1}\frac{d \ln [\eta]}{dT} - \frac{2\gamma}{3}(\alpha^2 - 1)[(5-\gamma)\alpha^2 - (3-\gamma)]^{-1}\left[(2\beta_2 - \beta_1) - ({}^1/_2 - \chi)^{-1}\frac{d\chi}{dT}\right] \quad (13)$$

Here β_1 and β_2 are the bulk expansion coefficients of solvent and liquid polymer respectively, and γ is given by $\alpha_\eta{}^3 = \alpha^\gamma$. Although this method is promising as it involves viscosity data in one solvent only, the uncertainties in the factor γ and the exact relation between α and χ make its application difficult. A comparison of K values obtained at $T = \Theta$ for the polymers PMMA and PEMA indicates that the unperturbed dimensions of

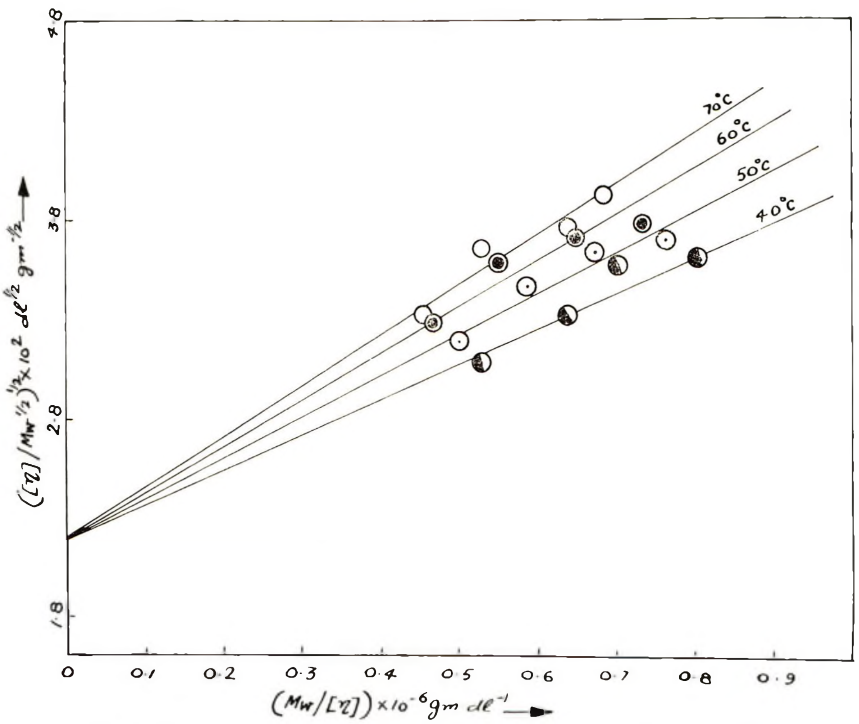

Fig. 5. Berry plots for PMMA in cyclohexane at 40, 50, 60, and 70°C.

TABLE III

K Values of Poly(ethyl Methacrylate) by Measurement of $[\eta]$ at $T \geq \Theta$

				$K \times 10^4$	
No.	Solvent	Θ, °C	T, °C	From $[\eta]_\Theta$	From S-F plots
1	Isopropanol	36.9	36.9	6.40	—
2	*n*-Butanol	45	45.0	5.80	—
3	Isoamyl acetate	−17	50.0	—	7.5
			80.0	—	6.1
4	Ethyl acetate	−223	35.0	—	5.0
			65.0	—	4.7
5	Methyl ethyl ketone	−99	23.0	—	6.3
			55.0	—	5.7
6	Methyl *n*-propyl ketone	0	40.0	—	11.5
			70.0	—	10.9
7	Benzene	−168	35.0	—	7.6
			60.0	—	7.0
8	*m*-Xylene	−3	50.0	—	7.7
			70.0	—	6.3
9	*n*-Butyl chloride	−13	40.0	—	5.0
			60.0	—	5.0
10	*n*-Butyl bromide	0	42.0	—	5.4 6.4 (F-F)
			65.0	—	5.0 6.5 (Berry)

PEMA are slightly greater than those of PMMA, probably because of the bulkier side group of the latter.

K from $[\eta]_\Theta$ Obtained Empirically

Various empirical and semiempirical methods suggested[16–24,26–31] for evaluation of $[\eta]_\Theta$ and hence K may be briefly touched upon. We have applied some of these methods to our data (Tables IV–VI, Fig. 6), and we conclude that these methods, though empirical, provide reasonable estimates of K and are sometimes more convenient for systems involving measurements at a single temperature or use of a single fraction of a polymer. For estimation of $[\eta]_\Theta$, Arichi[16] used eq. (14):

$$[\eta] = [\eta]_\Theta + 5 \times 10^{-3} A_2 M \tag{14}$$

where A_2 is the second virial coefficient.

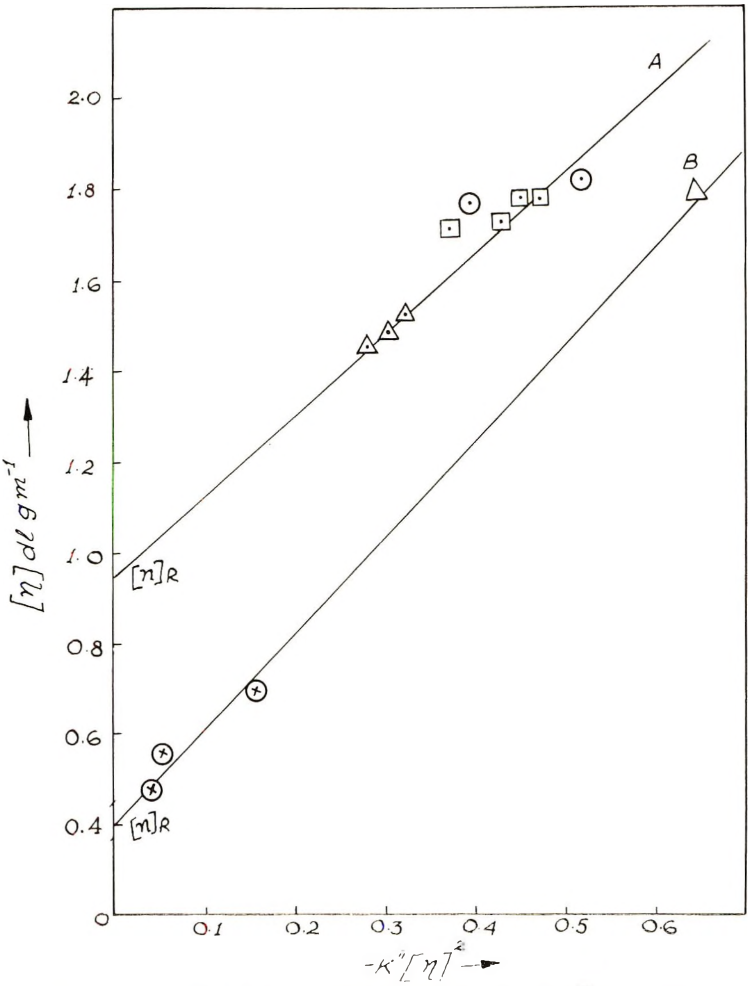

Fig. 6. Plots of $[\eta]$ vs. k'' $[\eta]^2$ for (A) PEMA, (A) fraction Ib ($\bar{M}_w = 14.45 \times 10^5$) and (B) PMMA fraction B5 ($\bar{M}_w = 9.42 \times 10^5$) in various solvents (⊙) n-butyl bromide; (△) benzene; (◬) isoamyl acetate; (⊡) m-xylene.

TABLE IV

K from Mark-Houwink Constants at 50°C

Polymer	Solvent	$K_m \times 10^4$	a	$K \times 10^4$
PMMA	p-Xylene	4.68	0.50	4.7
PMMA	Cyclohexanone	0.75	0.71	3.2
PEMA	n-Butanol	5.80	0.50	5.8
PEMA	n-Butyl bromide	1.35	0.67	4.3
PEMA	m-Xylene	1.35	0.67	4.3

TABLE V

$[\eta]_\Theta$ Obtained from $[\eta]$ and k' for PEMA Systems

Solvent	Temperature, °C	Fraction	$(\bar{M}_w)^{1/2}$	$[\eta]$	k'	$[\eta]_\Theta$
m-Xylene		Ia	1382.0	2.250	0.30	0.826
	70	Ib	1202.0	1.782	0.35	0.806
		IIa	822.0	1.230	0.30	0.452
Ethyl acetate		4	1159.0	2.000	0.35	0.905
		6	1038.0	1.515	0.32	0.606
	65	7	852.1	1.116	0.38	0.694
Isoamyl acetate		Ia	1382.0	2.159	0.31	0.828
		Ib	1202.0	1.519	0.37	0.744
	70	Id	829.9	1.030	0.29	0.362

TABLE VI

Comparison of $[\eta]_R$ and $[\eta]_\Theta$

Polymer	Solvent	Temperature, °C	Fraction	$\bar{M}_w \times 10^{-5}$	$[\eta]_R$	$[\eta]_\Theta$
PEMA	n-Butyl bromide	42–65	Ib			
	Isoamyl acetate	50–80		14.45	0.95	0.84[a],
	m-Xylene	47–61				0.85[b]
PEMA	n-Butyl bromide	42–65	Ic			
	n-Butyl chloride	47–61		10.05	1.00	—
	m-Xylene	47–70				
PMMA	n-Butyl bromide	35–58	5B	9.42	0.40	0.44[c]
	Benzene	23				
PMMA	o-Xylene	40–70	8B	6.93	0.40	0.41[d]
	Benzene	35				

[a] Measurement in isopropanol $\theta = 36.9°C$.

[b] Rao's empirical method.[21]

[c] Measured in p-xylene, $\theta = 50°C$, and m-xylene, $\theta = 30°C$.

[d] Measured in p-xylene, $\theta = 50°C$, and in m-butyl bromide, $\theta = 35°C$.

Bianchi and Peterlin[17] proposed $[\eta] = K_m M^a$ with the Mark-Houwink constant a for a polymer in good solvent decreasing with molecular weight. For $M < 10^4$ they recognized, an extended region over which $a = 0.5$ and $K_m \approx K$. Van Krevelen and Hoftyzer[18,19] proposed the relation:

$$[\eta] = 32K_\Theta(M/1000)^a = K_M M^a \tag{15}$$

From an application of these equations to our data (Table IV), we conclude that the agreement is satisfactory.

Kanide[20] has also suggested a new approach for determining unperturbed dimensions of the polymer from the Mark-Houwink parameters. Rao[21] used the empirical equation:

$$[\eta]_\Theta = [\eta]\{1 - (1 - 2k')^{1/2}\} \tag{16a}$$

for a single fraction of a polymer in several solvents.

Theoretical relations close to eq. (16a) have been proposed by Bhatnagar, Biswas, and Gharpurey[22] and Yamakawa.[23] Sakai[24] reviewed various theoretical equations and proposed for the Huggins constant:

$$k' = \frac{1}{2} + \frac{\bar{v}^2}{2[\eta]} - \frac{3(\alpha_n{}^2 - 1)}{4\alpha_n{}^4} \tag{16b}$$

where $0.5 < k_\Theta' \leq 0.7$; $k_\Theta' = k'$ at $T = \Theta$. Our values of k_Θ' are found[25] to be in the range 0.5–0.7. It may be emphasized that eq. (16b) does not predict a unique value of k_Θ' independent of solvent and molecular weight of the polymer. An application of eq. (16a) to our data on PEMA (Table V) indicates that the value of K compares well with that obtained by the S-F method within limits of experimental errors. Gundiah and Kapur[26] found that the value of $[\eta]_R$, the intrinsic viscosity at the precipitation point obtained from plots of $[\eta]$ versus $k''[\eta]^2$ could be related to M:

$$[\eta]_R = kM^{0.5} \tag{17}$$

Earlier they reported $[\eta]_R \approx [\eta]_\Theta$ and $k \approx K$ for polystyrene and some PMMA systems. Recently they reported[27] that for PMMA in benzene, chloroform, or acetone, $[\eta]_R > [\eta]_\Theta$. Our plot of $[\eta]$ versus $k''[\eta]^2$ (Fig. 6) for different fractions of PMMA and PEMA have yielded $[\eta]_R$ values which compared well within the corresponding $[\eta]_\Theta$ values obtained[28] at $T = \Theta$. We admit that extrapolations for $k''[\eta]^2 \leq 0.1$ if not available are hazardous. The error limits in k'' and $[\eta]_R$ were ± 0.03 and $+0.04$ respectively. The poor agreement reported[27] between $[\eta]_R$ and $[\eta]_\Theta$ may be due to the latter having been determined from F-F or S-F plots rather than by direct measurements at Θ.

References

1. J. M. G. Cowie, *Polymer*, **7**, 487 (1966).
2. T. Brandrup and E. H. Immergut, Eds., *Polymer Handbook*, Interscience, New York, 1966, p. 47.
3. G. V. Schulz and R. Kirste, *Z. Physik. Chem.* (Frankfurt), **30**, 171 (1961).
4. S. N. Chinai and C. W. Bondurant, Jr., *J. Polym. Sci.*, **22**, 555 (1956).
5. H. Lutje and G. Meyerhoff, *Makromol. Chem.*, **68**, 180 (1963).
6. T. G. Fox, *Polymer*, **3**, 111 (1962).
7. M. Bohdanecky, *Coll. Czech. Chem. Commun.*, **30**, 1576 (1965).
8. H. Inagaki and S. Kawai, *Makromol. Chem.*, **79**, 42 (1964).
9. M. Bohdanecky, *Coll. Czech. Chem. Commun.*, **34**, 407 (1969).
10. V. V. Varadaiah and V. S. R. Rao, *J. Sci. Ind. Res.*, **20B**, 280 (1961).

11. S. N. Chinai, J. D. Matlack, A. L. Resnick, and R. S. Samuels, *J. Polym. Sci.*, **17,** 391 (1955).

12. J. M. G. Cowie and S. Bywater, *Polymer*, **6,** 197 (1965).

13. W. R. Moore and R. J. Fort, *J. Polym. Sci. A*, **1,** 929 (1963).

14. S. Gundiah, R. B. Mohite, and S. L. Kapur, *Makromol. Chem.*, **123,** 151 (1969).

15. P. J. Flory, *Principles of Polymer Chemistry*, Cornell Univ. Press, Ithaca, N. Y., 1953.

16. S. Arichi, *Bull. Chem. Soc. Japan*, **39,** 439 (1966).

17. U. Bianchi and A. Peterlin, *J. Polym. Sci. A-2*, **6,** 1759 (1968).

18. D. W. Van Krevelen and P. J. Hoftyzer, *J. Appl. Polym. Sci.*, **11,** 1409 (1967).

19. D. W. Van Krevelen and P. J. Hoftyzer, *J. Appl. Polym. Sci.*, **10,** 1331 (1968).

20. K. Kanide, *Kobunshi Kagaku*, **25,** 781 (1968); *Chem. Abstr.*, **70,** 88348y (1969).

21. V. S. R. Rao, *J. Polym. Sci.*, **62,** S157 (1962).

22. H. L. Bhatnagar, A. B. Biswas, and M. K. Gharpurey, *J. Chem. Phys.*, **23,** 88 (1958).

23. H. Yamakawa, *J. Chem. Phys.*, **34,** 1360 (1961).

24. T. Sakai, *J. Polym. Sci. A-2*, **6,** 1535 (1968).

25. P. Vasudevan and M. Santappa, *Makromol. Chem.*, in press.

26. S. Gundiah, and S. L. Kapur, *J. Polym. Sci.*, **57,** 373 (1962).

27. S. Gundiah, R. B. Mohite, and S. L. Kapur, *Makromol. Chem.*, **123,** 151 (1969).

28. P. Vasudevan and M. Santappa, unpublished result.

29. P. C. Deb and S. R. Chatterjee, *Makromol. Chem.*, **120,** 49 (1968).

30. P. C. Deb and S. R. Chatterjee, *J. Ind. Chem. Soc.*, **46,** 468 (1969).

31. C. F. Cornet, *Polymer*, **6,** 373 (1966).

32. P. J. Flory and T. G. Fox, *J. Amer. Chem. Soc.*, **73,** 1904, 1915 (1951).

33. M. Kurata and H. Yamakawa, *J. Chem. Phys.*, **29,** 311 (1950).

34. M. Kurata and H. Utiyama, *Makromol. Chem.*, **34,** 139 (1959).

35. W. H. Stockmayer and M. Fixman, in *First Biannual American Chemical Society Polymer Symposium.* (*J. Polym. Sci. C*, **1**), H. W. Starkweather, Jr., Ed., Interscience, New York, 1963, p. 137.

36. H. Kurata and W. H. Stockmayer, *Fortschr. Hochpolym. Forsch.*, **3,** 196 (1963).

37. H. Kurata, W. H. Stockmayer, and A. Roig, *J. Chem. Phys.*, **33,** 151 (1960).

38. G. C. Berry, *J. Chem. Phys.*, **46,** 1338 (1967).

39. O. P. Ptitsyn, *Vysokomol. Soedin.*, **3,** 1673 (1963).

40. P. J. Flory and S. Fisk, *J. Chem. Phys.*, **44,** 2243 (1966).

41. H. Yamakawa and G. Tanaka. *J. Chem. Phys.*, **47,** 3991 (1967).

42. D. K. Sarkar and S. R. Palit, *Ind. J. Phys.*, **41,** 389 (1967).

43. N. Kuwahara, T. Okazawa, and M. Kaneko, *J. Chem. Phys.*, **47,** 3367 (1967).

44. H. Yamakawa, *J. Chem. Phys.*, **48,** 2103 (1968).

45. J. Norisuye, K. Kawahara, and H. Fujita, *J. Chem. Phys.*, **49,** 4330, 4339 (1968).

46. N. Kuwahara, T. Okawa, and M. Kaneko, *J. Chem. Phys.*, **49,** 4972 (1968).

47. M. Ueda and K. Kajitani, *Makromol. Chem.*, **109,** 22 (1967).

48. N. Kuwahara, *Kobunshi Kagaku*, **18,** 122 (1969).

49. M. Kurata, *J. Polym. Sci. A-2*, **6,** 1607 (1968).

50. T. Norisuye, K. Kawahara, and H. Fujita, *J. Polym. Sci. B*, **6,** 849 (1968).

51. W. Burchard, *Makromol. Chem.*, **50,** 20 (1961).

52. W. R. Krigbaum, *J. Polym. Sci.*, **28,** 213 (1958).

53. M. Ueda and K. Kajitani, *Makromol. Chem.*, **109,** 22 (1967).

54. H. Inagaki, H. Suzuki, and M. Kurata, in *U.S.-Japan Seminar in Polymer Physics* (*J. Polym. Sci. C*, **15**), R. S. Stein and S. Onogi, Eds., Interscience, New York, 1966, p. 409.

55. P. Vasudevan, Ph.D. Thesis, Madras University, India, 1968.

56. E. Cohn-Ginsberg, T. G. Fox, and H. F. Mason, *Polymer*, **3,** 97 (1962).

57. S. N. Chinai and R. J. Samuels, *J. Polym. Sci.*, **19,** 463 (1956).

58. S. N. Chinai, *J. Polym. Sci.*, **39,** 363 (1959).

59. G. C. Berry and T. G. Fox, *J. Amer. Chem. Soc.*, **36,** 3540 (1964).
60. M. Bohdanecky, *J. Polym. Sci. B*, **3,** 201 (1965).
61. S. Lifson and J. Oppenheim, *J. Chem. Phys.*, **33,** 109 (1960).
62. J. N. Majerus, *J. Polym. Sci. A-2*, **5,** 455 (1967).
63. C. Rossi, E. Bianchi, and E. Pedemonte, in *Macromolecular Chemistry Prague 1965* (*J. Polym. Sci. C*, **16**), O. Wichterle and B. Sedlàček, Eds., Interscience, New York, 1968, p. 2692.
64. J. M. G. Cowie, in *Macromolecular Chemistry Tokyo–Kyoto 1966*, (*J. Polym. Sci. C*, **23**), I. Sakurada and S. O. Kamura, Eds., Interscience, New York, 1968, p. 267.
65. T. A. Orofino and J. W. Mickey, *J. Chem. Phys.*, **38,** 2512 (1963).
66. T. A. Orofino and A. Ciferri, *J. Phys. Chem.*, **68,** 3136 (1964).
67. T. A. Orofino, *J. Chem. Phys.*, **45,** 4310(1960).
68. M. Ueda and K. Kajitani, *Makromol. Chem.*, **109,** 22 (1967).
69. C. V. Schulz, *Angew. Chem.*, **72,** 531 (1960).
70. U. Bianchi, *J. Polym. Sci. A-2*, **2,** 3083 (1964).
71. A. Ciferri, *J. Polym. Sci. A*, **2,** 3089 (1964).
72. P. J. Flory, A. Ciferri, and R. Chiang, *J. Amer. Chem. Soc.*, **83,** 1023 (1961).
73. M. Bohdanecky, V. Petrus, and P. Kratochvil, *Coll. Czech. Chem. Commun.*, **34,** 1168 (1969).

Received February 18, 1970
Revised September 9, 1970

JOURNAL OF POLYMER SCIENCE: PART A-2 VOL. 9, 499-515 (1971)

Dielectric and Rheo-optical Properties of Some Ethylene-Carbon Monoxide Copolymers

P. J. PHILLIPS,* G. L. WILKES,† B. W. DELF,‡ and R. S. STEIN§
Polymer Research Institute and Department of Chemistry,
University of Massachusetts, Amherst, Massachusetts 01002

Synopsis

Studies were made on films of copolymers of ethylene with 0.5 and 1.0 mole-% carbon monoxide. The carbon monoxide appeared negligibly to affect the degree of crystallinity, melting point, morphology, and dynamic mechanical spectra. Infrared dichroism showed that the orientation of the carbonyl groups was comparable with that of the crystalline CH_2 groups and indicated that the carbonyl groups are at least partially within the crystals. This is confirmed by x-ray measurements which indicate an expansion of the *a*-axis spacing and by an appreciable increase in the height of the α dielectric loss peak which has been assigned to crystalline motion. This α loss peak moves to a lower temperature with increasing carbonyl content, while the γ dielectric loss peak moves to higher temperatures. Activation energies of 25, 35, and 15 kcal/mole for the α, β, and γ peaks, respectively, were independent of carbonyl content and comparable with values for oxidized polyethylene.

INTRODUCTION

This paper involves a study of low-density polyethylene samples which contain small amounts of carbonyl groups introduced by copolymerization with ethylene. The purpose of studying such samples was twofold: (*1*) the carbonyl groups provide a polar indicator of molecular motion and orientation which may be observed from their dielectric relaxation and infrared dichroism; (*2*) the properties of the sample may be slightly modified as a consequence of the polar inclusion.

Initial samples prepared by high pressure polymerization of ethylene and copolymerization of ethylene with carbon monoxide containing 0.1, 0.5, and 1.0 mole-% carbonyl were kindly provided by Dr. J. E. Guillet of the University of Toronto, to whom they were supplied by Tennessee Eastman Co.,

---

* Present Address: Department of Materials, Queen Mary College, University of London, England.

† Present Address: Department of Chemical Engineering, Princeton University, Princeton, New Jersey.

‡ Present Address: Department of Physics, University College, Cardiff, Wales, Great Britain. This work was carried out while visiting the University of Massachusetts under the N.S.F. Visiting Foreign Scientist Program.

§ To whom correspondence should be sent.

Kingsport, Tenn. Additional amounts were provided by courtesy of Dr. R. L. Combs of the Tennessee Eastman Co. They are identical with the samples studied in a recent publication by Heskins and Guillet,[1] where they were reported to have a number-average molecular weight of 40,000 but were not characterized with respect to weight-average molecular weight or branching.

Compression-molded films of these samples were made at 180°C at 8000 psi. The annealed samples (AS) were left to cool at the natural cooling rate of the press. The quenched samples (QS) were made by removal from the press after 3–4 min and immediately quenching in a Dry Ice–ethanol bath. Samples for dielectric studies were compression-molded disks, 53 mm in diameter and 2 mm thick, made by pressing at 150°C at a pressure of 15,000 psi for 30 min followed by cooling under pressure over a period of 3–4 hr.

The degree of crystallinity of the samples used for dielectric studies was measured by the Mathews x-ray method[2] and found to be 51% for the 1.0% copolymer and 50% for the 0.5% copolymer.

LIGHT-SCATTERING PHOTOGRAPHS

The spherulitic nature of the samples was evaluated by using the photographic light-scattering technique and a He–Ne gas laser light source.[3] Typical H_V patterns are presented in Figure 1. The AS films show small "cloverleaf" patterns indicative of large spherulites. The QS films show no well-defined maximum in the lobe of the cloverleaf but show a much larger pattern. Thus it appears that while the AS films are definitely spherulitic in structure, the QS films have only poorly ordered spherulites and probably a higher content of amorphous material.

DYNAMIC-MECHANICAL BEHAVIOR

Dynamic-mechanical spectra were obtained on a Vibron direct reading viscoelastic spectrometer for the 0% and 1.0% carbonyl AS films at a frequency of 110 Hz. Data shown in Figure 2 indicates little difference between the two samples, both of which give results similar to those reported by Takayanagi[4] for branched polyethylene.

CALORIMETRY

Plots of specific heat versus temperature obtained with a Perkin-Elmer Model DSC 1B differential scanning calorimeter are shown in Figure 3 for 0% and 1.0% carbonyl AS samples. The weights of the two samples were very similar, so that the two plots may be compared with respect to the area under the curves. Heats of fusion determined from the areas were identical to within 1%, implying that the degree of crystallinity was essentially the same for both types of films.

The melting point depression caused by the carbonyl in the 1.0% sample was less than 0.5°C. A melting point depression may be calculated by using Flory's equation[5] for a random copolymer.

$$(1/T_m) - (1/T_m^\circ) = -(R/\Delta H_m)\ln X \qquad (1)$$

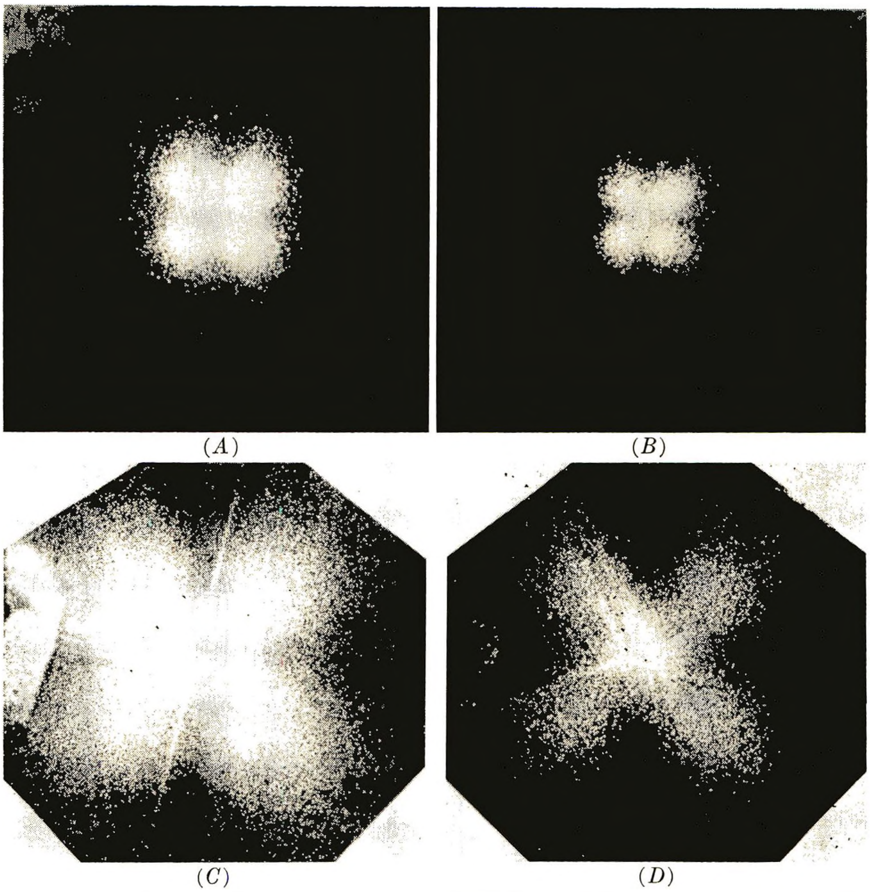

Fig. 1. H_V light scattering patterns of polyethylene ethylene–carbon monoxide copolymer films: (*A*) annealed, 0% carbonyl; (*B*) annealed, 1.0% carbonyl; (*C*) quenched, 0% carbonyl; (*D*) quenched, 1.0% carbonyl.

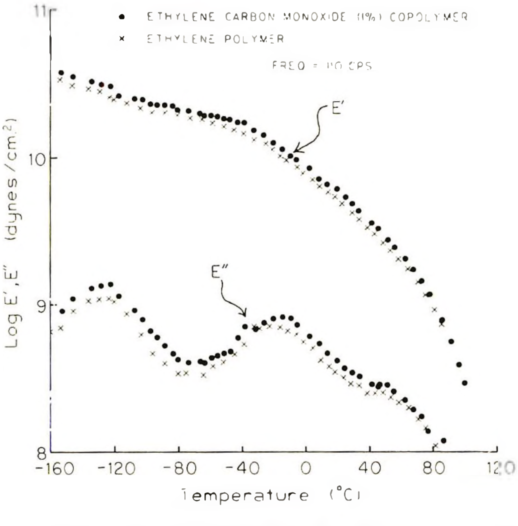

Fig. 2. Storage and loss Young's moduli as a function of temperature for a 0% and 10% carbonyl AS sample at 110 Hz.

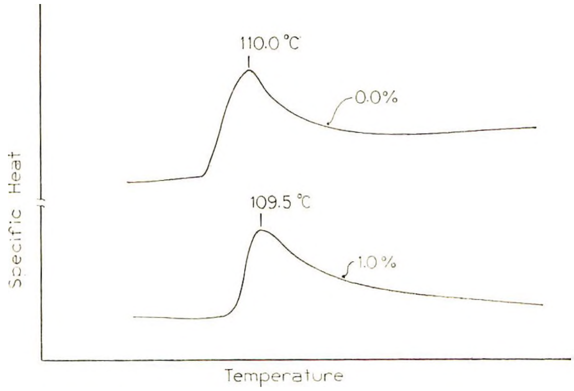

Fig. 3. Specific heat as a function of temperature for 0% and 1.0% carbonyl AS sample.

where T_m is the melting temperature of the copolymer, $T_m{}^\circ$ is the melting temperature of the pure crystalline homopolymer, R is the gas constant, ΔH_m is the heat of fusion, and X is the mole fraction of the crystallizable component in the copolymer. This gives a ΔT_m of 1.4°C for the 1.0% carbonyl copolymer, a value greater than the measured value by an amount exceeding experimental error (±0.5°C). The equation neglects melting point depression arising from finite crystal size which would lead to an even greater depression for the smaller crystals in the copolymer sample.

The Flory equation is based upon the assumption that impurities are rejected by the crystal. It is known that carbonyl groups may be incorporated into the crystal lattice[6] and that 1:1 ethylene–carbon monoxide alternating copolymer has a crystal structure not greatly different from that of polyethylene.[7] It is likely that the formation of such a mixed crystal leads to a lower melting-point depression than is predicted by the Flory equation. More extensive calorimetric studies of ethylene–carbon monoxide copolymers have been reported by Wunderlich, *et al.*[8] who have also concluded that the CO group is incorporated within the crystal lattice.

LATTICE PARAMETERS

Further evidence for inclusion of carbonyl groups within the crystal comes from precision measurement of the 200 and 110 lattice spacings of AS samples. These were compared with an internal standard of powdered Al_2O_3 dusted on the surface of the sample. The *d* spacings of the 1.0% carbonyl samples were greater than those of the 0% sample by $\Delta(200) = 0.004 \pm 0.001$ Å and $\Delta(110) = 0.0023 \pm 0.0007$ Å. This corresponds to an increase of 0.008 Å in the *a* spacing and a change in the *b* spacing too small to be observed.

Chatani et al.,[9] have reported lattice parameters for a series of polyketones. By interpolating linearly from their results at 22% carbonyl concentration to 1.0% carbonyl, we calculate a 0.007 Å increase in the *a* spacing and a negligible increase in the *b* spacing. This represents satisfactory agreement and is consistent with the assumption that carbonyl groups are included within the crystals of our samples. A somewhat larger increase of 0.016 Å is estimated by interpolation of the data of Wunderlich and Poland.[8]

X-RAY LINE BROADENING

The 200 diffraction from the 1.0% carbonyl AS sample shows a small but significant increase in breadth as compared with the base polyethylene. This could be due to a reduction in size of the ordered regions, but as the crystallinities are similar, it is almost certainly due to the lattice being strained by the presence of the carbonyl groups. An approximation to the magnitude of this strain may be obtained by measuring the half-widths (the width at half height) of the 1.0% and 0% samples, W_1 and W_0, respectively. Then, the breadth caused by the strain W_s is

$$W_s^2 = W_1^2 - W_0^2 \tag{2}$$

as the observed profiles are Gaussian to a good approximation. We can then obtain a value for the root-mean-square strain $\langle\epsilon\rangle$ from

$$\langle\epsilon\rangle = W_s/(4 \tan \theta) \tag{3}$$

where θ is the Bragg diffraction angle. This expression is not exact but will give a good approximation if the average crystal size is the same in both samples. We find that in units of 2θ, $W_1 = 1.255°$, $W_0 = 1.225°$ so that $W_s = 0.27°$ and $\langle\epsilon\rangle = 0.08\%$ strain in the direction perpendicular to the 100 plane. No broadening of the 110 line was detected, indicating that strain perpendicular to the 110 plane is small.

INFRARED SPECTRA AND DICHROISM

A typical polarized infrared spectrum for the 1.0% carbonyl sample stretched 1.6 times its unstretched length is given in Figure 4. The spectrum contains the bands arising from the ethylene as well as the carbonyl groups. We shall devote our attention to the bands at 720 cm^{-1} and at 1740 cm^{-1}.

The 720 cm^{-1} band arises from the CH_2 rocking of the ethylene sequences having a transition moment perpendicular to the chain axis.[10,11] At higher resolution, this band is seen to consist of two components, one at 720 cm^{-1} arising partly from a crystalline contribution with a transition moment along the *b* crystal axis and partly from an amorphous contribution from chains with a series of four or more carbon atoms in the *trans* conformation.[12] The second component at about 730 cm^{-1} arises entirely from the crystalline phase and has its transition moment along the *a* crystal axis.

The 1740 cm^{-1} band arises from a carbonyl stretching mode[13] with its transition moment directed along the C=O bond axis and hence perpendicular to the chain axis. Splitting of this band dependent upon the location

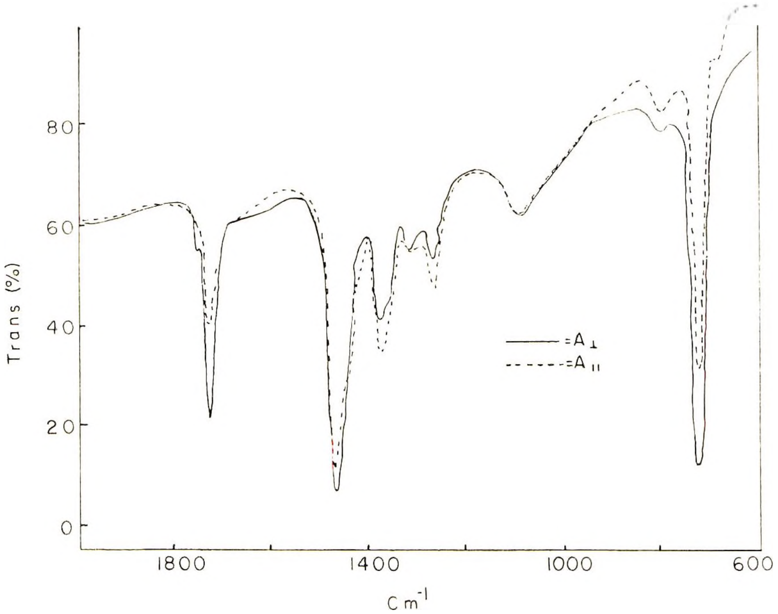

Fig. 4. Polarized infrared spectrum of a 1.0% carbonyl (AS) sample with an extension ratio of 1.6.

of the group in the crystalline or amorphous phase was not observed. The intensity of this band decreases with decreasing carbonyl content, and it is not observed in the 0% carbonyl sample. The high intensity of this band relative to that of the ethylene bands in a sample containing only 1.0% carbonyl is a consequence of the high relative value of the transition moment of the carbonyl stretching vibration.

It is noted from Figure 4 that both of the above bands exhibit greater absorption for radiation polarized perpendicularly to the stretching direction in accordance with the assignments of the transition moments in directions perpendicular to the ethylene chain.

The dichroism of a band is defined as

$$D = A_{\parallel}/A_{\perp} \tag{4}$$

where $A_{\parallel}$ and $A_{\perp}$ are absorbances for radiation polarized parallel and perpendicular to the stretching direction, respectively. This is related to the orientation function f_M of the transition-moment vector **M** of the absorbing group by[14,15]

$$(D - 1)/(D + 2) = f_M \tag{5}$$

where f_M is defined by

$$f_M = [3 \langle \cos^2 \theta_M \rangle_{av} - 1]/2 \tag{6}$$

The angle θ_M is that between the stretching direction and **M**.

If the transition-moment vector makes an angle α with the chain axis, then the orientation function of the chain axis is related to the dichroism by

$$f = C(D - 1)/(D + 2) \tag{7}$$

where

$$C = (D_0 + 2)/(D_0 - 1) \tag{8}$$

and

$$D_0 = 2 \cot^2 \alpha \tag{9}$$

For the two bands in question, **M** is perpendicular to the chain axis, so $D_0 = 0$ and $C = -2$. From the dichroism results, the calculated chain orientation functions are plotted against extension ratios in Figure 5. It is noted that the orientation functions are relatively high and are similar for the two bands, indicating a comparable degree of orientation of the portions of the chain containing the two groups. Since the 720 cm^{-1} band is known to be associated with crystalline regions or highly *trans* amorphous regions of the chain, this result indicates that the carbonyl groups are similarly located. Thus it is likely that the carbonyl groups are at least partly located within the crystalline regions.

Data reported by Read and Stein[16] on polyethylene containing 2.0% by weight of acrylonitrile are also given in Figure 5. It is noted that while the 720 cm^{-1} band exhibits orientation similar to that shown by the carbon monoxide copolymer, the 1740 cm^{-1} band orientation for the acrylonitrile

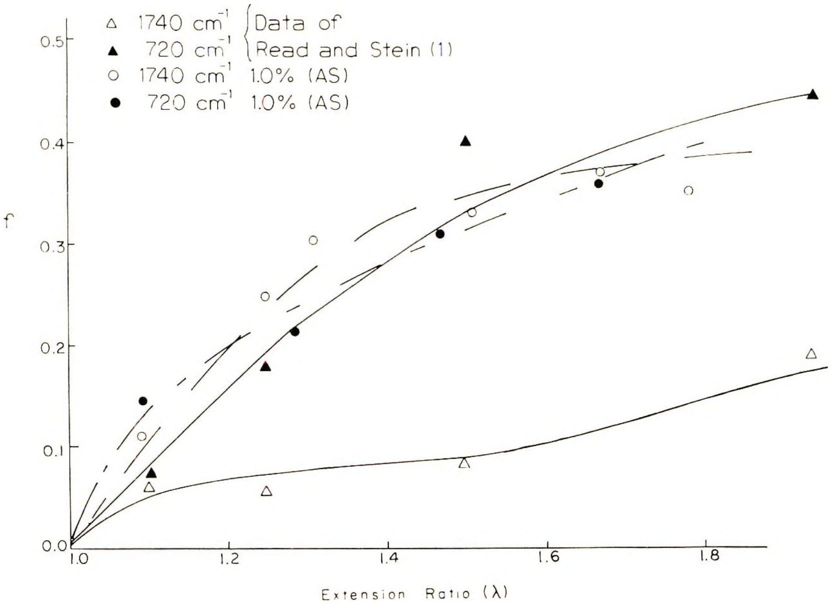

Fig. 5. Variation of the chain orientation function with extension ratio calculated from the dichroism of the 720 cm^{-1} band and the 1740 cm^{-1} band of the 1.0% carbonyl (AS) sample. Data of Read and Stein[14] for these bands are also given.

copolymer is appreciably lower. This may be a consequence of the carbonyl groups occurring primarily in the amorphous phase in this latter case. This seems likely since the carbonyl groups in the acrylonitrile copolymer probably arise from thermal oxidation which may predominate at chain ends or at chain folds occurring in amorphous regions.

DIELECTRIC STUDIES

Oxidized low-density polyethylene was first studied dielectrically by Oakes and Robinson,[17] who observed three relaxation regions comparable to the mechanical α, β, and γ relations. The origin of the losses has been attributed[18] to the relaxation of carbonyl groups situated in the main chain and produced by adventitious oxidation.

Milling of polyethylene at temperatures above 150°C in the presence of oxygen produces a greater concentration of carbonyl groups in the polymer. Samples treated in this way have been studied by Reddish and Barrie[19] and Tuijnman.[20]

The α peak was first assigned to the crystalline regions by Mikhailov[21] who showed that the α peak is not observed for polyethylene of low crystalline content. Annealed low-density polyethylene does show an α peak, and it was also observed by Mikhailov that the peak moves to higher temperatures on annealing. An important observation made by Reddish and Barrie was that the half-width of this peak was 1.75 decades and independent of temperature. Most amorphous polymers exhibit relaxations with half-width between 1.7 and 2.5 decades; crystalline polymers have much broader relaxation peaks, and a single relaxation process has a half-width of 1.14 decades. The α peak of polyethylene, therefore, has a relatively narrow distribution of relaxation times. Recent experiments of Tuijnman[20,22] and Booij[23] support the assignment of the peak to the crystalline regions.

The activation energy for the α peak has been well characterized[24] by a number of workers and is about 25 kcal/mole.

The β peak, by analogy with the mechanical β peak, is thought to arise from the amorphous regions, but no specific proposed mechanism for the process has yet been generally accepted. It is thought that the process involves motion of polymer segments containing side branches. Estimates of the activation energy of the process vary from 16 to 40 kcal/mole, but this variance may be due to the confused nomenclature of the past. Sandiford and Willbourn[25] obtained a value of 38 kcal/mole in both dielectric and mechanical experiments.

The mechanical γ peak can be separated into two components, one from the amorphous phase and one from the crystalline phase. The amorphous-phase relaxation is thought to be of the Schatzki[26,27] or Boyer[28] type or in view of more recent work,[29] may represent the primary glass transition. The crystalline-phase relaxation may be due to an endgroup mechanism.[30,31] One would expect the major part of the dielectric γ peak to come from the amorphous phase, owing to the small concentration of endgroups relative to carbonyls.

Up to the present, dielectric experiments have been carried out on samples containing carbonyl groups due either to adventitious oxidation or milling, and it cannot be said that the groups are randomly placed on the polyethylene chains and in the phases of the polymer. For this reason, it is useful to obtain data from samples containing randomly placed carbonyl groups as well as to study the effect of well defined increasing carbonyl content on the properties of polyethylene.

The copolymers show α, β, and γ relaxations similar to those observed for oxidized polyethylene samples. However, in this case, the magnitude of the α peak is much greater than in the adventitiously oxidized samples. This tends to confirm that the α peak is crystalline in origin as oxidation in the interior of a crystal is not expected to any great extent.

EXPERIMENTAL

The apparatus[24] consisted of a General Radio capacitance measuring assembly Type 1620-A. The frequency range of this instrument was from 50 Hz to 10 kHz. A three-terminal cell supplied by Balsbaugh Laboratories (Type LD-3) was used in conjunction with the bridge.

Temperature variation was achieved from room temperature to −130°C by cooling the interior of the cell with dry nitrogen which had previously been passed through a coil immersed in liquid nitrogen. Different temperatures were achieved by variation of the rate of flow of nitrogen gas.

Higher temperatures up to 100°C were obtained by heating the interior of the cell with dry air which had been passed through a coil immersed in an oil bath. Variation of temperature was again achieved by altering the flow of gas, as well as the oil bath temperature.

Experiments were carried out over the temperature range −130°C to +100°C and at frequencies of 50, 100, 200, and 500 Hz and 1, 2, 5, and 10 kHz on samples containing 1.0%, 0.5%, and 0% carbonyl groups.

RESULTS AND DISCUSSION

All the polymers show relaxation regions. For the polymers containing 1.0% and 0.5% carbonyl three distinct relaxations are apparent. The 0% polymer shows loss of very small magnitude in the regions of the α and γ relaxations, but these relaxations could not be measured accurately since the tan δ values were of the order of the experimental error. The reasons for this loss are probably (a) ester endgroups or (b) some partial oxidation incurred during molding.

Curves of tan δ versus temperature are shown for the 1.0% and 0.5% copolymers in Figures 6 and 7, respectively, at frequencies of 100 Hz, 1 kHz, and 10 kHz. Curves of tan δ versus frequency for the α peaks of both copolymers at various temperatures are shown in Figures 8 and 9.

It can be seen from Figures 6 and 7 that all three peaks vary in magnitude with carbonyl concentration and that the α peak also varies in position.

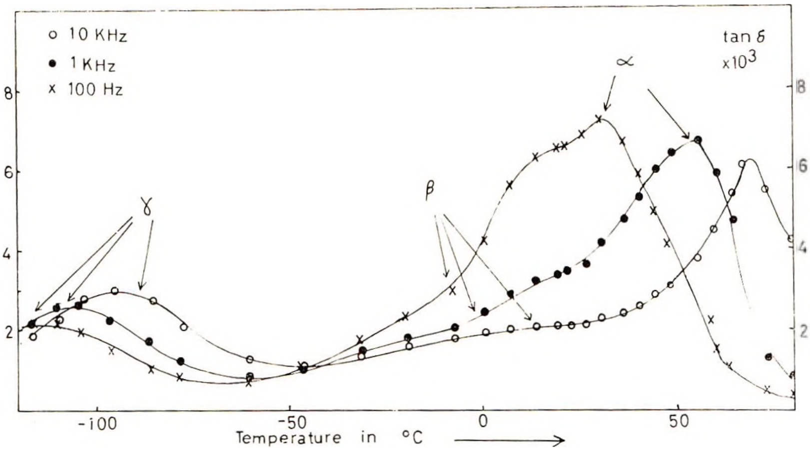

Fig. 6. Variation of the dielectric tan δ with temperature for the 1.0% copolymer.

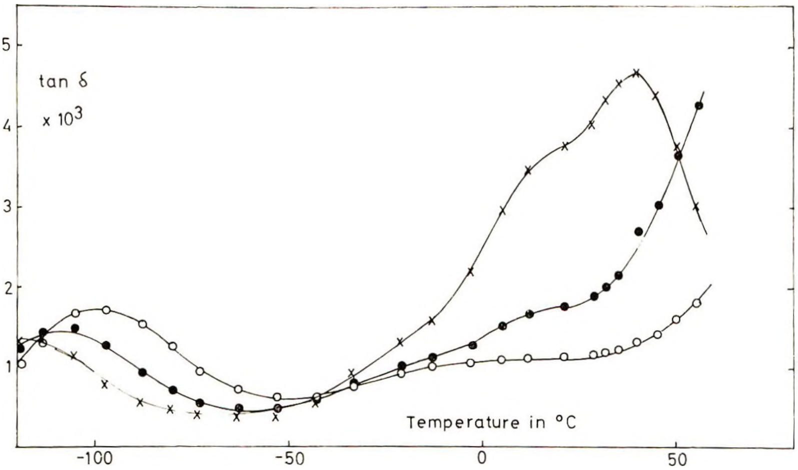

Fig. 7. Variation of the dielectric tan δ with temperature of the 0.5% copolymer: (○) 10 KHz; (●) 1 kHz; (×) 100 Hz.

α Peak

Figure 10 shows Arrhenius plots of the α peak for both copolymers, apparent points for the 0% samples, and points obtained by other workers for oxidized polyethylenes. Unfortunately, carbonyl concentrations were not specified by other workers.

As can be seen for the copolymers, as carbonyl content is increased the relaxation moves to lower temperatures. A similar occurrence is observed[18] on going from high-density to low-density polyethylene. Also, other workers[20,21] had observed that the relaxation moves to higher temperatures with annealing.

These observations are all in agreement with the assignment of the peak to the crystalline regions.

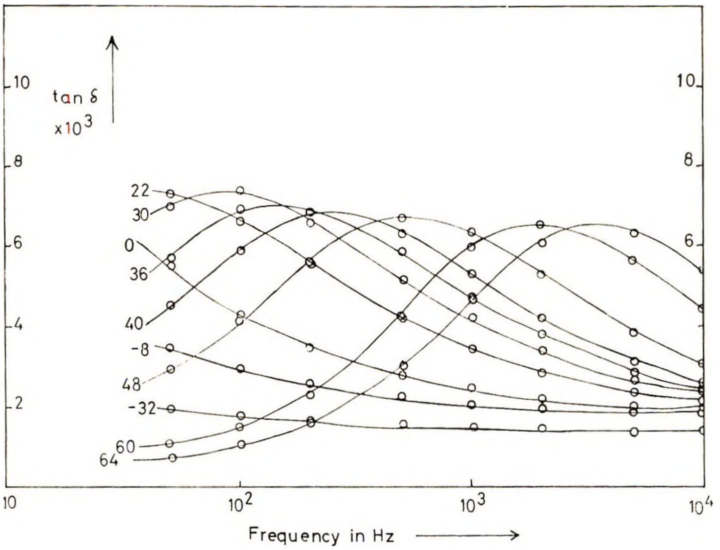

Fig. 8. Variation of the dielectric tan δ with logarithm of frequency in the region of the α loss peak for the 1.0% copolymer. Temperatures in °C are specified.

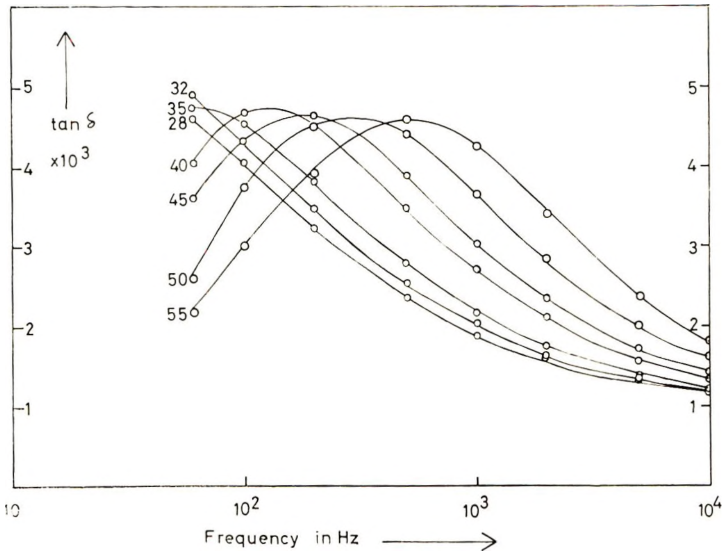

Fig. 9. Variation of the dielectric tan δ with logarithm of frequency in the region of the α loss peak for the 0.5% copolymer. Temperatures in °C are specified.

The activation energies obtained by various workers have been in the region of 23–28 kcal/mole. This work indicates values of 21–22 kcal/mole obtained from frequency-plane maxima and 25 kcal/mole from temperature-plane maxima. The plots appear to be linear over the two decades but there may be a slight curvature upwards at higher temperatures.

Cole-Cole plots[32] for the 1.0% copolymer at various temperatures are

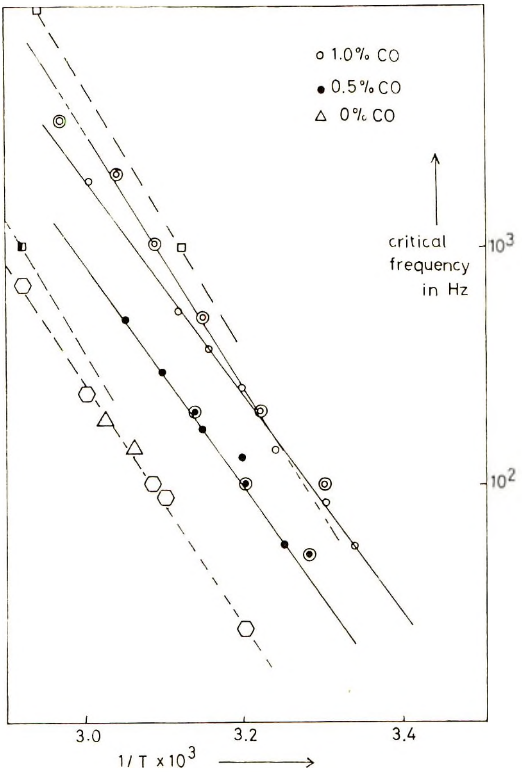

Fig. 10. Arrhenius plots of the α-peak data: (◎), 1.0% copolymer, temperature plane; (○) 1.0% copolymer, frequency plane; (⦿) 0.5% copolymer, temperature plane; (●) 0.5% copolymer, frequency plane; (△) 0% "copolymer"; (□) low-density polyethylene;[16,19] (◧) high-density polyethylene;[16,19] (⬡) milled high-density polyethylene.[17]

given in Figures 11 and 12. These appear to indicate that as the temperature is increased, the distribution of relaxation times becomes narrower, even to the extent of approaching a single relaxation time. There is, however, the possibility that we may have skewed-arc plots at the higher temperatures as the points available do not completely define the arc. Generally, there is a definite narrowing of the distribution of relaxation times as the temperature is increased.

This seems to imply that a variety of crystalline mechanisms is responsible for the dispersion and that as the temperature is increased many of these disappear leaving only the more stable of the processes. It is suggested that the less stable processes are associated with chain folds and loops and that the final process may be a combination chain-fold and chain-torsion mechanism. These suggestions are in line with experimental trends and activation energies. It is useful to note that a narrowing of the distribution relaxation times with increasing temperature is predicted by the barrier theory of Hoffman[33] for a chain torsion-transition mechanism.

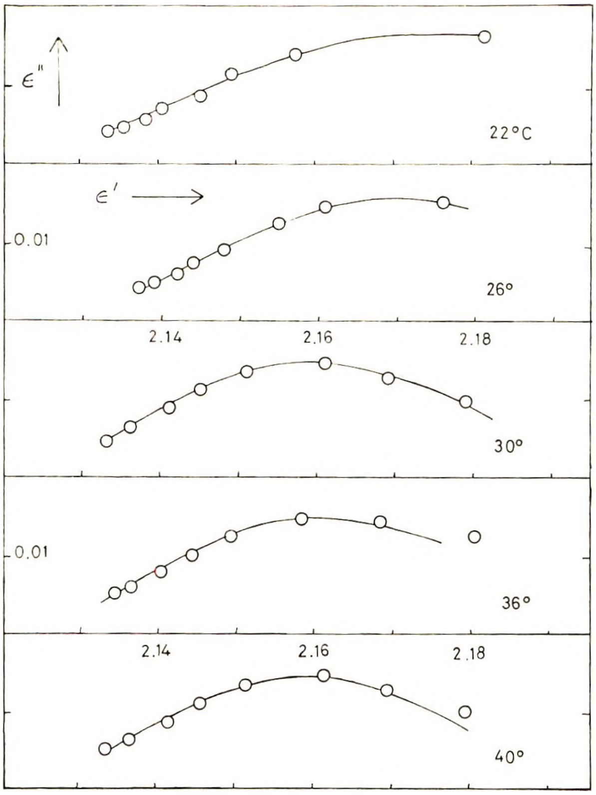

Fig. 11. Cole-Cole plot for the α peak for the 1.0% copolymer at various temperatures.

β Peak

The β peak appears as an intense shoulder on the low temperature side of the α peak. It is, in magnitude, about half the height of the α peak, in contrast to results of Mikhailov[20,21] in which the magnitude of the β peak was always considerably greater than that of the α peak.

An activation energy of about 35 kcal/mole was derived from the results which compares well with the value of 38 kcal/mole obtained by Sandiford and Willbourn.[25] The value of activation energy of the mechanical β peak for these copolymers has been obtained as 35–30 kcal/mole.

The above observations would seem to indicate that the dielectric and mechanical β peaks originate from the same mechanism. The high activation energies suggest that the motion involved is very hindered and could be due to motions in the amorphous phase between lamellae.[34,35]

γ Peak

This peak is reasonably sharp in the temperature plane but very broad in the frequency plane (see Figs. 13 and 14). Activation energies were

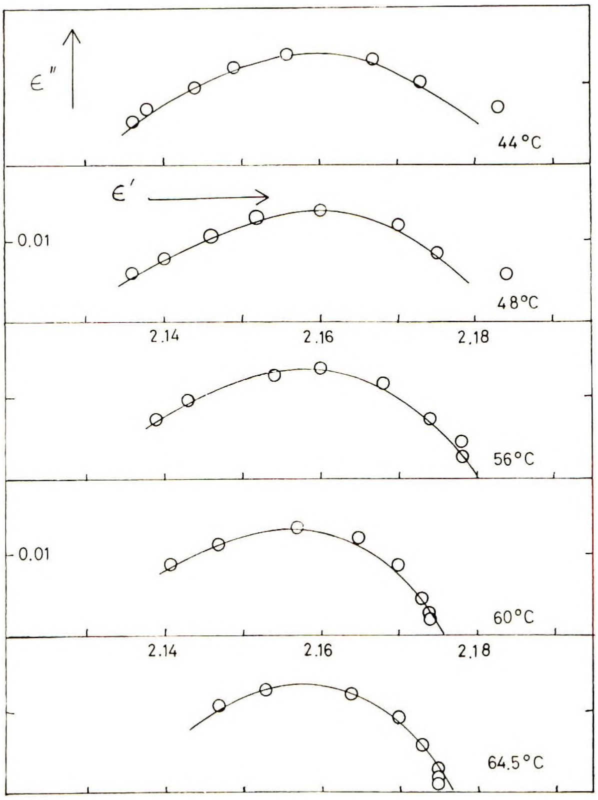

Fig. 12. Cole-Cole plot for the α peak for the 1.0% copolymer at various temperatures.

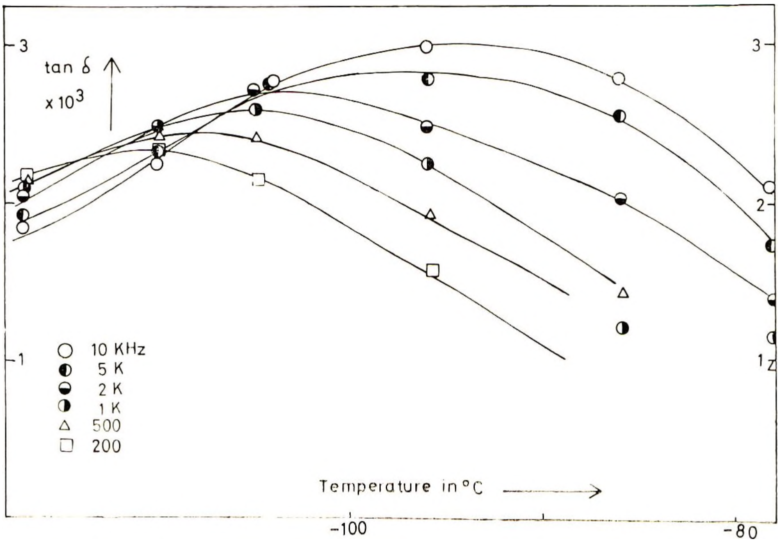

Fig. 13. Plot of tan δ vs. temperature for the γ peak region of the 1.0% copolymer.

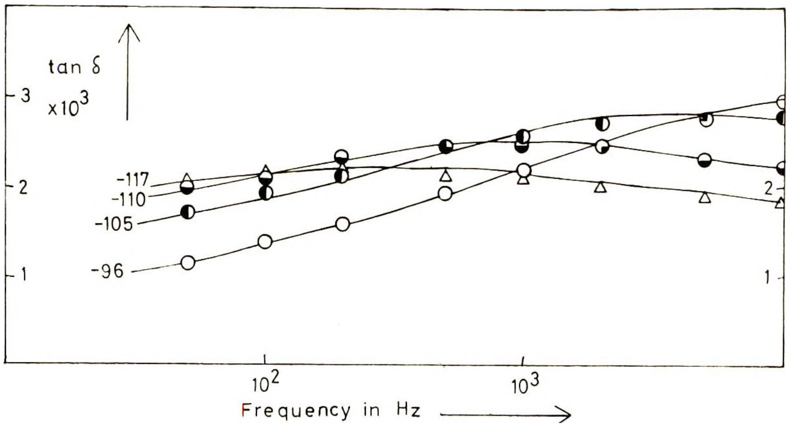

Fig. 14. Plot of tan δ vs. logarithm of frequency for the γ peak region of the 1.0% copolymer.

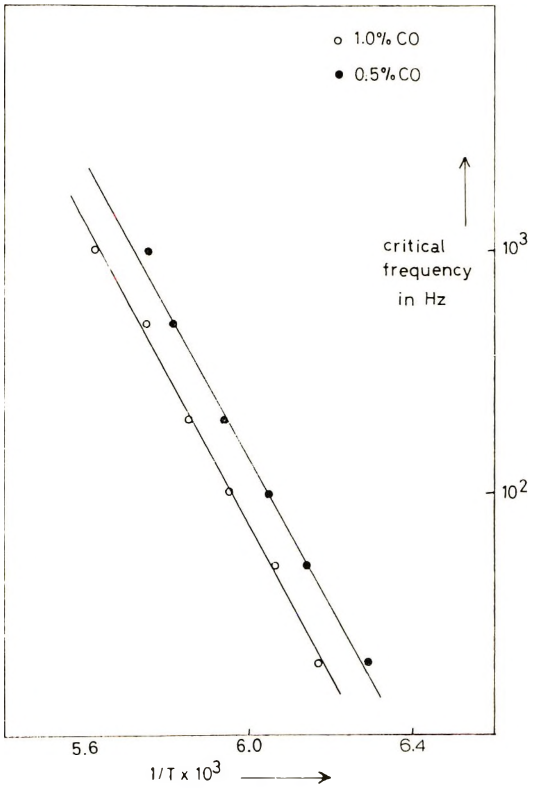

Fig. 15. Arrhenius plots of the γ peak data for both copolymers.

found to be 14.3 kcal/mole for the 1.0% copolymer and 14.1 kcal/mole for the 0.5% copolymer. The peak also shifted to higher temperatures as the carbonyl content was increased (see Fig. 15).

This seems to support the suggestion[29,36] that the γ_a relaxation in polyethylene is related to the glass transition. However, perhaps a more reasonable explanation is that the amorphous region becomes more tightly bonded as the concentration of polar groups increases, thereby causing the γ_a relaxation to occur at higher temperatures. This would therefore appear to support the assignment of the dielectric γ peak to the amorphous region. It is possible that the relaxation may be the amorphous equivalent[37] of the crystalline relaxation and may be due to motions of a —CH_2—CH_2—CO—CH_2—CH_2— section of the chain.

All of the results are consistent with the location of carbonyl groups in both crystal and amorphous regions. The crystalline and dielectric loss peak shifts to lower temperatures while the γ peak shifts to higher temperatures with increasing carbonyl content. Since the α loss peak is most certainly primarily of crystalline origin, it seems likely that the γ dielectric loss peak comes from an amorphous contribution.

This work was supported in part by a contract with the Office of Naval Research and in part by a grant from the Petroleum Research Fund of the American Chemical Society.

References

1. M. Heskins and J. E. Guillet, *Macromolecules*, **3**, 224 (1970).

2. J. L. Mathews, H. S. Pieser, and R. B. Richards, *Acta Cryst.*, **2**, 85 (1949).

3. P. F. Erhardt and R. S. Stein, *High Speed Testing, Volume VI: The Rheology of Solids* (*Appl. Polym. Symp.*, **5**), R. D. Andrews, Jr., and F. R. Eirich, Eds., Interscience, New York, 1967, p. 113.

4. M. Takayanagi, *Mem. Fac. Eng. Kyushu Univ.*, **23**, 1 (1963).

5. P. J. Flory, *Trans. Faraday Soc.*, **51**, 848 (1955).

6. C. W. Bunn and H. S. Pieser, *Nature*, **159**, 161 (1957).

7. Y. Chatani, T. Takizawa, S. Murahashi, Y. Sakata, and Y. Nishimura, *J. Polym. Sci.*, **55**, 811 (1961).

8. B. Wunderlich and D. Poland, *J. Polym. Sci. A*, **1**, 357 (1963).

9. Y. Chatani, T. Takizawa, and S. Murahashi, *J. Polym. Sci.*, **62**, S27 (1962).

10. S. Krimm, *Fortschr. Hochpolym. Forsch.*, **2**, 51 (1960).

11. R. S. Stein and G. B. B. M. Sutherland, *J. Chem. Phys.*, **22**, 1993 (1954).

12. R. G. Snyder, *J. Chem. Phys.*, **47**, 1316 (1967).

13. G. Herzberg, *Molecular Structure and Molecular Spectra, II. Infrared and Raman Spectra of Polyatomic Molecules*, Van Nostrand, New York, 1945, p. 195.

14. R. B. D. Fraser, *J. Chem. Phys.*, **21**, 1511(1953).

15. R. S. Stein, *J. Polym. Sci.*, **31**, 327 (1958).

16. B. E. Read and R. S. Stein, *Macromolecules*, **1**, 116 (1968).

17. W. G. Oakes and D. W. Robinson, *J. Polym. Sci*, **14**, 505 (1954).

18. G. P. Mikhailov, A. M. Lobanov, and B. I. Sazhin, *J. Tech. Phys.* (*USSR*), **24**, 1553 (1954).

19. W. Reddish and J. T. Barrie, paper presented at I.U.P.A.C. Symposium on Macromolecules, Wiesbaden, Kurzmitteilung 1A-3 (1959).

20. C. A. F. Tuijnman, *Polymer*, **4**, 259 (1968).

21. G. P. Mikhailov, S. P. Kabin, and T. A. Krylova, *Soviet Phys. Tech. Phys.*, **2**, 1899 (1957); *J. Tech. Phys* (*USSR*), **27**, 2050 (1957).

22. C. A. F. Tuijman, *Polymer*, **4**, 315 (1968).

23. H. C. Booij, in *Macromolecular Chemistry, Prague, 1965* (*J. Polym. Sci. C*, **16**), O. Wichterle and B. Sedláček, Eds. Interscience, New York, 1967, p. 1761.

24. P. J. Phillips and W. J. MacKnight, *J. Polym. Sci. A*-2, **8**, 727 (1970).

25. D. J. H. Sandiford and A. H. Willbourn, in *Polythene*, A. Renfrew and P. Morgan, Eds., Iliffe, London, Chap. 8.

26. T. F. Schatzki, *J. Polym. Sci.*, **57**, 496 (1962).

27. T. F. Schatzki, paper presented at American Chemical Society Meeting, September 1965, Atlantic City, N. J.; *Polym. Preprints*, **6**, 646 (1965).

28. R. F. Boyer, *Rubber Rev.*, **34**, 1303 (1963).

29. F. C. Stehling and L. Mandelkern, *Macromolecules*, **3**, 242 (1970).

30. K. M. Sinnott, in *Transitions and Relaxations in Polymers* (*J. Polym. Sci. C*, **14**), R. F. Boyer, Ed., Interscience, New York, 1966, p. 141.

31. J. D. Hoffman, G. Williams, and E. Passaglia, in *Transitions and Relaxations in Polymers* (*J. Polym. Sci. C*, **14**), R. F. Boyer, Ed., Interscience, New York, 1966, p. 173.

32. K. S. Cole and R. H. Cole, *J. Chem. Phys.*, **9**, 341 (1941).

33. J. D. Hoffman, *J. Chem. Phys.*, **22**, 156 (1954); *J. Chem. Phys.*, **23**, 1331 (1955).

34. Z. Stachurski and I. M. Ward, *J. Polym. Sci. A-2*, **6**, 1033 (1968).

35. Z. Stachurski and I. M. Ward, *J. Polym. Sci. A-2*, **6**, 1817 (1968).

36. A. H. Willbourn, *Trans. Faraday Soc.*, **54**, 717 (1958).

37. M. Takayanagi, *Mem. Fac. Eng. Kyushu Univ.*, **23**, 1 (1963).

Received June 29, 1970
Revised September 4, 1970

JOURNAL OF POLYMER SCIENCE: PART A-2 VOL. 9, 517-529 (1971)

Scattering of Light by Deformed Disordered Spherulites

R. S. STEIN and T. HASHIMOTO, *Department of Chemistry and Polymer Research Institute, University of Massachusetts, Amherst, Massachusetts 01002*

Synopsis

The change in the light-scattering patterns upon deforming two-dimensional disordered spherulites is shown to arise from four effects occurring upon stretching: (1) the change in shape of the spherulite, (2) the change in average orientation of the optic axes of the scattering volume elements, (3) the change in deviation of the optic axis orientation angle from its average value, and (4) the change in the distance over which this deviation is correlated. The effects of these contributions upon the experimental scattering patterns are analyzed.

Introduction

The change in light scattering patterns upon deforming perfect spherulites has been considered in two[1] and three dimensions.[2,3] The theories are based upon a model of affine deformation of an anisotropic sphere (or circle) to an ellipsoid (or ellipse) and lead to predicted scattering patterns which change shape with deformation in a manner which is approximately in agreement with experiment. The results are somewhat dependent upon the assumptions concerning the way in which the optic axes of the anisotropic elements constituting the spherulite change their orientation as the spherulite is deformed.

It has been observed that the scattered intensity from spherulites is superimposed on a background intensity which is believed to be primarily associated with the imperfect arrangement of crystalline lamellae constituting the spherulite.[4] Such background scattering has been observed with deformed spherulites[1,3] and has been subtracted from the experimental data to facilitate comparison with the spherulite deformation theory. It is our feeling that this background scattering conveys important information about the internal rearrangement of the spherulite so that its study is warranted. Measurements may be made under conditions (azimuthal scattering angle $\mu = 0°$ or $90°$ for H_V scattering) where the spherulitic contribution vanishes in which case the experiment yields direct information about the background. Such measurements are quite pertinent in studies of the dynamics of spherulite deformation where it is believed that the time scales for the spherulite deformation itself and the rearrangement of internal structure are different.

A theory for internal randomness of undeformed two-dimensional spherulites has been proposed in which optic axes are permitted to deviate from their ideal orientation in a manner described by an internal orientation correlation function.[5] Two simple cases, in which disorder in only the radial or only the tangential direction of the spherulite occurs, yield results that correspond to the experimentally observed deviations from perfect spherulite scattering.

In this paper, a similar analysis is carried out for the effect of disorder on the scattering from deformed spherulites.

Calculations

Consider a two-dimensional spherulite with the optic axes **a** lying in the plane of the spherulite at an angle β to the radius (Fig. 1). The plane of the spherulite lies perpendicular to the incident beam. The analyzer is assumed to be perpendicular to the incident beam as in a previous paper.[1] The angular coordinates of the radial vector **r** to a given scattering element are r and α. The H_V scattered amplitude is given by[1]

$$E_{H_V} = K \cos \rho_2 \int N_0 \sin [2(\alpha + \beta)] \cos [k(\mathbf{r} \cdot \mathbf{s})]d\mathbf{r} \qquad (1)$$

where, as before,[1] $\cos \rho_2 = \cos \theta / [\cos^2 \theta + \sin^2 \theta \sin^2 \mu]^{1/2}$, θ and μ are the scattering angles; $k = 2\pi/\lambda$; $\mathbf{s} = \mathbf{s}_0 - \mathbf{s}_1$, where $\mathbf{s}_0$ and $\mathbf{s}_1$ are unit incident and scattered ray vectors; N_0 is the density of scattering material at position **r** in the spherulite; K is the product of a number of physical constants and the birefringence of the spherulite. Upon deformation of the spherulite, this becomes

$$E_{H_V} = K \cos \rho_2 \int N(r', \alpha') \sin [2(\alpha' + \beta')] \cos [k(\mathbf{r}' \cdot \mathbf{s})]d\mathbf{r}' \qquad (2)$$

where the primed quantities designate the deformed state. The scattering density $N(r', \alpha')$ is generally a function of position in the spherulite, as is the angular orientation of the optic axis with respect to the radius.

As before,[1] we shall assume an affine deformation such that all parts of he spherulite deform with the same strain with an extension ratio λ_3 in

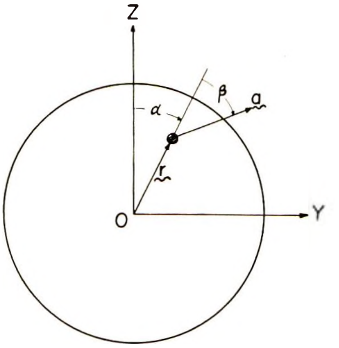

Fig. 1. Coordinates of optic axes within a two-dimensional spherulite.

the stretching direction (vertical and parallel to the direction of polarization of the incident light) and λ_2 in the transverse direction. It is usual but not necessary to assume that these spherulite extension ratios correspond to the sample extension ratios. This affine deformation results in the following transformations:[1]

$$r' = r[\lambda_2^2 \sin^2 \alpha + \lambda_3^2 \cos^2 \alpha]^{1/2} \tag{3}$$

$$\sin \alpha' = \frac{\lambda_2 \sin \alpha}{[\lambda_2^2 \sin^2 \alpha + \lambda_3^2 \cos^2 \alpha]^{1/2}} \tag{4}$$

and

$$\cos \alpha' = \frac{\lambda_3 \cos \alpha}{[\lambda_2^2 \sin^2 \alpha + \lambda_3^2 \cos^2 \alpha]^{1/2}} \tag{5}$$

It is then convenient to define an angle γ such that

$$\sin \gamma = \frac{\lambda_2 \sin \mu}{[\lambda_2^2 \sin^2 \mu + \lambda_3^2 \cos^2 \mu]^{1/2}} \tag{6}$$

and

$$\cos \gamma = \frac{\lambda_3 \cos \mu}{[\lambda_2^2 \sin^2 \mu + \lambda_3^2 \cos^2 \mu]^{1/2}} \tag{7}$$

and a variable q such that

$$q = kr \sin \theta \; [\lambda_2^2 \sin^2 \mu + \lambda_3^2 \cos^2 \mu]^{1/2} \tag{8}$$

in which case, we have

$$k(\mathbf{r}' \cdot \mathbf{s}) = q \cos \psi \tag{9}$$

where $\psi = \alpha - \gamma$. It also follows that $rdr = (R^2/X^2)qdq$, where

$$X = kR \sin \theta \; [\lambda_2^2 \sin^2 \mu + \lambda_3^2 \cos^2 \mu]^{1/2}$$

and R is the initial (undeformed) radius of the spherulite.

We shall also adopt the assumption of case I of the previous paper[1] that the total density of scattering material remains constant at every point within the spherulite so that $N_0 rdrd\alpha = N(\alpha', r')r'dr'd\alpha'$. Upon substituting eqs. (3)–(9) into eq. (2) one obtains

$$E_{Hv} = K_1 \int_{q=0}^{X} \int_{\psi=0}^{2\pi} [B(\alpha) \cos 2\beta' + C(\alpha) \sin 2\beta'] \times \cos [q \cos \psi] d\psi q dq \tag{10}$$

where

$$K_1 = {}^1/_2 K \cos \rho_2 N_0 (R^2/X^2)$$

$$B(\alpha) = \lambda_2 \lambda_3 \sin 2\alpha / [\lambda_2^2 \sin^2 \alpha + \lambda_3^2 \cos^2 \alpha] \tag{11}$$

and

$$C(\alpha) = (\lambda_3^2 \cos^2 \alpha - \lambda_2^2 \sin^2 \alpha)/[\lambda_2^2 \sin^2 \alpha + \lambda_3^2 \cos^2 \alpha] \tag{12}$$

Case of Angular Disorder

We shall assume that at a given polar angle α' within the deformed spherulite, the optic-axis angle β' is independent of r and hence of q. In this case, eq. (10) may be integrated over q, ψ being held constant. Let us define a function $f(\psi)$ by

$$f(\psi) = \frac{1}{X^2}\int_{q=0}^{X} \cos[q \cos \psi] q dq$$

$$= \frac{\cos[X \cos \psi] - 1}{[X \cos \psi]^2} + \frac{\sin[X \cos \psi]}{X \cos \psi} \tag{13}$$

Then eq. (10) becomes

$$E_{HV} = K_1 X^2 \int_{\psi=0}^{2\pi} [B(\alpha) \cos 2\beta' + C(\alpha) \sin 2\beta'] f(\psi) d\psi \tag{14}$$

If β' is constant, this integral may be evaluated numerically to give results equivalent to those previously published (for $\beta' = 0$) for uniform spherulites. Numerical integration can also be carried out for the case where β' is a function of α in the deformed state.

The case of interest here is that where there is heterogeneity in β' in the deformed state. As in the earlier paper,[5] we shall adopt the correlation function approach involving squaring eq. (14) prior to integration to obtain for the scattered intensity

$$I_{HV} = K_2 K_1^2 \int_{\psi_2=0}^{2\pi}\int_{\psi_1=0}^{2\pi} [B(\alpha_1) \cos 2\beta_1' + C(\alpha_1) \sin 2\beta_1'] [B(\alpha_2) \cos 2\beta_2' + C(\alpha_2) \sin 2\beta_2'] f(\psi_1) f(\psi_2) d\psi_1 d\psi_2$$

$$= K_2 K_1^2 [I_1 + I_2 + 2I_3] \tag{15}$$

where

$$I_1 = \int_{\psi_2=0}^{2\pi}\int_{\psi_1=0}^{2\pi} B(\alpha_1) B(\alpha_2) \cos 2\beta_1' \cos 2\beta_2' f(\psi_1) f(\psi_2) d\psi_1 d\psi_2 \tag{16}$$

$$I_2 = \int_{\psi_2=0}^{2\pi}\int_{\psi_1=0}^{2\pi} C(\alpha_1) C(\alpha_2) \sin 2\beta_1' \sin 2\beta_2' f(\psi_1) f(\psi_2) d\psi_1 d\psi_2 \tag{17}$$

and

$$I_3 = \int_{\psi_2=0}^{2\pi}\int_{\psi_1=0}^{2\pi} B(\alpha_1) C(\alpha_2) \cos 2\beta_1' \sin 2\beta_2' f(\psi_1) f(\psi_2) d\psi_1 d\psi_2 \tag{18}$$

We may now assume, as before, that $\beta_1' = \beta_{01}' + \Delta\beta_1'$ where β_{01}' is the average value of β_1' in the deformed state at the angular location corresponding to α_1, and $\Delta\beta_1'$ is the fluctuation from the average at this position. Then, we have

$$\cos 2\beta_1' \cos 2\beta_2' = \cos 2\beta_{01}' \cos 2\beta_{02}' \cos (2\Delta\beta_1') \cos (2\Delta\beta_2') + \sin 2\beta_{01}' \sin 2\beta_{02}' \sin (2\Delta\beta_1') \sin (2\Delta\beta_2') - 2 \sin 2\beta_{01}' \cos 2\beta_{02}' \sin (2\Delta\beta_1') \cos (2\Delta\beta_2') \quad (19)$$

Now if

$$\Delta\beta_{12}' = \Delta\beta_2' - \Delta\beta_1'$$

it follows that

$$\cos (2\Delta\beta_1') \cos (2\Delta\beta_2') = \cos^2 (2\Delta\beta_1') \cos (2\Delta\beta_{12}') - \sin (2\Delta\beta_1') \cos (2\Delta\beta_1') \sin (2\Delta\beta_{12}') \quad (20)$$

We shall adopt the previous assumptions that (1) the fluctuation $\Delta\beta_{12}'$ is independent of $\Delta\beta_1'$ and (2) positive and negative fluctuations of $\Delta\beta_{12}'$ are equally probable. Thus, for a given ψ_1 and ψ_2, Eq. (20) becomes

$$\langle\cos (2\Delta\beta_1') \cos (2\Delta\beta_2')\rangle_{\psi_1,\psi_2} = \langle\cos^2 (2\Delta\beta_1')\rangle_{\psi_1} \langle\cos (2\Delta\beta_{12}')\rangle_{\psi_1,\psi_2} \quad (21)$$

Similarly, it follows that

$$\langle\sin (2\Delta\beta_1') \sin (2\Delta\beta_2')\rangle_{\psi_1,\psi_2} = \langle\sin^2 (2\Delta\beta_1')\rangle_{\psi_1} \langle\cos (2\Delta\beta_{12}')\rangle_{\psi_1,\psi_2} \quad (22)$$

and

$$\langle\sin (2\Delta\beta_1') \cos (2\Delta\beta_2')\rangle_{\psi_1,\psi_2} = 0 \quad (23)$$

We shall now define a correlation function

$$G(\psi_1, \psi_2) = \langle\cos (2\Delta\beta_{12}')\rangle_{\psi_1,\psi_2} = G(\psi_1, \psi_{12}) \quad (24)$$

Then, eq. (19) becomes

$$\langle\cos (2\beta_1') \cos (2\beta_2')\rangle_{\psi_1,\psi_2} = [\cos 2\beta_{01}' \cos 2\beta_{02}' \langle\cos^2 (2\Delta\beta_1)\rangle_{\psi_1} + \sin 2\beta_{01}' \sin 2\beta_{02}' \langle\sin^2 (2\Delta\beta_1)\rangle_{\psi_1}] G(\psi_1,\psi_{12}) \quad (25)$$

and similarly,

$$\langle\sin (2\beta_1') \sin (2\beta_2')\rangle_{\psi_1,\psi_2} = [\sin 2\beta_{01}' \sin 2\beta_{02}' \langle\cos^2 (2\Delta\beta_1)\rangle_{\psi_1} + \cos (2\beta_{01}') \cos (2\beta_{02}') \langle\sin^2 (2\Delta\beta_1')\rangle] G(\psi_1,\psi_{12}) \quad (26)$$

and

$$\langle\sin (2\beta_1') \cos (2\beta_2')\rangle_{\psi_1,\psi_2} = \{\sin 2\beta_{01}' \cos 2\beta_{02}' [\langle\cos^2 (2\Delta\beta_1')\rangle_{\psi_1} - \langle\sin^2 (2\Delta\beta_2')\rangle_{\psi_2}]\} G(\psi_1, \psi_{12}) \quad (27)$$

The evaluation of the integrals I_1, I_2, and I_3 then depends upon the way in which quantities such as β_{01}', $\langle\sin^2 (2\Delta\beta_1')\rangle$ and $G(\psi_1, \psi_2)$ depend upon angular position within the spherulite. Let us consider first a simple case where $\beta_{01}' = \beta_0$ and is independent of position within the spherulite. Then for the simple case where $\beta_0 = 0$, the integrals become

$$I_1 = \int_{\psi_2=0}^{2\pi}\int_{\psi_1=0}^{2\pi} B(\alpha_1)B(\alpha_2)\,\langle\cos^2(2\Delta\beta_1')\rangle_{\psi_1} \times G(\psi_1, \psi_{12})f(\psi_1)f(\psi_2)d\psi_1 d\psi_2 \qquad (28)$$

$$I_2 = \int_{\psi_2=0}^{2\pi}\int_{\psi_1=0}^{2\pi} C(\alpha_1)C(\alpha_2)\,\langle\sin^2(2\Delta\beta_1')\rangle_{\psi_1} \times f(\psi_1)f(\psi_2)G(\psi_1, \psi_{12})d\psi_1 d\psi_2 \qquad (29)$$

and $I_3 = 0$. The integration next depends upon the way in which terms like $\langle\sin^2(2\Delta\beta_1')\rangle_{\psi_1}$ depend upon ψ_1 and upon the functional form of $G(\psi_1, \psi_{12})$. A simple assumption to study first is that where the angular dependence of disorder is not affected by the deformation so that these terms are independent of ψ_1, in which case

$$I_1 = \langle\cos^2(2\Delta\beta_1')\rangle \int_{\psi_2=0}^{2\pi}\int_{\psi_1=0}^{2\pi} B(\alpha_1)B(\alpha_2)f(\psi_1)f(\psi_2)G(\psi_{12})d\psi_1 d\psi_2 \qquad (30)$$

$$I_2 = \langle\sin^2(2\Delta\beta_1')\rangle \int_{\psi_2=0}^{2\pi}\int_{\psi_1=0}^{2\pi} C(\alpha_1)C(\alpha_2)f(\psi_1)f(\psi_2)G(\psi_{12})d\psi_1 d\psi_2 \qquad (31)$$

One may assume that $G(\psi_{12})$ may be represented exponentially as in the previous work so that

$$G(\psi_{12}) = \exp\{-|\psi_{12}|/c\} \qquad (32)$$

where c is an angular correlation distance. It is noted that $\psi_{12} = \alpha_{12}$ The quantity $|\psi_{12}|$ is defined such that if $|\psi_{12}| > \pi$, its supplement $(2\pi - |\psi_{12}|)$ is used.

If disorder is dependent upon deformation, quantities like $\langle\sin^2(2\Delta\beta_1')\rangle_{\psi_1}$ depend upon position within the spherulite. A simple assumption is an ellipsoidal variation with the angle α

$$\langle\cos^2(2\Delta\beta_1')\rangle_{\psi_1} = g_0(1 + \sigma\sin^2\alpha_1) \qquad (33)$$

so that $\langle\cos^2(2\Delta\beta_1')\rangle$ increases from g_0 in the polar part of the spherulite to $g_0(1 + \sigma)$ in the equatorial part. When $\sigma = 0$, this reduces to the previous case.

Similarly, the correlation distance varies with α so that as a simple assumption

$$G(\gamma_1, \gamma_{12}) = \exp\{-|\gamma_{12}|/c(1 + \rho\sin^2\alpha_1)\} \qquad (34)$$

These equations may then be used in the evaluation of the integrals in eqs. (28) and (29), where σ and ρ are parameters describing the effect of orientation on the random contribution to the scattering. These parameters each vary with elongation.

Results

Calculations of H_V intensities for various values of the parameters have been carried out by using the CDC 3600 computer of the University of

Massachusetts Research Computing Center. The calculations were made for uniaxial deformation at constant volume so that $\lambda_3 = \lambda_s$ and $\lambda_2 = \lambda_s^{-1}$. Values of the undeformed spherulite radius $R_0 = 3\ \mu$ and wavelength of light in the medium $\lambda' = 0.364\ \mu$ were chosen (corresponding to the mercury green line in air $\lambda_0 = 0.546\ \mu$ with refractive index $n = 1.5$). The angular disorder correlation distance c was assumed to be independent of angle and elongation and was taken to be 0.7 π radians. The proportionality constant $K_1{}^2K_2/\cos^2\rho_2$ was arbitrarily set at 10^5. The values of parameters corresponding to the various figures are summarized in Table I. The intensity contours are indicated by numbers which are related to relative intensities as shown in Table II.

TABLE I
Summary of Parameters for Scattering Calculations

λ_3	g_0	σ	Figure	Comments
1.0	1.0	0.0	3 *a*	Contour diagrams
1.0	0.9	0.0	3 *b*	Contour diagrams
1.0	0.7	0.0	3 *c*	Contour diagrams
1.0	0.9	0.0	4 *a*	θ Dependence
1.5	0.8	0.0	5 *a*	Contour Diagrams
1.5	1.0	0.0	5 *b*	Contour Diagrams
1.5	1.0	−0.2	5 *c*	Contour Diagrams
1.5	1.0	−0.5	5 *d*	Contour Diagrams
1.5	0.5	1.0	5 *e*	Contour Diagrams
1.5	1.0	0.0 to −0.5	7	θ Dependence at $\mu = 0°$
1.5	1.0	0.0 to −0.5	8	θ Dependence at $\mu = 90°$

TABLE II
Designation of Constant-Intensity Contours

Contour no.	Relative intensity
1	1.4×10^5
2	1.0×10^5
2′	8.0×10^4
3	7.0×10^4
3′	6.0×10^4
4	5.0×10^4
5	4.0×10^4
6	3.0×10^4
7	2.0×10^4
8	1.0×10^4

It is seen from a comparison of the undeformed perfect two-dimensional spherulite pattern of Figure 2 with the patterns of Figure 3 for the undeformed disordered spherulite that, as has previously been pointed out,[5] the effect of disorder is to give a "tennis-racket" type pattern with a build-up of intensity toward the center of the pattern as disorder increases of a type described by Kawai, et al.[6] This is further seen in the plot of Figure 4 for the variation of intensity with θ. The absolute intensity of scattering

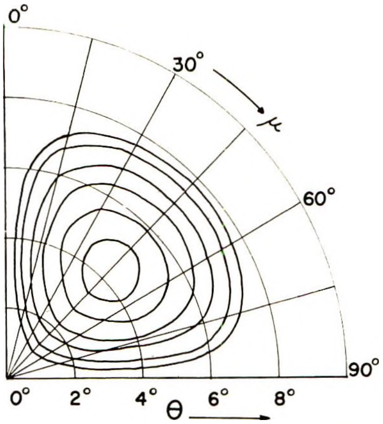

Fig. 2. H_V scattering pattern corresponding to an undeformed perfect two-dimensional spherulite.

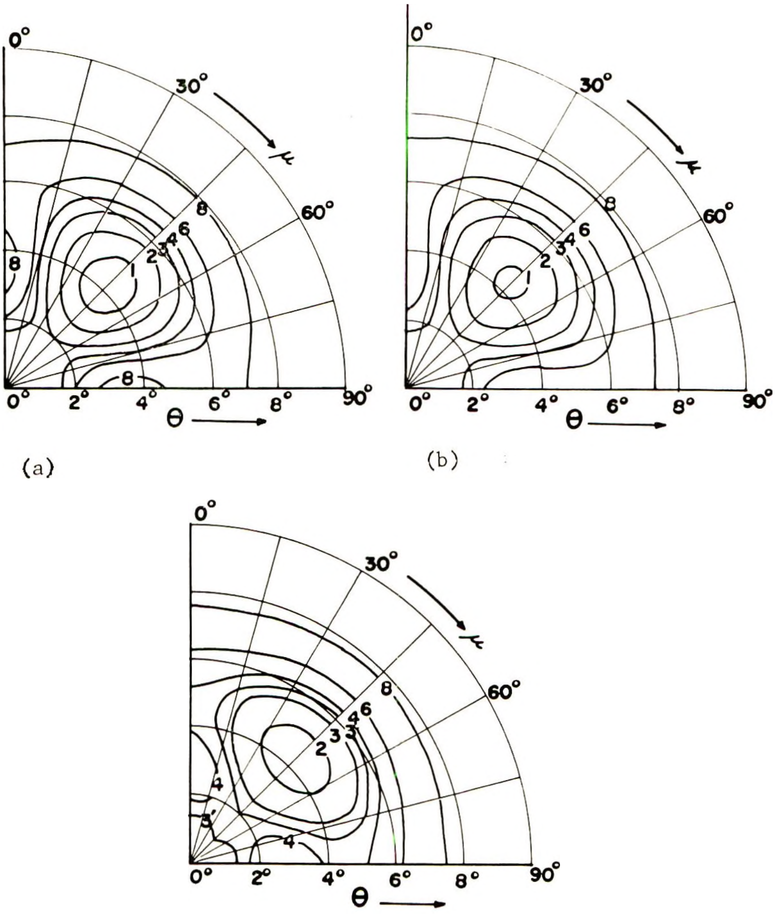

Fig. 3. Intensity contour diagram for an undeformed spherulite ($\lambda_s = 1.0$) for various values of the mean-square orientation fluctuation parameter g_0: (*a*) $g_0 = 1.0$; (*b*) $g_0 = 0.9$; (*c*) $g_0 = 0.7$.

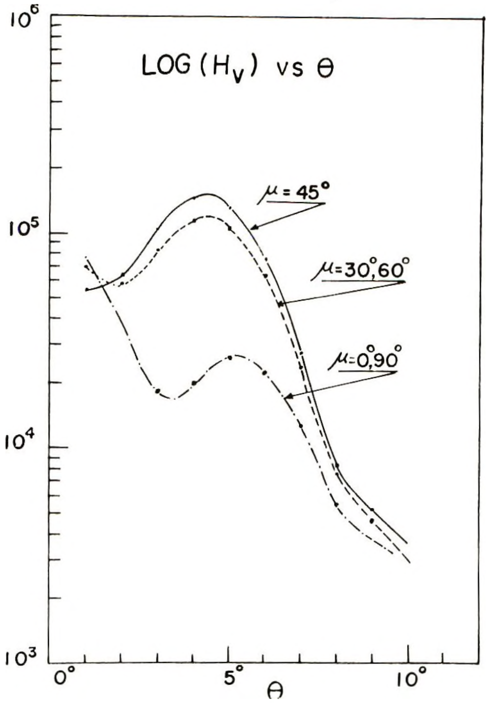

Fig. 4. Variation of scattering intensity with θ for an undeformed spherulite with g_0 = 0.9 for azimuthal angles of 0° (90°), 45°, and 30° (60°).

tends to decrease with increasing disorder. For the perfect spherulite, the scattered intensity is zero at $\theta = 0$ and at all values of θ along $\mu = 0$ and 90°. For the disordered spherulite, there is a build-up of intensity at these values of μ.

The next set of figures are for the case of a spherulite deformed by an elongation ratio $\lambda_s = 1.5$. In Figures 5*a* and 5*b*, $\sigma = 0$ designates an angular variation of $\langle\cos^2(2\beta_1)\rangle_{\psi_1}$ which is independent of direction in the film. The disorder parameter in Figure 5*a* is 0.8 while it is 1.0 in Figure 5*b*.

It is seen that the patterns undergo a characteristic change in shape with deformation as has been previously pointed out,[1] with the intensity maxima moving toward higher values of μ and θ. For the undeformed spherulite, the maximum occurs at $\mu = 45°$ and $\theta = 4.4°$ while at an elongation ratio of 1.5, it occurs at $\mu = 60°$ and $\theta = 4.8$ for $g_0 = 1.0$. It is seen that with increasing disorder, as g_0 goes from 1.0 to 0.8, the pattern assumes a more "deformed tennis racket" appearance with an increase in intensity at small values of θ and at $\mu = 0°$ and 90°.

The effect of an angular dependence of $\langle\cos^2 2\Delta\beta_1'\rangle$ is seen in Figures 5*c* and 5*d*, where σ is allowed to assume values of -0.2 and -0.5 while g_0 is kept constant at 1.0. The variation of $\langle\cos^2 2\Delta\beta_1'\rangle$ corresponding to these values of σ is shown in Figure 6. These negative values of σ correspond to spherulites in which the disorder is greater in the lateral region than the polar region. Figure 5*e* corresponds to $g_0 = 0.5$ and $\sigma = 1.0$ which, as shown in Figure 6, is where the disorder is greatest in the polar region of the spherulite.

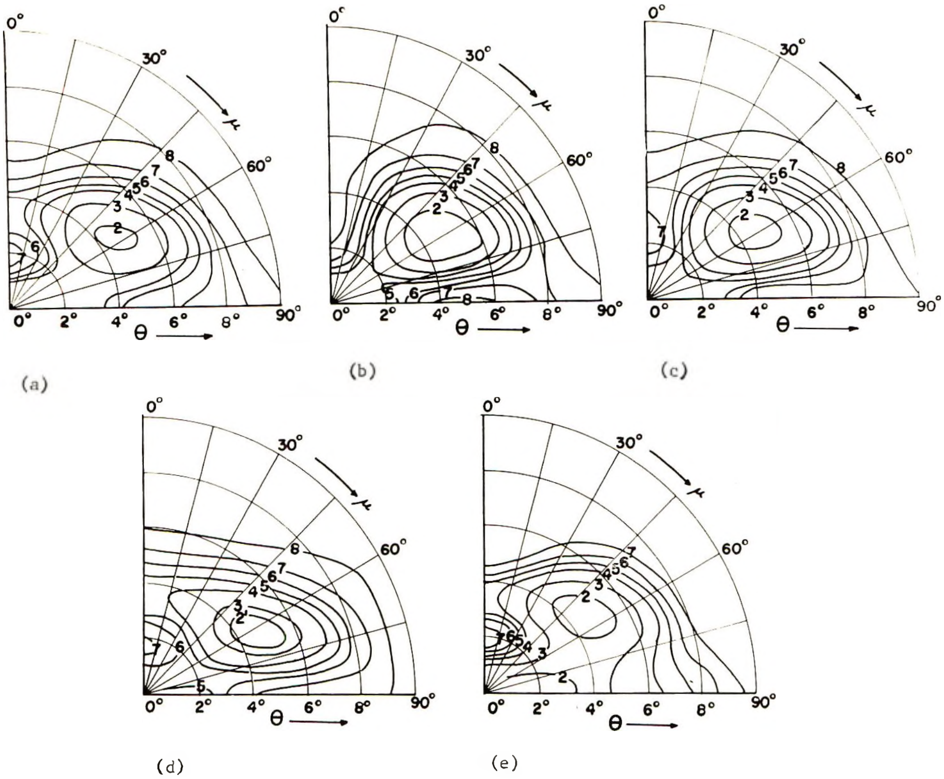

(a) (b) (c)

(d) (e)

Fig. 5. Scattering intensity contour diagrams of a deformed spherulite with $\lambda_s = 1.5$ and (*a*) $g_0 = 0.8$ and $\sigma = 0$ no angular dependence of fluctuation amplitude and for $g_0 = 1.0$ with angular dependence of fluctuation amplitude characterized by values of σ of (*b*) 0, (*c*) -0.2, (*d*) -0.5, and (*e*) for $g_0 = 0.5$ and $\sigma = 1.0$.

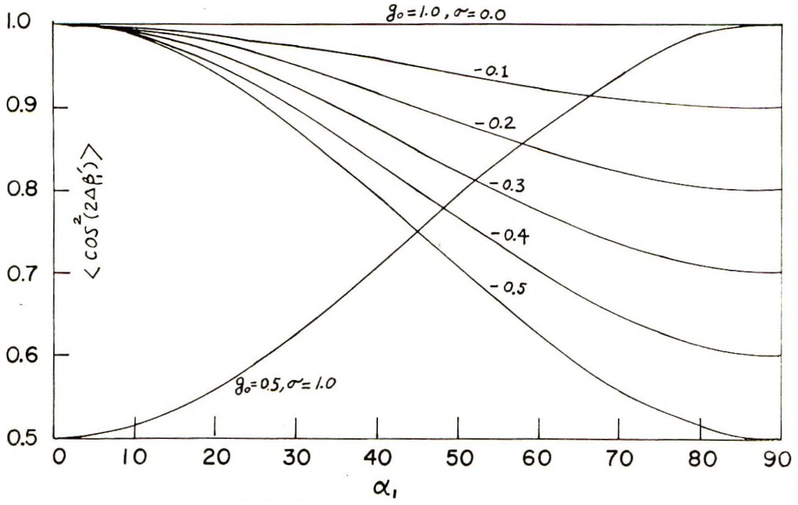

Fig. 6. Variation of $\langle \cos^2 2\Delta\beta_1' \rangle$ with α corresponding to $g_0 = 1.0$ and $\sigma = 0, -0.1, -0.2, -0.3, -0.4, -0.5$ and for $g_0 = 0.5$ with $\sigma = 1.0$.

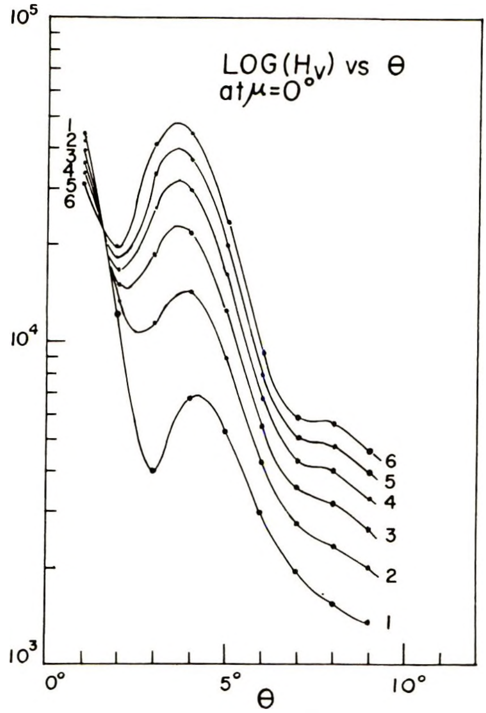

Fig. 7. Variation of scattering intensity with θ for a deformed spherulite ($\lambda_s = 1.5$) at azimuthal angle $\mu = 0$ for $g_0 = 1.0$ and (*1*) $\sigma = 0$, (*2*) $\sigma = -0.1$; (3) $\sigma = -0.2$, (*4*) at $\sigma = -0.3$; (*5*) $\sigma = -0.4$; (*6*) $\sigma = -0.5$.

It is noted that the μ and θ at which the maximum scattering occurs is rather insensitive to the disorder parameters. As the amplitude of the orientation fluctuations becomes larger in the equatorial regions of the spherulites, there is a build-up of intensity in the polar region of the scattering pattern (at $\mu = 0°$). This may be seen in Figure 7, representing a plot of the variation of H_V scattered intensity with θ at $\mu = 0°$ for a deformed spherulite with $\lambda_s = 1.5$, $g_0 = 1.0$ and σ changing from 0 to -0.5, which may be compared with Figure 8, showing the corresponding variation in the equatorial region of the scattering pattern at $\mu = 90°$. The changes in the equatorial region of the pattern are more complex. The effect of such angular dependence of disorder is greater at $\mu = 0°$ and 90° than at the μ corresponding to the intensity maximum.

Similarly, a comparison of Figures 5*b* and 5*e* reveals that an increase in the amplitude of the orientation fluctuation in the polar region of the spherulite leads to a pronounced increase in intensity at the equator of the scattering pattern (at $\mu = 90°$).

Experimental scattering patterns from deformed polyethylene[6] more closely resemble theoretical patterns like Figure 5*c*, suggesting that larger fluctuations occur in the equatorial region of the deformed spherulite.

In these calculations, the angular correlation distance was kept constant.

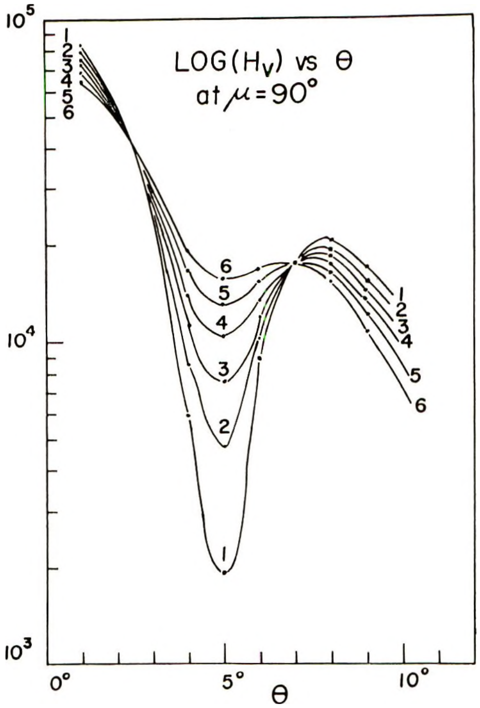

Fig. 8. Variation of scattering intensity with θ for a deformed spherulite ($\lambda_s = 1.5$) at azimuthal angle $\mu = 90°$ for $g_0 = 1.0$ and the same values of σ as for Fig. 7.

An angular variation of this is expected to have effects similar to those produced by an angular variation of the amplitude of the fluctuation. Also, it has been assumed that the average optic-axis tilt angle, β_0', is independent of the angle α in the deformed state. A more thorough analysis would allow β_0' to vary with α, perhaps in the manner of the empirical equation of van Aartsen et al.[2] These additional variations are not included in this paper because of the desire to avoid introducing an unmanageable number of empirical parameters.

Conclusions

The introduction of nonrandomness into the theory of the scattering from deformed spherulites produces changes in the predicted scattering patterns analogous to those predicted for undeformed spherulites. The disorder results in an increase in scattered intensity as small values of the scattering angle θ as well as nonzero intensities at $\mu = 0°$ and $90°$. The relative effect on the intensity at $\mu = 0°$ and $90°$ depends upon the angular dependence of the amplitude and correlation distance associated with the fluctuations from orientational order within the spherulite. The experimental observations of scattering patterns from stretched polyethylene indicate that a greater degree of disorder occurs in the equatorial part of the spherulite.

This work was supported in part by a contract with the Office of Naval Research and in part by a grant from the Petroleum Research Fund of the American Chemical Society.

References

1. S. Clough, J. J. van Aartsen, and R. S. Stein, *J. Appl. Phys.*, **36**, 3072 (1965).
2. J. J. van Aartsen and R. S. Stein, *J. Polym. Sci. A-2*, **9**, 295 (1971).
3. R. J. Samuels, in *U.S.-Japan Seminar in Polymer Physics* (*J. Polym. Sci. C*, **15**), R. S. Stein and S. Onogi, Eds., Interscience, New York, 1966, p. 37.
4. A. E. M. Keijzers, J. J. van Aartsen, and W. Prins, *J. Amer. Chem. Soc.*, **90**, 3167 (1968).
5. R. S. Stein and W. Chu, *J. Polym. Sci. A-2*, **8**, 1137 (1970).
6. M. Motegi, T. Oda, M. Moritani, and H. Kawai, *Polym. J.* (Japan) **1**, 209 (1970).

Received July 17, 1970
Revised September 15, 1970

JOURNAL OF POLYMER SCIENCE: PART A-2 VOL. 9, 531-541 (1971)

Morphology of Polyethylene Crystallized by Solution Stirring

A. M. RIJKE,* J. T. HUNTER, and R. D. FLANAGAN, *Department of Chemistry, University of the Witwatersrand, Johannesburg, Republic of South Africa*

Synopsis

Dilatometric and calorimetric studies have been made of the fusion process of linear polyethylene crystallized by stirring xylene solutions at elevated temperatures. It is shown that the melting point of the crystals increases rapidly from 139.5°C to 145°C in the crystallization temperature range of 100–103°C and levels off to 146 ± 0.5°C, provided that very slow heating rates are employed. Stirrer-crystallized samples treated with fuming nitric acid show higher crystalline contents. Comparison of their enthalpies of fusion and melting points indicate that higher molecular order along the fiber axis is associated with higher crystallization temperatures. This is in general agreement with corresponding results of other modes of crystallization. The attack of fuming nitric acid on stirrer crystals is characterized by weight-loss curves similar to those of dilute-solution crystals and bulk polyethylene. The linear molecular weight dependence on time of exposure to nitric acid suggests that the oxidation proceeds mainly from the chain ends at a constant rate for samples stirred in the lower crystallization range, but an increased rate is observed for a sample stirred from xylene at 105°C. It is suggested that the lamellar overgrowths, most evident at low crystallization temperatures, are epitaxially attached to the fiber axis, whereas the smaller crossbandings observed at higher crystallization temperatures are possibly made up of elements of chains that are only partly incorporated in the highly ordered fibrous core.

Introduction

The formation of fibrillar polyethylene crystals, as originally reported by Pennings and Kiel,[1] has been the subject of study by several workers during recent years. The fibrils are formed by stirring solutions at temperatures[2–7] above the precipitation temperature, by ultrasonic cavitation,[8] through heterogeneous Ziegler-Natta catalysis,[9,10] in some extruded melts,[2] and in crystallized melts of polyethylene–paraffin mixtures.[12] It is now well established that the chain axis of the fibrils is preferentially oriented parallel to the fiber axis. Further evidence of the fibrillar character is provided by electron microscopic studies, which show the fine details of the structures and their dependence upon the crystallization temperature.[1,3,13]

When crystallized from xylene solutions in the 94–99°C range, the fibers

---

* Present address: Department of Materials Science, University of Virginia, Charlottesville, Virginia 22901.

show under the electron microscope central ribbonlike filaments onto which lamellalike platelets are attached in a dense, more or less regular array. By treatment with fuming nitric acid the fibrillar nature is easily destroyed, and debris consisting of lamellar units only is obtained after a sufficiently long time of exposure.[3]

The properties of these fibers, when crystallized from xylene at about 100°C or higher are significantly different. Here, the lamellar units are much less pronounced. The relatively smooth fibers appear to be constructed of cross-banded structures, approximately 200–400 Å wide, along a fine central core.[4] This core can be observed directly when the material is selectively dissolved after treatment with fuming nitric acid. The oxidation appears to leave the structures seemingly unaltered, but close examination shows that much of the amorphous material between the cross-banding has been removed and the finer elements stand out more clearly. The core is very resistant to the nitric acid, and little breakage occurs as a result of the oxidative attack until just before the oxidation has been completed.

The electron microscopic observations and results from fuming nitric acid treatment and selective dissolution provide the evidence on which the morphological concept of solution-stirred fibrils is based, viz., at crystallization temperatures under 100°C, lamellar platelets of dimensions comparable to dilute-solution single crystals are attached at regular intervals to a central core consisting predominantly of folded chains. At crystallization temperature above 100°C the core consists of extended chains and much smaller overgrowths of folded chains with interlamellar tie molecules. Considerable support for this concept is provided by the gel-permeation chromatographic studies of Willmouth et al.[4] These authors exposed fibrils, stirred at 100°C, to fuming nitric acid for various treatment times. Their chromatograms show peaks at large elution volumes corresponding to single traverse lengths of the molecule, and two folds thereof, in agreement with the striation periods as measured from the electron micrographs. In addition, a persistent tail at low elution volumes, indicative of the presence of high molecular weight material, can be identified with the resistant, extended-chain core as suggested by the electron microscopic studies. Thus, the dual character of the fibrils has been well established, and all the major experimental features can be satisfactorily explained by this model. Closer examination, however, reveals some difference in detail which may be a consequence of variation in crystallization temperature. First, it is well known that considerable fractionation occurs over the whole crystallization temperature range. Pennings has reported[14] a strong dependence of intrinsic viscosity on crystallization temperature. Although a difference in molecular weight does not necessarily imply a difference in morphology, several experimental results on other crystalline polymer systems seem to indicate that molecular weight plays a significant role in the kinetically controlled nucleation.[15,16] Second, the melting behavior of carefully annealed fibrils shows a marked dependence on crystallization temperature.[13] The ultimate melting points of samples stirred at 95, 102, and 105°C increases from approximately 138°C to 146°C. This indicates that more perfect, and possibly larger, crystallites are formed as the crystallization temperature is increased. Third, the ease with which the oxidized overgrowths can be removed by selective dissolution appears to vary greatly with crystallization temperature.[14] Wikjord and St. John Manley,[3] working with fibrils stirred in xylene at 100°C, encountered no problems when trying to remove the overgrowths completely by using only very short exposures to the toluene vapor. Even when unoxidized fibrils were subjected to the vapor, most of the overgrowth could be washed away selectively, leaving filamentary ribbons with adhering material at random sites along their length. Willmouth et al.,[4] on the other hand, working with fibrils stirred at 102.8°C and 103.2°C, were unable to wash away the oxidized overgrowths with either refluxing toluene or xylene at 109°C. Some of their material clearly dissolved, but very resistant strings of beads remained behind which could be dissolved only as a whole. No separation at all could be made between the structural elements of the fibrils of the unoxidized material. It is unlikely that a difference in molecular weight distribution could account for the observed variation in susceptibility to selective dissolution, particularly when most of the amorphous material in the overgrowths has been oxidized. It is reasonable to assume, therefore, that a difference in morphological detail, not observed in the electron microscope, causes the fibrils crystallized at higher temperatures to be more resistant to selective dissolution.

In order to investigate these details somewhat further, we have studied polyethylene fibrils stirred from xylene in a temperature range between 95°C and 105°C by calorimetry, dilatometry, and nitric acid treatment. Our object was to correlate the results of these studies to arrive at a molecular architecture of backbone and overgrowth capable of satisfactorily explaining the observed properties.

Experimental

The polyethylene fibrils were stirred from 3% xylene solutions of Marlex-50 at 95, 97, 99.5, 101.5, 102, 103.5, and 105°C following previously reported techniques.[13] In order to determine the melting behavior of each sample, conventional, mercury-filled dilatometers which held about 150 mg of sample were used. They were immersed in silicone oil baths maintained constant to ±0.1°C. The mercury level was read with a sensitive cathetometer accurate to 0.01 mm. The samples were brought rapidly to 134°C and the temperature was subsequently raised at 0.5°C intervals, but not until the level of the mercury had become constant for each temperature setting. Typically, in the range above 139.5°C, the scale reading would increase during the first few days and then level off to a constant value over the next three to five days or so. Consequently, extremely slow heating rates were applied by this method,[13] more than adequate to suppress superheating effects and sufficient for annealing involving volume changes to occur.

In another experiment 100–150 mg of each sample stirred at 95°C (M-95), 102°C (M-102), and 105°C (M-105) was mechanically dispersed and treated with 93% fuming nitric acid (specific gravity 1.50) at 80°C for various lengths of time. The ratio of polyethylene to fuming nitric acid was 0.5 g/100 ml. The mixtures were then poured out into excess distilled water, stirred, filtered, washed with water and then with absolute alcohol, and finally dried *in vacuo* at 50°C. In a separate experiment, designed to remove the lamellar overgrowth completely, samples M-95 and M-105 were treated with red fuming nitric acid, (Baker's reagent) at 80°C for 5 hr. A 2–4 mg portion of each of these oxidized samples was heated in a Perkin-Elmer DSC-1B at a heating rate of 10°C/min. The enthalpy of fusion ΔH^* was calculated by comparing the area under the fusion curve with that obtained with a known weight of indium heated under the same conditions. After the initial melting was completed the samples were subsequently recrystallized by rapid cooling to room temperature and were melted in the DSC again following the same heating schedule.

Results and Discussion

For the samples crystallized from xylene solutions under 100°C, the fusion process, as studied in detail by the previously described dilatometric procedures, was very similar to what is found with carefully crystallized bulk polyethylene.[17] The fusion curves joined the liquidus lines in the vicinity of 138.5°C. This, of course, does not mean that this temperature can be identified with the melting temperature of the highest melting component of the system, but rather indicates that the fusion process has been sufficiently slow to allow the original sample to be transformed into bulk polyethylene through the process of melting and recrystallization. The actual melting temperature characteristic of these fibrils is expected to be very dependent on heating rate.

Higher melting points were found for samples stirred from solutions above 100°C. For samples crystallized at 103°C and higher, two melting points were observed, the bulk of the material melting near 139°C, followed by renewed melting with an ultimate melting point several degrees higher.

The results are presented in Figure 1. It is seen that a sharp increase in melting temperature T_m occurs in a narrow crystallization temperature range around 100°C, which coincides with the temperature range in which major morphological changes were observed in the electron microscope.[3,4] However, there is no *a priori* reason why these features are correlated, because the increase of melting temperature with crystallization temperature T_c is likely to hold at T_c below 99°C as well and would be observed if recrystallization could be prevented.

The occurrence of two melting points for samples crystallized in the higher temperature ranges indicates that the dual character of these fibrils is even more pronounced. It is feasible to assume that the high melting

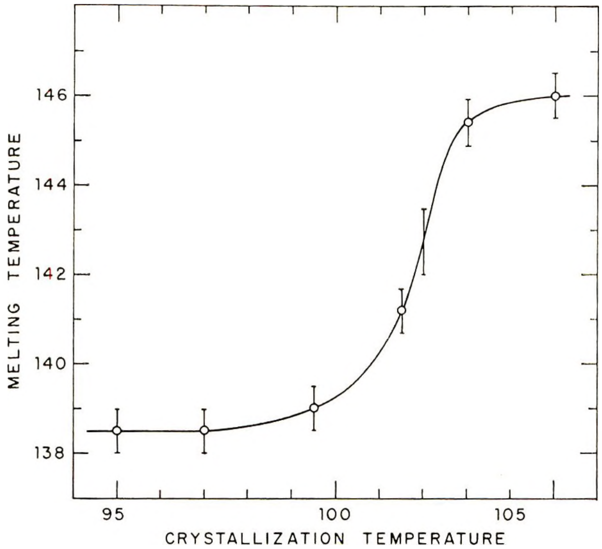

Fig. 1. Melting temperature as a function of crystallization temperature for linear polyethylene crystallized from xylene solutions at very slow heating rates. The melting temperature of the sample stirred at 102°C was earlier found to lie between 142 and 143.5°C.[13]

fraction can be identified with at least part of the annealed, nitric-acid-resistant core, whereas the low-melting bulk would be made up of the cross-banded striations. The perfection and possibly the sizes of the crystallites are likely to increase with crystallization temperature. It is interesting to note therefore that the curve in Figure 1 levels off to T_m = 146.0 ± 0.5°C. This melting temperature is very close to the theoretical value predicted by Flory and Vrij[18] and the results of Gopalan and Mandelkern[19] on the extrapolated melting temperature of high molecular weight polyethylene as a function of the crystallization temperature. It also stands in good accord with the value determined from the analysis of the critical annealing temperatures of dilute-solution single-crystals as a function of initial crystallite thickness.[20] However, it is realized that a high melting temperature is not necessarily an indication of the presence of extended-chain crystals. A reduced interfacial free energy in a state of high axial orientation relative to that of crystallites produced by more conventional methods of crystallization could equally well account for the increased melting temperature. An analysis of these data in terms of crystallite size and interfacial free energy is in want of experimental verification.

In an attempt to distinguish between the crystallite sizes present in samples of different crystallization temperature samples M-105 and M-95 were subjected to red fuming nitric acid. The oxidation was allowed to progress considerably into the crystalline regions before the samples were tested in the calorimeter. Previous efforts to determine the melting points in mercury-filled dilatometers were unsuccessful as a result of the continuous evolution of gas during the whole of the fusion process.

The fusion curves from the DSC show very similar, single peaks without shoulders[21] for the samples both before and after cooling from the melt. Only the peak of oxidized sample M-105 was somewhat taller than its fusion curve after recrystallization. The data are shown in Table I. Values for the enthalpy of fusion ΔH^* of the unoxidized samples lie well within the range observed previously[13] for these types of structures, but significantly higher ΔH^* values were recorded for the oxidized samples in which the amorphous regions have been removed by selective oxidation.[11] On the basis of these enthalpies of fusion we can calculate a degree of crystallinity, $\Delta H^*/H_u$, of 76 and 82% for samples M-95 and M-105, respectively, but these percentages have at best relative value due to the high oxygen content of the samples. The presence of oxygen at the interfaces, mainly in the form of nitro groups and carboxylic acids,[22] will tend to yield lower ΔH^* values on a per weight basis, but the strong intermolecular interaction between these groups will increase the enthalpy of fusion and melting temperature. A recent study on nitric-acid-treated single crystals has shown that ΔH^* may drop by about 10 cal/g when the oxygen-containing groups have been removed chemically.[22] This effect should be less for paraffins with longer chains, as in our case, but nevertheless indicates that values for enthalpies of fusion and melting temperatures of unmodified nitric acid treated crystals cannot be related directly to degree of crystallinity and molecular chain length. However, a comparison of the relative magnitudes of ΔH^* shows a significantly higher ΔH^* for M-105 than for M-95. This supports our previously expressed opinion that the molecular order along the fiber axis in solution-stirred polyethylene crystals is associated with higher crystallization temperatures. This is also borne out by the observation that the last traces of crystallinity on the fusion curves disappear at a lower temperature for sample M-95 than for M-105. The depression of the observed melting temperature ΔT from its equilibrium value T_m°, reads

TABLE I
Enthalpies of Fusion and Melting Temperatures of Nitric Acid-Treated Polyethylene Crystallized by Stirring[a]

	Sample M-95	Sample M-105
Recovered after oxidation, %	54	42
ΔH^* of unoxidized material, cal/g	45.3	48.5
ΔH^* of oxidized material, cal/g	53.7	56.8
ΔH^* of oxidized material after cooling and recrystallization from melt, cal/g	50.1	49.3
T_m of oxidized material, °C	127	136
T_m of oxidized material after cooling and recrystallization from melt, °C	125	131.5

[a] Data not corrected for instrument lag and oxygen content.

$$\Delta T = 2\sigma_{ec}T_m{}^\circ/\zeta\Delta H_u \tag{1}$$

where ζ is the crystallite size, in repeating units, along the chain direction, and σ_{ec} is the interfacial free energy per sequence emerging from the 001 plane. The observed difference in ΔT values for the samples M-105 and M-95 can therefore be attributed to a difference in either ζ or σ_{ec} or both. The interfacial free energy associated with the 001 planes of the unoxidized samples may depend on morphological detail and therefore on the crystallization temperature. It is, however, feasible to assume that the spatial arrangement of the chains emerging from the 001 planes, and therefore the value of σ_{ec}, will vary only slightly, if at all, once all amorphous material has been removed and the oxidation has progressed well into the crystalline phase in the directions normal to the 001 planes. This would mean that the observed difference in ΔT of the two samples is a consequence of difference in crystallite sizes only. The validity of this proposal is substantiated by the observation that ΔH^* of sample M-95, measured after cooling and recrystallization from the melt, has decreased only slightly, whereas a much larger drop in ΔH^* is observed for recrystallized sample M-105. This is in keeping with expectation for it is well known that polyethylene of low molecular weight crystallizes readily in a molecular crystal habit, which, after repeated melting and recrystallization, shows a constant melting point peculiar to the crystal size. Viscosity studies on decalin solutions of oxidized sample M-95 yield $[\eta] = 0.129$ which corresponds to $\bar{M}_w = 2050$. According to the molecular weight–melting temperature relations reported by Fatou and Mandelkern[17] for chains of uniform lengths, a molecular crystal of this molecular weight melts at 126°C, in accord with our calorimetric melting temperature, but the agreement may well be fortuitous, as no correction for instrument lag or for oxygen content of the sample has been made. On the other hand, the higher molecular weight chains in the oxidized sample M-105 will, after cooling from the melt, not recrystallize into a molecular crystal of the same dimensions, but a new morphology will be established with smaller crystallite sizes and chains emerging from the 001 planes in an amorphous fashion. These smaller crystallites will show lower ΔH^* values and melt at lower temperatures in agreement with our experimental findings.

Although these results supply substantial evidence for the existence of increasingly larger crystallite sizes with increasing crystallization temperatures, these data do not allow an estimate of the crystallite sizes as they actually occur in our unoxidized samples. The low melting point of oxidized sample M-105 indicates quite clearly that oxidation into the crystalline regions has already progressed considerably in this particular experimental procedure. Studies on oxidized samples recovered after various times of exposure to nitric acid will not only provide evidence for the crystal sizes in the unoxidized material, but could also give access to an estimate of the excess free energy involved in the 001 interfaces of the various samples. Our results for samples M-95, M-102 and M-105 are

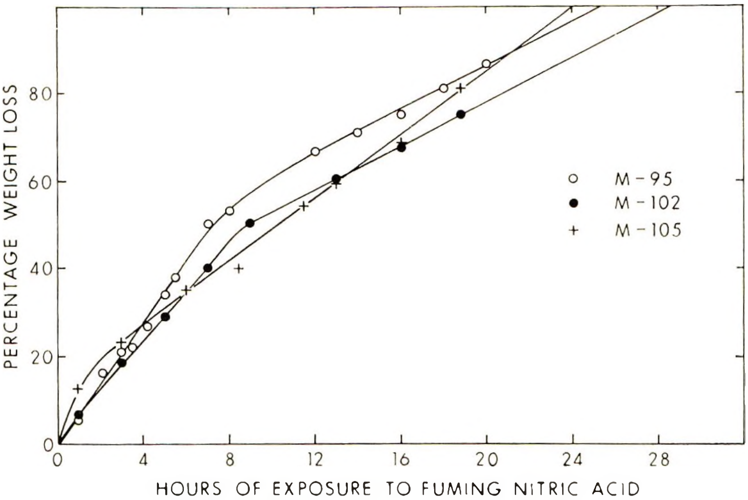

Fig. 2. Plots of percentage weight loss vs. time of exposure to fuming nitric acid for samples M-95, M-102, and M-105.

shown in Figure 2, where the percentage weight loss is plotted against time of exposure to fuming nitric acid. For samples M-95 and M-102 there is a linear decrease in weight with time for about 8 hr, the slope being slightly steeper for M-95 than for M-102. After 8 hr, the slopes become smaller and virtually parallel. The digestion has been completed after 25 and $28^1/_2$ hr, respectively. The results for sample M-105 are rather similar. An initial steep rise of the curve is followed after 2 hr by a linear decrease of weight with time. The slope of the second part of the curve is smaller than that of the first part, but significantly steeper than the corresponding parts for samples M-95 and M-102. These changes of slope in the weight loss curves indicate a change in the crystalline properties as the oxidation proceeds from the surface to the interior. It is feasible to assume that all of the amorphous material has been digested at the inflection points and that from there on the rate of weight loss is representative of the crystal dimensions. Similar conclusions were drawn from observations on oxidized single crystals grown from dilute solutions.[23]

The initial rate of weight loss is larger for sample M-95 than for M-102, the ratio being the same as that of the weight loss at the inflections, which occur after about the same period of time. This can be interpreted as further experimental evidence in favor of the assumption that the amorphous regions are first accessible to the acid as a result of their lower density. After the amorphous material has been removed the rate of weight loss is reduced to approximately the same value. From the positions of the inflection points a crystalline content of roughly 43 and 51% is calculated for samples M-95 and M-102, respectively. These values are somewhat lower than those calculated on the basis of their enthalpy of fusion as determined from calorimetric measurements which yielded 66% for both samples.[13] Plots of the molecular weights of the samples against time of

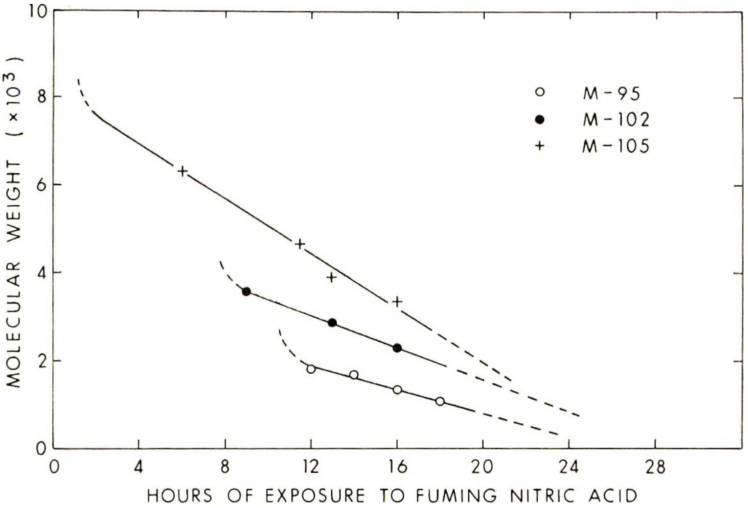

Fig. 3. Viscosity molecular weights vs. time of exposure to fuming nitric acid for oxidized samples M-95, M-102, and M-105.

exposure to nitric acid are shown in Figure 3 for the regions where all of the amorphous material has been removed. The number-average molecular weights were calculated by Tung's equation,

$$[\eta]_{\text{decalin, } 135^\circ \text{C}} = 5.86 \times 10^{-4} \bar{M}_n^{0.725} \tag{2}$$

derived for fractions obtained by fractional precipitation.[24] Straight lines are obtained for all samples which extrapolate to about the same times of complete digestion as shown in Figure 2. The linearity in the experimentally observed molecular weight range suggests that the chains in the lattice are predominantly attacked at the 001 surfaces and that the rate of oxidation remains constant throughout the lattice. If we assume this rate to be α units of length per time unit then we can write for the number-average chain length $\bar{l}$ in the crystallites:

$$\bar{l} = \frac{n_1(l_1^\circ - \alpha\tau) + \ldots}{n_1 + n_2 + \ldots} = \bar{l}^\circ - \alpha\tau \tag{3}$$

where τ is the time and n_1 is the number of chains with length $l_1 = l_1^\circ - \alpha\tau$ etc. Inasmuch as the molecular weights in Figure 3 are properly described by eq. (2), the linearity of the plots in Figure 3 indicates that α remains constant in this molecular weight range and is about the same for samples M-95 and M-102, but larger for sample M-105. Sample M-105 shows rapid weight loss during the first 2 hr of exposure to acid, indicating that all of its amorphous regions are more accessible to acid than those of M-102 and M-95. The oxidative degradation subsequently proceeds at a rate still larger than that of M-95 and M-102, which suggests a more effective diffusion of acid and oxidation products as a result of differences in morphology. A nonlinear relation between chain length and exposure time would be observed for all cases where the oxidative attack included effective chain cutting, even if this occurred only at the crystallite surfaces. The admittedly scarce experimental data, particularly in the region of high exposure times does not rule this out; but the fact that the lines in Figure 2 and 3 ultimately extrapolate to the same time for complete digestion, does not support this possibility. A break in the straight lines of Figure 3 would be observed if the degradation of a major, low molecular weight component were completed before all of the material had been digested.

The larger oxidation rate α for sample M-105 seems contradictory to the expectation that only 001 planes are accessible to oxidative attack and that the occurrence of extended-chain crystallites, and therewith increased resistance to nitric acid, becomes more likely as the crystallization temperature is increased. In actual practice, however, the degradation proceeds relatively fast (see also Table I), although the fibrous character and some morphological detail persists until the oxidation is almost completed. At the present stage, the observed difference in oxidation rate can at best only be explained on the basis of difference in dimensionality of the diffusion mechanism.

The rapid increase in melting temperature, at least partly due to larger crystallite sizes, and the larger difference in susceptibility to fuming nitric acid and selective dissolution, as the crystallization temperature in xylene is increased from 100°C to 105°C, form the basis of our conclusion that major morphological changes, not observed in the electron microscope, occur in this temperature range. For T_c in the vicinity of 100°C, it is possible that the crossbanding is made up of relatively low molecular weight material epitaxially grown onto the central core, which consists of high molecular weight material of increasing molecular order as the crystallization temperature is increased. This would explain the high melting point, the ease with which the overgrowth can be dissolved selectively, the same α as for M-95, and the larger $\bar{l}^{\circ}$. On the other hand, crystallization at temperatures higher than about 102°C would prevent epitaxial nucleation of solute molecules, but instead the crossbandings are here composed of elements of chains that are only partly incorporated in the highly ordered central core. This would explain, besides the aforementioned characteristics, the increased resistance to selective dissolution before and after oxidation.

An estimate of the crystalline dimensions in the direction of the chain axes can be made from the plots in Figure 3, if we assume that the inflections in the weight-loss curves signal the onset of the oxidative attack on the crystallites. A molecular weight of 2500 can be derived for sample M-95, which corresponds to a chain length of 220 Å, in agreement with the thickness of the platelets, as measured from the electron micrographs. Molecular weights of 3750 and 7500 are found for M-102 and M-105, respectively, and somewhat larger values if we calculate the molecular weights according to the probably more accurate relation between the intrinsic viscosity and molecular weight due to Chiang.[25] However, these molecular weights are averages of the various crystalline components and do not provide information on the dimensions of the largest crystals with the highest melting temperature. Consequently, an evaluation of the interfacial free energy of the high-melting crystallites must await experimental verification until the central core can be isolated in sufficient quantity.

References

1. A. J. Pennings and A. M. Kiel, *Kolloid-Z.*, **205**, 160 (1965).
2. A. Keller and M. J. Machin, *J. Macromol. Sci.*, **B1**, 41 (1967).
3. A. G. Wikjord and R. St. John Manley, *J. Macromol. Sci.*, **B2**, 501 (1968).
4. F. M. Willmouth, A. Keller, I. M. Ward, and T. Williams, *J. Polym. Sci. A-2*, **6**, 1627 (1968).
5. K. Monobe, Y. Yamashita, and Y. Fujiwara, *Mem. School Eng. Ikayama Univ.*, **3**, 77 (1968).
6. B. Wunderlich, C. M. Cormier, A. Keller, and M. J. Machin, *J. Macromol. Sci.*, **B1**, 93 (1967).
7. T. W. Huseby and H. E. Bair, *J. Polym. Sci. B*, **5**, 265 (1967).
8. D. A. Blackadder and H. M. Schleinitz, *Nature*, **200**, 778 (1963).
9. P. Blais and R. St. John Manley, *Science*, **153**, 539 (1966).
10. H. Chanzy, A. Day, and R. H. Marchessault, *Polymer*, **8**, 567 (1967).
11. M. J. Richardson, *Polymer*, **10**, 950 (1969).
12. H. D. Keith, F. J. Padden, Jr., and R. G. Vadimsky, *J. Polym. Sci. A-2*, **4**, 267 (1966).
13. A. M. Rijke and L. Mandelkern, *J. Polym. Sci. A-2*, **8**, 225 (1970).
14. A. J. Pennings, in *Macromolecular Chemistry, Prague* **1965**, (*J. Polym. Sci. C*, **16**), O. Wichterle and B. Sedlàček, Eds., Interscience, New York, 1967, p. 1799.
15. L. Mandelkern, J. G. Fatou, and K. Ohno, *J. Polym. Sci.*, **6**, 615 (1968).
16. E. G. Lovering, *J. Polym. Sci. A-2*, **8**, 1831 (1970).
17. J. G. Fatou and L. Mandelkern, *J. Phys. Chem.*, **69**, 417 (1965).
18. P. J. Flory and A. Vrij, *J. Amer. Chem. Soc.*, **85**, 3548 (1963).
19. M. R. Gopalan and L. Mandelkern, *J. Phys. Chem.*, **71**, 3833 (1967).
20. L. Mandelkern, R. K. Sharma, and J. F. Jackson, *Macromolecules*, **2**, 644 (1969).
21. G. Meinel and A. Peterlin, *J. Polym. Sci. B*, **5**, 197 (1967).
22. A. Keller and Y. Udagana, *J. Polym. Sci. A-2*, **8**, 19 (1970).
23. A. Peterlin and G. Meinel, *J. Polym. Sci. B*, **3**, 1059 (1965).
24. L. H. Tung, *J. Polym. Sci.*, **24**, 333 (1959).
25. R. Chiang, *J. Phys. Chem.*, **69**, 1645 (1965).

Received July 10, 1970

JOURNAL OF POLYMER SCIENCE: PART A-2 VOL. 9, 543-555 (1971)

Ultraviolet Photoelectric Effects in Polyethylene

L. A. VERMEULEN,* H. J. WINTLE, and D. A. NICODEMO,
Department of Physics, Queen's University, Kingston, Ontario, Canada

Synopsis

Photocurrents developed in polyethylene in the wavelength range 360–180 nm have been measured. The action spectra show features which can be related to the corresponding features in the absorption spectrum, and in addition there is electron injection from the metal electrode at a wavelength determined by the electrode material. The time dependence of the response indicates that a long-lived space charge is formed in the material.

INTRODUCTION

Photoconduction in polyethylene has been reported under ultraviolet illumination[1,2] and more recently for white light illumination.[3,4] The previous work in the ultraviolet region was carried out by using lines from the mercury arc spectrum and indicated that some form of barrier layer might exist close to the surface of the polyethylene film,[5] in addition to there being bulk photoconduction. In order to explore more fully the processes taking place, we have investigated the photoelectric behavior by using monochromatic light in the near-ultraviolet region (360–185 nm) and have correlated our results with the known absorption spectrum of this material. We have discovered that there is both a time dependence of the response and an electron injection at a wavelength governed by the electrode metal. These results are relevant to the photodegradation and the static electrification properties of the material.

EXPERIMENTAL

Materials

The material used was taken from one roll of 1-mil-thick 503M low-density polyethylene free of antioxidants and other additives. Other thicknesses and samples were available, but the results obtained were sufficiently complex for attention to be focussed on only one material in one thickness at this stage.

---

* On leave from Department of Physics, University of the Witwatersrand, Johannesburg, South Africa.

Apparatus

Polyethylene specimens were cut from the roll with a minimum of handling and were washed with Freon TF solvent to remove surface grease. Semitransparent silver electrodes, 1.0 in. in diameter, were evaporated on to the polyethylene films which were then mounted in a vacuum chamber similar to that used by earlier workers[1,6,7] and clamped between guard rings. Contact to the silver electrodes on the specimen was made with a soft iron disk and a button magnet which were gold-plated to eliminate the possibility of differential work functions giving rise to spurious offset voltages. Construction details of the contact system and vacuum chamber system have been given by Nicodemo.[8]

The vacuum chamber was provided with a Chance-Pilkington OW1 glass window so that the specimens could be illuminated with monochromatic ultraviolet light from a Bausch and Lomb high-intensity monochromator with a xenon arc source. The grating was driven by a synchronous motor and scanned the range from 360 to 180 nm. A spectral band width of 10 nm was normally employed. A liquid nitrogen trap was incorporated into the vacuum system to prevent contamination of the specimens by diffusion-pump-oil vapor. The pressure could be reduced to 3×10^{-5} torr. All readings were taken at room temperature.

Optical absorption spectra were measured with a Cary 1501 spectrophotometer and the photocurrents with Keithley 603, 610B, and 610C electrometers.

Photoelectric emission from the metallic parts of the specimen environment and the contact system gave rise to a spurious effect which could be recorded even in the absence of a specimen in the vacuum chamber. This "apparatus effect" was eliminated by spraying a Teflon skin onto the interior of the vacuum chamber and by covering all the signal carrying leads with Teflon spaghetti. In the course of the present investigation, frequent checks were made to ensure that the apparatus effect remained insignificant.

RESULTS

The search for photoelectric effects in polyethylene in fact covered the range 1.6 μm–180 nm. The silver-polyethylene sandwich specimens described above are sensitive to infrared and ultraviolet light. No effects could be detected in the visible region when the high-order ultraviolet spectra were filtered from the light in that range. The infrared effects found confirm in greater detail the findings of Tanaka and Inuishi[4] and Partridge and Avery[9] and are reported elsewhere.[10]

Action Spectra

Two successive action spectra obtained in air with the illuminated electrode positive are shown in Figure 1. These spectra are not corrected for the variation of lamp intensity with wavelength. The dark current is of

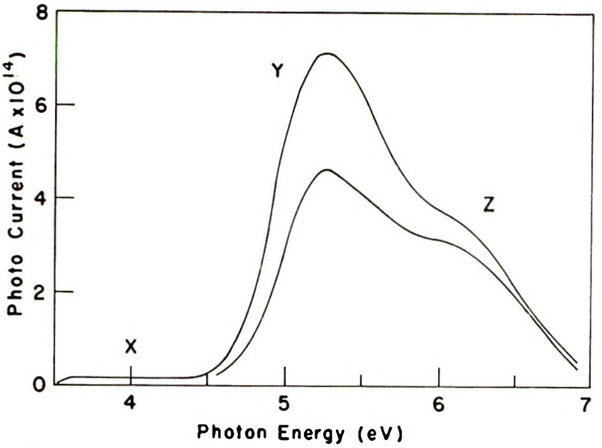

Fig. 1. Plot of two successive photocurrent action spectra for 1-mil polyethylene film. Illuminated face at +90 V.

the order of 1 fA. The illumination was run from 360 nm to 180 nm at a sweep rate of 0.92 nm/sec. The photocurrent has been plotted as function of the energy of the illumination. In a preliminary subdivision we recognize three features.

(1) X is a tail extending from less than 3.44 eV to 4.6 ± 0.2 eV. Its development is most prominent in the first spectrum obtained from any polyethylene specimen. The sensitivity in this region is specimen- and history-dependent. In many specimens the feature is too small to be observed in second and subsequent action spectra.

(2) Y is an intermediate feature with its threshold at 4.6 ± 0.2 eV.

(3) Z is a feature overlapping with Y at energies less than 5.6 eV.

The relative heights of the Y and Z features vary somewhat from specimen, but the curves shown are representative of several hundred similar action spectra obtained from 22 different specimens, with varying thicknesses of electrode material (optical absorbance of the silver in differential optical absorption measurements in the range 0.11 OD to 0.36 OD at 200 nm). Similar action spectra are obtained *in vacuo* (after due allowance for the absorbance of the window), at atmospheric pressure, and when the vacuum chamber is pressurised with helium, nitrogen, or oxygen.

The photocurrents in the action spectrum are in the direction of the applied field if the latter is parallel to the incident illumination, i.e., with the front illuminated face at a positive potential and the electrometer connected to the back face; or the electrometer connected to the front face and the back face at a negative potential. With the illuminated face at a negative potential, there is rectification, in that the action spectrum in this mode is nearly an order of magnitude smaller than in the other arrangements, although this is a difficult matter to establish quantitatively because of the history dependence discussed below. In this mode it can often happen that the current measured in the external circuit apparently flows against the applied field at applied field strengths of 3.4×10^4 V/cm. The data discussed below all refer to measurements taken with the front face positive. By using two electrometers and floating power supplies, we have established[11] that these results refer to conduction across the thickness of the specimen and do not have any significant contribution from surface currents.

Time Dependence

The action spectrum is transient, in that its magnitude decreases in successive sweeps. To describe this behavior, the spectra have been numerically integrated to obtain the charge $Q(n)$ passed during the nth sweep. The charge falls hyperbolically with the sweep number, and from experiments conducted with unequal doses ΔD of energy incident during each sweep, we have been able to establish that the proper quantity to consider is the reciprocal charge sensitivity $\Delta D/Q(n)$, which increases linearly with the total dose deposited, as shown in Figure 2.

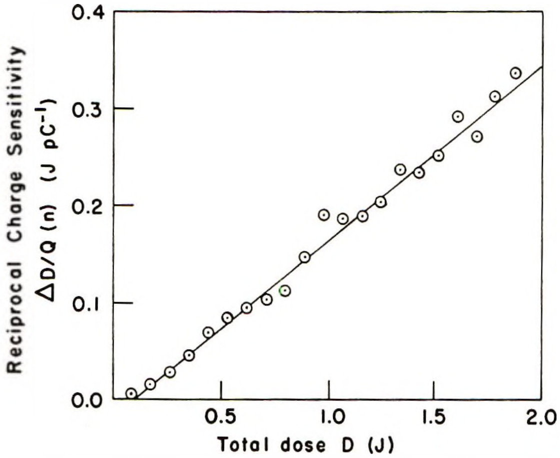

Fig. 2. Graph showing the linear dependence of the incremental dose per unit charge $[\Delta D/Q(n)]$ against the total ultraviolet dose incident upon the specimen.

After leaving the specimen resting in the dark with the voltage applied for periods of several minutes or more, the charge passed recovers towards its initial value, but then on succeeding sweeps it again falls in the manner described by Figure 2.

Ambient Effects

A considerable decrease in the magnitude of the action spectrum can be observed when going from vacuum (3×10^{-5} torr) to atmospheric ambient. This is shown in Figure 3. A number of sweeps establish the trend of the $Q(n)$ versus n curve *in vacuo*. Opening the system to air decreases $Q(n)$ by one order of magnitude, although the general trend is still preserved. The effect is reversible within the limitations imposed by the transient behavior noted above.

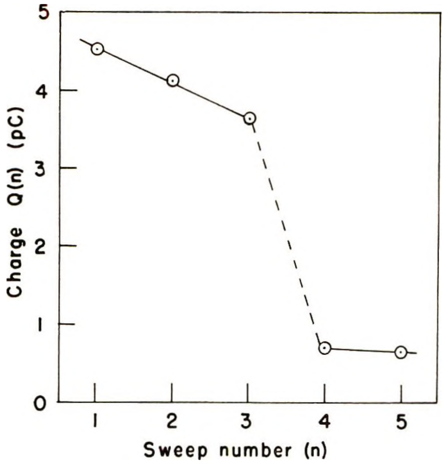

Fig. 3. Atmospheric quenching effect. The charge per sweep $Q(n)$ is plotted against sweep number. The experiment was begun at a pressure of 2×10^{-4} torr. Between sweeps 3 and 4, the vacuum chamber was opened to the atmosphere.

One set of readings taken on a specimen equilibrated for several days in helium showed a much slower decrease of the charge $Q(n)$ than is normal for air ambient. On replacing the helium with nitrogen, a fall in the charge yield similar to that recorded in Figure 3 took place, and a further reduction occurred when the nitrogen was replaced by oxygen. Subsequent trials with a helium atmosphere did not reproduce the slow decrease, presumably because the specimen had by now absorbed significant quantities of the more reactive gases.

Other Treatments

We have also investigated both gold and aluminum as electrode materials. The main changes are that with aluminum, the Y peak moves to lower energies. With gold it remains in the same place, but the Z peak disappears. In addition, the gold system shows a discharge current immediately when the light is cut off; and the charge $Q(n)$ passed during the ultraviolet light exposure is recovered within a few minutes. A similar rapid recovery is also observed with gold electrodes in the infrared region of the spectrum and is not understood as yet.

We have subjected some specimens to a hexane soak of several minutes duration or longer. Such a soak leaches out "oxidation products" and has a profound influence on both the optical absorption and thermoluminescence spectra.[12,13] As far as the electrical properties are concerned, there are likely to be two effects, a reduction in the concentration of ionizable centers and also a reduction in the concentration of traps. In addition, a treatment in alcohol[14,15] apparently removes static electrification, and we believe a similar discharge occurs on soaking in any nonreacting liquid that penetrates into the polymer.[16,17] The effect is to enhance the resolution of the Y peak and to increase the total charge injected, as shown in Figure 4.

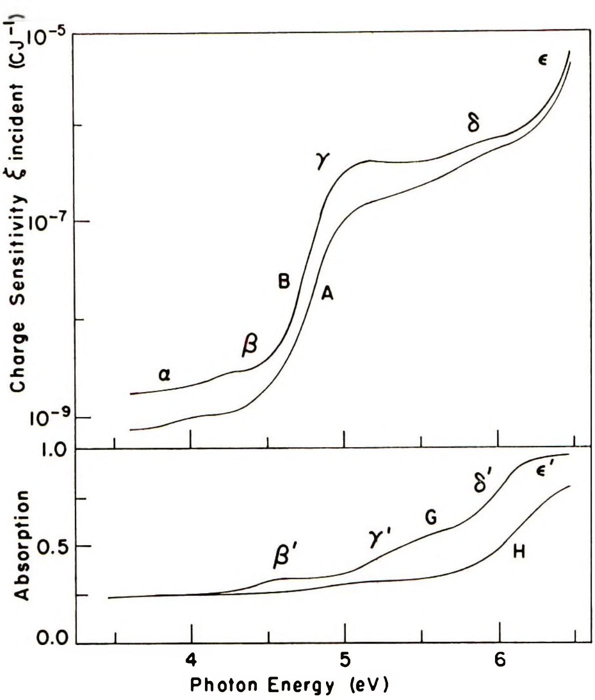

Fig. 4. Normalized spectra of charge sensitivity ξ_{incident} (charge passed per unit incident energy) as a function of photon energy: (*A*, *B*) spectra from the same specimen before and after hexane treatment, respectively; (*G*, *H*) corresponding optical absorption curves. The labeled features are discussed in the text.

A somewhat similar improvement in resolution was found to occur if a gentle warming was employed between ultraviolet sweeps. In a number of cases we have exposed specimens to infrared radiation (1.6–0.7 μm wavelength) between successive ultraviolet exposures. The material shows a photoelectric response in this infrared range,[10] but we have not been able to detect any major effect on the ultraviolet response after an infrared exposure, though the time dependence would cause any variation of less than 30% of the total ultraviolet response to be obscured.

Normalized Spectra

The action spectra have been normalized by dividing the observed photocurrent by the photon flux incident on the polyethylene (due allowance being made for the absorbance of the window and of the front silver electrode). In carrying out this procedure we have assumed, in the absence of further knowledge, that the photocurrent is proportional to the incident light intensity. The normalized spectra are plotted as a relative "quantum efficiency" ξ versus the energy of the light; ξ is equal to the number of elementary charges apparently transported across the thickness of the specimen per incident photon. The errors in ξ are compounded from uncertainties in our measurements of the photocurrent, exposed electrode

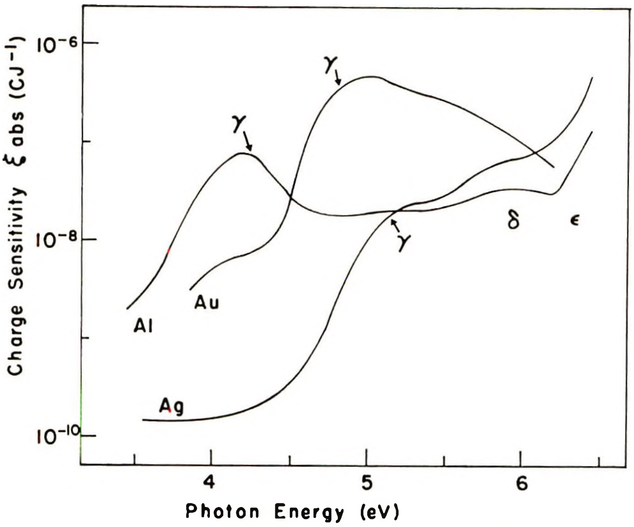

Fig. 5. Effect of changing the electrode material. Normalized spectra of charge sensitivity ξ_{abs} (charge passed per unit absorbed energy) as a function of photon energy. Three different metals (Al, Au, and Ag) were employed in the form of semitransparent evaporated films.

area of the specimens, the cross section of the light beam, loss of power from the monochromator output due to defocussing, and the absorbances of the OW1 window and of the metal electrodes. There is a systematic error in ξ, in that the figures supplied by the manufacturers for a typical radiant output flux from the monochromator were assumed applicable throughout in our experiments. We have also ignored effects due to light scattered into the sample from the surroundings and variations of the ambient absorption when the pressure is varied. The range of ξ in our measurements is from 10^{-11} to 10^{-5} elementary charges per incident photon, and we believe our values to be correct to within an order of magnitude.

The quantum efficiencies of a specimen before and after a hexane soak are shown in Figure 4, together with the absorption of the polyethylene before and after the hexane soak. These absorption measurements confirm that our material is comparable to that used by other workers.[12,18,19] In Figure 5 we give the quantum efficiencies for specimens with the three different electrode materials.

DISCUSSION

The photoelectric response of polyethylene is quite complex, but some of the features in the action spectrum can be accounted for in a relatively simple manner.

The Y Feature (4.6–5.6 eV, Silver Electrodes)

This is labeled γ when the action spectrum is normalized with respect to the incident light intensity. It includes the range of excitation of the

γ' centers in the optical absorption spectrum, (curve G of Fig. 4) of polyethylene containing oxidation products. It has a well defined threshold at 4.6 ± 0.2 eV. This is just the photoelectric work function of silver. We think this development is the consequence of two processes.

Photoelectric emission of electrons by the silver cathode into polyethylene. The energetics of electron photoinjection require that[20,21]

$$E_{\mathrm{w}} - E_{\mathrm{x}}^* - (I_{\mathrm{A}} - E_{\mathrm{G}}) < 0$$

where E_{w} is the work function of the electrodes, E_{x}^* the incident quantum energy, I_{A} the solid-state ionization energy of polyethylene, E_{G} the intrinsic sorption edge of polyethylene. Putting in the values, $E_{\mathrm{w}} = 4.7$ eV for silver, $E_{\mathrm{G}} = 7.6$ eV, and $I_{\mathrm{A}} = 10$ eV,[22] we find the threshhold for photoinjection of electrons into the conduction band of polyethylene to be 2.3 eV, although this value should be modified to take into account band bending at the metal–insulator contact. In the absence of severe bending of the bands, we have more than enough excitation energy to satisfy this requirement.

Ionization of the γ' Centers. The γ' absorption is due to one or more of the "oxidation products" in polyethylene.

The existence of photoinjection is supported by the observation that the efficiency is increased by a factor of 4 after a hexane soak (Fig. 4), which has leached out some trapping impurities and thus enhanced the macroscopic mobility. More important is the fact that with aluminum electrodes the threshold of γ was shifted to 3.9 eV, and now lies outside the range of the γ' absorption peak.

Ionization of γ' centres is also contributing to the photoconduction because there is still an effect in this spectral region when photoinjection at the same energies is avoided by the use of aluminum electrodes (Fig. 5). The aluminum injection is an order of magnitude more efficient than the γ' ionization process. When silver electrodes are used, the efficiencies appear to be of similar magnitude (Fig. 4). We can still see that with silver electrodes (Fig. 4, curve B) there is a region extending from about 5.2 eV upwards in energy which cannot be accounted for by the trailing edge of the silver injection peak, and this must also be ascribed to ionization of the γ' centers.

The difference between the samples soaked in hexane and those not treated indicates a complex behavior. The luminescence and absorption of the oxidation products in polyethylene have been studied by Partridge,[12,22] who found that these impurities can be removed by the soaking. This is also shown by the optical absorption spectra (G and H of Fig. 4). The corresponding photoconduction spectra before and after soaking are curves A and B. Now the injection peak increases fourfold, indicating that traps have been removed. However, over the rest of the spectrum, there is an overall sensitization by a factor rather smaller than 4, so that the enhancement due to the removal of traps has been offset by the removal of some, but not all, of the ionisable impurities giving rise to photocarriers. A similar partial removal of impurities has been reported by Boustead and Charlesby.[23] On the basis of their work one might tentatively suggest that the carriers are produced largely in the crystalline regions, the energy required coming from absorption in the benzoic acid located in these regions, while trapping arises from the aromatic residues which provide the bulk of the absorption in the γ' region.[12] Ionization arising from the energy absorbed by these residues cannot, however, be ruled out. Since they can be removed by evaporation at quite modest temperatures,[12] the increase in resolution of Y and Z after warming also points to their influence on the photoconduction process.

The *Z* Feature ($E_x^* > 5.6$ eV)

Light is strongly absorbed in this region of the spectrum, as is shown by the features labeled δ' and ϵ'. The δ' feature is due to carbonyl groups and some components of the "oxidation products" while the ϵ' feature is the beginning of the absorption peak due to double bonds in the material.[12] While there may be some contribution from leachable impurities, we believe that the photoelectric response occurs as the result of absorption of photons in the bulk of the material, followed by an ionization process. Such a process might be expected to be biphotonic, but we have been unable to make satisfactory measurements of response as a function of the intensity because of interference from the transient behavior. Electrons freed by such a process might be expected to be present in progressively decreasing concentration in going more deeply into the material, so that the resulting diffusion current would correspond to electron flow from front to back of the specimen. The opposite polarity is observed, and this suggests that there may be an efficient electron trapping process at the front surface, giving rise to a concentration profile of the form[24] shown in Figure 6. The steep leading edge of this distribution would give rise to a diffusion current with a direction agreeing with that found in practice. The fact that this feature preserves the same polarity, though is reduced in magnitude, when the external field is reversed is also consistent with our suggestion of a diffusion process.

Fig. 6. Qualitative representation of the free-electron concentration as a function of the distance x into the specimen. Front surface at $x = 0$, back surface at $x = d$.

The X Feature (3.4 eV < E_x^* < 4.6 eV)

The feature X becomes α and β in the normalized spectra. β appears to be related to ionization of the β' centres of the optical absorption spectrum of oxidized polyethylene. Part of the β' absorption is removable with hexane treatment. This is the fraction associated with the amorphous regions of the material. The part associated with the crystalline regions is unaffected by the hexane treatment, as is the shape of the rising portion β of the normalized action spectrum. Consequently some part of the β feature may be attributable to ionization of β' centers associated specifically with crystalline polyethylene. We can find no clear origin for the α feature and therefore are unable to present a model for the X feature at this stage. The energy involved is in theory sufficient for photoinjection to occur, but the irregular nature of the feature and the fairly clear evidence of injection in the Y feature lead us to discount this possibility.

The transient behavior illustrated in Figure 2 can be accounted for by an Elovitch (or Roginsky-Zeldovich) equation

$$(D + b)/(D_0 + b) = \exp\{a(Q - Q_0)\}$$

where D is the total dose, Q is the total charge passed and a, b, D_0, and Q_0 are constants. The implication is that once some charge has been introduced, the motion of further charge is inhibited, presumably because the earlier charge is not transferred across the specimen from one electrode to the other, but rather forms a space charge. The field set up by this space charge will act in a sense that will prevent further charge migration. The recovery on resting and the observation of a discharge with gold electrodes support the space charge hypothesis.

The effect of oxygen and nitrogen presents a problem. The equilibration time for our specimens is about 6 sec,[25] much shorter than the duration of the experiments, so the gas content of the sample can always be assumed to be the equilibrium concentration. On the one hand, a specimen irradiated in air gives an action spectrum quite comparable to that obtained in a vacuum, except that the charge transferred per sweep, $Q(n)$, falls more abruptly when the gas is present. One might ascribe this behavior to a more efficient trapping of carriers when the gas is present. On the other hand, when either oxygen or nitrogen is let into the vacuum system following vacuum irradiation, the quenching which occurs is very strong and leads to subsequent spectra which are similar in shape but much smaller than those obtained after the same number of exposures in air. We infer that the processes giving rise to charge release are the same in all cases, but that an even more efficient trap is formed during the quenching operation. As with the oxygen effect in thermoluminescence,[25] the quenching is removed under only modest pumping (less than 10^{-3} torr). The responses to illumination at a fixed frequency vary as a function of time in the manner outlined by Heijne[26] for adsorption processes and, coupled with the reversible behavior under change in pressure and the occurrence of the Elovitch type of equation, provide strong circumstantial evidence that gas adsorption also plays an important role.

It is not possible to make an unequivocal identification of the nature of the charge carrier excited in these experiments. The carrier mobilities which have been measured in the dark are very low and thermally activated,[27–30] and it has been inferred from the thermoluminescence work that electrons are the carriers.[31] The quenching effect of oxygen effectively rules out oxygen ions as carriers, even though the neutral molecules have a diffusion coefficient more than adequate to account for the observed mobilities in the range 10^{-7}–10^{-11} cm^2/V-sec. It is possible to construct models in which holes are the mobile carriers. However, it is hard to see how oxygen, which has an electron affinity of 0.33 eV in polyethylene[32] and which is likely to act as an electron trap, or perhaps even an acceptor center, will quench a hole-photocurrent in this material, whereas in anthracene, which is known to be *p*-type, the presence of oxygen increases the hole-photocurrent[33,34] as is to be expected. In our discussion we have consequently made the assumption that electrons are involved. The sources are (1) bulk-generated electrons and (2) photoinjected electrons from the cathode. The bulk-generated electrons are extrinsic in origin, since the energy of excitation used here was less than 7.6 eV, which is the fundamental absorption edge of polyethylene;[22] since there is no evidence of exciton absorption in polyethylene at these energies,[35] the charge carriers are not generated by exciton decomposition, as in anthracene. The concentration of electrons during illumination at the short wavelength end has been postulated to have the distribution shown in Figure 6. This picture is qualitatively valid if the diffusion length of the charge carrier is small compared with the dimension of the specimen. We have $L = (D\tau)^{1/2} = (\mu kT\tau/q)^{1/2}$, where L is the diffusion length, D the diffusion constant, τ the lifetime of the charge carriers, k is Boltzmann's constant, T the absolute temperature, and q the electronic charge. Taking $\mu = 10^{-11}$ cm^2/V-sec and Fowler's[36] upper limit for $\tau = 10^{-7}$ sec, we find $L \approx 10^{-9}$ cm, whereas the thickness of our specimens is 2.5×10^{-3} cm, so the required condition is easily satisfied.

Work has recently been published by Binks et al.[37] on photocurrents in polymers. Their work contains a number of rather similar measurements which appear to be at variance with our results. These discrepancies are (a) that their currents are largest with the illuminated face negative rather than positive, (b) no photocurrents are observed at wavelengths longer than 310 nm (silver electrodes), and (c) that under steady illumination their currents rise with time and then become steady, rather than decreasing with time. Their front electrodes are semitransparent metal films evaporated on quartz, and their rear electrode is brass. These electrodes are held in mechanical contact with the specimen. By introducing a gap between specimen and electrode they show conclusively that they are not dealing with photoconduction in the polymer but with the effect of bombarding the polymer with a stream of low-energy electrons sent off from the front electrode by external photoemission. The fact that their rear electrode is not a good emitter accounts for (a). Their lowest reported current is 3×10^{-14} A, while the currents we detect in the X feature are an order of magnitude smaller, so (b) arises from the overall sensitivity, which may be governed more by the electrical noise levels than by the electrometer specifications. Our experiments show space charge storage and recovery effects at illumination levels of around 10 μW/cm². The work of Binks et al. does not indicate such effects for levels up to 15 mW/cm², but does under pulsed light conditions for which the intensity is roughly 60 W/cm² (as estimated from their blank cell currents). Thus point (c) appears to be a quantitative rather than a qualitative difference, and may be due either to the different grade of polyethylene or to the somewhat different manner in which the experiments are conducted. It is clear that the electron yield in the external photoemission experiments[37] is much larger than in our case in which we believe internal photoemission occurs from the electrode directly into the polymer.[38] We are thus able to observe the effect impurities have on the photoconduction, both as traps and as sources of carriers.

The present work reports the first measurements of the ultraviolet photoconduction action spectrum of polyethylene. The excited charge carrier is probably an electron, though we cannot entirely rule out other species. We have detected a number of different regions in the response and made tentative assignments of these to the corresponding features in the optical absorption spectrum. In addition, we have identified an injection peak. It is clear that further experimental work is required to clarify the relative roles of reversible physical processes and irreversible photochemical degradation before detailed mechanisms can be presented.

The authors would like to thank Mr. M. Wenger for the careful preparation of specimens, Mr. J. Turner for the construction of the vacuum chamber, and Mr. K. O. Lim for numerical calculations. Discussions with Drs. M. Sayer, A. T. Stewart, and F. R. L. Schöning have been very helpful. We are indebted to Canadian Industries Ltd. for the gift of specimens. One of us (D. A. N.) has held a Province of Ontario Graduate Fellowship, while another (L. A. V.) has received a travel award from the South African C.S.I.R. Financial support for this project has been provided by the Ontario Department of University Affairs and by the National Research Council of Canada.

References

1. H. J. Wintle and A. Charlesby, *Photochem. Photobiol.*, **1**, 231 (1962).
2. M. Kryszewski, A. Szymanski, and A. Wtochowicz, in *Macromolecular Chemistry Prague 1965* (*J. Polym. Sci. C*, **16**), O. Wichterle and B. Sedláček, Eds., Interscience, New York, 1969, p. 3921.
3. T. Tanaka and Y. Inuishi, *Japan. J. Appl. Phys.*, **5**, 974 (1966).
4. T. Tanaka and Y. Inuishi, *Japan. J. Appl. Phys.*, **6**, 1371 (1967).
5. H. J. Wintle, *Photochem. Photobiol.*, **4**, 803 (1965).
6. W. L. McCubbin, *Trans. Faraday Soc.*, **58**, 2307 (1962).
7. A. Weinreb, N. Ohana, and A. A. Braner, *J. Chem. Phys.*, **43**, 701 (1965).
8. D. A. Nicodemo, M.Sc. Thesis, Queen's University, Kingston, Ontario, Canada, 1969.
9. R. H. Partridge and A. J. Avery, private communication.

10. L. A. Vermeulen and H. J. Wintle, *J. Polym. Sci. A-2*, in press.

11. D. A. Nicodemo, H. J. Wintle, and L. A. Vermeulen, *1969 Annual Report, Conference on Electrical Insulation and Dielectric Phenomena*, NAS-NRC, Washington, 1970, p. 31.

12. R. H. Partridge, *J. Chem. Phys.*, **45**, 1679 (1966).

13. I. Boustead and A. Charlesby, *Europ. Polym. J.*, **3**, 459 (1967).

14. R. H. Partridge, *J. Polym. Sci. B*, **5**, 205 (1967).

15. E. L. Zichy, *Conference on Static Electrification*, Institute of Physics and the Physical Society, London, 1967, p. 52.

16. D. K. Davies, private communication.

17. J. D. Comins, to be published.

18. H. J. Wintle, *Photochem. Photobiol.*, **3**, 249 (1964).

19. W. L. McCubbin and J. C. Weeks, *J. Appl. Phys.*, **37**, 3644 (1966).

20. H. Kallmann and M. Pope, *J. Chem. Phys.*, **32**, 300 (1960).

21. H. Kallmann and M. Pope, *Nature*, **186**, 31 (1960).

22. R. H. Partridge, *J. Chem. Phys.*, **45**, 1685 (1966).

23. I. Boustead and A. Charlesby, *Proc. Roy. Soc.* (London), **A316**, 291 (1970).

24. J. N. Murrell, *Discussions Faraday Soc.*, **28**, 36 (1959).

25. A. Charlesby and R. H. Partridge, *Proc. Roy. Soc.* (London), **A271**, 188 (1963).

26. L. Heijne, *Philips Tech. Rev.*, **29**, 221 (1968).

27. D. K. Davies, *Conference on Static Electrification*, Institute of Physics and the Physical Society, London, 1967, p. 29.

28. E. H. Martin and J. Hirsch, *Solid State Commun.*, **7**, 783 (1969).

29. O. Dehoust, *Z. Angew. Physik.*, **27**, 268 (1969).

30. H. J. Wintle, *J. Appl. Phys.*, **41**, 4004 (1970).

31. R. H. Partridge, *J. Polym. Sci. A*, **3**, 2817 (1965).

32. A. Charlesby and R. H. Partridge, *Proc. Roy. Soc.* (London), **A283**, 312 (1965).

33. A. G. Chynoweth and W. G. Schneider, *J. Chem. Phys.*, **22**, 1021 (1954).

34. D. C. Northrop and O. Simpson, *Proc. Roy. Soc.* (London), **A244**, 377 (1958).

35. R. H. Partridge, *J. Chem. Phys.*, **49**, 3656 (1968).

36. J. F. Fowler, *Proc. Roy. Soc.* (London), **A236**, 464 (1956).

37. A. E. Binks, A. G. Campbell, and A. Sharples, *J. Polym. Sci. A-2*, **8**, 529 (1970).

38. A. M. Goodman, *J. Electrochem. Soc.*, **115**, 276C (1968).

Received July 16, 1970
Revised September 25, 1970

JOURNAL OF POLYMER SCIENCE: PART A-2 VOL. 9, 557–567 (9971)

Segmental Motion in Polyoxymethylene*

B. CRIST and A. PETERLIN, *Camille Dreyfus Laboratory,*
Research Triangle Institute, Research Triangle Park, North Carolina 27709

Synopsis

The proton spin-lattice relaxation times (T_1) of melt-crystallized, solution-crystallized, and solid-state-polymerized polyoxymethylene (POM) were measured between −60 and +150°C. The three types of samples each have a pronounced T_1 minimum near room temperature which is a high-frequency manifestation of the γ process. From the quantitative dependence of the relaxation intensity on crystallinity as well as from the absolute magnitude of the relaxation times, it is concluded that the γ process in POM arises from hindered rotation of noncrystalline chain segments. The relation between the relaxation times and the long period indicates that these noncrystalline segments constitute disordered lamellar surface layers, the thickness of which depends on thermal history of the material. The temperature dependence of the motion of the relatively thin surface layers of solution crystallized POM is quite straightforward. The γ process in the bulk-crystallized material involves cooperative motion, however, leading to temperature-dependent kinetic parameters.

INTRODUCTION

Polyoxymethylene (POM) displays multiple relaxation processes, as do many semicrystalline polymers. These relaxations have been extensively studied by mechanical and dielectric loss techniques[1] and by wide-line NMR.[2–6] The high-temperature α relaxation is associated with motion in the crystalline regions, probably involving rotation and translation of the helical chain segments.[1,7] A weak β relaxation process is generally observed above room temperature. Though the β intensity is known to be sensitive to moisture and thermal history[8] as well as comonomer content,[9] the relaxation mechanism for this process is uncertain. The γ relaxation has been most thoroughly investigated, having been measured over a frequency range of 12 decades. From the qualitative dependence of the apparent relaxation intensity on density, the γ process has been attributed to motion in the noncrystalline regions.[8] Proposed mechanisms for this relaxation include an amorphous glass–rubber transition,[10,11] local mode relaxation on the disordered lamellar surfaces[7] or in defects within the crystals.[12] From dielectric loss measurements it appears that the γ relaxation is a composite process, having components associated with both the amorphous and crystalline regions.[13–15] Two additional relaxations

---

* Presented in part at the Meeting of the American Physical Society, Dallas, Texas, March 1970.

have recently been reported in POM: a very low-temperature (48°K) mechanical loss maximum[16] and a high-frequency dielectric dispersion in the melt.[17]

Relatively few systematic investigations of relaxation effects in polymers have been made by utilizing nuclear magnetic spin-lattice relaxation times (T_1). Previous work on polyethylene (PE) has shown that the spin-lattice relaxation times of the entire sample can be explained by motion of a relatively small fraction of chain segments.[18,19] In the limit when the spin diffusion mechanism which couples the mobile and immobile spins is very efficient, the observed relaxation time in the polymer is given by[20,21]

$$1/T_1 = X_m/T_1^m \qquad (1)$$

where x_m is the fraction of nuclear spins whose motion is responsible for the relaxation, and T_1^m is the intrinsic relaxation time of the mobile spins, which depends on the relative motional frequency of neighboring nuclei and on the internuclear distance. For thermally activated motion, T_1^m is temperature-dependent, having a minimum value when the average motional frequency is comparable to the NMR frequency. Thus, from the temperature dependence of the observed spin-lattice relaxation, the mobility of certain chain segments or functional groups can be followed. In addition, the absolute value of T_1 enables one to estimate the number of mobile segments which give rise to the relaxation.

Trappeniers et al.[22] have shown that the T_1 minimum observed in POM around room temperature is related to the γ process in this material. We have investigated the T_1 behavior in POM samples of widely varying preparations and thermal history. The observed relaxation effects have been interpreted in terms of the morphology of the material.

EXPERIMENTAL

Methods

The pulsed NMR apparatus has been described previously.[18] All the POM samples displayed a single exponential spin-lattice relaxation, and the relaxation times were measured by the t_{null} technique. The relaxation times were perfectly reversible with respect to temperature.

Densities were obtained at 20°C by the flotation technique with liquid mixtures of xylene and tetrachloroethylene. The noncrystalline mass fractions ($1 - \alpha_m$) were calculated from a two-phase model with the crystal density[23] $\rho_c = 1.492$ g/cm^3 and the amorphous density[24] $\rho_a = 1.25$ g/cm^3.

The long periods of the POM samples were evaluated by applying Bragg's law to the low-angle x-ray scattering maxima.

Samples

All the POM samples except sample F were prepared from Delrin 500 (Du Pont), having a number-average molecular weight $\bar{M}_n$ of approximately 40,000. After the preparative treatments outlined below, about 0.2 g of the material was thoroughly degassed ($<10^{-5}$ torr), then sealed under 0.5 atm helium. Annealing was done under a helium atmosphere.

Sample A was formed by quenching a molten, compression-molded film (1 mm thick) in ice water.

Sample B was prepared by cooling a 1-mm compression-molded film from the melt at 1°C/min.

Sample C resulted from annealing the quenched film (sample A) at 173°C for 7 hr.

Sample D was isothermally crystallized at 141°C from a 0.05% solution in cyclohexanol. After filtering, the single-crystal mat was dried under high vacuum at 56°C.

Sample E resulted from annealing the single-crystal mat (sample D) at 168°C for 3.5 hr.

Sample F was prepared by the solid-state polymerization of trioxane and will be referred to as extended chain POM. The material was annealed at 179°C under vacuum to eliminate twinning.

The characteristics of these samples are summarized in Table I.

TABLE I
Physical Properties of POM Samples

Sample	Description	ρ_{20}, g/cm^3	$1 - \alpha_m$	L, Å
A	Quenched	1.406	0.32	138
B	Slowly cooled	1.437	0.20	185
C	Annealed	1.444	0.17	230
D	Single crystals	1.462	0.11	125
E	Annealed single crystals	1.452	0.14	190
F	Extended chain	1.475	0.06	—

RESULTS

The temperature dependence of the proton spin-lattice relaxation rate $1/T_1$ in the POM samples is shown in Figures 1 and 2. The experimental values of $1/T_1$ for the slowly cooled specimen (sample B) were consistently 13% greater than those for annealed sample C and have been omitted for the sake of clarity. All six of the POM samples display a pronounced relaxation maximum near room temperature, signifying that some large-scale thermally activated motion attains a frequency comparable to the NMR frequency (38 MHz in these experiments) in this temperature region.

It is seen from Figure 1 that the intensity of this relaxation centered at 15°C is density-dependent, while the shape of the relaxation peak is identical for the three bulk-crystallized POM samples. The relaxation rate is greatest in the specimen with the lowest density, suggesting that segmental motion in the density-deficient, disordered regions of the polymer is responsible for the observed relaxation.

The POM single-crystal and extended-chain samples, despite their ap-

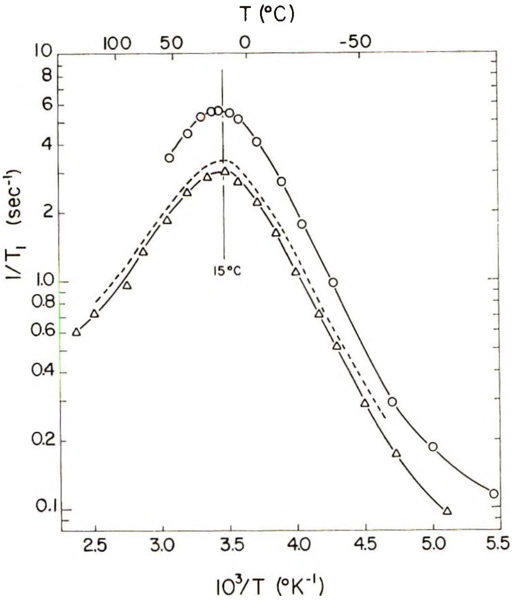

Fig. 1. Temperature dependence of the spin-lattice relaxation rate for bulk crystallized POM: (O) quenched, (---) slowly cooled, and (△) annealed specimens.

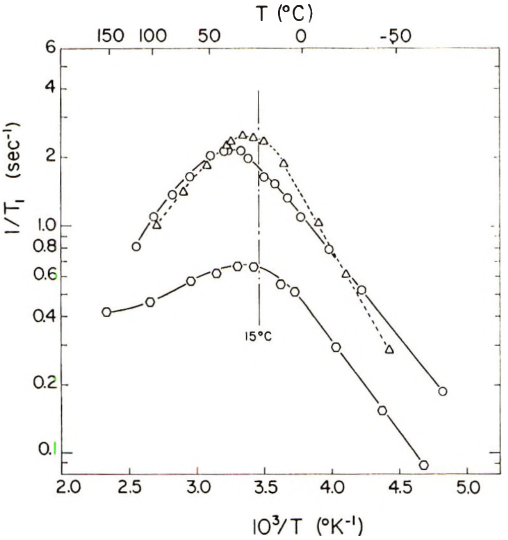

Fig. 2. Temperature dependence of the spin-lattice relaxation rate for POM: (O) single crystals as grown, (△) annealed, and (⬡) solid-state-polymerized POM.

preciably different morphologies, have relaxation curves (Fig. 2) essentially similar to those of the melt-crystallized samples. In addition, the qualitative density dependence of the relaxation intensity, as measured by the maxima of the relaxation curves, is followed by samples D, E, and F.

Small differences do exist, however, in the shape of the relaxation curves. The temperature of the relaxation maximum for the single crystals as grown (sample D) is some 20°C higher than that in the bulk-crystallized specimens. This implies that the average mobility of the chain segments whose motion gives rise to the relaxation is observably less in the single crystals. The low-temperature slopes of the relaxation peaks for the single crystals (sample D) and extended-chain POM (sample F) are some 30% lower than those found in the bulk-crystallized specimens. These slopes reflect the activation energy of the motion in the different types of samples, as will be discussed in the next section. It may be noted that the high-temperature slopes for samples A–E are quite similar. After annealing the single crystals (sample E), both the temperature of the maximum and the low-temperature slope approach the values found in melt-crystallized POM. These parameters of the relaxation curves are summarized in Table II. It should be remembered that the apparent activation energies derived from Figures 1 and 2 are too low, as the relaxation peaks are broadened by a distribution of correlation times.[25]

TABLE II
Spin-Lattice Relaxation of POM

Sample	$(1/T_1)_{\max}$, sec^{-1}	$T_{\max}$, °C	Slope, kcal/mole: Low temperature	Slope, kcal/mole: High temperature
A	5.58	15	5.4	—
B	3.40	15	5.4	3.7
C	3.00	15	5.4	3.7
D	2.15	35	3.1	3.5
E	2.45	24	4.8	3.5
F	0.58	~25	3.4	—

The pronounced asymmetry of the relaxation curve for the extended-chain sample F is thought to result from a relaxation mechanism originating in the crystalline regions. This interference contributes about 0.1–0.2 sec^{-1} to the relaxation rate above room temperature and is virtually unobservable in samples A–E.

DISCUSSION

The spin-lattice relaxation maximum in POM being considered in this work has previously been associated with the γ relaxation found in mechanical and dielectric loss experiments.[22] The relaxation map shown in Figure 3 confirms this assignment: the points for both the bulk-crystallized and as-grown single crystals coincide quite well with the loci of the dielectric loss maxima of similar samples. Neither the very weak β relaxation nor the crystalline α relaxation is observable at the high frequency of the NMR experiment. It is realized that the location of the

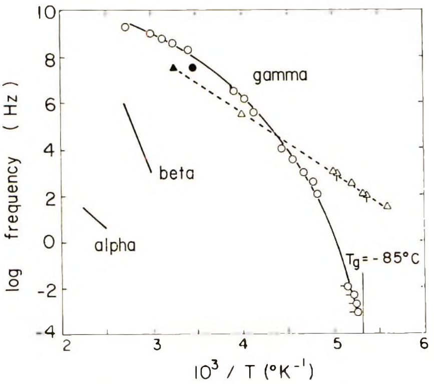

Fig. 3. Relaxation map for POM: (——) from dielectric loss data on bulk-crystallized samples,[1] with experimental points from (O) Read and Williams[10] and (-O) Williams;[26] (---) for (Δ) single crystals[13] and (Δ) solid-state-polymerized POM;[15] (●) points for bulk-crystallized and (▲) solution-crystallized specimens (this work).

γ loss maximum is subject to rather small systematic differences which depend on the type of measurement (dielectric or mechanical)[11] and the technique used (isochronal or isothermal).[11,12] The relaxation map in Figure 3 has therefore been compiled from isochronal dielectric loss maxima $\epsilon''(T)$, as data of this type are most complete and correspond to the constant-frequency T_1 measurements.

From this relaxation map it is seen that the apparent activation energy for the γ process in melt-crystallized POM is highly temperature-dependent, decreasing from 60 kcal/mole at −80°C to 8.6 kcal/mole above room temperature. Certain authors have attributed this curvature of the relaxation line to a temperature dependent distribution of relaxation times, and assert that the true activation energy can be derived only from isothermal loss maxima.[1,10,27] After a critical review of the literature, we have concluded that the curvature of the solid line in Figure 3 reflects the glass transition of semicrystalline POM, which has been observed by calorimetry[28] and measurements of thermal expansion.[29,30] These data place the glass transition temperature T_g at -85 ± 2°C, which agrees very well with the lowest temperature at which the γ relaxation has been observed in melt-crystallized POM (see Fig. 3).

The low-temperature relaxation in the POM single crystals, on the other hand, shows no characteristics of a glass transition down to −95°C. The locus of the relaxation from this work is correlated with the lower-frequency dielectric data of Kakizaki et al.[13] by an Arrhenius expression with an activation energy of 12 kcal/mole. Also included in Figure 3 are the data of Ishida[15] for solid-state-polymerized POM. We have not plotted our result for the similar sample F, as we are uncertain of the exact temperature of the maximum, but it is certainly in the range 3.25–3.40×10^{-3} °K^{-1}, indicating kinetic parameters very similar to those of the single crystals.

For the sake of convenience, the low-temperature relaxation in all three types of POM will be referred to as the γ relaxation or the γ process. The different kinetics of this relaxation in bulk-crystallized POM as opposed to solution-crystallized and solid-state-polymerized specimens are substantiated by the temperature dependence of T_1 in Figures 1 and 2. The temperature-dependent activation energy of the γ process in samples A, B, and C is indicated by the difference between the high-temperature and low-temperature slopes (Table II). The relaxation peak for the single crystals, however, is nearly symmetric, reflecting the constancy of the activation energy over the temperature range covered. The equivalence of the low-temperature slopes for the single crystals and the solid-state-polymerized POM agrees with the observation that the loci of the dielectric loss maxima of these materials overlap. Also, the high-temperature slopes of samples A–E are virtually identical, reflecting the fact that the two γ-relaxation lines in Figure 3 are nearly parallel above room temperature. Regarding these points it can be seen that the behavior of the annealed single crystals is intermediate between that of the melt-crystallized POM and of the single crystals as grown.

The relation between the nature of the γ relaxation and sample morphology will now be considered in more detail. Mechanical and dielectric loss measurements both display a low-temperature (γ) relaxation in bulk-crystallized, solution-crystallized and solid-state-polymerized POM;[5,12–14] in addition, the relative intensities of the relaxation qualitatively agree with those found in this study. To examine this trend more quantitatively, the relaxation intensities of the POM samples given by the peak heights in Figures 1 and 2 are plotted as a function of the noncrystalline content in Figure 4. The points for the bulk-crystallized and solution-crystallized samples all fall very close to a straight line of unit slope. This demonstrates that the segmental motion responsible for this relaxation is associated with the density-deficient regions of POM. The relaxation rate for the extended-chain sample F is some 30% below the line. It is quite probable that time required for spin diffusion to the dilute noncrystalline regions is not negligible in this material, and thus the observed spin-lattice relaxation

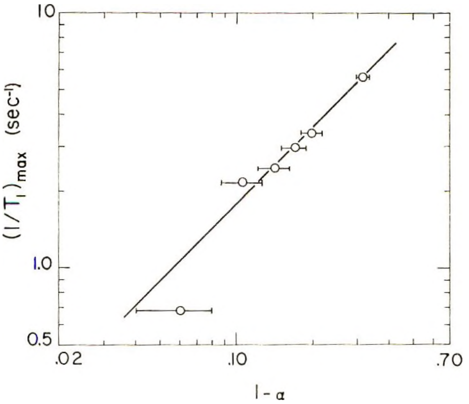

Fig. 4. Dependence of the maximum relaxation rate on noncrystalline mass fraction.

time is increased. A similar effect has been noted in extended-chain, highly crystalline PE.[18]

Though the two-phase crystalline–amorphous model was assumed in calculating the noncrystalline fractions in Figure 4, the linearity of the experimental points does not in itself prove that the relaxation originates from motion of amorphous chain segments; the motion could be associated with any density-deficient regions, including crystal defects. The γ relaxation observed in these experiments would nonetheless vanish in a (hypothetical) 100% crystalline sample. The identical result is obtained if one similarly plots the mechanical loss intensities (maximum logarithmic decrement) observed by McCrum.[31] Therefore it will be assumed throughout the remainder of this discussion that the γ relaxation in POM results from a single motional process. Some authors[13–16] have argued on the basis of the asymmetry of the isochronal loss peak that this relaxation is a superposition of two or more components. From the present results and those of McCrum, it is apparent that the various components, if they indeed exist, have approximately the same density dependence. In the cases of linear polyethylene and polychlorotrifluoroethylene, which are known to have composite mechanical and dielectric low temperature (γ) relaxations, the relaxation intensity extrapolates to a finite value in the limit of 100% crystallinity.[32,33] Such is not the case with POM. Perhaps the various components could be resolved by very low frequency, low temperature relaxation experiments.

The two-phase model, however, is supported by the absolute value of the observed relaxation times. If it is assumed that the γ relaxation results from motion of all the amorphous segments, eq. (1) can be rewritten as

$$1/T_1 = (1 - \alpha_m)/T_1^{m} \qquad (2)$$

Here, the fraction of mobile protons which relaxes the entire sample is given by the noncrystalline mass fraction $1 - \alpha_m$. From the absolute value of the maximum relaxation rates plotted in Figure 4, the experimentally derived value of T_1^{m} is 57 msec, which agrees quite well with the value of 43 msec calculated for an isolated methylene proton pair undergoing hindered rotation about a fixed axis. The disagreement of ca. 30% is not considered serious, as the effects of a distribution of correlation times and extra-pair dipolar interactions have been neglected in this extremely simple model.

A more stringent test of the two-phase model is based on the lamellar morphology of POM. By adoption of the "sandwich" model of Fischer and Schmidt,[34] in which the crystalline cores of the lamellae are separated by disordered surface layers, the volume fraction noncrystallinity of the sample can be expressed as

$$1 - \alpha_v = l/L \qquad (3)$$

In this expression l is twice the thickness of a disordered surface layer, and L is the long period characteristic of the lamellar structure. After accounting for the small (ca. 20%) difference between mass and volume crystallinities, substitution of eq. (3) into eq. (2) yields the expression (4) the relaxation:

$$1/T_1 = (\rho_a/\rho)l/T_1{}^{m}L \tag{4}$$

It can be seen that eq. (4) predicts that the relaxation rate depends on the ratio l/L; the quantity (ρ_a/ρ) varies by less than 5% for samples A–F and hence does not sensibly affect $1/T_1$.

In Figure 5 the data are plotted in accordance with eq. (4). The point for the extended-chain sample F is omitted, as it is not expected that this material is described by the lamellar model. The open circles for the three bulk-crystallized POM samples fall within 10% of a straight line passing through the origin, as predicted by the two-phase lamellar model. These specimens were each crystallized or annealed around 170–175°C, and would thus be expected to have similar values of l.[34] It is quite apparent that the data for the single crystals as-grown fall well below this line. In terms of the lamellar model in question, this implies that the disordered surface layers of POM crystallized from solution at 141°C are significantly thinner than those formed at higher temperatures. After annealing the single crystals at 168°C, the surface layer apparently thickens as indicated by the shift upward and to the left in Figure 5 toward the line for the melt crystallized samples. The increase in l on annealing is also reflected in an increased mobility of the surface layer, as the γ temperature shifts down toward the 15°C value found for samples A, B, and C (see Fig. 2). Applying the two-phase model and eq. (4) to these data, one obtains a surface-layer thickness ($l/2$) of 24 Å for the melt-crystallized POM, 10 Å for the single crystals as grown, and 17 Å for the annealed single crystals. This

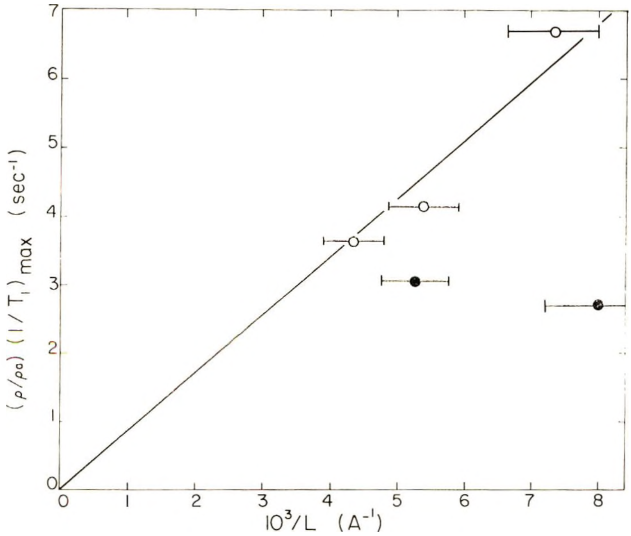

Fig. 5. Relaxation rate as a function of reciprocal long period for (○) bulk-crystallized and (●) solution crystallized POM.

dependence of the surface-layer thickness and mobility on thermal history exactly parallels the behavior of bulk-crystallized and solution-crystallized linear PE.[18]

It is believed that these different surface layer thicknesses are responsible for the two γ-relaxation curves in Figure 3. The disordered surface layers in the as-grown single crystals are thought to consist of relatively tight folds and a few excluded chain ends. The thermally activated motion of the relatively ordered segments on these surfaces can be described by a classical Arrhenius expression with temperature-independent parameters, giving rise to the straight dashed line on the relaxation map. The thicker surfaces of the bulk-crystallized lamellae are composed of interlamellar tie molecules as well as chain ends and large, irregular folds. These regions more closely resemble an amorphous state; the motions of the segments within them are clearly cooperative and result in the curved solid line for the γ process in Figure 3. Stehling and Mandelkern[30] have noted that many solution-grown polymers, including POM, display mechanical relaxations which are qualitatively similar to those found in corresponding melt-crystallized specimens. In those cases in which the mechanical loss is associated with a glass transition in bulk-crystallized samples, they conclude that a glass transition also exists in the single-crystal preparations. The present study shows that this argument cannot be applied to POM single crystals as grown.

The situation with the extended-chain sample F is less clear. From the temperature position and low temperature shape of the relaxation curve in Figure 2, as well as the qualitative correspondence between noncrystallinity and the relaxation strength in Figure 4, it seems that the motion occurring in this material is similar to that described above for the lamellar POM. As there are presumably no fold surfaces or tie molecules in the extended-chain sample, it is tempting to associate motion of the chain ends with the γ process.[5,14] If the present T_1 results are to be explained by this model, one reaches the unlikely conclusion that some 100–150 repeat units are associated with the mobile terminal segments of each extended-chain molecule having an estimated molecular weight of 100,000.[5,35] It is more probable that this motion originates in disordered regions within the crystals, as is indicated by the anisotropy of the dielectric loss maximum found by Ishida.[15]

The authors gratefully acknowledge the financial support of the Camille and Henry Dreyfus Foundation. We are also indebted to Dr. A. Chapiro of Laboratorie de Chimie des Radiations, Bellevue, France, for supplying the sample of solid-state-polymerized POM.

References

1. N. G. McCrum, B. E. Read, and G. Williams, *Anelastic and Dielectric Effects in Polymeric Solids*, Wiley, New York, 1967, pp. 540 ff.

2. W. P. Slichter, *Makromol. Chem.*, **34**, 67 (1959).

3. H. G. Olf and A. Peterlin, *J. Appl. Phys.*, **35**, 3108 (1965).

4. K. Hikichi and J. Furuichi, *J. Polym. Sci. A*, **3**, 3003 (1965).
5. N. Yamada, Z. Orito, and S. Minami, *J. Polym. Sci. A*, **3**, 4173 (1965).
6. T. Hideshima and M. Kakizaki, *Repts. Progr. Polym. Phys. Japan*, **6**, 201 (1963).
7. K. Arisawa, K. Tsuge, and Y. Wada, *Japan. J. Appl. Phys.*, **4**, 138 (1965).
8. N. G. McCrum, *J. Polym. Sci.*, **54**, 561 (1961).
9. L. Bohn, *Kolloid-Z. Z. Polym.*, **201**, 20 (1965).
10. B. E. Read and G. Williams, *Polymer*, **2**, 239 (1961).
11. R. E. Wetton and G. Allen, *Polymer*, **7**, 331 (1966).
12. M. Takayanagi, *Mem. Fac. Eng. Kyushu Univ.*, **23**, 1 (1963).
13. M. Kakizaki, Y. Morita, K. Tsuge, and T. Hideshima, *Repts. Progr. Polym. Phys. Japan*, **10**, 397 (1967).
14. Y. Morita, M. Kakizaki, K. Tsuge, and T. Hideshima, *Repts. Progr. Polym. Phys. Japan*, **11**, 349 (1968).
15. Y. Ishida, *J. Polym. Sci. A-2*, **7**, 1835 (1969).
16. Y. S. Papir and E. Baer, *Bull. Am. Phys. Soc.*, **15**, 352 (1970).
17. C. H. Porter, J. H. L. Lawler, and R. H. Boyd, *Macromolecules*, **3**, 308 (1970).
18. B. Crist and A. Peterlin, *J. Polym. Sci. A-2*, **7**, 1165 (1969).
19. B. Crist and A. Peterlin, *J. Macromol. Sci. B*, **4**, 791 (1970).
20. J. E. Anderson and W. P. Slichter, *J. Phys. Chem.*, **69**, 3099 (1965).
21. U. Haeberlen, *Polymer*, **9**, 50 (1968).
22. N. J. Trappeniers, C. J. Gerritsma, and P. H. Oosting, *Physica*, **30**, 997 (1964).
23. G. Carazzolo, *J. Polym. Sci. A*, **1**, 1573 (1963).
24. C. F. Hammer, T. A. Koch, and J. F. Whitney, *J. Appl. Polym. Sci.*, **1**, 169 (1959).
25. T. M. Connor, *Trans. Faraday Soc.*, **60**, 1575 (1964).
26. G. Williams, *Polymer*, **4**, 27 (1963).
27. M. E. Baird, *J. Phys. Chem.*, **72**, 1462 (1968).
28. F. S. Dainton, D. M. Evans, F. E. Hoare, and T. P. Meliu, *Polymer*, **3**, 263 (1962).
29. B. E. Read, cited by G. Williams, *Polymer*, **4**, 27 (1963).
30. C. F. Stehling and L. Mandelkern, *J. Polym. Sci. B*, **7**, 255 (1969).
31. N. G. McCrum, *J. Polym. Sci.*, **54**, 561 (1961).
32. R. W. Gray and N. G. McCrum, *J. Polym. Sci. A-2*, **7**, 1329 (1969).
33. J. D. Hoffman, G. Williams, and E. Passaglia, in *Transitions and Relaxations in Polymers* (*J. Polym. Sci. C*, **14**), R. F. Boyer, Ed., Interscience, New York, 1966, p. 173.
34. E. W. Fischer and G. F. Schmidt, *Angew. Chem.*, **1**, 488 (1962).
35. M. Jaffe and B. Wunderlich, *Kolloid-Z. Z. Polym.*, **216–217**, 203 (1967).

Received August 24, 1970

JOURNAL OF POLYMER SCIENCE: PART A-2 VOL. 9, 569-576 (1971)

Photocurrents in Simple Polymer Systems. II

G. McGIBBON, A. J. ROSTRON, and A. SHARPLES, *Inveresk Research International, Musselburgh, Midlothian, Scotland*

Synopsis

Large photocurrents have been observed in films of some simple polymers (containing no π-orbitals), of which poly(vinyl fluoride) is a typical example. Not only are the currents large (up to 10^{-5} A/cm^2) but also they are capable of being excited by light in the visible wavelength region where absorption by the polymer is too low to be detectable. The results indicate that the effects are electronic, rather than ionic, in nature.

INTRODUCTION

It is now well established that relatively high electrical conductivities can be observed in certain classes of polymers. Thus polyacetylene, which is a typical conjugated double-bond polymer, has a conductivity of ca. 10^{-4} ohm^{-1}-cm^{-1}, and the charge transfer complex formed between the poly-1-methyl 2-vinylpyridinium ion and the strong electron acceptor tetracyanoquinodimethane has a similar value[1]. Simple polymers on the other hand, by which is meant uncomplexed polymers with no double bonds in the main chain, are typical insulators, although band structures have been proposed to account for the very small dark currents which can be observed.[2] Polyethylene itself, for example, has a conductivity of 10^{-18} ohm^{-1}-cm^{-1}.

In an earlier paper,[3] however, it was nevertheless shown that significant increases in current can be observed in a wide range of simple polymers, if they are irradiated with ultraviolet light. Typically, polymer films of ca. 50 μ thickness show dark current densities of ca. 10^{-14} A/cm^2 on application of 100 V, which increase to ca. 10^{-10} A/cm^2 in the presence of ultraviolet radiation from a mercury lamp, with intensities of the order of a few mW/cm^2. It was deduced that the conduction process is electronic and that the charge carriers arise from photoemission from the electrodes. With a semitransparent silver electrode, for example, the photoeffect ceases at ca. 340 nm—the photoemissive edge for silver. It is probable that the photoconductivity in vinyl polymers recently reported by Kryszewski et al.[4] can also be accounted for by this mechanism.

In this paper it is shown that a much more restricted range of simple polymers[5] can show even higher photocurrents, (up to ca. 10^{-5} A/cm^2), and that in some cases quite high dark currents can also be observed, arising from charge carriers which are electronic in nature. The results reported are aimed primarily at characterizing these unexpected effects, in broad terms, for a number of polymers. A detailed study of the dependence of the currents on voltage, thickness, light intensity, and wavelength will be discussed in a later paper in relation to possible mechanisms.

EXPERIMENTAL

Sample Preparation

The polymer samples were all studied in film form, with thicknesses generally in the region of 30 μ. The more conducting ionic polymers, which are included for comparison, were in fact generally thicker; but as it has been previously established that the conductivity in these particular materials is ohmic at low field strengths,[6] the effect of thickness can be calculated in order to enable comparisons to be made with the electronically conducting polymers.

The samples and sources are listed in Table I.

TABLE I
Sources of Polymers Used and Method of Film Preparation

Polymer	Source	Film
Poly(vinyl fluoride)	Du Pont Tedlar	Commercial film sample
Viton (a copolymer of hexafluoropropylene and vinylidene fluoride)	Du Pont, Viton C10	Cast from ethyl methyl ketone solution
Poly(vinyl alcohol)	Du Pont, Elvanol	Cast from aqueous solution
Poly(vinyl acetate)	Shawinigan, Gelva V7	Cast from chloroform solution
Nylon 610	ICI Maranyl range	Hot pressed film
Nylon 66	Polymer Consultants Ltd.	Hot pressed film
Poly(ethylene oxide)	Union Carbide Ltd., Polyox WSR 35	Hot pressed film
Poly(trimethylene oxide)	From T. P. Hobin, Ministry of Aviation	Film
Poly(ethylene imine)	BASF U.K. Ltd., Polymin H.S.	Cast from aqueous solution

No attempt was made to eliminate impurities, with the exception of the solvents used to prepare the laboratory-cast films. The presence of residual solvent generally was found to be important in determining dark conductivity, and this of course was particularly true for the case of water in poly(vinyl alcohol). Consequently, solvent was removed by heating *in vacuo*, and its absence was confirmed by the use of differential thermal analysis.

The electrodes in general were formed by evaporating silver onto each side of the polymer to form circular electrodes, 3 cm^2 in area. The light-facing electrode was semitransparent and transmitted 70% of the light at 320 nm (the transmission maximum). None of the polymer films was colored, and the small reduction in transmitted light intensity which did occur was accountable for in terms of reflection and scattering, at least above 250 nm.

Light Sources

The standard sources of light used were as follows. The ultraviolet source was a 125 W MB/U mercury lamp, positioned 13 cm from the film. The overall intensity was 10 mW/cm^2, and since the outer envelope of the lamp was removed, the energy emission ranged from 185 nm to long wavelengths. Light from this source is effective in causing photoemission into vacuum from silver, although only the energy below 340 nm (corresponding to the photoemissive edge) is utilized.

The visible wavelength light source was a 100-W tungsten–iodine lamp, filtered with an OY1 filter to remove all the radiation capable of causing photoemission from silver and with a water cell to remove infrared radiation. The intensity falling on the polymer film was 10 mW/cm^2, and the spectral range of the energy was from 550–4000 nM.

Experiments with the use of thick, nontransparent silver electrodes on the light-facing side established the fact that heating of the films by this radiation was negligible and could not account for the observed photoeffects.

Current Measurements

The currents resulting from the applied voltages (usually 120 V) were determined in a cell similar to that described in a previous paper.[6] All the measurements were made in a vacuum of less than 10^{-3} torr. The measuring instrument was a Vibron 33C electrometer, capable of detecting currents down to 10^{-14} A.

RESULTS

Control Experiments

In previously reported work on photocurrents in simple polymer systems,[3] it was proposed that the source of the charge carriers is the light-facing electrode, which produces electrons by photoemission. This suggests that considerable care should be taken in the preparation of this electrode, if reproducible results are to be obtained.

In this work the light-facing electrode was prepared by evaporation of silver to form a thin, semitransparent film. The reproducibility of the process was established by determining the photoemissive current in the absence of any polymer, from silver deposited on quartz, by irradiating through the quartz with a standard ultraviolet mercury light source. The current was determined *in vacuo* with a brass anode 1.8 mm distant. It was found that by standardizing the conditions in the evaporator, reproducible silver layers could be obtained whose photoemissive currents increased to a maximum with increasing film thickness and then decreased owing to the progressive attenuation of the light by the silver. At the optimum thickness, which was subsequently used as standard, this blank photoemissive current in the absence of a polymer was 10^{-7} A, which corresponds to an efficiency of ca. 10^{-4}. This low value is accounted for partly by the fact that the incident light was only partially absorbed by the silver; and partly because the silver was exposed to the atmosphere during transfer to the conductivity cell and so became partially oxidized. This contamination appeared to occur to a reasonably constant extent, however, as photocurrents could be reproduced to a factor of 2. These currents were obtained of course when the light-facing electrode was negative, and although a voltage of 120 V was normally used, the photoemissive currents were roughly independent of voltage, as would be expected.

When the back electrode was coated with a thick silver layer and irradiated through a semitransparent front electrode, photoemissive currents could also be observed if this back electrode was negatively charged, with current levels about one third lower.

When polyethylene film 25 μ thick was used as a polymer control and coated on one side with thick silver and on the other with a semitransparent layer, a photocurrent was observed on irradiation with the standard ultraviolet light source of 5×10^{-10} A, with -120 V on the light-facing electrode. With the field reversed, the current was 2×10^{-10} A. These results were taken after 100 sec when the photocurrents were approximately constant. The corresponding dark currents under these conditions were ca. 10^{-13} A, although these currents continued to decrease over a period of hours, in a way typical of absorption currents.

These figures were found to be typical of a wide range of polymer films with thicknesses in the 20–50 μ range, including polyethylene, poly(propylene), poly(styrene), poly(ethylene terephthalate), cellulose acetate, poly-4-methylpentene-1, poly(vinyl chloride), and polyvinylpyrrolidione, and support the findings reported in the previous paper.[3]

Dark Currents and Ultraviolet Photocurrents in More Highly Conducting Simple Polymers

The photoeffects for the polymers listed in the previous section, although significant, are not high. In the course of more recent work, higher photocurrents, and in some cases high dark currents, have been observed in a limited number of simple polymers, again with ultraviolet light as the source of stimulating radiation. The results for these and also for some other relevant polymers are given in Table II.

The first six materials in Table II are simple polymers which show much higher photocurrents than those listed in the previous section. Generally these photocurrents are at least two orders higher, and in addition they approach the blank photocurrent of 10^{-7} A arising from photoemission from the electrode.

The observed dark currents were invariably time-dependent, owing in part to contributions from the reversible absorption currents. Steady state currents were eventually observed, however, after $<10^4$ sec in Viton,

TABLE II
Ultraviolet Photocurrents and Dark Currents in a Range of Polymer Films

Polymer	Voltage, V	Thickness, μ	Dark current (after 10^4 sec), A	Photo-current (after 10 sec), A[a]
Poly(vinyl fluoride)	120	29	2.7×10^{-10}	2.3×10^{-8}
Poly(vinyl acetate)	120	28	1.1×10^{-12}	4.1×10^{-8}
Poly(vinyl alcohol)	120	35	1.8×10^{-9}	2.4×10^{-8}
Viton	120	70	1.0×10^{-8}	1.6×10^{-8}
Viton	9.4	70	3.0×10^{-10}	5.8×10^{-9}
Nylon 6.6	120	70	2.8×10^{-10}	4.4×10^{-8}
Nylon 610	120	30	3.0×10^{-10}	1.3×10^{-8}
Poly(ethylene oxide)[b]	9.4	100	3.3×10^{-7}	4.1×10^{-7}
Poly(trimethylene oxide)[b]	120	230	3.5×10^{-7}	4.0×10^{-7}
Poly(ethylene imine)[b]	1.5	60	5.4×10^{-4}	5.4×10^{-4}

[a] Photocurrent is defined as total current in the presence of light.

[b] Ionically conducting polymers.

poly(vinyl fluoride), and poly(vinyl alcohol). The values for these three polymers are at least three orders higher than those observed in typical insulating polymers, and the figure for Viton is particularly high.

One possibility, of course, is that ionic transport is responsible for the conduction process, and for this reason the last three polymers are included for comparison. Poly(ethylene oxide) and poly(trimethylene oxide) have previously been established as ionically conducting polymers,[6] and poly(ethylene imine) shows even larger ionic conductivity. The important point is that large photoeffects are unlikely to occur in polymers whose dark conductivity arises from ionic charge carriers, and these last three polymers can be seen from Table II to show negligible photoeffects. The open-circuit voltages, measured with a high impedance Lindemann electrometer, after applying the field and briefly short-circuiting, were large (>12 V) for the polymers which showed high photoconductivity and small (ca. 1 V) for the three ionically conducting polymers. The high voltages are consistent with electronic space charges and the low voltages typical of those arising from discharge of an electrolytic cell formed by polarization at the electrodes.[6] Consequently, it seemed reasonable to conclude that both the high dark currents and the high photocurrents observed for the first six polymers in Table II involve an electronic transport process.

The explanation which has been proposed[3] to account for the ultraviolet photocurrents in polyethylene and similar low dark-conductivity polymers is that the charge carriers are electrons which arise by unmodified photoemission from the electrode, and that the subsequent velocity of these electrons is limited by their low mobility within the polymer and hence by the resulting space charge. It is implicit in this picture that even if the mobility could be increased, there would be a limit to the current, determined by the rate of photoemission from the electrode. This current is the blank photocurrent in the absence of polymer; and for the conditions so far considered, it has a value of 10^{-7} A, as reported in the previous section.

In an attempt to increase the photocurrents given in Table II, a mercury light source of higher intensity was used in conjunction with an increased voltage of 960 V, and applied to a film of poly(vinyl fluoride), with the normal silver electrodes. The blank current under these conditions was increased to 1.2×10^{-6} A, but the polymer photocurrent was increased disproportionately to 1.2×10^{-5} A, one order greater than that of the blank. From this it is evident that, at least for this particular polymer, the photoeffect must involve a different mechanism from that proposed above. With this indication that an additional part of the energy spectrum of the mercury light source is being used, it was instructive to carry out measurements at wavelengths higher than the photoemissive edge for silver.

Long Wavelength Photocurrents in Simple Polymers

The source of radiation used for these experiments was a compact source filament lamp, filtered to eliminate ultraviolet radiation and peaking at 1200 nm. The intensity was similar to that arising from the normal mercury lamp source used in the previous section. Blank experiments confirmed that no photoemission occurs when silver is irradiated with this source. In addition, none of the polymers of low dark conductivity discussed in the earlier paper[3] and listed in Table I showed significant photocurrents. Several of the polymers given in Table II, however, gave quite large effects, as shown in Table III, and the steady-state photocurrents were at least five orders greater than the transient photocurrents occurring in polyethylene, observed by Tanaka and Inuishi.[7]

TABLE III

Visible Light Photocurrents and Dark Currents in a Range of Polymers

Polymer	Voltage, V	Thickness, μ	Dark current, A	Photo-current, A
Poly(vinyl fluoride)	120	29	2.4×10^{-10}	1.8×10^{-8}
Poly(vinyl acetate)	120	28	1.1×10^{-12}	1.1×10^{-9}
Poly(vinyl alcohol)	120	35	2.0×10^{-9}	1.3×10^{-7}
Viton	120	70	1.0×10^{-8}	1.2×10^{-8}
Viton	9.4	70	3.0×10^{-10}	3.5×10^{-10}
Nylon 66	120	70	2.8×10^{-10}	8.5×10^{-10}
Nylon 610	120	30	3.0×10^{-10}	3.5×10^{-10}
Poly(ethylene oxide)	9.4	100	4.0×10^{-7}	4.4×10^{-7}
Poly(ethylene imine)	1.5	60	5.4×10^{-4}	5.4×10^{-4}

Thus, poly(vinyl fluoride) gave a long-wavelength effect which was similar in magnitude to that observed with ultraviolet radiation, while poly(vinyl alcohol) showed even higher photocurrents. Viton, the polyamides, and the ionically conducting polymers, on the other hand, showed negligible effects. As in the case of the ultraviolet effect, the use of a light source of higher intensity (3×), resulted in even higher photocurrents. Thus poly(vinyl fluoride) at 120 V gave a photocurrent of 1.1×10^{-7} amp.

These visible light effects occur in a region of the spectrum where there is no photoemission from the silver electrode into vacuum, and also where there is no detectable absorption of energy by the polymer itself. For the polymers listed in Table III there is no significant absorption above 250 nm. Significant absorption does occur at the electrodes, but as indicated above this cannot lead to unmodified photoemission.

One feature of this visible light photoeffect is that it was found to be strongly dependent on the physical nature of the contact between the polymer and the electrode. Thus, when a silver coated quartz disk was pressed into light contact with poly(vinyl fluoride), the photocurrent was reduced by two orders compared with that using an evaporated silver electrode. For the ultraviolet photoeffect, on the other hand, the reduction was negligible (Table IV). This can be accounted for if in the latter case the electrons are emitted by the electrode, whereas in the former case they arise either within the polymer or at the polymer–electrode interface.

TABLE IV
Photocurrents in 29 μ Thick Poly(vinyl Fluoride) Film with Pressed and Evaporated Silver Electrodes (-120 V on Front Electrode)

Light source	Electrode	Photocurrent, A
Ultraviolet	Evaporated	5.3×10^{-8}
Visible	Evaporated	2.8×10^{-8}
Ultraviolet	Pressed	1.8×10^{-8}
Visible	Pressed	6.0×10^{-10}

DISCUSSION

It has been established that large photocurrents (up to 10^{-5} A) can be observed in certain simple polymers. Unlike the effects which have been previously reported in a wide range of low conductivity polymers, as exemplified by polyethylene, large, steady-state photocurrents in these exceptional polymers can be excited by visible light radiation and so cannot be accounted for in terms of unmodified photoemission from the electrodes. Whatever the mechanism involved, it is obviously of considerable interest that such high currents can be observed in polymers which do not contain conjugated double bonds, especially in view of the fact that the carriers appear to be electronic rather than ionic in nature. There has not previously been experimental evidence to indicate that high currents can be obtained at room temperature in such polymers.

The detailed facts relevant to mechanism will be discussed in a later paper, but it is of interest to speculate at this stage on the possible origin of the photocurrents which occur in the long-wavelength region and where photon absorption is negligible. In general there would appear to be three possibilities.

(*1*) Impurity donors present at a low concentration may be ionized by the light, and so give rise to charge carriers within the polymer.

(*2*) Photoemission may occur at the electrode, but the effective work function of the metal may be reduced by contact with the polymer.

(*3*) Injection may occur in the dark from electrodes which are effectively ohmic and so give rise to space-charge-limited currents. The effect of light would then be to increase the mobility of the charge carriers, perhaps by a trap-emptying process, and so increase the space charge limited currents which are determined directly by mobility.

No evidence is offered at this stage to favor any one of these possibilities In any case it should be appreciated that the simple classification into two distinct types of polymers is not necessarily justifiable. The polymers studied previously and typified by polyethylene show small dark currents and ultraviolet photocurrents which, although significant, are still small when compared with the blank photoemissive currents from the electrodes in the absence of any polymer. Of the polymers reported in this paper, Viton shows large dark currents but small photoeffects; poly(vinyl fluoride) shows large photocurrents, in both the visible and ultraviolet regions, and significant dark currents; the polyamides show large dark and photocurrents in the ultraviolet region but negligible photoeffects in the visible region; and poly(vinyl acetate) shows large ultraviolet photocurrents but low dark currents. It is thus possible that more than one process is operative, depending upon the nature of the polymer and also on the conditions under which the experiment is operated.

However, whatever the mechanism, the points to be stressed are that unexpectedly high current densities—in the region of 10^{-5} A/cm^2—can be obtained in simple transparent polymers containing no π-orbitals, and that these currents result from the effect of visible or higher wavelengths acting in a region where there is negligible absorption by the polymer itself.

References

1. D. A. Seanor, *Fortschr. Hochpolym. Forsch.*, **4**, 317 (1965).
2. W. L. McCubbin and I. C. Gurney, *J. Chem. Phys.*, **43**, 983 (1965).
3. A. E. Binks, A. G. Campbell, and A. Sharples, *J. Polym. Sci.*, *A-2*, **8**, 529 (1970).
4. M. Kryszewski, A. Szymanski, and A. Wlochowicz, *Macromolecular Chemistry Prague 1965* (*J. Polym. Sci.*, *C*, **16**), O. Wichterle and B. Sedláček, Eds., Interscience, New York, 1968, p. 3921.
5. A. Sharples, A. J. Rostron, and G. McGibbon, Brit. Prov. Pat. Spec., No. 41382/68 (August 1968).
6. A. E. Binks and A. Sharples, *J. Polym. Sci. A-2*, **6**, 407 (1968).
7. T. Tanaka and Y. Inuishi, *Jap. J. Appl. Phys.*, **6**, 1371 (1967).

Received August 4, 1969
Revised September 28, 1970

The *Journal of Polymer Science* publishes results of fundamental research in all areas of high polymer chemistry and physics. The *Journal* is selective in accepting contributions on the basis of merit and originality. It is not intended as a repository for unevaluated data. Preference is given to contributions that offer new or more comprehensive concepts, interpretations, experimental approaches, and results. Part A-1 *Polymer Chemistry* is devoted to studies in general polymer chemistry and physical organic chemistry. Contributions in physics and physical chemistry appear in Part A-2 *Polymer Physics.* Contributions may be submitted as full-length papers or as "Notes." Notes are ordinarily to be considered as complete publications of limited scope.

Three copies of every manuscript are required. They may be submitted directly to the editor: For Part A-1, to C. G. Overberger, Department of Chemistry, University of Michigan, Ann Arbor, Michigan 48104; and for Part A-2, to T. G Fox, Mellon Institute, Pittsburgh, Pennsylvania 15213. Three copies of a short but comprehensive synopsis are required with every paper; no synopsis is needed for notes. Books for review may also be sent to the appropriate editor. Alternatively, manuscripts may be submitted through the Editorial Office, c/o H. Mark, Polytechnic Institute of Brooklyn, 333 Jay Street, Brooklyn, New York 11201. All other correspondence is to be addressed to Periodicals Division, Interscience Publishers, a Division of John Wiley & Sons, Inc., 605 Third Avenue, New York, New York 10016.

Detailed instructions on preparation of manuscripts are given frequently in Parts A-1 and A-2 and may also be obtained from the publisher.

Coming soon from Wiley-Interscience—

The Second Edition of the Most Comprehensive Book in the Field of Polymer Science

TEXTBOOK OF POLYMER SCIENCE
Second Edition

By FRED W. BILLMEYER, JR., *Rensselaer Polytechnic Institute*

In the last 50 years, the field of polymer science has developed into a discipline essential to most aspects of our modern technology. Because this development has been so rapid, it has been difficult for educational systems and texts to keep pace. *Textbook of Polymer Science* was originally published in 1962 to help fill this gap, and this new Second Edition continues to supply up-to-date information on the field.

To up-date the original treatment of the theory and practice of all major phases of polymer science, engineering, and technology, the author has made extensive revisions and additions throughout the entire work.

Part I:
An introduction to concepts and characteristics of macromolecules, Part I now includes material on solubility parameters, free-volume theories of polymer solution thermodynamics, gel-permeation chromatography, vapor-phase osometry, and scanning electron microscopy.

Part II:
The advances gained from new data on the crystalline nature of polymers are now treated in a thorough discussion of the structure and properties of bulk polymers.

Part III:
The format and content of Part III, concerned with polymerization kinetics, have been revised to include recent advances and new references, as well as further data and explanations of recently discovered processes.

Part IV:
The material on commercially important polymers has been rearranged, and now includes information on aromatic heterochain, heterocyclic, ladder, and inorganic polymers.

Part V:
The comprehensive discussion of polymer processing in Part V now includes many new references for plastics, fiber, and elastomer technology.

1971 In Press

wiley

WILEY-INTERSCIENCE
a division of JOHN WILEY & SONS, Inc.
605 Third Avenue, New York, New York 10016
In Canada: 22 Worcester Road, Rexdale, Ontario

- 6 W.A. 25